Studies of Elastic and Inelastic Scattering of 50 MeV. Protons by Zirconium Isotopes

by

D.T.Jones

A thesis submitted to the
Victoria University of
Manchester in support of
an application for the degree
of Doctor of Philosophy.

June, 1970.

(EF90V)

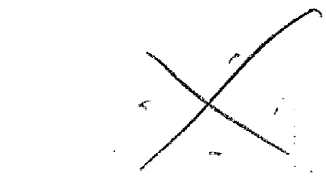

Th28020

Preface

The author holds the degree of B.Sc. with Honours (Physics) conferred by the Victoria University of Manchester in 1965 and the Diploma for Advanced Studies in Science also conferred by this University in 1966.

None of the work described in this thesis has been submitted in support of an application for a degree at this or any other University.

D.T.Jones

June 1970

Abstract

The scattering of polarised and unpolarised 50 MeV. protons by Zr^{90}, Zr^{91}, Zr^{92}, Zr^{94} and Zr^{96} has been studied using an acoustic spark chamber in conjunction with a magnetic spectrometer. The elastic scattering cross-sections and asymmetries have been analysed by an Optical Model parameter search program. A D.W.B.A. analysis of the inelastic scattering was carried out in terms of both the Collective and Shell models of the nucleus. In the former case the value of the deformation parameter for each excited state has been measured, and tentative assignments of the orbital angular momentum transfer made. In the Shell model analysis, a value of the strength of the effective interaction has been found which gave reasonable agreement with the cross-sections of each of the states of the $(g_{9/2})^2$ configuration in Zr^{90}. Possible configurations for many of the other states of this nucleus in the 0 to 5 MeV. range are also discussed.

In addition, an energy level scheme for each isotope has been obtained and compared with previous experiments.

Contents

Chapter 1

A series of experiments to investigate the scattering of 50 MeV. protons has recently been completed by the Manchester University group at the Rutherford High Energy Laboratory. The angular distributions of the cross-sections of elastic and inelastic scattering have been measured for a large number of nuclei ranging from Li^{6} to Pb^{208}. In addition, the asymmetry in the elastic scattering for many of the nuclei has been measured using a polarised proton beam. The analysis of the experimental data is being carried out in terms of both the collective model and the shell model picture of the nucleus.

The work described in this thesis comprises the part of these studies concerned with isotopes of Zirconium. In all, five isotopes have been investigated, namely Zr^{90}, Zr^{91}, Zr^{92}, Zr^{94} and Zr^{96}. The elastic scattering data was analysed in terms of the optical model. The resulting phenomenological potentials were used to generate the elastic scattering wave functions in a Distorted Wave Born Approximation (D.W.B.A.) analysis of the inelastic scattering.

The D.W.B.A. theory expresses the reaction in terms of a transition of the projectile between

elastic scattering states. The transition may be regarded as being caused by an effective interaction whose form will depend on the particular nuclear model under consideration. By using phenomenological wave functions generated by optical potentials known to give a good account of the elastic scattering, any strong absorbtion by the nucleus is automatically taken into account. An allowance is also made for the effects of coulomb repulsion, which may be important for heavy nuclei.

Diffraction effects introduced by the use of distorted waves play a large part in determining the broad features of the angular distributions. However, different optical potentials which gave similar predictions for the elastic scattering gave similar results when used in D.W.B.A. calculations. Hence, within the limitations of the optical model analysis, the elastic scattering uniquely determines the distorted waves, and most of the interest in inelastic scattering studies lies in the investigation of the interaction.

The excitation of a nucleus by the inelastic scattering of a nucleon projectile can involve a number of processes. For instance, the incident

nucleon may interact with a large number of the target nucleons, exciting cooperative modes of motion such as vibrations or rotations. Such excitations may be appropriately described in terms of the collective model. Here, the optical model potential is generalised to include non-spherical terms containing coordinates describing the deformation of the nuclear surface. The expansion of the potential in terms of these coordinates produces a sum of interactions causing transitions between the various nuclear states. For the purposes of the present analysis, only first order or single step interactions were considered. All of the terms of the optical potential were deformed and the interaction was in general complex. The deformations of the spin-orbit potential also introduced the possibility of a spin transfer between the projectile and the nucleus.

Such collective states may also be described by the shell model in terms of a superimposition of a number of hole-particle configurations. Each configuration is considered to be formed by the interaction of the projectile with one of the nucleons in the core, exciting it to vacancies in the higher orbits. These configurations, and

others formed by the transition of nucleons outside the closed shells may also be involved in the excitation of single particle states. In such cases, the shell model picture is more appropriate, although in practice there may be some mixing between the various configurations. The present analysis has been confined to single configurations in both the initial and final states.

In the shell model description of inelastic scattering the interaction of the projectile with the target nucleus is assumed to take place through a sum of two body interactions with the target nucleons. At sufficiently high energies for the impulse approximation to be valid, the effect of the other nucleons on the two particle force may be neglected and the interaction is simply the free nucleon-nucleon scattering potential. At lower energies this potential will be modified by the presence of the other nucleons and the reaction must be described phenomenologically using an "effective" interaction. This has the disadvantage of introducing further parameterisation into the transition amplitude. As this quantity involves the matrix elements of the interaction between single

particle states any deficiencies in the shell model wave functions used to describe these states may be compensated by modifications to the parameters.

The effects of these shortcomings are less serious in a study of Zr^{90}. This nucleus has been the subject of a large number of investigations using a variety of reactions and techniques. It is known to possess a set of excited states which are well described in terms of relatively pure configurations of protons in the outer shells. Since the ambiguity between the single particle wave function and the effective interaction applies principally to the shape of the angular distribution, the relative magnitudes of the cross-sections for the various levels may give some indication of the consistency of the interaction parameters.

Apart from the distorted waves, the factor having most effect on the general shape of the angular distributions is the orbital angular momentum transfer. In the shell model description the allowed values of the transfer for a given configuration are limited by the triangulation rules and the conservation of parity. The number of expected configurations in a given

energy range is also limited. Consequently, a comparison of the number and detailed shapes of the experimental angular distributions corresponding to a given angular momentum transfer with the theoretical predictions may yield some insight into the structure of the corresponding levels.

The distinction between collective and single particle states made in the above discussion is not neccesarily observed experimentally. The 2.18 2^+ MeV. level in Zr^{90} described by the shell model as a $(1g_{9/2})^2$ configuration may be regarded by the collective model as a quadrupole vibration. In practice, the level excited by proton scattering may include contributions both from the simple shell model configuration and from collective excitation of the core. At present the effects of such core polarisation have been taken into account by modifying the strength of the two body interaction potential. It is intended in future analyses to calculate this contribution specifically.

The strength of the single particle configurations may be studied using deuteron stripping reactions. However there are severe limitations on the type of levels which can be

excited in this way. Inelastic scattering of heavier particles may also be used to investigate the structure of the nucleus, and alpha scattering has the advantage that only zero spin and isospin transfer is allowed. In this case, however, the mathematical formulation is more difficult because of the complications introduced by the presence of the additional nucleons.

A similar study to the one described in this work has been carried out into the scattering of 19 MeV. protons by Zirconium (reference 1). At this energy a greater approximation is involved in the use of an effective nucleon-nucleon interaction. On the other hand, core polarisation effects might be lower at lower incident energies. The comparison of the results at 50 MeV. and 19 MeV. should give an indication of the energy dependance of these effects.

The shell model, as discussed above, apart from neglecting core polarisation also fails to take into account the effects of the excitation of particles to continuum states. Both these processes would result in an imaginary term in the effective interaction. Such a term arises naturally in the collective model and also in the impulse approximation. A further important

defect in the description is the neglect of exchange terms in the interaction. These arise from total antisymmetrisation between the incoming particle and the nucleus and from exchange forces. Such terms would result in "knock-on" type reactions with the outgoing nucleon being different from the projectile. Again, it is hoped to consider such effects in future analyses.

All the experimental work described in this thesis was carried out at the Rutherford High Energy Laboratory, Chilton, Berks. The Proton Linear Accelerator was used to supply unpolarised and polarised beams of protons. The scattered protons were momentum analysed by a doubly focussing magnetic spectrometer. The distribution of particles in the focal plane of the spectrometer was determined using an acoustic spark chamber. The overall resolution of the system including the momentum spread of the beam and straggling in the target was better than 80 keV., well below the level spacing of the Zirconium isotopes which was typically about 100 keV. The experimental apparatus and the setting up procedure are described in Chapter 2. The procedure followed during the experiment is described in Chapter 3.

The preliminary analysis of the raw data to obtain absolute quantities, also described in Chapter 3, and the theoretical analysis described in Chapter 6 were carried out using a suite of programs written for the IBM 360/75 computer at the Laboratory. Details of most of these programs may be obtained from the sources indicated in the text. The theory of the optical model is described in Chapter 4 and the D.W.B.A. theory in Chapter 5. The results, conclusions and discussion are presented in Chapter 6.

Chapter 2

The experimental part of this work was carried out using the 50 MeV. beam of the Proton Linear Accelerator at the Rutherford Laboratory, Chilton, Berkshire. The scattering of the protons was analysed by a magnetic spectrometer used in conjunction with an acoustic spark chamber. In this chapter, the characteristics of the accelerator, spectrometer and the particle detection system are described and details are given of the procedure followed in preparing the experimental apparatus for use. The ancilliary equipment used to measure the beam energy and polarisation and to record the total integrated beam current is also described.

Further details of the spark chamber and its associated electronics may be found in reference 3. The rest of the experimental apparatus is described either in reference 2 or in the relevant user guides published by the Laboratory.

Section 2i: The Proton Linear Accelerator

The Proton Linear Accelerator (PLA) consists of three radio-frequency accelerating tanks which may be used in combination to produce proton beams with nominal energies of 10, 30 or

50 MeV. It is not possible to sustain the radio-frequency field continuously on the tanks, because the power dissipation of the system is limited. Consequently the r.f. power is pulsed at repetition rates of either 50 or 25 pulses per second. The proton pulses produced in each case are 200 and 600 μsecs. long, giving respective duty cycles of 1% and 1½%. The phase bunching effect of the accelerating field imposes an additional fine structure on the proton pulses, consisting of 0.3 nsec pulses at a separation of 5 nsecs.

Both unpolarised and polarised proton beams can be produced by the PLA. The unpolarised source can produce mean currents, measured at the output of the machine, of up to 5 μamps. with a 1% duty cycle and 7 μamps. with a 1½% duty cycle. The corresponding mean currents obtained using the Polarised Proton Source (PPS) are only 0.1 namps. and 0.15 namps. However, the beam produced by the PPS is up to 55% polarised. The direction of polarisation is perpendicular to the scattering plane and the orientation of the proton spin may be up or down.

After the beam leaves the final accelerating

tank, it passes through the debuncher. This is a resonant cavity device, to which is applied a r.f. field of the same frequency as the accelerating field. By adjusting the phase angle between the device and the accelerator, the debuncher may be used to reduce the energy spread of the beam at the expense of its spatial distribution. The energy spread of the beam measured at the target without the debuncher is typically about 270 keV. With the debuncher in operation, this can be reduced to below 80 keV.

The Spectrometer Beam Line

After leaving the debuncher, the beam enters the spectrometer beam line. The transport of the beam through the flight tubes is effected by a system of seven quadrupole lenses and a bending magnet. A diagram illustrating the arrangement of the beam line is shown in figure 2.1. Two pairs of slits, one pair before the bending magnet and the other pair after it, define the profile of the beam in the horizontal and vertical planes. The slits are used in conjunction with the bending magnet to restrict the range of momenta transmitted through the beam line.

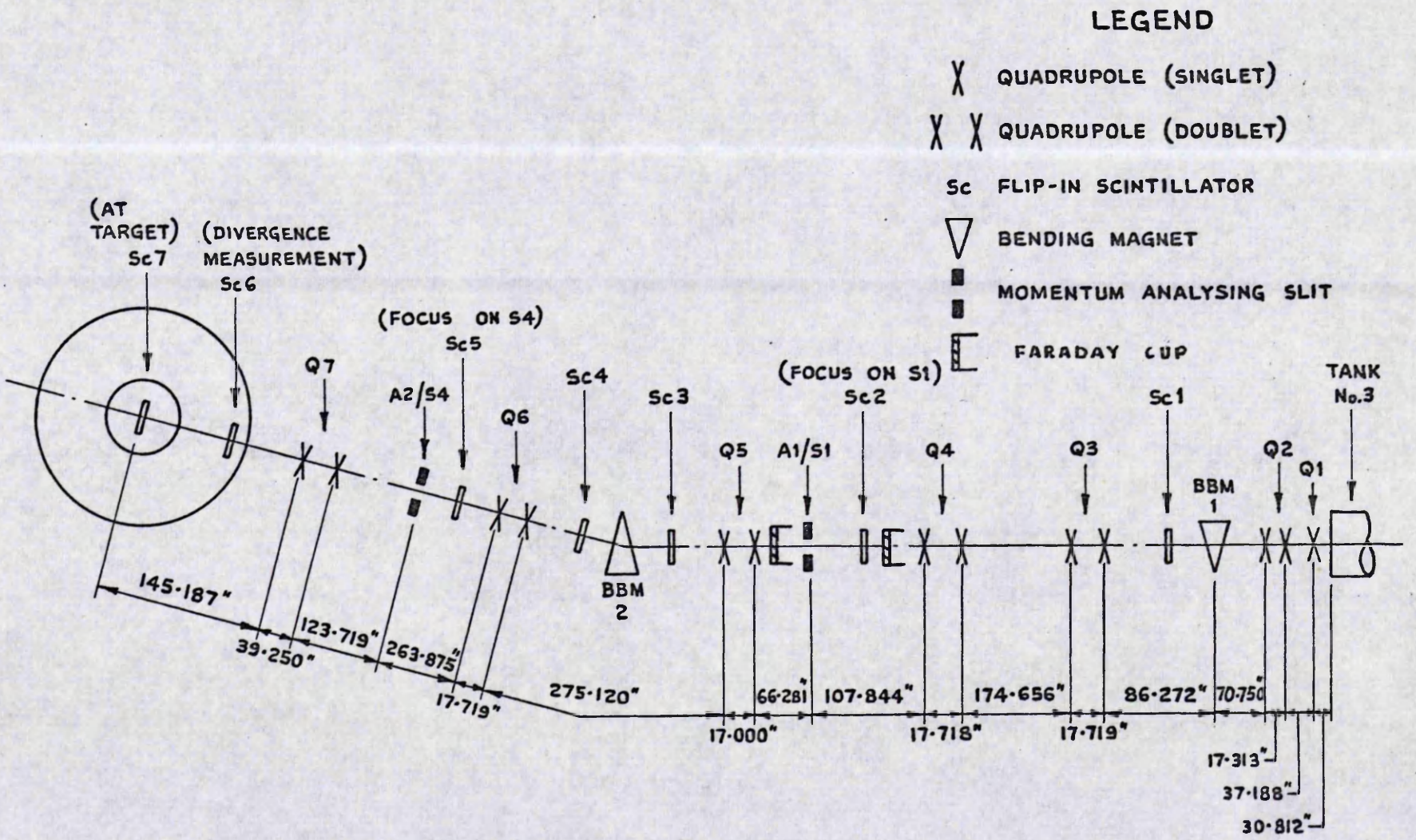

Figure 2.1 The Spectrometer Beam Line

Some of the quadrupole lenses are made up of doublet pairs, to give focussing in both the vertical and horizontal planes. In addition, quadrupoles Q4, Q6, Q7 and Q8 are wound in such a way that they can be used to steer the beam. Similar steering quadrupoles are also mounted within the third accelerating tank of the machine, on drift tubes 19 and 26. The system is used to obtain a well focused beam spot, centrally placed on the target. The profile and energy spread of the beam at the target depends mainly on the dimensions of the slits used. An improvement in the resolution of the beam can generally be obtained only at the expense of beam intensity, particularly if the debuncher is not in operation.

To assist in the setting up procedure, the beam line is equipped with a set of retractable scintillators placed at convenient positions. The profile of the beam on each scintillator is viewed by a closed circuit television camera and relayed to the counting room.

Setting up the Spectrometer Beam Line

The currents in the quadrupoles and the bending magnet were set up to give the optimum transmission using the following procedure.

The current in each quadrupole was first set to an approximate value obtained from a previous experiment. The "flip-in" scintillators were then used to examine the profile of the beam along the flight tube. Starting from the accelerator end of the beam line, the quadrupole and bending magnet currents were systematically adjusted to obtain the expected shape and position of the beam on each scintillator. The profile and alignment of the beam spot on the target were observed on a scintillator placed in the target position.

The next stage was the optimisation of the transmission. The currents in Q1, Q2 and the drift tube quadrupoles were adjusted until the maximum intensity was obtained on a Faraday cup placed before the bending magnet. The transmission through the rest of the flight tube was optimised by systematically varying the currents in the remaining quadrupoles. The current passing through the target was monitored by a Faraday cup in the scattering chamber. Finally, the steering quadrupoles were used, if neccesary, to position the beam centrally on the target.

The result of badly set up beam transport

is usually the collision of the beam with the structure of the flight tubes or the accelerator. This not only causes a high background radiation but also produces a flux of neutrons which interferes with the scintillation detectors (see section 2v). Throughout the optimisation process, therefore, care was taken to ensure the radiation levels in the vicinity of the accelerator remained within tolerable limits. As a final check, the spectrum of particles in the focal plane of the spectrometer was recorded, using scattering by a suitable target. This spectrum was examined to see if the required resolution had been obtained and to check that the background was at a reasonable level.

The transmission efficiency is defined as the fraction of the beam, measured at the end of the third accelerating tank, which passes through the target. A typical value of the efficiency obtained by the above procedure was about 2%, with the appropriate momentum slits and with the debuncher in operation. Under these conditions, the resolution of the beam on the target was 50 keV. With no momentum slits, a transmission of 5% at 70 keV. resolution was obtained.

Section 2ii: The Beam Energy Monitor

The absolute energy of the beam was measured using the Beam Energy Monitor. The mechanical arrangement of the Monitor is shown in figure 2.2. The beam passes through two degrading systems and enters the double ion chamber. The parallel sided degrader is used to reduce the energy of the beam from 50 MeV. to 30 MeV. The amount of energy lost by the beam in the double wedge system however, depends on the relative positions of the wedges. Thus, by altering the position of the retractable wedge, it is possible to change the energy of the particles entering the ion chambers.

The double ion chamber consists of three parallel electrodes perpendicular to the beam. Both sections of the chamber are filled with air at atmospheric pressure. The thickness of the first section is 5/7ths of the thickness of the second. Potentials of 1.0 kV. and -1.4 kV. are applied to the first and third electrodes respectively, so that there is the same potential gradient in each section.

At a certain beam energy, the amount of ionisation in each section is the same, and the output current from the centre electrode is zero.

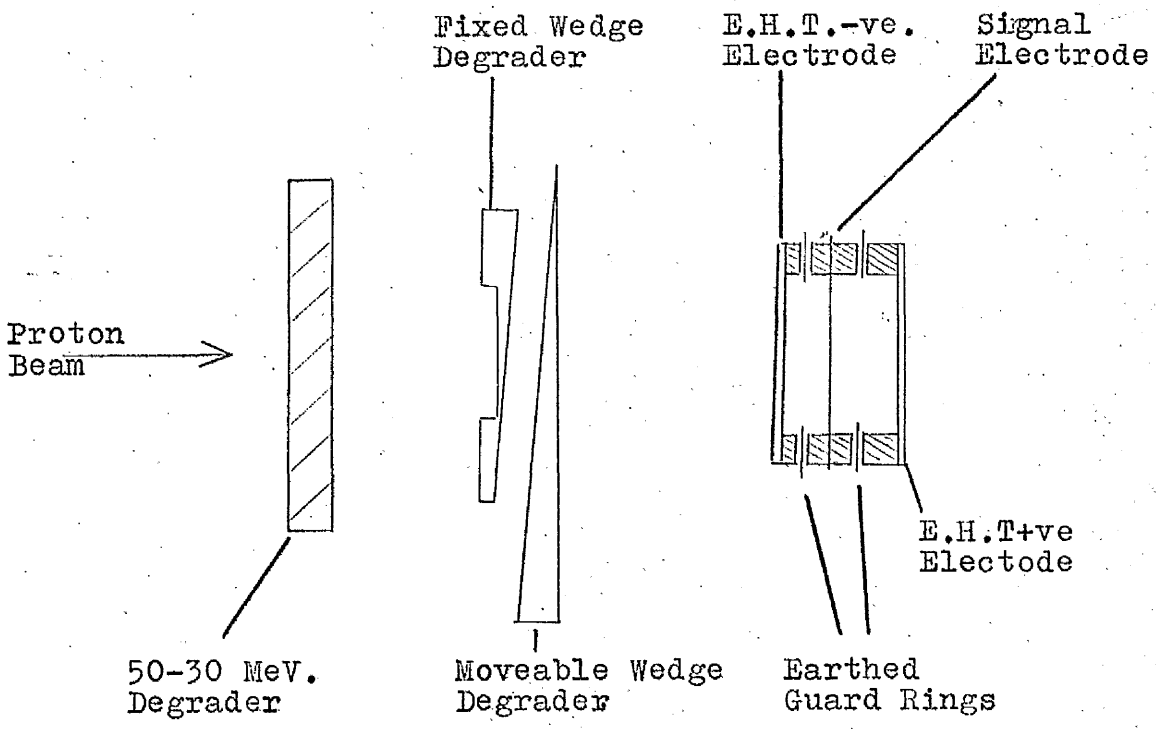

Figure 2.2 Schematic Lay-out of the Beam Energy Monitor

If the beam energy is higher than this critical value, more protons penetrate to the second chamber, giving a negative output current. Conversely, lower energy protons give rise to a positive current.

A set of tables, relating the wedge position and the energy of the particles entering the monitor has been compiled using a time of flight method. The procedure for using the monitor therefore was to adjust the wedge position until the current on the central electrode of the ion chamber was zero. The incident beam energy was then obtained from the table.

Section 2iii: The Double Focussing Spectrometer

The magnetic spectrometer used to analyse the scattered protons has a field index $n = \frac{1}{2}$. It is doubly focussing so that monochromatic particles from a point source are focused at a point and not in a line. At a given field setting the foci of particles of differing energies lie in a plane inclined to the vertical at an angle depending on the magnetic rigidity of the particles. For the 50 MeV. protons studied in this experiment, the focal plane is inclined at 57° to the vertical. A special evacuated vessel is used to attach particle detection systems to the spectrometer.

The aperture of the vessel lies in the focal plane and is sealed with a thin mylar foil. Brackets are provided so that particle detection devices can be mounted so that they lie in the focal plane.

The trajectories of the particles which pass through the aperture have a mean radius of 40 inches. The median line representing the mean trajectory extends horizontally to bisect the focal plane. The centre of the focal plane is marked to facilitate the correct alignment of detection systems placed in it. The aperture is 50 cm. long, allowing a momentum range of 15% of the median momentum to be detected at a given field setting. For protons at 50 MeV. this corresponds to a range of 5 MeV.

The magnet is attached to its scattering chamber by a sliding foil arrangement which allows the magnet to be rotated through 120° while maintaining a vacuum in the scattering chamber and in the spectrometer. However, there are four entrance ports to the scattering chamber at 60° intervals, which extend the angular range in the scattering plane to 150° to -150° to the beam. The spectrometer is illustrated in plate 1.

The entrance aperture to the magnet is

Plate 1. A General View of the Doubly-focussing Spectrometer.

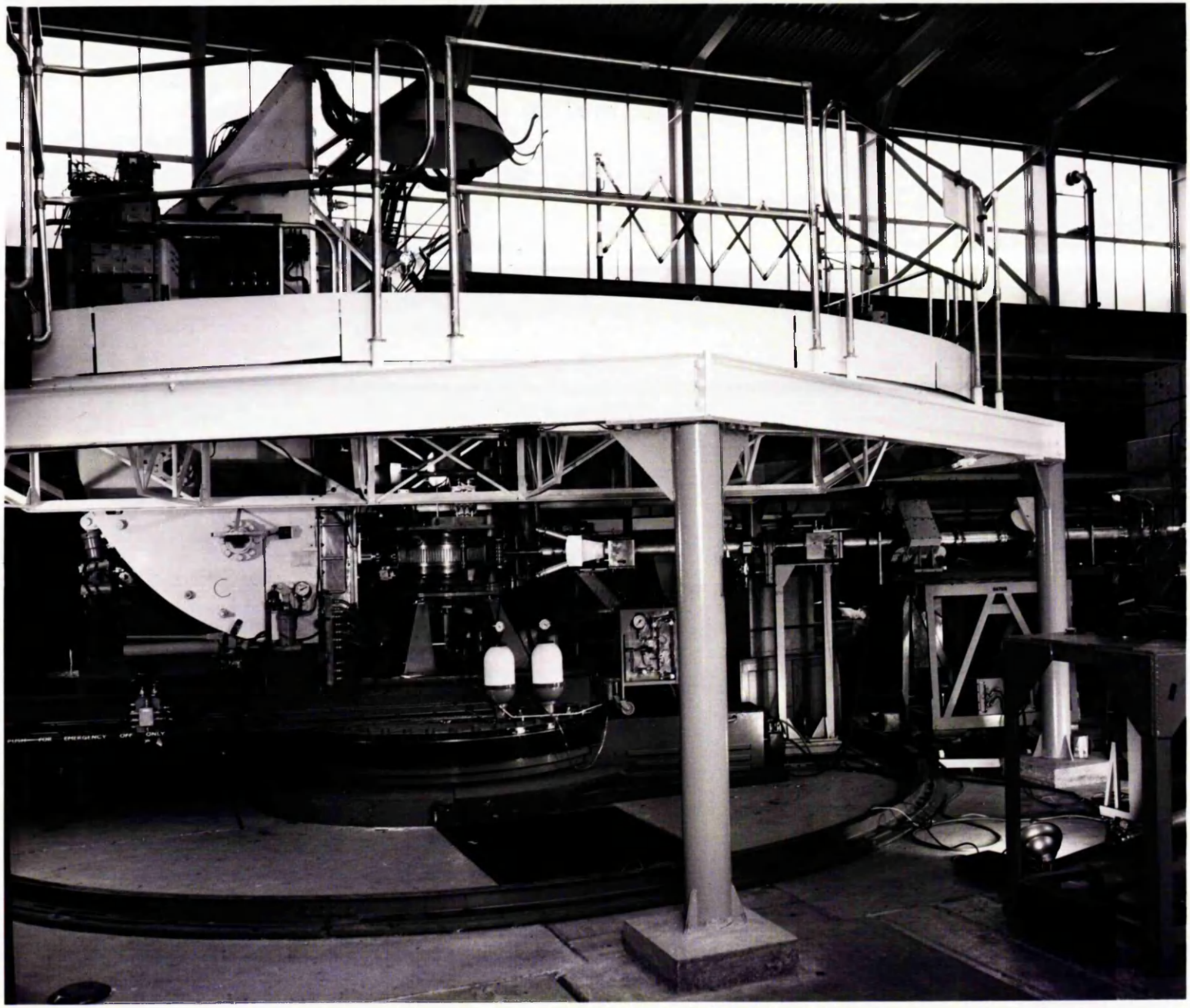
EMERGENCY OFF ONLY

defined by a detachable vertical slit. The solid angle defined by the slit at the centre of the target was calculated from its dimensions and its distance from the centre of the target. The slit used for all the experiments performed in this work was a rectangle 0.411 inches wide by 2.47 inches high and was 23.71 inches from the centre of the target. These dimensions correspond to a solid angle of 1.805 millisteradians.

The scattering chamber has provision for the mounting of targets in special cassettes. The targets are bolted to a semicircular vane which can be rotated out of the cassette and located positively into position by remote control. Up to eleven targets at a time can be mounted in a cassette, and a given target selected without entering the experimental area. The cassettes, which may be sealed, were filled with an inert gas to protect the targets from contamination by the atmosphere.

The field in the spectrometer is indicated by the Hall voltage measured across a plate suspended in the spectrometer gap. The plate is maintained at a uniform temperature by a specially designed oven. Although the Hall

plate voltage gives an absolute indication of the field at one point in the magnet, the variation of the field over the pole pieces depends on the magnetic history of the spectrometer. To ensure consistent results from the spectrometer, a given field setting was always obtained by changing the magnet current in the same direction.

The actual energy spread, or aberration, observed in the focal plane of the spectrometer is the aggregate of several contributions. The first of these, the energy spread of the beam, is discussed in section 2i. A typical value is 50 keV. at 50 MeV. The other important contribution is linearly dependant on the height of the target beam spot. The spectrometer acts as a lens with a magnification of almost unity. The image of a 2 mm. high beam spot will consequently be about 2 mm. long in the focal plane. As the dispersion of the spectrometer is 4 cm. for 1% change in momentum, this corresponds to 50 keV. aberration in energy. Other contributions are due to second order effects, and for 50 MeV. protons amount to less than 0.03% of momentum. The total aberration is found by adding these contributions in quadrature. The overall

aberration obtained, using the above figures, is 75 keV. which is close to the experimentally observed aberration of 80 keV.

Section 2iv: The Charge Monitoring System

The charge passing through the target is collected by a Faraday cup mounted in the scattering chamber behind the target. The collision of the beam with the target causes the emission of electrons. These, together with any which come down the beam pipe, are repelled from the Faraday cup by a negative potential applied to a guard ring electrode. The guard ring also prevents the emission of secondary electrons caused by the beam colliding with the cup.

The resulting current from the Faraday cup is fed into an amplifier. The amplified current is integrated by a specially designed unit (Harwell 3008 Integrating Amplifier) which registers every time a given amount of charge has been collected. There are seven ranges of amplification for maximum currents of between 10^{-11} and 10^{-5} amps. These are used in conjunction with 5 integration ranges of between 10^{-9} and 10^{-5} coulombs per cycle.

The integration ranges are nominal and

require calibration before absolute cross-sections can be calculated. A precision current source capable of producing a range of currents between 8×10^{-6} amps 8×10^{-11} amps was used to supply current to the amplifier input. The operation of the source was checked by a null method using a sensitive galvanometer, before it was used.

A correction factor C was calculated for each range from the time taken to record a nominal amount of charge Q with a source current I. Then,

$$C = \frac{IT}{Q} = \frac{IT}{NR} \qquad 2.1$$

where N is the number of cycles and R the number of coulombs/cycle.

The operation of the integrator was such that every time it completed a cycle, a dead time of 100 μseconds is imposed on the charge collection system. At count rates below 1 cycle per second, the resulting correction is less than 0.01% and may be negligible. During the experiment the integrator was generally used at rates lower than, or close to, 1 cycle per second. Similar count rates were therefore maintained during the calibration process.

The 8×10^{-6} amps and 8×10^{-7} amps ranges

of the current source were more accurate than the lower ranges. The higher ranges however, could not be used to calibrate the lowest ranges of the integrator as this would result in high count rates requiring a dead time correction. The following procedure was adopted to obtain the corrections to the lower current ranges of the source.

The integrator was set to the 10^{-6} coulombs per cycle range. A current of 8×10^{-7} amps was supplied to the amplifier input, and the time for 1000 cycles was recorded. The procedure was then repeated for 100 cycles at 8×10^{-8} amps. The true current for the 8×10^{-8} amps range could then be obtained by comparing the two readings. This procedure of cross calibration was used to obtain correction factors for all the integrator ranges.

The beam intensity obtained from the Polarised Proton Source is too low to be monitored by the above method. An ion chamber was therefore used in place of the Faraday cup to provide an amplification factor of approximately 400. The chamber used consists in fact of two "split" ion chambers placed in tandem. Each split ion chamber consists of three equally

spaced parallel electrodes, the electrodes of the front chamber being in the horizontal plane, those of the rear chamber being in the vertical plane. The axis of the beam lies in the plane of each of the central electrodes. Equal voltages are applied to the outer electrode. If both voltages have the same polarity, and are set at a level below the saturation voltage of the ion chamber, the current drawn from the central electrode varies linearly with the total number of charged particles entering the ion chamber. If, on the other hand, the voltages have opposite polarity, the current depends on the difference in the numbers of protons entering the opposing halves of the ion chamber. Thus, a centrally placed beam will give zero output current. In this mode, the ion chamber can be used to indicate the position of the beam on the target. This was useful because at these low intensities it was often difficult to observe the beam spot on the target scintillator.

During the polarisation experiments carried out in this work, the horizontal ion chamber was used to monitor the total charge. The integrator system described above was used to integrate the output current. The vertical ion chamber was used

in a position sensitive mode, to indicate the horizontal position of the beam. Its output current was recorded on a chart recorder as a check that the beam transport was stable , and independant of the direction of polarisation.

Section 2v: The Polarimeter

The polarisation of the beam produced by the Polarised Proton Source was measured with the Polarimeter. This device uses the elastic scattering of 15.7 MeV. protons by carbon to measure the polarisation. A sheet of high density graphite is used to degrade the beam from 50 to 15.7 MeV. The protons scattered from a carbon target are detected in the horizontal and vertical planes by four symmetrically mounted scintillation detectors. Each detector subtends an angle of 46.6° to the beam. Both the target and degrader were mounted on wheels rotating on a common shaft. The wheels were mounted in such a way that, as they rotated the degrader and target were struck by only one in ten of the proton pulses from the accelerator.

The scintillation detector pulses are discriminated so that only the elastic scattering pulses were recorded. When the beam is polarised in the vertical plane there is an asymmetry in the

number of protons detected in the left hand and right hand detectors. The numbers of pulses detected by the upper and lower detectors are the same. If L_+ and R_+ are the number of left hand and right hand protons for proton spin up, and L_- and R_- the corresponding values for spin down, the beam polarisation P_S is given by

$$\frac{L_+ R_-}{L_- R_+} = \frac{(1 + P_B P_S)^2}{(1 - P_B P_S)^2} = \left[\frac{1 + \epsilon}{1 - \epsilon}\right]^2 = \alpha \qquad 2.2$$

so that

$$P_B P_S = \frac{\alpha^{\frac{1}{2}} - 1}{\alpha^{\frac{1}{2}} + 1} \qquad 2.3$$

where P_B is the analysing power of the polarimeter. A table of values of $P_B P_S$ for a range of values of α is given in reference 4. Equations 2.2 and 2.3 only hold if the angles of the detectors are correctly set, and if the spin up polarisation equals the spin down polarisation. Care was also taken in setting up the discriminator levels on the scintillation detectors.

The analysing power P_B of the Polarimeter was calculated using the Birmingham Polarimeter, which used double proton scattering at 15.7 MeV. A correction to this value was obtained with the use of a helium gas polarimeter for 10 MeV. protons

at a laboratory scattering angle of 116.5°. The value obtained for the analysing power was 0.574.

Section 2vi: The Particle Detection System

The total number of particles entering the focal plane of the spectrometer was recorded by the scintillation detector system. The output pulses from the detectors were used to trigger an acoustic spark chamber which gave the distribution of the particles in the focal plane.

The Scintillation Detectors

The arrangement of the scintillation detector assembly is illustrated by figure 2.3 and plate 2. Each of the two vertical scintillators is viewed by two photomultipliers, and the outputs are added. The height of the resultant pulse is proportional to the energy loss of the particle in the scintillator. Deuterons and heavier particles lose a greater proportion of their energy in the first (E_1) scintillator, and consequently give rise to higher output pulses. This enables the two detector arrangement to be used as a particle identification system.

The electronic circuitry of the system is shown in figure 2.4. Both the E_1 and E_2 outputs are first amplified, then discriminated against

Plate 2. The Focal Plane Particle Detection System and Associated Electronics.

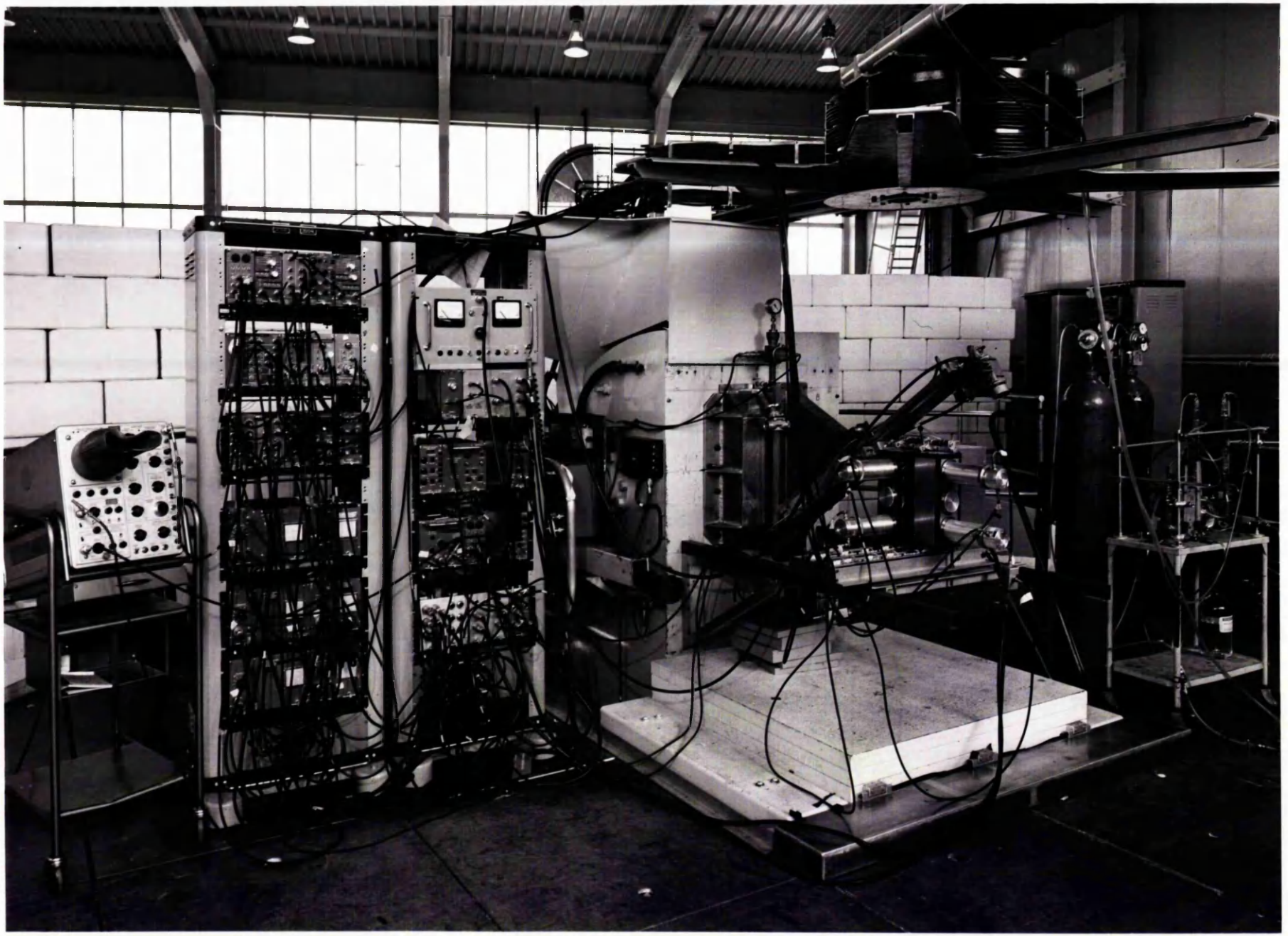

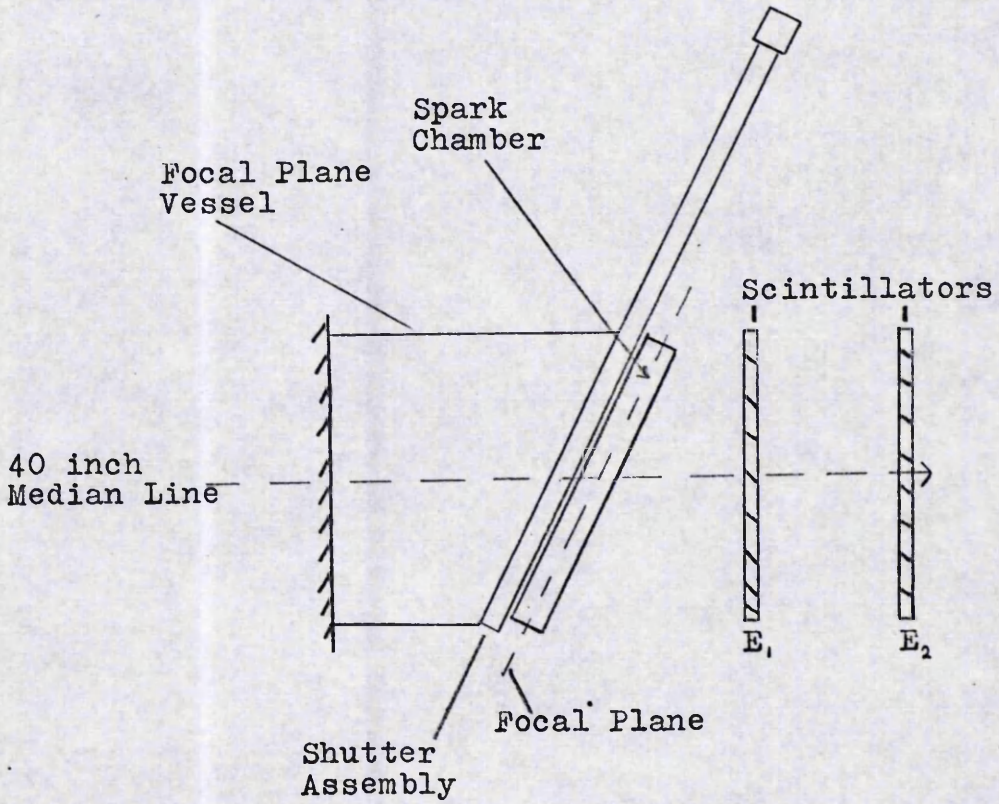

Figure 2.3 Arrangement of the Spark Chamber and Scintillation Detectors.

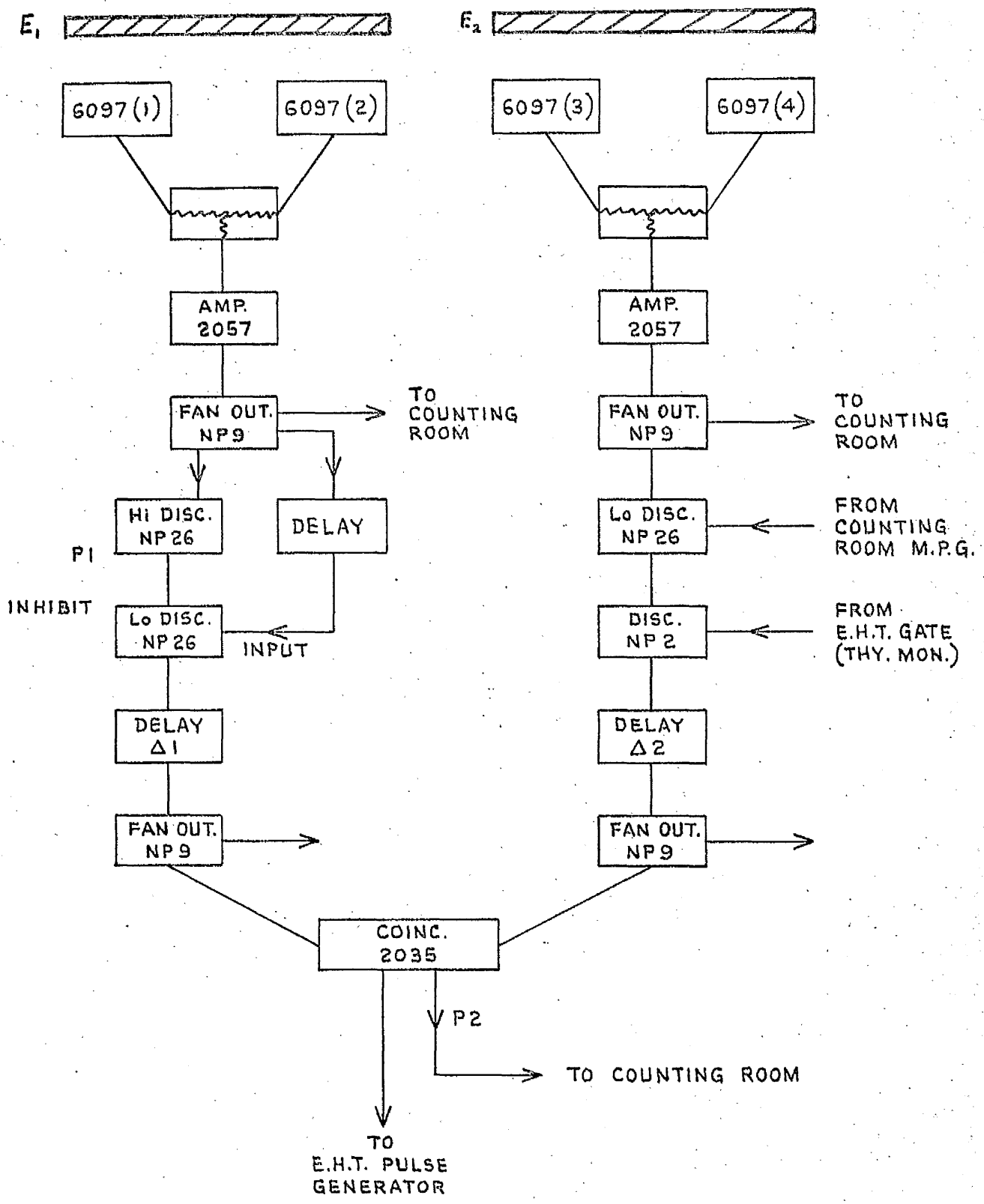

Figure 2.4 The Particle Identification Electronics

the low amplitude noise background. The E_1 pulses are further analysed by an upper limiting arrangement of two discriminators, (see reference 3), to eliminate pulses from heavier particles.

Coincidences are taken between the analysed outputs of the E_1 and E_2 detectors. The coincidence output pulses therefore, almost entirely correspond to genuine proton events. If the number of E_1 and E_2 pulses is high, however, there is a possibility of a coincidence between two different events occuring within the resolving time of the coincidence system. An estimate of the number of these accidental events is obtained by introducing a relative delay between the E_1 and E_2 pulses so that they were no longer in coincidence, and recording the number of coincidences so obtained.

Setting Up

The first stage of setting up the scintillation detection system was to adjust the E.H.T. bias on the respective photomultiplier tubes of each detector to ensure that the pulse height of a particle of given energy was the same whatever its position in the focal plane. A suitable target was selected and the spark chamber was used to position the elastic scattering peak near one end of the focal plane. A pulse height spectrum of the undiscriminated

summed output of one pair of photomultipliers was recorded in a Laben Pulse Height Analyser, (P.H.A.). The spectrometer field was adjusted so that the elastic peak was near the other end of the focal plane. A second spectrum was then accumulated in a different section of the P.H.A. memory.The positions of the proton peaks in the spectra were compared. If there was significant disparity between the peak positions, the E.H.T. bias on the photomultiplier viewing the corresponding section of the scintillator was adjusted. This process was continued until the peak positions did coincide, indicating that the pulse height was uniform along the scintillator. Finally the elastic peak was swept across the focal plane, and the pulse height compared at each position. A variation of less than 10% in the pulse height with position was obtained.

The next step was to set the bias on the discriminators to ensure that all the protons are detected, with noise and other particles eliminated as much as possible. The elastic scattering peak was placed centrally in the focal plane, and an analogue spectrum recorded on the pulse height analyser. In this case the analyser was used in its "coincident" mode. The required external

gating pulses were obtained from the discriminator output from the corresponding detector. Consequently, all the events appearing in the spectrum corresponded to discriminator pulses. A typical spectrum is given in figure 2.5. The "low" discriminator bias was then increased until most of the noise was cut off. Similarly, for the E_1 detector the high amplitude discriminator bias was reduced until the deuteron and heavy particle peaks in the spectrum had disappeared. However, neither bias level was set so that it cut off any part of the proton peak. An alternative method of obtaining the correct bias was by drawing integral-bias curves. The total number of analysed pulses for a given amount of beam charge was measured for a series of increasing values of the discriminator bias. These numbers were plotted against the discriminator bias voltages. A typical integral-bias curve is shown in figure 2.6. The discriminator bias level was then set at the value at the centre of the plateau.

Finally, the coincidence and accidental coincidence circuits were set up. A relative delay was introduced between the E_1 and E_2 pulses and the number of coincidences obtained for a given number of Faraday cup cycles was measured. The length of the delay was changed and the measurement

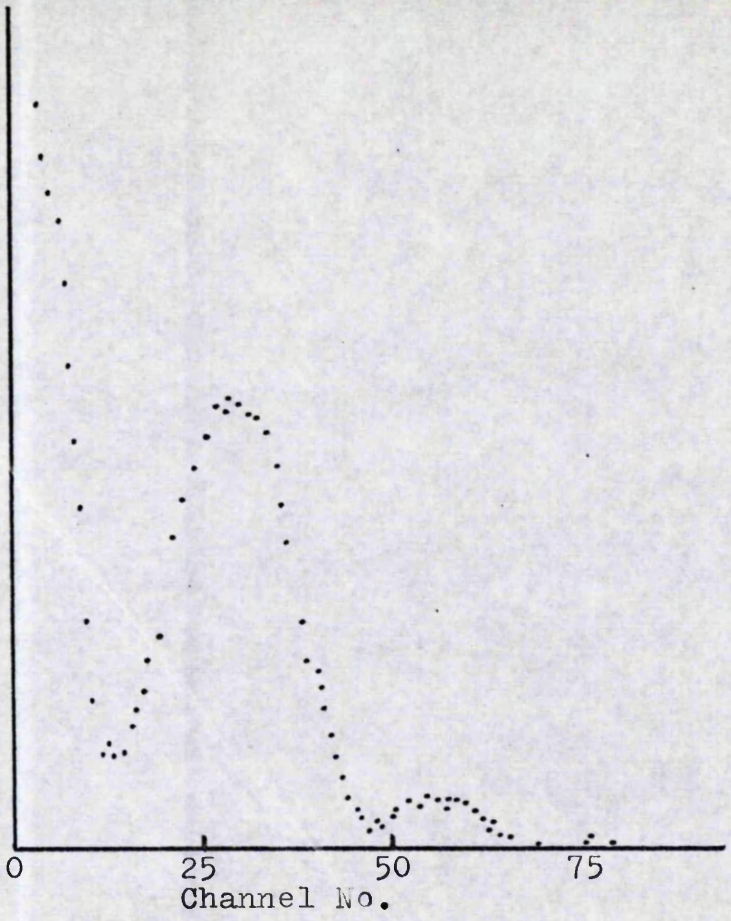

Figure 2.5 A Typical E_1 Spectrum.

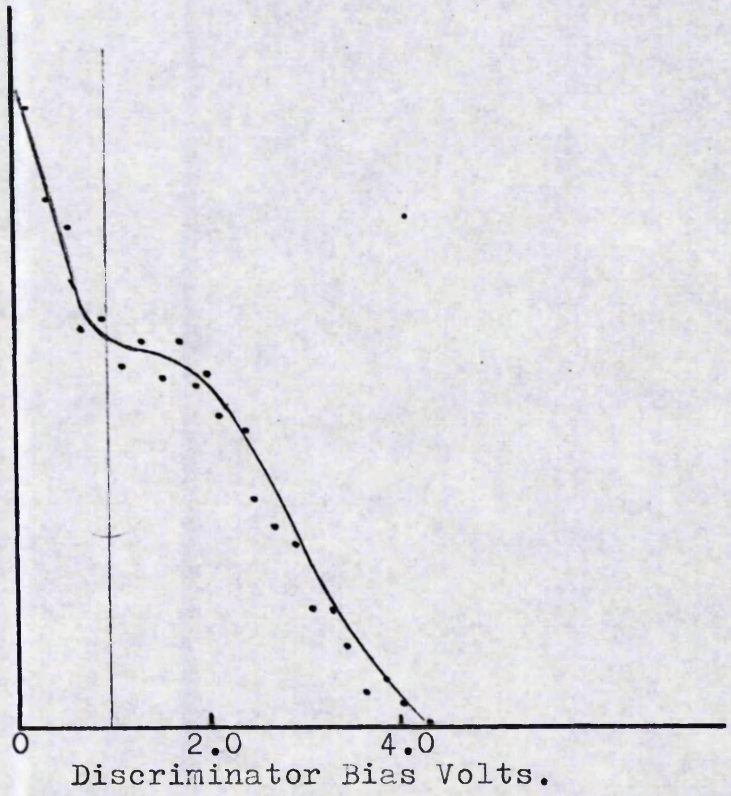

Figure 2.6 A Typical Integral-bias Curve.

repeated. A graph was drawn between relative delay and coincident rate. It has the form of figure 2.7. The coincidence delay was set at the midpoint value of the plateau. The accidental coincidence delay was set at a value well away from the plateau.

The Spark Chamber

Details of the construction of the spark chamber and associated components are given in reference 3. This reference also gives a more detailed description of the working of the spark chamber electronics.

The spark chamber is attached to the focal plane vessel of the spectrometer so that it lies in the focal plane. Its ionisation characteristics are improved by passing a mixture of Argon and Ethanol vapour through it. When a particle enters the spark chamber and an E.H.T. potential is applied, it breaks down along the ionisation trail of the particle causing a spark. A low constant potential is applied to the spark chamber. This serves to clear away the ionisation caused by the spark and also sweeps away most, but not all, of the ionisation caused by an incoming particle. This tends to locate the resulting spark more precisely to the position of the incoming particle.

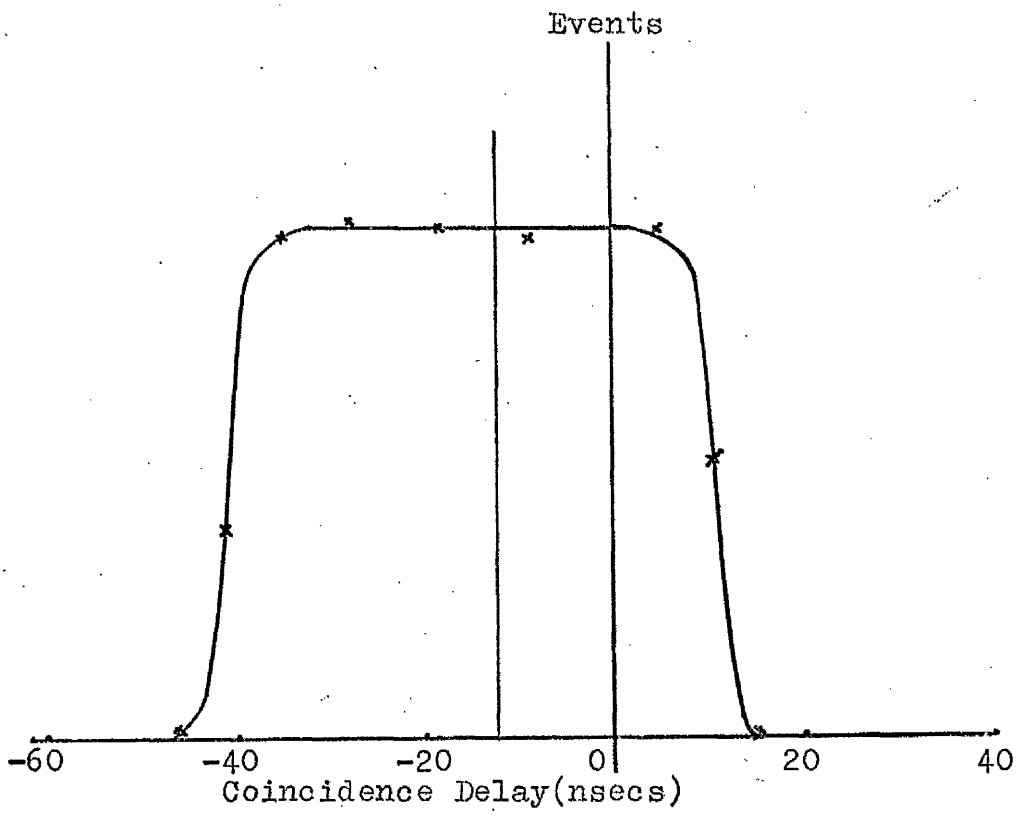

Figure 2.7 Coincidence Delay Curve.

to the position of the incoming particle.

The coincidence pulses are used to generate "start" pulses. The start circuitry (see figure 2.8) also applied the E.H.T. to the spark chamber after a delay of 400 nsecs. The resulting spark generates a 100 kilocycle sound wave which is detected by a microphone at one end of the spark chamber. The interval between the "start" pulse and the subsequent detection of the acoustic signal may be as great as 1.8 msecs., much longer than the beam pulses from the accelerator. Therefore the start circuit is self inhibiting for 5 msecs. to prevent particles detected during the remainder of the beam pulse from triggering the spark chamber. The start circuit also generates a 1 μsec. pulse which inhibits the E.H.T. pickup in the scintillator detector amplifiers and a 5 μsec. pulse which inhibits both electrostatic pickup by the microphone, and the signal caused by the mechanical transmission of the noise of the spark by the spark chamber structure.

The output from the microphone is discriminated to provide a "stop" pulse. However, each negative going edge of the acoustic signal gives an output from the discriminator. A single stop pulse is obtained by inhibiting subsequent pulses with a

3 msecs. pulse generated by the first pulse.

Under the application of the E.H.T. sparks occur along all the ionisation trails in the spark chamber. Consequently, more than one spark may be generated if a particle enters the spark chamber in the interval between the initial event and the application of the E.H.T. Only the event nearest to the microphone will be detected, so that the resultant spectrum will be distorted towards the microphone end. The same effect occurs if particles normally eliminated by the particle detection system enter the spark chamber just before the initial proton. In this case insufficient time can elapse for the clearing field to eliminate the trail of the first particle before the E.H.T. is applied. The effects are minimised by "vetoing" such events. The output from the E_1 detector is split by means of a fan-out amplifier. One output is used in the coincidence circuit, the other is separately discriminated to give a "veto" pulse for any particle entering the system. The "veto", "stop" and "start" pulses are fed into a special unit. If a veto pulse occurs within the period from 1 μ sec. before to 1 μ sec. after the initial event, the stop pulse is inhibited. Each such event is recorded by a "lost"

scaler. The ionisation from particles which occur more than 1 second before the initial event is swept away by the clearing field before the E.H.T. is applied. The method described below was used to set the clearing field bias so that this condition was always satisfied.

The start and stop pulses are fed into the Laben T.V. 45 time of flight unit. Each event is stored in a channel whose number depends linearly on the interval between the start and stop pulse. This quantity depends linearly on the position of the detected particle. Thus a spectrum of "number of events" versus position is obtained. The position of a particle depends on its momentum, which over this range of energy varies almost linearly with energy. The P.H.A. spectrum can therefore be regarded as an energy spectrum. Further discussion on this point is given in Chapter 3.

There are dead areas at both ends of the spark chamber. The dead area at the microphone end is partly caused by the 5 μsecs. inhibit, and partly by the distortion caused by the shock wave from the spark at small distances. It is shielded by a brass shutter. At the other end, the microphone pulses may be so attenuated

they are unable to fire the discriminator. A moveable brass shutter sliding in the plane end of the spark chamber is provided. Its position is registered by a counter and is therefore reproduceable. It may be used to reduce the spark chamber to any required length.

Most of the relevant quantities are recorded on scalers, a list is given in table 2.1.

Setting up the Spark Chamber

In order to reduce the interval between the detection of a particle and the subsequent firing of the spark chamber, the scintillation detector coincidence circuitry (figure 2.4) and the pulser circuit (figure 2.8) were placed adjacent to the spark chamber within the experimental area. The discriminator bias levels and the coincidence delays were remotely controlled from the counting room, and were set up using the proton beam. Because of the high radiation levels in the experimental area the remainder of the electronics was set up using an intense, well collimated beta source to provide a stream of ionising particles.

Using the source, the discriminator bias levels were set to give a reasonable number of coincidences and the timing and lengths of the

Scaler No.	
1.	Scaler Simulator Unit*
2.	
3.	
4.	Accelerator Proton Pulses.
5.	Charge Integrator Cycles.
6.	E_1 Singles Total.
7.	E_2 Singles Total.
8.	Coincidences.("T+A")
9.	Accidental Coincidences.("A")
10.	Start Pulses.("START")
11.	Stop Pulses.("STOP")
12.	Pulses Entered In the PHA. Memory.("ADD 1")
13.	Number of Vetoed "STOP" pulses.("LOST")
14.	E_1 Analogue Pulses.
15.	E_2 Analogue Pulses.

*The Scaler Simulator behaved like three pseudo-scalers, allowing three preset 6 digit numbers to be printed out at the same time as the other scalars. It was used to maintain a record of quantities such as Target mass, Run number and Spectrometer angle.

Table 2.1 List of Scaled Quantities.

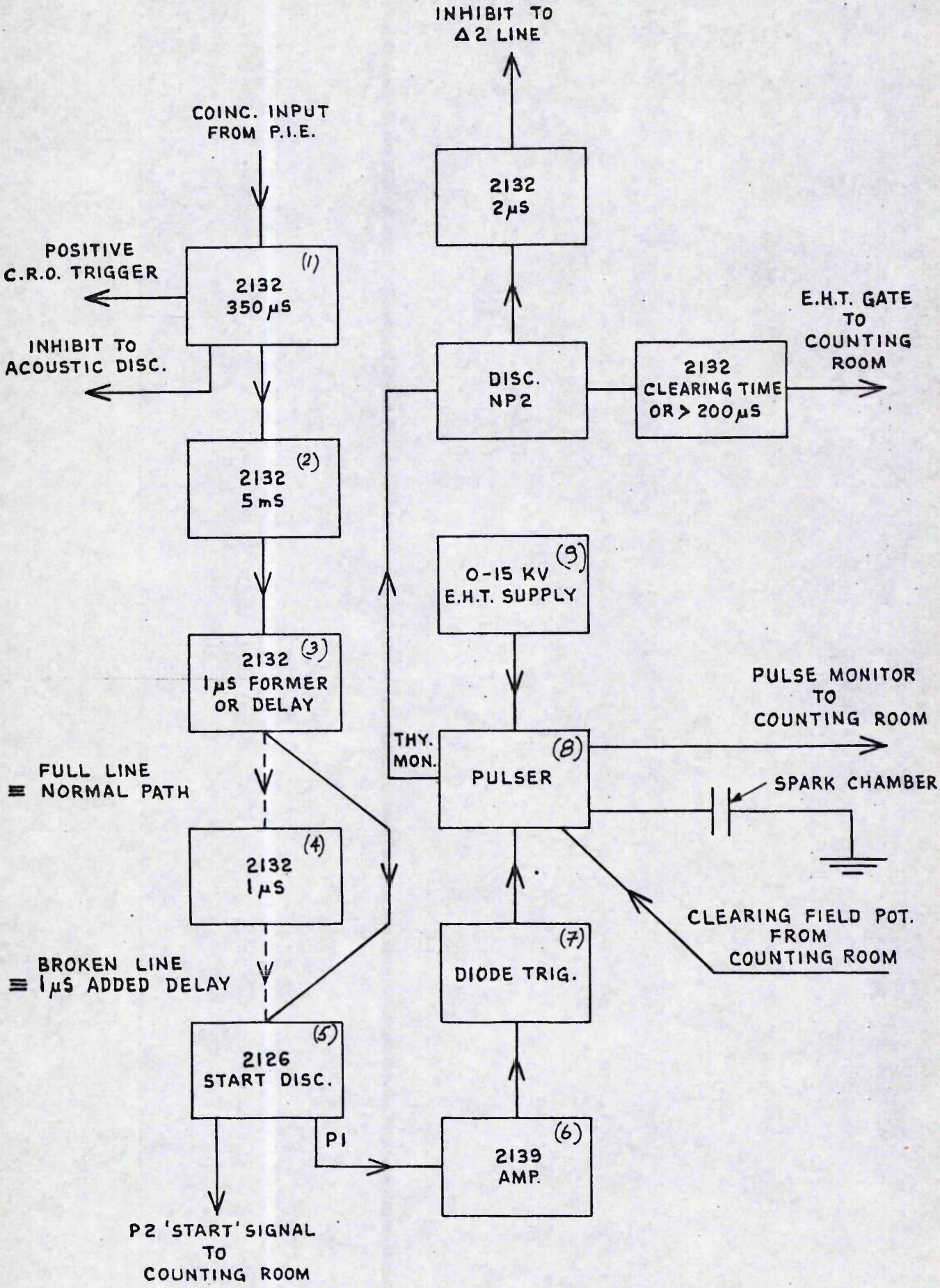

Figure 2.8 E.H.T. Pulser Electronics

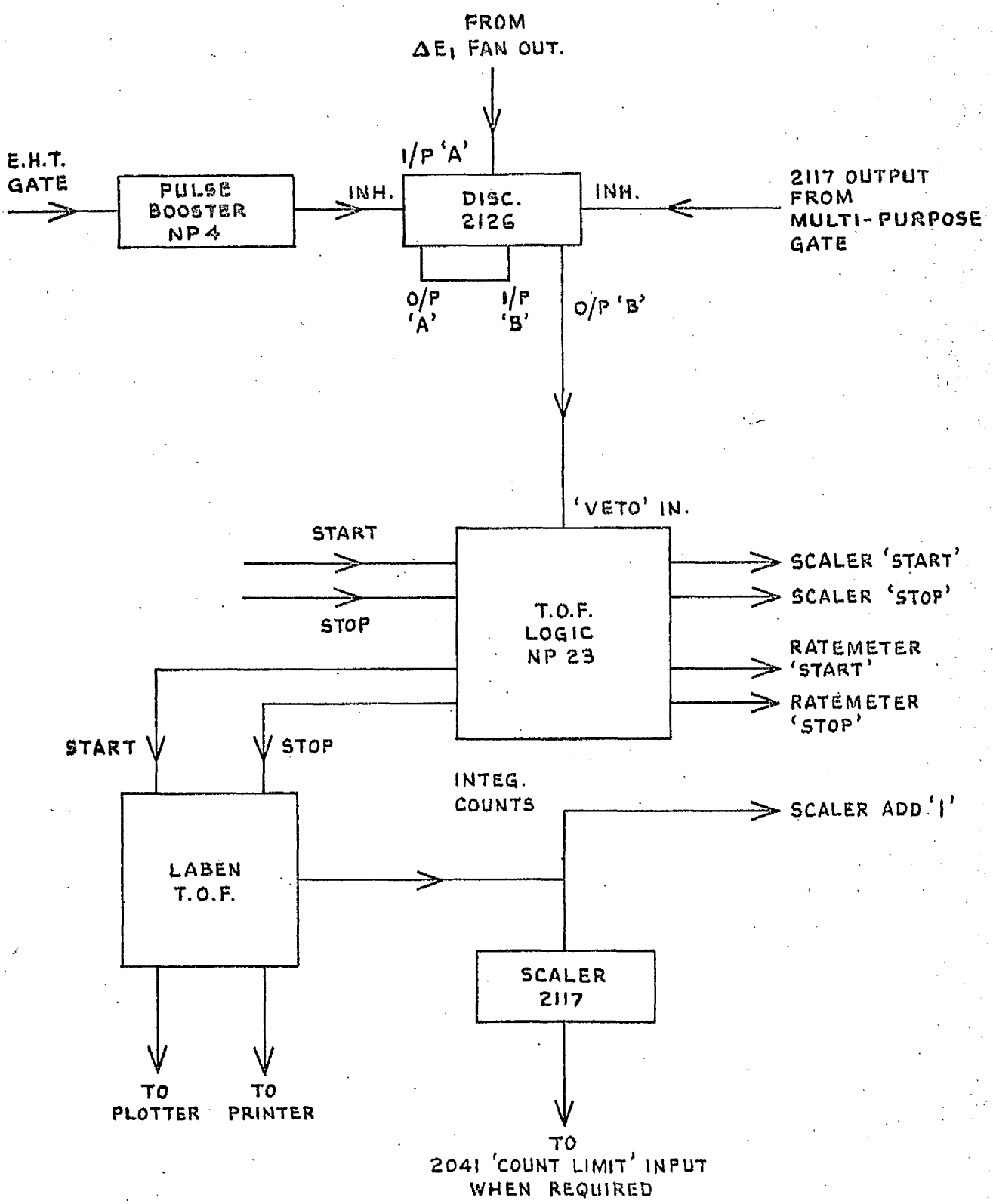

Figure 2.9 Time-of-flight Electronics in the Counting Room

inhibit pulses were set using an oscilloscope.

The gas mixture flowing through the spark chamber was also adjusted using the source. The proportion of ethanol to argon was progressively altered until the threshold voltage at which the spark chamber just fires was 6.5 kV. The E.H.T. bias was then set at 8 kV.

With the spark chamber in operation, the next stage was the setting of the bias level of the acoustic discriminator. It was imperative to ensure that the discriminator fired at the first negative-going edge of the microphone signal, wherever the sound pulse originated in the spark chamber, otherwise ambiguities may occur in the positioning of the particle. On the other hand, the bias had to be sufficiently high to prevent the discriminator being fired by stray noise pulses on the acoustic line. The bias was set to a high level and the source placed near the microphone end of the spark chamber. The microphone signal and the output from the discriminator were simultaneously fed into an oscilloscope. The signals were added internally. It was easy to see from the resulting trace at which points the discriminator was firing. The bias was slowly reduced until the discriminator always fired at

the leading negative edge. The source was then moved progressively further away from the microphone and the procedure repeated at each point. As the acoustic wave is attenuated over distance, it was generally neccesary to reduce the bias slightly. When the whole length of the spark chamber had been covered, the bias was left at its final value, and the firing condition rechecked at various positions in the focal plane.

The veto discriminator was set up using the beam with a suitable target selected and the spectrometer field chosen so that the elastic scattering peak was in the spark chamber. The procedure followed was the same as that for the E_1 and E_2 discriminators above.

The operation of the veto logic unit may be followed in figure 2.10. Briefly, the $NAND_A$ gate prevents the vetoing circuit from being fired by veto pulses arising from the same particle that initiated the start pulse. The delays were adjusted so that the relevant pulses were in coincidence. The AND_A gate tests whether a pulse arrived in the interval 1μsec. after a start pulse. The AND_B gate detects a non-coincident start pulse arriving in the interval 1μsec. after a veto pulse.

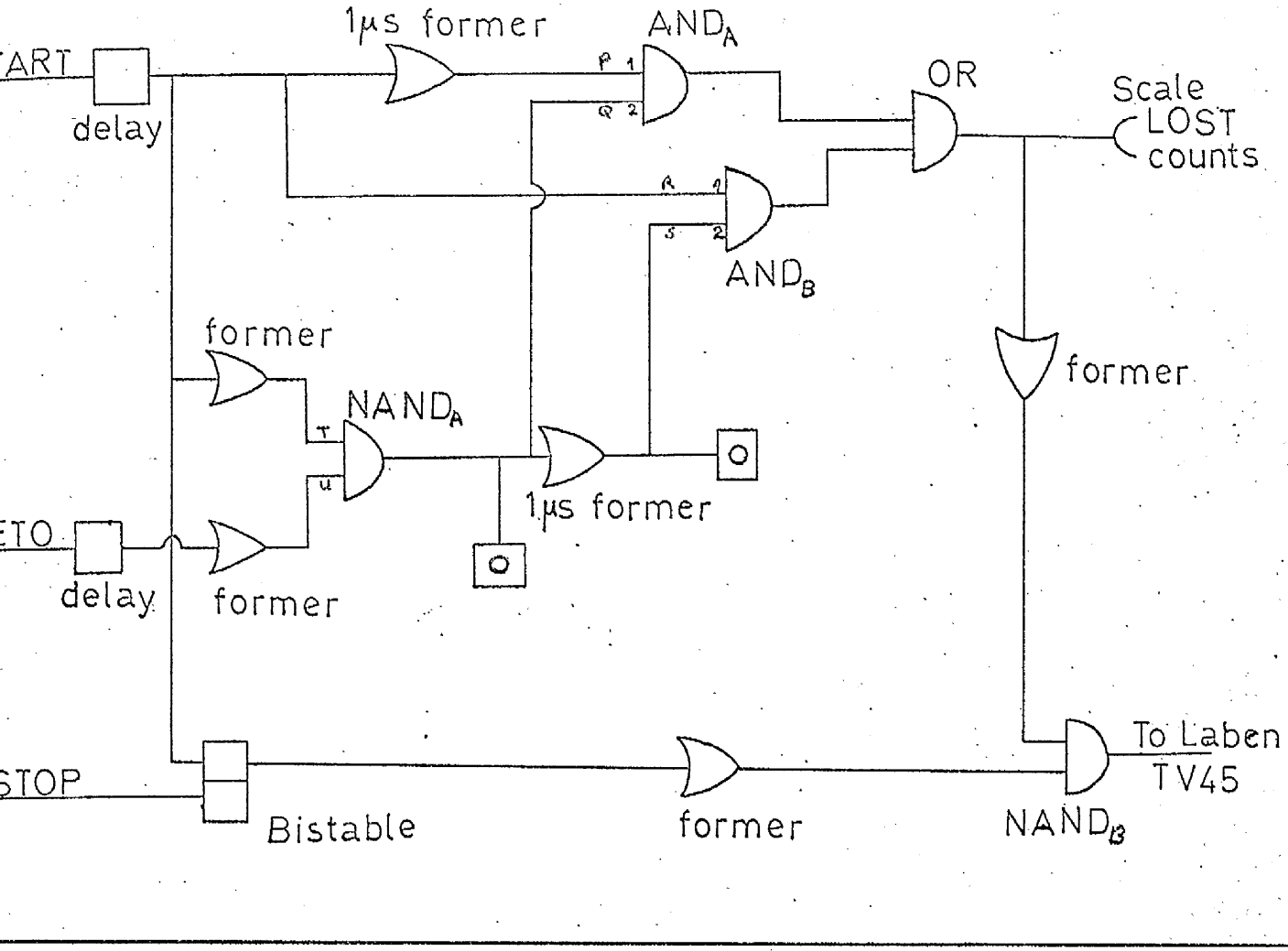

Figure 2.10 Veto Logic Unit

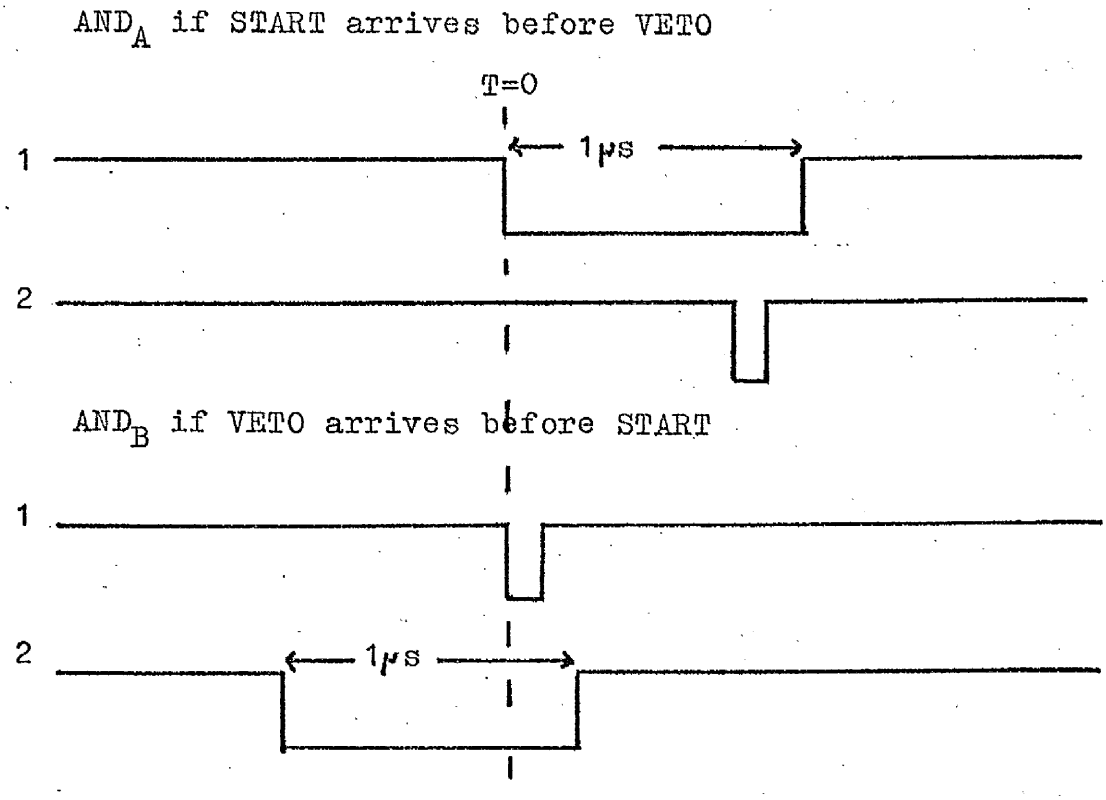

In either case a TRUE result increments the lost scaler by one, and inhibits the stop pulse for 5 milliseconds via the $NAND_B$ gate. The pulses at points P, Q, R, S, T, and U were monitored by an oscilloscope and the unit adjusted until the correct timing was achieved.

The efficiency of the spark chamber is defined as the ratio of "stops" and "lost" to "starts". As the clearing field is increased, the efficiency remains constant until a critical value is reached. At this field intensity, the ionisation trails of some of the incoming particles are being completely swept away before the E.H.T. is applied. Increasing the field further quickly reduced the efficiency to zero. For proper operation of the spark chamber the field should be set below the knee of the resulting characteristic wave. If, on the other hand, a delay of 1 μsec. is introduced between the detection of a particle and the subsequent firing of the spark chamber, the knee of the curve will occur at a lower potential, as the field has more time to clear away the ionisation. The clearing field is set at a level where, under these conditions, the efficiency is zero. Thus, all particles which occur more than 1 μsec. before the initial

true event, will not be detected by the spark chamber. Events occuring within this time are dealt with by the veto circuit.

The clearing field was progressively increased until the efficiency was zero. At each level of the field, a measurement of the efficiency was made. A graph was drawn between efficiency and clearing bias. The procedure was repeated with the application of the E.H.T. delayed by 1 μsec. The resulting graphs are depicted in figure 2.11. The correct bias was set by choosing a level between the knees of the two curves.

Limitations of the Spark Chamber

It can be seen from the above description that the spark chamber system had a dead time of 5 msecs. This limits the maximum count rate to 1 event per machine cycle. Hence the rate of accumulation of events in a spectrum is independant of the beam above a certain intensity. The spark chamber therefore is most efficient when used to find the distribution of particles along the focal plane. The total number of scattered particles is measured by the scintillation detectors. The absolute cross-sections of each of a number of levels present in the spark chamber may therefore

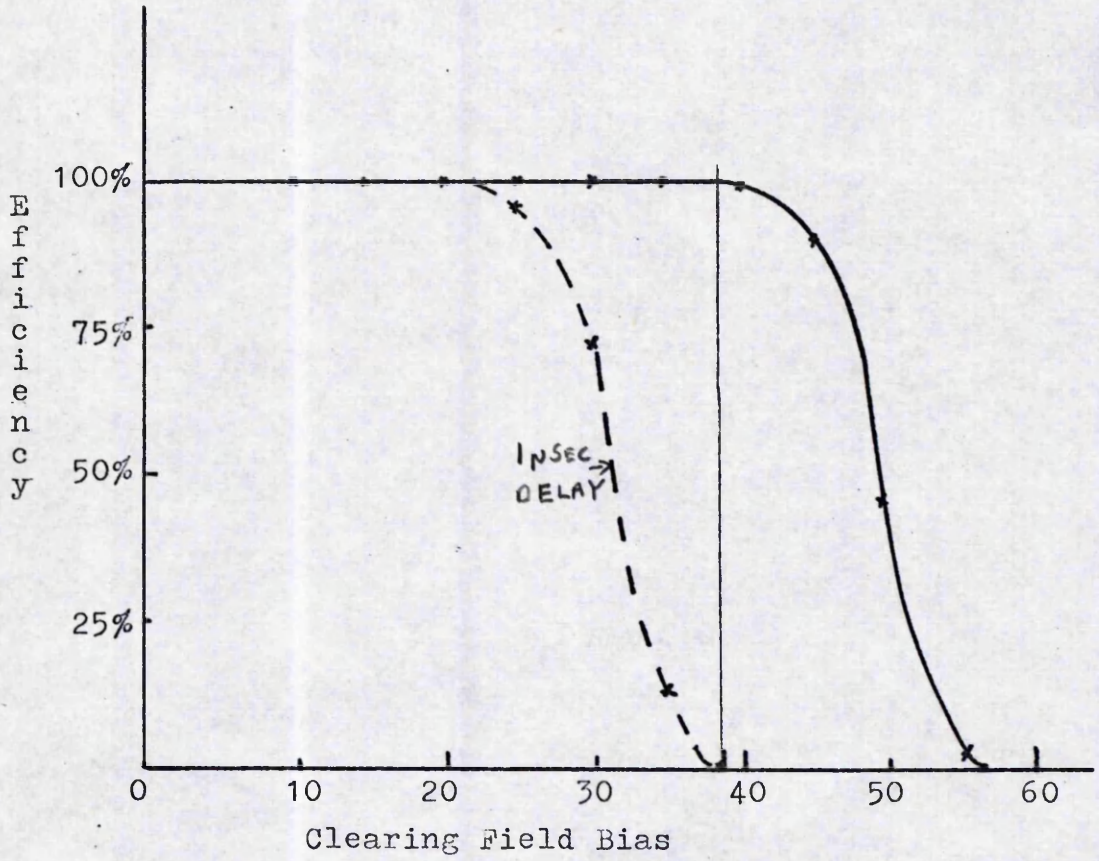

Figure 2.11 Efficiency versus Clearing Field Bias

easily be found, by multiplying this total by the proportion of events detected by the spark chamber which are in the relevant peak. However, a consequence of the very long dead time of the spark chamber occurs when part of the spectrum has a very much greater cross-section than an adjacent part. In order to measure the smaller cross-section part in detail, a disproportionately long time would be required, as most of the events recorded would be in the high cross-section parts of the spectrum. In addition there are limitations in the count rate of the coincidence system. At very high count rates, pile-up effects are encountered. To ensure that these effects are always negligible, the beam was maintained at a level such that the count rate was less than four coincidences per machine cycle. Even at such count rates, the risk of a failure of the veto circuit to detect "double" events is relatively great. For these reasons, if the spark chamber was being used to measure relative cross-sections, it was never allowed to count at a rate greater than one event every two machine cycles.

Chapter 3

In this work, four aspects of the scattering of 50 MeV. protons by Zirconium isotopes were studied. Experiments were performed to find the excited states of each isotope, and to obtain the angular distribution of elastic and inelastic scattering. The angular distributions of the asymmetry in elastic scattering were also measured. This chapter describes the procedure followed during each experiment and also discusses the reduction of the experimental data to obtain the absolute quantities.

Section 3i: Targets

Both Zirconium metal and Zirconium oxide targets were used during the experiments. The metal targets were manufactured from highly enriched Zirconium isotopes at the Oak-Ridge National Laboratories, Oak-Ridge, Tennessee. They were in the form of self-supporting foils, two centimetres square, with nominal thicknesses of 2 mgm./cm^2. The actual thicknesses are listed in table 3.1, which also gives the concentrations of the principal impurities.

The targets were transferred from their sealed containers to the scattering chamber

Target	Thickness	% Composition				
	mgm./cm .	Zr^{90}	Zr^{91}	Zr^{92}	Zr^{94}	Zr^{96}
Zr^{90}	2.0	97.8	0.95	0.65	0.49	-
Zr^{91}	2.0	4.95	91. 65	2.51	0.62	0.07
Zr^{92}	2.0	2.86	1.29	94.50	1.15	0.14
Zr^{94}	2.1	1.67	0.42	0.76	96.93	0.22
Zr^{96}	1.8	14.64	2.80	4.21	5.88	72.47

Table 3.1 Target thicknesses and the concentrations of principal impurities.

cassette under an atmosphere of dry argon. The cassette itself was filled with argon at slightly above atmospheric pressure. These precautions were designed to prevent contamination of the targets by the atmosphere. However, the experiment subsequently showed that there was some degree of oxidation of all the targets.

In most cases, these targets were thick enough to allow accurate data to be collected in a reasonable time. However, for polarisation measurements at large angles, the low intensity of the polarised beam coupled with the relatively small cross-sections at these angles made accurate measurements of the polarisation prohibitively lengthy. This problem was overcome by using Zirconium oxide targets approximately 20 mgm./cm^2. thick. These were made by the Electromagnetic Separation Group at the Atomic Energy Research Establishment, Harwell, Berkshire. They consisted of compressed oxide powder supported by thin mylar foils. These targets could not be used for cross-section measurements as their exact thicknesses were unknown. They were also unsuitable for use at forward angles because of the difficulty of resolving the oxygen and zirconium elastic

scattering peaks. In practice they were used only for measurements above 70°, where the oxygen and zirconium peaks were well separated. Measurements of the polarisation below 70° were made using the metal targets.

Section 3ii: Elastic Scattering

Forward angle scattering

The inelastic peaks observed in the proton scattering spectrum of each isotope were well separated from the elastic peak. This simplified the measurement of elastic scattering cross-sections as it was possible to set up the detection system so that only elastic events were recorded. The field in the spectrometer was set so that the elastic peak was near the low energy end of the focal plane. In this position the inelastic part of the spectrum was cut off by the edge of the spark chamber. The focal plane shutter, which operates from the high energy end of the focal plane, was then used to reduce the active length of the spark chamber. The aperture which remained was sufficiently wide to ensure that no part of the elastic peak was cut off by either the shutter or the edge of the spark chamber. The spark chamber was used only to ensure that the elastic peak was placed near the centre of

the aperture and was not required for accurate measurements of the distribution of particles in the focal plane. Consequently, the rate at which data could be acquired was determined only by the maximum count rate of the scintillation detector system (Section 2vi).

With this arrangement of the detector system, the cross-sections could be evaluated from the number of events detected by the scintillation detectors. This number however, included contributions from the elastic scattering by the oxygen contaminant of the target and from a background flux of neutrons present in the experimental area. The method used to extract the zirconium cross-sections from the quantities obtained during the experiment is described below.

All the forward angle measurements were made with the target at an angle of 135° to the beam (see figure 3.1). This ensured that measurements could be made up to 90° without causing the spectrometer to be moved into the "shadow" of the target. The oblique position of the target, however, increased the effective thickness of the target by a factor of 1.414 (Sec 45°) which had to be taken into account when calculating the cross-sections.

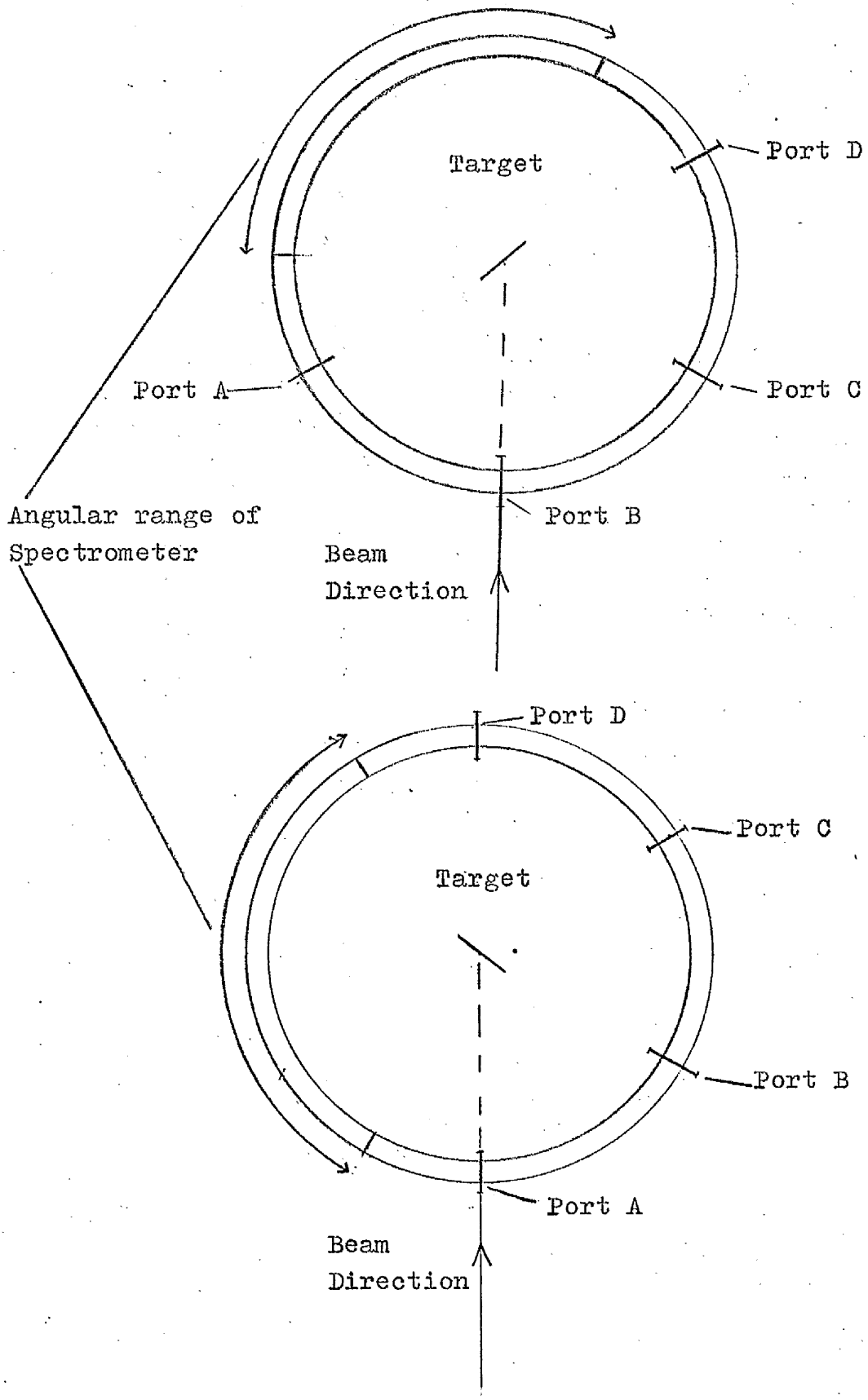

Figure 3.1 Diagram Illustrating Target and Spectrometer Angle.

During this part of the experiment the differential cross-sections of each isotope were measured at 2.5° intervals from 7.5° to 87.5°. As a check against the development of systematic errors, consecutive measurements were made at alternative angles. The spectrometer angle was first increased in 5° steps from 7.5° and then decreased in similar steps from 85°. At each angle, the following procedure was adopted. The position of the elastic peak was obtained using the spark chamber. If neccesary the spectrometer field was adjusted to position the peak near the centre of the focal plane aperture. The beam intensity was set to a level such that the count rate was slightly less than four events per machine cycle. The system was allowed to count for a number of integrator cycles sufficient to obtain a reasonable statistical error in the number of events recorded. In practice, about 7000 coincidences were recorded at each angle. Finally, the spark chamber spectrum was printed out and the contents of each scalar noted.

Correction for oxygen contamination

The oxygen peak began to separate out of the zirconium peak at 17.5° and was completely resolved at 20°, 22.5° and 25°. At angles greater

than 25° it was cut off by the edge of the spark chamber. At 20° and 25°, the oxygen peak was much smaller than the zirconium peak, oxygen events forming less than five per cent of the total number in the spectrum. At 22.5°, however, there is a diffraction minimum in the zirconium cross-section and the proportion of oxygen events was as high as 30%.

The actual degree of oxygen contamination was estimated from the observations at 20°, 22.5° and 25°, using the oxygen cross-sections of Fannon et al (reference 5). It was then possible to calculate the number of events at each angle arising from oxygen elastic scattering.

For the angles 20° to 25°, the estimation was made directly, without referring to the oxygen cross-sections. The proportion of coincidences which were oxygen events was assumed to be the same as the proportion of events in the spark chamber spectrum which were in the oxygen peak. Although the rate at which the system was allowed to count was too high for the spark chamber to be a completely reliable guide to the distribution of particles in the focal plane, any errors introduced by making this assumption were expected to be small. In any case, a 20% error in the number of oxygen events would

lead to an error of less than 1% in the cross-sections. An allowance for any such errors was made when calculating the total error in the cross-section. At 22.5°, however, the uncertainty in the number of oxygen events made a large contribution to the error, and the estimate of the error was increased to take this into account.

The number of events $I(\Theta)$ in the oxygen peak was found by adding the appropriate channels of the spectrum. The total number of events in the spectrum $A(\Theta)$ was obtained from the "add 1" scalar (see table 2.1). The number of coincidences and the number of accidentals were also obtained from the appropriate scalars. If $T_T(\Theta)$ is the number of true coincidences, then the number of oxygen events $T_o(\Theta)$ in T_T is given by

$$T_o(\Theta) = \frac{I(\Theta)\, T_T(\Theta)}{A(\Theta)} \qquad 3.1$$

With the proviso that the quantities used are normalised to the same amount of incident beam we can say that $T_o(\Theta)$ will vary linearly with the cross-section of oxygen elastic scattering $\sigma(\Theta)$ that is

$$\frac{T_o(\Theta)}{\sigma_o(\Theta)} = K \qquad 3.2$$

For each target a mean value of K was found

from the values of T_o and σ_o at 20°, 22.5° and 25°. The number of oxygen events at angles below 20° is given by

$$T_o(\theta) = K \sigma_o(\theta) \qquad 3.3$$

The corrected number of zirconium events at each angle T_z was then given by

$$T_z(\theta) = T_T(\theta) - T_o(\theta) \qquad 3.4$$

Background correction

The number of zirconium events T_z obtained from equation 3.4 still includes a number of background events. When the spark chamber is operating with 100% efficiency the number of stops should equal the number of starts. However, during the experiment, it was noticed that at large angles the ratio of stops to starts, which was unity at forward angles, fell short of unity by an amount which increased with decreasing cross-section. This was an effect of a beam dependant background of neutrons in the region of the scintillation detectors. Some of the energetic protons produced by collisions of the neutrons with protons in the scintillators and the surrounding structure were detected by both scintillators. The resulting coincidence pulse occasionally initiated a start pulse. The absence of a corresponding ionisation trail meant that no spark and consequently no

stop pulse would be produced. For a given beam intensity this effect was constant in time and independant of angle. Consequently it was of greater importance at larger angles where it was neccesary to count for longer periods in order to obtain the required number of events. The start circuitry fires with equal probability for any coincidence pulse so that the proportion of genuine events in the total was given by the ratio of stops to starts.

Calculation of absolute cross-sections

The differential cross-section transformed to the centre-of-mass frame is given by the following formula

$$\left(\frac{d\sigma}{d\Omega}\right)_{cm} = \frac{T_2(\theta).\,ST(\theta).\,SAC.}{SR(\theta).N_T.\Omega.\,C.R.F_R.}$$

$$\times \frac{10^{27}}{6.242 \times 10^{18}} \cos(\phi) \text{ mbarns/steradian} \qquad 3.5$$

where $SR(\theta)$ and $ST(\theta)$ are the numbers of starts and stops, N_T is the number of atoms per sq. cm. in the target, Ω is the solid angle subtended by the spectrometer and C, R, and F_R are the number of cycles, the number of coulombs per cycle and the range correction factor respectively. The factor 6.242×10^{18} is the number of incident protons in a coulomb of beam. ϕ is the target angle and SAC is a kinematical correction to the solid angle.

The total statistical error in the measurement of the cross-section was evaluated by adding in quadrature the errors in the quantities $ST(\theta)$, $SR(\theta)$ and $T_z(\theta)$ of equation 3.5. This was an over-estimate of the error as ST, SR and to a lesser extent T_z are not strictly independant variables. However, a fixed error of 4% was included in the estimate of the total error in the cross-section. As the total statistical error was rarely greater than 3%, the effect of ignoring the dependance of ST and SR was to increase the total error by less than 1⅓%. The fixed error represented an estimated upper limit to the aggregate of all errors, other than statistical, arising during the experiment. It includes the uncertainties introduced by the oxygen correction (see above) and by neglecting the correction for the finite width of the solid angle defining aperture (see below). The formula used to obtain the total error was:

$$\Delta = \frac{d\sigma}{d\Omega} \times \left\{ \left(\frac{\Delta T_z}{T_z}\right)^2 + \left(\frac{\Delta SR}{SR}\right)^2 + \left(\frac{\Delta ST}{ST}\right)^2 + 0.0016 \right\}^{1/2} \qquad 3.6$$

where ΔT_z, the error in T_z was taken to be equal to $T_z^{1/2}$. Similarly $\Delta ST = (ST)^{1/2}$ and $\Delta SR = (SR)^{1/2}$.

Finite solid angle correction

The differential cross-section $\sigma_a = \frac{d\sigma}{d\Omega}(\theta)$

is defined for an infinitesmal solid angle $d\Omega$. The spectrometer, however, subtended at the centre of the target nominal angles of 1° in the horizontal plane, and 6° in the vertical plane. Consequently, the quantities measured by the spectrometer are the cross-sections averaged over an angle of 1°. The finite height of the aperture meant that the values of the cross-sections also included a contribution from out-of-the-plane scattering. However, the absolute cross-section at the centre of the aperture is related to the average cross-section by the following equation

$$\sigma_A(\theta) = \sigma_{exp}(\theta) + \frac{\beta^2}{24\,\mathrm{Tan}\theta}\frac{d\sigma_{exp}}{d\theta} + \frac{\alpha^2}{24}\frac{d^2\sigma_{exp}}{d\theta^2} \qquad 3.7$$

where α is the horizontal angle and β the vertical angle subtended by the aperture. σ_{exp} is the experimentally observed cross-section.

The solid geometry of the problem is discussed in reference 6 where equation 3.7 is derived. At forward angles, where $\tan\theta$ is small and the cross-section changes fairly rapidly, the second term in equation 3.7 is about 10% of the total cross-section. The gradient of the angular distribution at a given point was taken to be the gradient of

the straight line joining the two adjacent points. The contribution of the third term was not calculated specifically, as it was not possible to obtain an accurate value of $\frac{d^2\sigma}{d\theta^2}$. However it was expected to be fairly small, and an allowance for it was made when calculating the error in the cross-sections.

Target impurities

The principal impurities in each target, apart from oxygen, were the other isotopes of zirconium. The observed cross-section $\sigma_a(A)$ of an isotope A therefore included contributions from the impurities. The cross-sections $\sigma'_a(A)$ of each pure isotope were calculated using the concentrations of the various impurities given in table 3.1.

As the Zr^{90} target had the lowest concentration of impurities, the cross-section of pure Zr^{90} was calculated first, using the equation

$$\sigma'(90) = \{100\,\sigma_a(90) - 0.95\,\sigma_a(91) - 0.65\,\sigma_a(92) - 0.49\,\sigma(94)\}/97.8 \qquad 3.8$$

Similar equations were written for the remaining isotopes. The corrected cross-sections of the other isotopes were calculated in descending order of purity. The new values obtained for the purer isotopes were used in calculating the

corrections to the less pure isotopes. The set of corrected cross-sections obtained in this way were then used to perform more accurate calculations of the absolute cross-sections by the same method. The procedure was reiterated until a consistent set of cross-sections of the pure isotopes had been obtained.

Large angle cross-sections

Measurements of the cross-sections were extended to angles greater than 87.5° using a slightly different procedure to that used at forward angles. At backward angles, the zirconium cross-sections are relatively small. Consequently the count rate of the system was well below the limiting value for making accurate measurements with the spark chamber. It was therefore possible to record elastic and inelastic events together. The distribution of events between the elastic and various inelastic channels was given by the distribution of events between the corresponding peaks in the spark chamber spectrum. The cross-section was therefore given by the expression of equation 3.5 multiplied by the ratio of events in the elastic peak to the total in the spectrum. That is

$$\frac{d\sigma}{d\Omega}(\theta) = \frac{A(\theta) \cdot T_z(\theta) \cdot ST(\theta) \cdot SAC}{SP(\theta) \cdot SR(\theta) \cdot N_T \cdot \Omega \cdot C \cdot R \cdot F_R} \times \frac{10^{27}}{6.242 \times 10^{18}} \cos\phi \text{ mbarn/str.} \qquad 3.9$$

where $A(\theta)$ is the area of the elastic peak, obtained by adding the contents of the appropriate channels. $SP(\theta)$ is the total number of events in the spectrum, obtained from the "add 1" scalar. The cross-sections of the 2.75 MeV. 3^- level were given by a similar equation.

The cross-section was measured at 5° intervals from 70°. At each angle, the system was allowed to count until there were at least 300 events in the 3^- peak in the spark chamber spectrum. The target was set at 45° to the beam, so that the spectrometer viewed the target in reflection mode (see figure 3.1). The change in target position introduced the possibility of differing normalisation between the data at forward and backward angles. However, the two parts of the angular distribution had overlapping points at 70°, 75°, 80° and 85°. A normalisation factor was given by the mean ratio of the values of the cross-sections calculated by the method described in the first part of this section to the values obtained by the above method. The backward angle cross-sections were multiplied by this factor to give a consistent angular distribution from 7.5° to 140°.

A computer code was used to perform all of the calculations described in this section, except

the correction for oxygen contamination. The program also converted the angle, cross-section and error to the centre-of-mass system. The elastic scattering angular distributions are depicted in the diagrams illustrating Chapter 6. The solid lines in these diagrams are predictions of the optical model theory described in Chapter 4.

Normalisation errors

Apart from the errors in the measurement of the cross-section at each angle, there was an error in the absolute normalisation of each angular distribution. This error arose mainly from uncertainty in the measurements of the target thicknesses which were estimated to be accurate only to within 5%. Other smaller contributions came from the measurement of the solid angle and the calibration of the charge integrator system. However, the total normalisation error was estimated to be better than 10%.

Section 3iii: Polarisation Measurements

The asymmetry $\delta(\theta)$ in the elastic scattering of polarised protons at an angle was given by

$$\delta(\theta) = \frac{1 - \sigma_{\downarrow}/\sigma_{\uparrow}}{1 + \sigma_{\downarrow}/\sigma_{\uparrow}} \qquad 3.10$$

where $\sigma_{\uparrow}$ and $\sigma_{\downarrow}$ are the elastic scattering cross-sections, measured with proton spin up and with

proton spin down respectively.

During the experiment, the asymmetries of each isotope were measured at 2.5° intervals from 7.5° to 65°. Measurements were also made at 5° intervals from 65° to 100° for all the isotopes except Zr^{91}. The relative values of $\sigma_{\uparrow}$ and $\sigma_{\downarrow}$ were measured, in the same way as the backward angle cross-sections. However, in this case two spectra were accumulated at each angle, one for each spin orientation. The amount of incident beam was measured by the split ion chamber, which had an unknown multiplication factor. However, the spectra were accumulated for equal numbers of integrator cycles so that $\sigma_{\downarrow}/\sigma_{\uparrow} = T_{\downarrow}/T_{\uparrow}$ where $T_{\uparrow}$ and $T_{\downarrow}$ are given by

$$T(\theta) \qquad \frac{A(\theta) \cdot ST(\theta) \cdot T_r(\theta)}{SP(\theta) \cdot SR(\theta)} \qquad 3.11$$

Because of the low intensity of the polarised beam, measurements at all except forward angles took several hours to complete. As the beam polarisation changed with time, the spin orientation was changed at intervals of about 20 minutes. The spectra were accumulated in different parts of the analyser memory, avoiding the neccesity of erasing the memory each time the spin orientaion was changed. Each time, however, the contents of the scalers

were noted and the accumulated spectrum was printed out. This avoided an unneccesary loss of data if a fault developed in the system. After each spin up-spin down cycle, approximate values of the asymmetry and the beam polarisation were calculated and checked for consistency with the values from previous cycles. At angles greater than 70°, it was neccesary to use thicker ZrO targets (Section 3i) in order to complete the measurements in a reasonable time.

Calculation of polarisation

At each angle the asymmetry was calculated from equations 3.10 and 3.11. The error $\Delta\delta$ in the asymmetry was given by the expression

$$\Delta\delta \simeq \left(\frac{1}{T_\uparrow + T_\downarrow} + \frac{T_\uparrow + T_\downarrow}{T_\uparrow - T_\downarrow}\right)\delta \qquad 3.12$$

This estimate did not take into account the experimental uncertainties in the measurement. To allow for these, a fixed error of 4% was included in the total error. The beam polarisation was calculated from the polarimeter readings, using equations 2.2 and 2.3 (see section 2v). The polarisation of elastic scattering of the target, $P(\theta)$, was then given by

$$P_B(\theta)\, P(\theta) = \delta(\theta) \qquad 3.13$$

The results of this experiment are shown in

the diagrams illustrating Chapter 6. The angular distributions of elastic scattering polarisation are shown, together with the predicted values of the optical model.

Section 3iv: Energy Levels

The energy levels excited by inelastic proton scattering were investigated by two different methods. The first method, which is described in this section, required the calibration of the spectrometer. The absolute energy of a proton group in the focal plane was determined in relation to its position in the spectrum and to the field in the spectrometer.

In the second method, the energy levels were obtained from the spectra recorded during inelastic scattering measurements (see section 3v). The energies of several prominent and unambiguous peaks were obtained from measurements by other workers and used to calculate the relative energies of the remaining peaks.

Calibration of the spectrometer

The spectrometer was calibrated by finding an expression relating E_n, the energy of a proton detected in a given channel, to the channel number n and the Hall voltage V.

The energy of a proton detected in the central

channel of the spectrum n_o was given by the following expression

$$E_o^{1/2} = A + BV + CV^2 \qquad 3.14$$

where A, B and C are constants. Higher order terms were assumed to be negligible.

The energy E_n of protons detected in channel n was related to the central channel energy by

$$E_n^{1/2} = E_o^{1/2} + D(n-n_o) + E(n-n_o)^2 \qquad 3.15$$

where again D and E are constants and higher order terms were neglected. Substituting for $E_o^{1/2}$ in equation 3.15

$$E_n^{1/2} = A + BV + CV^2 + D(n-n_o) + E(n-n_o)^2 \qquad 3.16$$

The coefficients A, B, C, D and E were evaluated using the elastic scattering of protons by beryllium. A light nucleus was used to give a wide kinematical variation of energy with scattering angle. The beryllium target was the most suitable available, as interference from the excited states, which are well separated from the ground state, was negligible.

The spark chamber was attached to the focal plane of the vessel in a position such that the central channel of the spectrum coincided with the mid point of the focal plane. The spectrometer was set at an angle of 10° to

the beam. The spectrometer field was systematically varied so that the elastic peak moved across the length of the spark chamber. The number of the central channel of the peak was recorded for each value of the field. The procedure was repeated for spectrometer angles at intervals of 5° between 10° and 85°.

The energies of the protons in the peak at each angle were obtained from kinematical tables. In this way a table of related values of E_n, V and n was built up, for values of n which covered all parts of the spectrum and for values of E_n extending from 35 MeV. to 50 MeV. This table was used by a program written for the IBM 360/75 computer to calculate the coefficients of equation 3.16. The program used a least squares method to find the set of values of A, B, C, D and E which gave the best fit to the experimental data. The minimum value of the quantity χ^2 was found where

$$\chi^2 = \frac{1}{N} \sum_{N} (E_{exp} - E_{th})^2 \qquad 3.17$$

E_{th} is the energy calculated from equation 3.16 and E_{exp} the corresponding experimentally observed energy. N is the number of data points. The program calculated the final value of χ^2 and also listed the contribution of each data point.

The equation used to calculate the energy spectra was ($n_o = 145$)

$$E_n^{1/2} = 0.1684 + 0.001159(n - 145) + 0.1384 \times 10^{-5}(n - 145)^2 + 0.004020V - 0.2158 \times 10^{-6} V^2 \qquad 3.18$$

with a total value of χ^2 of 0.6716 for 40 data points.

Excitation spectra

The spectrum of proton scattering up to an excitation of 10 MeV. was measured for each isotope at scattering angles of 20° and 40°. The acceptance range of the spectrometer is only 5 MeV. It was therefore neccesary to link together a series of spark chamber spectra, each covering a different energy range of inelastic scattering.

The spectrometer was placed at an angle of 20° to the beam and the appropriate target selected. The spectrometer field was set so that the elastic peak was centrally placed in the spectrum. The spark chamber was allowed to count over 100 integrator cycles at 10^{-7} coulombs per cycle. Because of the relatively high cross-section of elastic scattering the inelastic peaks in the spectrum were barely discernable. In order to obtain a reasonable number of events for inelastic levels close to the ground state, the next spectrum was recorded over a range

of energy starting just above the ground state. The field in the spectrometer was reduced until the elastic peak was just cut off by the high energy end of the spark chamber. A spectrum was accumulated over 400 charge cycles at 10^{-7} coulombs/cycle. The field was then reduced again until the new spectrum overlapped the previous one by about 80 channels. The spectrum was again recorded over 400 integrator cycles. A series of overlapping spectra was obtained in the same way until the desired range of excitation energy had been achieved.

Each spectrum gives the relative cross-sections of the levels included in the range of excitation energy. There was, however, no correspondance between the cross-sections of peaks in different spectra. The overlapping sections of the spectra enabled the normalisation factors between them to be calculated. The wide overlap between the spectra also made it possible to neglect the end channels of each spectrum, which were subject to edge effects.

A computer program read in the relevant spectra and converted each one into an energy spectrum of 100 channels at intervals of 5 keV. using equation 3.18. The program then calculated the normalisation factors between the energy spectra by comparing the average contents of overlapping channels. Finally, the

normalised spectra were linked together to form a single spectrum calculated at 50 keV. intervals from the ground state up to about 7 MeV. excitation.

The above procedure was repeated for each isotope. A similar set of spectra was also obtained at a scattering angle of 40°. This was to assist in the observation of levels with forward peaked cross-sections and also enabled peaks belonging to light impurities to be identified by their kinematical shifts.

The energy level diagram for each isotope obtained in this way had a similar structure to the appropriate set of energy levels given in references 1 and 22. However, there was poor agreement between the actual energies. The reason for this discrepancy probably lay in the calibration process. The beryllium target had a thickness of 10 mgm./cm. and the elastic scattering peak was correspondingly broad. This made it very difficult to identify the exact position of the peak. There was also a considerable energy loss in the target which varied slightly with scattering angle. A more consistent set of energies for the low lying states was obtained from the inelastic scattering cross-section measurements. This method is described in the next section.

Section 3v: Inelastic Scattering

In this part of the experiment, the angular distributions of the cross-sections of inelastic scattering were measured for the low lying excited states in each isotope.

Inelastic scattering spectra

Spectra of inelastic scattering were obtained using the spark chamber at angles between 7.5° and 87.5°. The measurements were made at 2.5° intervals for Zr^{90} and at 5° intervals for the other isotopes. The number of levels which could be studied was limited by the active length of the spark chamber. The spectra extended from just below the lowest discernable inelastic peak to about 5 MeV. At each angle, the spectrum was accumulated at a rate of less than one event every two machine cycles. Consequently, the relative cross-sections of the inelastic levels were given by the ratios of the areas of the corresponding peaks. The number of events in each spectrum was sufficient to ensure that the majority of the peaks contained at least 300 to 400 events.

The spectra were printed out, and recorded on 5-hole punched paper tape. The tapes were read by the computer, and the spectra written on to a magnetic tape file.

The cross-section of each level was given by equation 3.9 where $A(\theta)$ was the area of the appropriate peak in the spark chamber spectrum. The values of $A(\theta)$ were found by a non-linear parameter search program written for the IBM 360/75 computer by Mr.G.S.Mani. This method was adopted because the large number of overlapping peaks in the spectrum made straightforward addition very difficult.

The approximate shape of each peak in the spectrum was assumed to be Gaussian. The program generated a theoretical spectrum from the equation

$$Y_I = \sum_N P_N \exp[-(Q_N - I)^2/R_N^2] + S \qquad 3.19$$

S represents a uniform background. The program found the set of values of P_N, Q_N, R_N and S which gave the best fit to the experimental data. The minimum of the quantity χ^2 was found where

$$\chi^2 = \sum_I \left(\frac{Y_I - X_I}{\Delta X_I} \right)^2 \qquad 3.20$$

X_I represents the contents of the I-th channel in the experimental spectrum and ΔX_I is the statistical error in X_I.

The logic and operation of this program is described in appendix A1.

The program explored the χ^2-space in the

vicinity of a set of initial values of P, Q, R and S, which were fed in at the start of the calculation. In practice, only the peak positions Q, expressed in integer form, were read in by the program. The initial value of the width for each peak was assumed to be standard at 5 channels, and the height of the peak was taken to be X_Q, the contents of the Qth channel in the experimental spectrum.

The function $\chi^2(P, Q, R, S)$ may have several minima. Considerable care had to be taken in selecting the initial values of Q to ensure a physically reasonable result.

The spectra belonging to each angular distribution were treated as a set. The members of each set all had the same basic structure. Thus, although the spectra were usually displaced with respect to one another, the relative positions of the peaks were generally the same. At angles above 40°, however, there was generally a prominent oxygen elastic scattering peak in each spectrum. The peak moved through the spectrum as the angle increased. At some angles it obscured or considerably overlapped one of the inelastic peaks. As it was sometimes not possible to extract the cross-section of the inelastic level in such cases, there

are corresponding gaps in the angular distributions.

The spectrum in each set with the most clearly defined set of peaks was chosen as a standard. The standard spectrum was fitted first. After several attempts, a set of initial parameters was found which gave a satisfactory fit. The displacement of each of the remaining spectra from the standard was estimated by comparing the positions of the prominent 3^- peaks. The initial values of Q for each spectrum were then calculated by adding the displacement to the best fit values of Q obtained for the standard spectrum. These parameters were used to obtain a set of preliminary fits for each isotope.

Before the values of $A(\theta)$, calculated from equation

$$A_N(\theta) = P_N \cdot R_N \cdot T_{\frac{1}{2}} \qquad 3.21$$

could be used to evaluate the cross-sections, it was neccesary to examine the consistency of the fitting procedure in each spectrum. This process commenced with the set of Zr^{90} spectra. Initially, an assessment of the quality of the fit to each peak was made for every member of the set. The energy interval associated with the separation between two given peaks was then found by assuming a linear relationship between energy and channel

number. The energy interval ΔE per channel was assumed to be constant throughout the spectrum. To within the 2 to 3 keV. accuracy required, this assumption appeared to be justified. An energy level diagram for Zr^{90} was compiled from references 1 and 21. As many peaks as possible in the standard spectrum were identified with levels in the diagram. The energies of two or three well defined levels were also obtained from the diagram. Using the positions of these peaks and the prominent 3^- level as a reference, an approximate value of ΔE was calculated. ΔE was then used to obtain the energies of the remaining peaks in the spectrum. The value of ΔE was adjusted to obtain the best agreement between the energies of the peaks and the energies of the corresponding levels in the diagram. During this process, particular weight was given to peaks which were experimentally well defined and where a good theoretical fit had been obtained. The energies of the peaks in the remaining theoretical spectra were then calculated.

If the fitting process and the experimental data had been perfect, the energy of a peak corresponding to a given level would have been the same in all the spectra. However, in practice, some variation in the peak energies was observed.

The decision whether or not to accept the fitting of a particular peak as consistent was made on a subjective basis. Both the quality of the fit and the definition of the experimental peak were taken into account. Generally, however, up to 10 keV, variation in peak energy was considered acceptable. Exceptionally, well defined peaks with good fits were accepted even if the energy was up to 20 keV. different from the standard.

The spectra containing inconsistent fits or badly fitted peaks were refitted with new starting parameters. The process of refitting and assessment was continued until a consistent set of fitted spectra had been obtained. In these spectra, the energies of most of the corresponding peaks agreed to within acceptable limits. However, for some peaks it was not possible to obtain a consistent fit in every spectrum. These were mainly in regions where there were many overlapping peaks, or where the cross-sections of the corresponding levels were very small.

The energy of each level was found by averaging over the values obtained for the energy of the relevant peak in the different spectra. Values for spectra where the fit to the peak was poor or inconsistent were not included in the average. The resulting energy levels are given in figure 6.35.

The same process was applied to the spectra of Zr^{92} and Zr^{94}, using the value of ΔE calculated for Zr^{90}. The analysis of Zr^{91} and Zr^{96} has not yet been completed. A comparison of the energy levels of Zr^{92} with those of other workers is shown in figure 6.36. The diagram for Zr^{94} is given in figure 6.37.

The cross-sections were evaluated from the values of $A(\theta)$ from the final set of "best fit" parameters for each spectrum. Graphs of the angular distributions of the observable levels in Zr^{90}, Zr^{92}, and Zr^{94} are given in figures 6.20 to 6.26. The continuous lines on the graphs are theoretical predictions of the cross-sections given by the collective model or by the microscopic model. (See Chapter 6).

Chapter 4

An optical model analysis of the elastic scattering data was carried out. Several forms of the optical potential were used, and in each case the parameters of the potential were varied until the best agreement between the theoretical and experimental data had been obtained.

Section 4i: Theory and Limitations of the Model

Introduction

The optical model replaces the complicated many body interaction between a nucleon and a nucleus by a simple potential well. The component of the total wave function of the particle with angular momentum can then be expressed asymptotically in terms of an incoming wave I_ℓ and an outgoing wave O_ℓ where

$$\Psi_\ell = I_\ell - S_\ell O_\ell \qquad 4.1$$

S_ℓ is defined as the scattering matrix element between the incoming and outgoing channels. It represents the change in amplitude and phase of the ℓth partial wave. Hence the ratio of the initial and final flux densities in a channel is given by $|S_\ell|^2$. The scattering matrix is unitary, so we may write

$$S_\ell = e^{-2i\delta_\ell} \qquad 4.2$$

where δ_ℓ is a phase shift in the ℓth partial wave.

In a system where no reaction or inelastic channels exist in addition to the elastic channel the angular distribution can be described in terms of a purely real potential. For a real potential well, δ_ℓ is real and $|S_\ell|^2 = 1$. This is a reflection of the fact that for pure elastic scattering the flux in each channel is conserved.

In a physically realistic system, particles are removed from the incident channels by a variety of reaction processes. In the case of the optical model, the effect of these processes is approximated by including an imaginary component in the scattering potential. This leads to an attenuation in each channel as the phase shifts δ_ℓ are complex, so that $|S_\ell|^2 < 1$.

Limitations of the model

The approximations made by the optical model are not valid in all cases. If the nucleus has a strongly excited reaction channel, the reaction processes can no longer be regarded as a peturbation on the elastic scattering. Also, at low energies the elastic scattering may be affected by the presence of compound nuclear states. If the energy spread of the incident beam is less

than the separation of the compound nuclear levels, the cross-sections will tend to be characteristic of one of these levels. Furthermore, at low energies only a few compound channels are open, and the probability of re-emittence of the particle into the elastic channel is relatively high. Such compound elastic scattering may be comparable to the shape elastic scattering from which it is experimentally indistinguishable. This applies particularly to light nuclei which generally have fewer compound states.

Therefore, the optical model can be expected to give best results for heavier nuclei at intermediate energies. Also, the large number of levels generally found in heavy nuclei means that compound elastic scattering can usually be neglected. The utility of the model at energies above about 300 MeV. is also restricted, partly because of the large number of partial waves which have to be taken into account and partly because relativistic effects become significant.

Form of the optical potentials

The potential well used by the model is characterised by a depth and a geometrical shape. Its simplest expression is

$$V_{opt} = (U + iW) f(r) \qquad 4.3$$

where V and W are the depths of the real and imaginary components. $f(r)$ is a radial form factor with a characteristic radius and shape parameter. The potential of equation 4.3 is given more flexibility by allowing different geometries for the real and imaginary parts.

$$V_{opt} = U f(r, r_r, a_r) + i W f(r, r_i, a_i) \qquad 4.4$$

where r_r, a_r and r_i, a_i are respectively the real and imaginary radii and shape parameters. In some cases, better results are obtained with an imaginary potential which is peaked at the nuclear surface. This is physically reasonable because the effect of the Pauli exclusion principle within the nucleus limits the number of states into which the projectile can scatter. In this analysis, imaginary potentials with both volume and surface components were used. The volume component had a similar geometry to the real potential. The radial form factor of the surface term was obtained by differentiating the volume form factor.

The potential of equation 4.4, however, does not take into account several important features of the particle-nucleus interaction. If the incident particles have non-zero spin, coupling of the projectile spin to its angular

momentum polarises the scattered particles. If this is to be accounted for by the optical model, there must be a spin orbit term proportional to $\underline{\ell}.\underline{\sigma}$ in the potential. Such a spin orbit term was used in this work, given by

$$V_{so}(r) = \left(\frac{\hbar}{m_\pi c}\right)^2 U_{so}\, \underline{\ell}.\underline{\sigma}\, \frac{f'(r)}{r} \qquad 4.5$$

where U_{so} is the potential depth and $f'(r)$ a derivative form factor.

Finally, if the projectiles are charged there is a coulomb term in the potential. This was taken to be the potential of a uniformly charged sphere, so that

$$V_c = \frac{Z_1 Z_T}{2R_c}\left(3 - r^2/R_c\right); \qquad r < R_c$$

$$V_c = \frac{Z_1 Z_T}{r} \qquad r > R_c \qquad 4.6$$

The optical model potential in its complete form can now be written:

$$V(r) = V_c(r) - U f(r, r_r, a_r) - i W_S f(r, r_i, a_i) - i W_D f'(r, r_i, a_i)$$

$$+\left(\frac{\hbar}{m_\pi c}\right)^2 \left\{U_{so} + i W_{so}\right\} \underline{\ell}.\underline{\sigma}\, \frac{1}{r} f'(r, r_{so}, a_{so}) \qquad 4.7$$

where W_S and W_D are the imaginary volume and surface well depths. r_r, a_r; r_i, a_i and r_{so}, a_{so} are the geometry parameters of the real, imaginary

and spin orbit terms respectively.

In this analysis, the radial form factor $f(r)$ was given a Saxon-Woods form, so that

$$f(r) = \frac{1}{1 + \exp[(r - r_r A^{1/3})/a_r]}$$

and

$$f'(r) = \frac{4 \exp[(r - r_r A^{1/3})/a_r]}{\left(1 + \exp[(r - r_r A^{1/3})/a_r]\right)^2} \qquad 4.8$$

Calculation of observables

The total wave function Ψ of the system is obtained from the solution of the Schroedinger Equation for the optical model potential.

$$\frac{\hbar^2}{2\mu} \nabla^2 \Psi + \left(E - V_{opt}(r)\right) \Psi = 0 \qquad 4.9$$

where $V_{opt}(r)$ is the optical model potential and μ is the reduced mass. μ is given by

$$\mu = \frac{A_I A_T}{A_I + A_T} \qquad 4.10$$

The wave function may be expanded in terms of radial, angular and spin components, so that

$$\Psi(r, \theta, \phi) = \sum_{jem} u_{je}(r) (2j+1)^{1/2} r^{-1} i^{\ell} Y_e^{\Lambda}(\theta, \phi) \chi_s^{\nu}$$
$$\times (-)^{\ell - s + \nu} \begin{pmatrix} \ell & s & j \\ m & \lambda & -\nu \end{pmatrix} \qquad 4.11$$

Setting $\rho = kr$, the radial and angular parts of equation 4.9 can be separated, so that we may write

$$\frac{d^2 u_\ell(\rho)}{d\rho^2} + \left\{1 - \frac{V(r)}{E} - \frac{\ell(\ell+1)}{\rho^2}\right\} u_\ell(\rho) = 0 \qquad 4.12$$

In the region outside the range of the nuclear forces, the incident particle experiences only the coulomb field. Hence, equation 4.12 becomes

$$\frac{d^2 u_\ell}{d\rho^2} + \left\{1 - \frac{2\gamma}{\rho} - \frac{\ell(\ell+1)}{\rho^2}\right\} u_\ell = 0 \qquad 4.13$$

where

$$\gamma = \frac{Z_I Z_T e^2}{k\hbar^2} \qquad 4.14$$

The solutions of this equation are the regular and irregular coulomb wave functions, F_ℓ and G_ℓ. The asymptotic form of these functions, for large ρ is

$$F_\ell(\rho) \sim \sin(\rho - \gamma \ln 2\rho - \tfrac{1}{2}\ell\pi + \sigma_\ell)$$
$$G_\ell(\rho) \sim \cos(\rho - \gamma \ln 2\rho - \tfrac{1}{2}\ell\pi + \sigma_\ell) \qquad 4.15$$

The total wave function in this region can now be written in the form of equation 4.1

$$\psi_\ell = F_\ell(\rho) + i G_\ell(\rho) + S_\ell(F_\ell(\rho) - i G_\ell(\rho)) \qquad 4.16$$

Within the nucleus there are two expressions of equation 4.12, depending on how the particle spin couples with its angular momentum. Thus, for a spin $\frac{1}{2}$ particle, the total angular momentum j has two values $\ell+\frac{1}{2}$ and $\ell-\frac{1}{2}$. The corresponding eigen values of $\underline{\ell}.\underline{\sigma}$ are ℓ and $-(\ell+1)$ giving the

following equations:

$$\frac{d^2 u_\ell^+(\rho)}{d\rho^2} + \left\{ 1 - \frac{V_c}{E} - \frac{U_r}{E} f(\rho, r_r, a_r) + \frac{i\left(W_s f(\rho, r_i, a_i) + W_0 f'(\rho, r_i, a_i)\right)}{E} - \ell\left(\frac{\hbar}{m_\pi c}\right)^2 \frac{U_{so} f'(\rho, r_{so}, a_{so})}{E\rho} - \frac{\ell(\ell+1)}{\rho^2} \right\} u_\ell^+(\rho) = 0 \qquad 4.17$$

and

$$\frac{d^2 u_\ell^-}{d\rho^2} + \left\{ 1 - \frac{V_c}{E} - \frac{U_r}{E} f(\rho, r_r, a_r) + \frac{i\left(W_s f(\rho, r_i, a_i) + W_0 f'(\rho, r_i, a_i)\right)}{E} + (\ell+1)\left(\frac{\hbar}{m_\pi c}\right)^2 \frac{U_{so} f'(\rho, r_{so}, a_{so})}{E\rho} - \frac{\ell(\ell+1)}{\rho^2} \right\} u_\ell^- = 0 \qquad 4.18$$

For each value of ℓ, the nuclear wave functions are evaluated at a point well outside the range of the nuclear forces. At the matching radius the boundary condition imposed on the wave function in both regions is that the logarithmic derivatives at that point should equal. Therefore

$$\frac{F_\ell + i G_\ell + S_\ell^{\mp}(F_\ell - i G_\ell)}{F_\ell' + i G_\ell' + S_\ell^{\mp}(F_\ell' - i G_\ell')} = \frac{u_\ell^{\mp}}{u_\ell'^{\mp}} \qquad 4.19$$

where the presence of a prime implies differentiation of the appropriate quantity. Equation 4.19 may be used to evaluate S_ℓ^+ and S_ℓ^-. The scattering amplitudes are then given by

$$A(\theta) = f_c(\theta) + \frac{1}{2ik}\sum_{\ell=0}^{\infty}\left\{(\ell+1)S_\ell^+ + \ell S_\ell^- - 2\ell + 1\right\} e^{2i\delta_\ell} P_\ell(\cos\theta) \qquad 4.20$$

and

$$B(\theta) = \frac{1}{2ik}\sum_{\ell=0}^{\infty}(S_\ell^+ - S_\ell^-)\, e^{2i\delta_\ell} P_\ell'(\cos\theta) \qquad 4.21$$

where $P_\ell'(\cos\theta)$ is the associated Legendre polynomial, f_c is the Rutherford scattering amplitude and σ_ℓ the coulomb phase shift.

The cross-section $\frac{d\sigma}{d\Omega}(\theta)$ may be evaluated from $A(\theta)$ and $B(\theta)$ using the equation

$$\frac{d\sigma}{d\Omega} = |A(\theta)|^2 + |B(\theta)|^2 \qquad 4.22$$

and the polarisation $P(\theta)$ is given by

$$P = \frac{2\,\mathrm{im}\,A B^*}{|A(\theta)|^2 + |B(\theta)|^2}\,\underline{n} \qquad 4.23$$

where $\underline{n}$ is a unit vector perpendicular to the scattering plane.

Numerical methods

The coulomb phase shifts and the coulomb wave functions were evaluated using recurrence relations. In the case of the phase shifts σ_ℓ, the relation

$$\sigma_\ell = \sigma_{\ell+1} - \tan^{-1}\left(\frac{\gamma}{\ell+1}\right) \qquad 4.24$$

where γ is defined in equation 4.14, is used for increasing values of ℓ. Therefore, the value of σ_ℓ was found for $\ell = 50$ using the asymptotic expansion for large ℓ (reference 7, equation 2.53). The phase shifts for smaller values of were then found by recurring downwards using equation 4.24.

The regular and irregular coulomb wave

functions were evaluated using the expressions of Froeberg (reference 7). The irregular function $G_\ell(\rho)$ and its derivative $G_\ell'(\rho)$ were evaluated using the asymptotic expressions at a radius ρ_a where the asymptotic condition is satisfied. Equation 4.13 was then integrated inwards from ρ_a to the matching radius ρ_m, to give the values of $G_\ell(\rho_m)$ and $G_\ell'(\rho_m)$.

The regular coulomb functions $F_\ell(\rho)$ were evaluated by Miller's method. The value of $F_{\ell 0}(\rho)$ was set equal to zero, and the value of $\alpha F_{\ell q}$ set equal to ϵ, a small number. α is a constant which had to be determined. Recurrence relations were used to obtain the values of $\alpha F_\ell(\rho)$ and $\alpha F_\ell'(\rho)$ for values of ℓ down to $\ell = 0$. The value of α was then obtained from the Wronskian for $\ell = 0$.

$$F_\ell'(\rho)\, G_\ell(\rho) - F_\ell(\rho)\, G_\ell'(\rho) = 1 \qquad 4.25$$

The same recurrence relations were used to find the rest of the $F_\ell(\rho)$ and $F_\ell'(\rho)$.

When all the F_ℓ, F_ℓ', G_ℓ and G_ℓ' had been calculated, the accuracy of the evaluation for each value of ℓ was checked by calculating the Wronskian. If the value of the Wronskian differed from unity by more than 0.0001, the calculation of the wave functions was repeated using a larger

value of ρ_a.

The values of $u_\ell(\rho_m)$ for both values of j were found by the numerical integration of equations 4.17 and 4.18 from the origin out to ρ_m. The corresponding derivatives of $u_\ell(\rho_m)$ were determined, both by Simpsons rule quadrature of $\frac{d^2u}{d\rho^2}$ in equations 4.17 and 4.18 and by direct numerical differentiation of u_ℓ. The accuracy of the integration could then be checked by comparing the values obtained by the two methods. If they failed to agree, the integration of the radial wave equations was repeated using a shorter step-length.

The values of F_ℓ, G_ℓ, u_ℓ and their derivatives were used to solve equation 4.19. The values of S_ℓ obtained in this way were used to evaluate the scattering amplitudes $A(\theta)$ and $B(\theta)$ from equations 4.20 and 4.21. The cross-sections and polarisations were then calculated using equations 4.22 and 4.23.

The optical model parameter search code

The calculations described above were performed by a computer code based on a program written by F.G.Perey. Details of the original program are given in references 8 and 9. The non-local part of the program has been deleted. In addition to calculating the cross-sections and

polarisations, the code searched over the parameters of the optical potential to obtain the best fit to the experimental data. The following description of the search procedure is based on that given in reference 9 .

The program read in a set of M experimental quantities X_i and ΔX_i where X_i is a cross-section or a polarisation and ΔX_i the experimental error in X_i . A set of N optical model parameters a_n was also read in, and theoretical values Y_i of the cross-sections and polarisations corresponding to X_i were calculated. The program searched over the parameters a_n until it obtained the minimum of the quantity χ^2 where

$$\chi^2 = \sum_{i=1}^{M} \left(\frac{Y_i - X_i}{\Delta X_i} \right)^2 \qquad 4.26$$

The program calculated a new set of parameters a_n' by changing each of the initial parameters a_n by an amount δa_n so that.

$$a_n' = a_n + \delta a_n \qquad 4.27$$

The step-lengths δa_n were obtained by solving the normal equations. These are derived as follows.

If Y_i' represents the new values of the theoretical quantities, then we can write

$$Y_i' = Y_i + \delta Y_i \qquad 4.28$$

If the new parameters a_n' give the minimum value

of χ^2, then the equation

$$\frac{\partial}{\partial a_n}\left(\sum_{i=1}^{M}\frac{1}{(\Delta X_i)^2}(X_i - Y_i)^2\right) = 0 \qquad 4.29$$

must hold for all n. Substituting 4.27 into 4.28

$$\frac{\partial}{\partial a_n}\left\{\sum_{i=1}^{M}\frac{1}{(\Delta X_i)^2}(Y_i+\delta Y_i - X_i)^2\right\} = \sum_{i=1}^{M}\frac{2}{(\Delta X_i)^2}(Y_i+\delta Y_i - X_i)\frac{\partial Y_i}{\partial a_n} \qquad 4.30$$

If the changes δa_n in a_n are small we write (to the first order in δa_n)

$$\delta Y_i = \sum_{s=1}^{N}\frac{\partial Y_i}{\partial a_n}\delta a_n \qquad 4.31$$

so that

$$\sum_{i=1}^{M}\frac{1}{(\Delta X)^2}\frac{\partial Y_i}{\partial a_n}\sum_{s=1}^{N}\frac{\partial Y_i}{\partial a_s}\delta a_s = \sum_{i=1}^{M}\frac{1}{(\Delta X)^2}(X_i - Y_i)\frac{\partial Y_i}{\partial a_n} \qquad 4.32$$

This is the normal equation for δa_n. A similar equation exists for each value of n. As the quantities Y_i are functions only of the scattering matrix elements, the derivative terms $\frac{\partial Y_i}{\partial a_n}$ in equation 4.32 were proportional to the quantities $\frac{\partial S_\ell}{\partial a_n}$. These were calculated analytically from the equation (reference 9),

$$\frac{\partial S_\ell}{\partial a_n} = \frac{i}{2k}\left[F_\ell(\rho_m) + i\,G_\ell(\rho_m) + S_\ell(F_\ell(\rho_m) - i\,G_\ell(\rho_m)\right]^2$$

$$\times \int_0^{\rho_m} u_\ell^2(\rho)\frac{\partial f_\ell}{\partial a_n}\,d\rho \qquad 4.33$$

where

$$f_\ell = k^2 - \frac{\ell(\ell+1)}{\rho^2} + V_C(\rho) + V_N(\rho)$$

The cross-sections and polarisations were calculated using the new set of parameters and the value of χ^2 obtained. The procedure was reiterated until the values obtained for χ^2 were stationary. Sometimes, where the change in δa_n was greater than about 10%, the approximation made in equation 4.31 failed, and the new set of parameters gave no improvement in the fit. In this case the program calculated two additional values of χ^2 for values of a_n along the predicted shift direction. A parabolic fit was made to the three points, and the new value of a_n taken at the minimum of the parabola.

Conclusion

The results of the optical model analysis are discussed in Chapter 6. In general, the model was very successful in describing the observed elastic scattering and polarisation. The optical model potentials which gave the best fit to the experimental data were used to generate scattering wave functions in D.W.B.A. calculations. (See Chapters 5 and 6).

Chapter 5

In this chapter the Distorted Wave Born Approximation theory of inelastic scattering is developed. Expressions are derived for the differential cross-sections using both the Collective model and the Shell model of the nucleus.

Section 5i: The Transition Amplitude

The D.W.B.A. form of the transition amplitude of the reaction

$$A(a, a')A' \qquad 5.1$$

is given by

$$T_{fi} = \int \psi_{a'}^{(-)*}(\underline{k}_{a'}, \underline{r}) \langle a' A' | V | a A \rangle \psi_a^{(+)}(\underline{k}_a, \underline{r})\, d\underline{r} \qquad 5.2$$

where $\psi_a^{(+)}(\underline{k}_a, \underline{r})$ is an incoming elastic scattering wave in the incident channel and $\psi^{(-)}(\underline{k}_{a'}, \underline{r})$ the corresponding outgoing wave in the exit channel. V is the interaction causing the transition between the initial and final state. The term $\langle a' A' | V | a A \rangle$ is the matrix element of V over the internal states of the nucleus. It behaves like an effective interaction inducing transitions between the initial and final elastic scattering states.

Methods of evaluating the nuclear matrix element using the collective model and the nuclear shell model are given below.

Section 5ii: Collective Model Form Factors

The theory described in this section is based on the treatment given in the Ph.D. thesis of H.Sherif, submitted to the University of Seattle, Washington, 1968. (reference 10)

The transition amplitude of equation 5.2 may be written

$$T_{fi} = \langle \psi^{(-)}(\underline{k}_a, \underline{r}) | \langle I M | \Delta U | 00 \rangle | \psi^{(+)}(\underline{k}_a, \underline{r}) \qquad 5.3$$

where the discussion has been restricted to transitions between a ground state of spin and parity 0^+ and a collective state of spin I and projection M.

The interaction potential ΔU is obtained by deforming the optical potential of equation 4.7, keeping terms to the first order in the deformation parameter. It may be separated into its coulomb, real, imaginary and spin orbit parts, so that

$$\Delta U = \Delta U_c + \Delta U_r + \Delta U_i + \Delta U_{so} \qquad 5.4$$

The forms of ΔU_r and ΔU_i are obtained by making the radial parameters in the functions $f(r, r_n, a_n)$ depend on the nuclear orientation giving

$$r_n \longrightarrow r_n + \alpha_n(\hat{\underline{r}})$$

Expanding $f(r, r_n, a_n)$ by Taylor Series -

$$f(r, r_n + \alpha_n(\hat{r})) \approx f(r, r_n, a_n) + \alpha_n(\hat{\underline{r}}) \left(\frac{\partial f}{\partial r_n}\right) \qquad 5.5$$

and

$$\Delta U_r = - \alpha_r(\hat{r})\, V_0 \frac{\partial}{\partial r_r} f(r, r_r, a_r) \qquad 5.6$$

$$\Delta U_i = - i \alpha_i(\hat{r}) \left(W_S - 4 a_i W_D \frac{\partial}{\partial r_i} \right) \frac{\partial}{\partial r_i} f(r, r_i, a_i) \qquad 5.7$$

There are several forms of the deformed spin dependant term (reference10). The form proposed by the Oak-Ridge group (reference11) is a similar expansion to equations 5.6 and 5.7

$$\Delta U_{so} = \left(\frac{\hbar}{m_\pi c}\right)^2 (V_{so} + i W_{so}) \frac{1}{r} \frac{\partial^2}{\partial r \partial r_{so}} f(r, r_{so}, a_{so})$$

$$\times \frac{1}{2} \left\{ \alpha_{so}(\hat{r})\, \underline{\sigma}.\underline{\ell} + \underline{\sigma}.\underline{\ell}\, \alpha_{so}(\hat{r}) \right\} \qquad 5.8$$

The symmetrisation of the final term in equation 5.8 is required by the Hermitian property of ΔU_{so} when $W_{so} = 0$.

The Thomas form expresses ΔU_{so} as the sum of two terms

$$U_{s,def}(1) = \left(\frac{\hbar}{m_\pi c}\right)^2 (V_{so} + i W_{so})\, \alpha_{so}(\hat{r})$$

$$\times \frac{1}{r} \frac{\partial}{\partial r} \left(\frac{\partial f}{\partial r_{so}} \right) \underline{\sigma}.\underline{\ell} \qquad 5.9$$

and

$$U_{s,def}(2) = \left(\frac{\hbar}{m_\pi c}\right)^2 (V_{so} + i W_{so}) \frac{\partial f}{\partial r_{so}}$$

$$\times \underline{\sigma}.\left\{ \underline{\nabla}\, \alpha_{so}(\hat{r}) \times \frac{1}{i} \underline{\nabla} \right\} \qquad 5.10$$

$U_{s,def}(1)$ is very similar to ΔU_{so} as given by equation 5.8.

The optical model wave functions of equation 5.2 have been given no explicit dependance on spin.

However, because of the spin orbit term in the optical model potential the ψ's are matrices in spin space. For example

$$\psi^{(+)}(\underline{k}_a, \underline{r}) = \sum_{m_b} |1/2, m_b\rangle \psi^{(+)}_{m_b m_a}(\underline{k}_a, \underline{r}) \qquad 5.11$$

where m_b is the spin. Terms with $m_b \neq m_a$ allow the possibility of spin flip.

The deformation parameters α_{rn} are expanded in a multipole series

$$\alpha(\hat{\underline{r}}) = \sum_{\ell m} \beta_{\ell m} Y_\ell^{m*}(\hat{\underline{r}}) \qquad 5.12$$

The nuclear matrix element can now be written

$$\langle IM | \alpha(\hat{\underline{r}}) | 00 \rangle = \frac{\beta_I r_n}{(2I+1)^{1/2}} Y_I^{M*}(\hat{\underline{r}}) \qquad 5.13$$

where, for rotational excitations, β_I is the deformation parameter and r_n is the radius parameter.

The transition amplitude can be expressed as follows

$$T_{fi} = A_0 + A_1 + A_2 \qquad 5.14$$

where A_0 is the contribution due to the $\Delta U_c + \Delta U_r + \Delta U_\ell$ parts of the interaction, A_1 arises from $U_{s,def}(1)$ and A_2 from $U_{s,def}(2)$.

Then

$$A_0 = \frac{\beta_I r_r}{(2I+1)^{1/2}} \sum_{m_b m_{b'}} \left\langle \psi^{(-)}_{m_{a'} m_{b'}}(\underline{k}_{a'}, \underline{r}) \right| \left\langle \tfrac{1}{2} m_{b'} \right| \mathcal{F}(r) Y_I^{M*}$$

P.T.O

$$\times \left| \tfrac{1}{2} m_b \right\rangle \left| \psi^{(+)}_{m_a m_b} (\underline{k}_a, \underline{r}) \right\rangle$$

5.15

$$A_1 = \frac{\beta_I^{so} r_{so}}{(2I+1)^{1/2}} \sum_{m_b m_{b'}} \left\langle \psi^{(-)}_{m_{a'} m_{b'}} (\underline{k}_{a'}, \underline{r}) \right| \left\langle \tfrac{1}{2} m_{b'} \right| \mathcal{J}_1 (r) Y_I^{M*} (\hat{\underline{r}}) \, \underline{\sigma} \cdot \underline{\ell}$$

$$\times \left| \tfrac{1}{2} m_b \right\rangle \left| \psi_{m_a m_b} (k_a, r) \right\rangle$$

5.16

and

$$A_2 = \frac{\beta_I^{so} r_{so}}{(2I+1)^{1/2}} \sum_{m_b m_{b'}} \left\langle \psi^{(-)}_{m_{b'} m_b} (\underline{k}_{a'} \underline{r}) \right| \left\langle \tfrac{1}{2} m_{b'} \right| \mathcal{J}_2 (r)$$

$$\times \underline{\sigma} \cdot \left\{ \underline{\nabla} Y_I^{M*} (\hat{\underline{r}}) \times \frac{1}{i} \nabla \right\} \left| \tfrac{1}{2} m_b \right\rangle \left| \psi^{(+)}_{m_a m_b} (\underline{k}_a, \underline{r}) \right\rangle$$

5.17

The radial form factors are given by:

$$\mathcal{J}_0 = (r_c / r_0) \, g_I (r_c, r) - V_0 \frac{\partial}{\partial r_r} f (r, r_r, a_r)$$

$$- i (r_i / r_0) \left(W_s - 4 a_i W_0 \frac{\partial}{\partial r} \right) \frac{\partial}{\partial r_i} f (r, r_i, a_i)$$

5.18

$$\mathcal{J}_1 = (\hbar / m_\pi c)^2 (V_{so} + i W_{so}) \frac{1}{r} \frac{\partial^2}{\partial r \, \partial r_{so}} f (r, r_{so}, a_{so}) \qquad 5.19$$

$$\mathcal{J}_2 = (\hbar / m_\pi c)^2 (V_{so} + i W_{so}) \frac{\partial}{\partial r_{so}} f (r, r_{so}, a_{so}) \qquad 5.20$$

where g_I is the contribution from the coulomb potential, given by

$$g_I (r_c, r) = \frac{3 Z_1 Z_T e^2}{r_c^2 (2I+1)} \begin{cases} 0 & r < r_c \\ (r_c / r)^{I+1} & r \geq r_c \end{cases} \qquad 5.21$$

The cross-sections are related to the transition amplitude T_{fi} by equation 5.61 . The calculation

of A_0 and A_1 from the above expressions is similar to the method used to evaluate the shell model transition amplitude described in the next section. The evaluation of A_2 is described in reference 10.

Section 5iii: Shell model form factors

The nuclear matrix element $\langle a'A'|V|aA\rangle$ may be expressed as follows

$$\langle a'A'|V|aA\rangle = \langle s_{a'} m_{a'}, t_{a'} \tau_{a'}, T_{A'} \tau_{A'}, J_{A'} M_{A'}|V| s_a m_a, t_a \tau_a, T_A \tau_A, J_A M_A\rangle \qquad 5.22$$

The scalar interaction V can be expanded in terms of multipoles acting on the isospin spaces of the projectile and the target (reference 12).

$$V = \sum_T V^{(T)} O_T = \sum_{T\tau} (-)^\tau V^{T\tau} O_{T,-\tau} \qquad 5.23$$

$V^{(T)}$ is a tensor of rank T which produces a change of T in the isospin of the target. O_T is a similar tensor of rank T acting on the isospin space of the projectile. T is restricted to the $2t_a + 1$ values between 0 and $2t_a$. For $T = 0$, O_T is a scalar, and leaves the isospin of the projectile unchanged. We may therefore take it as the unit operator. Similarly the vector may be represented by the Pauli isospin operator, so that

$$O_0 = \underline{1} \quad ; \quad O_1 = \underline{\tau} \qquad 5.24$$

The operator $V^{(\tau)}$ is a scalar in coordinate and spin space. Therefore it may be expanded in the following series

$$V^{(\tau)}(r, \xi_a, \xi_A) = \sum_{LSJM} (-)^M V^{(\tau)}_{LSJM}(r, \xi_A)\, T_{LSJ,-M}(\theta, \phi, \xi_a) \qquad 5.25$$

ξ_a and ξ_A are the internal coordinates of a and A respectively, M is the projection of J, and r, θ and ϕ are the relative coordinates of the target and projectile.

The irreducible tensor $T_{LSJM}(\theta, \phi, \xi_a)$ is a composite tensor formed from the product of the irreducible spin tensor $S_S(\xi_a)$ and the angle tensor $i^L Y_L(\theta, \phi)$ so that T_{LSJM} can be written

$$T_{LSJM} = \sum_m i^L Y_L(\theta, \phi)\, S_{S,M-m}(\xi_a) \times (-)^{L-S+M} \hat{J} \begin{pmatrix} L & S & J \\ m & M-m & -M \end{pmatrix} \qquad 5.26$$

where $\hat{p} = (2p+1)^{\frac{1}{2}}$

Each term in the expansion 5.25 corresponds to the amounts of angular momenta L, S and J transferred to the target nucleus during inelastic scattering. L arises from a change in the orbital motion of the projectile in the multipole field Y_L^M, and the spin transfer S from coupling to the projectile spin. Terms with $S \neq 0$ may be

referred to as "spin-flip". J is the vector resultant of L and S. The parity change is given by $(-)^L$, and, for a 0 spin ground state, J must equal the spin of the residual nucleus.

The adjoint $T^\dagger$ of a sperical tensor is defined as

$$T^\dagger_{LSJ\,N} = (-)^{J+N}\, T_{L\,S\,J,\,-N}$$

so that

$$T_{LSJ,-N} = (-)^{-J-N} \sum_m (-)^{2N-m}\, \hat{J}\, i^L\, Y_L^{m*}\, \zeta_{S,\,m-N} \begin{pmatrix} L & S & J \\ m & N-m & -N \end{pmatrix} \quad 5.27$$

Using equations 5.27, 5.25 and 5.23, equation 5.22 becomes

$$\langle a'A' | V | aA \rangle = \Big\langle s_a\, m_{a'},\, t_a\, \tau_{a'},\, T_{A'}\, \tau_{A'},\, J_{A'}, M_A \Big| \sum_{\Gamma L S J} \sum_{N m \tau}$$

$$\Big\{ (-)^{2N-m-J}\, i^L\, Y_L^{m*}(\theta,\phi)\, \hat{J}\, V^{T,\tau}_{LSJN}(r, \xi_A)\, S_{S,\,m-N}(\xi_a)\, O_{T,\,-\tau}$$

$$\begin{pmatrix} L & S & J \\ m & N-m & -N \end{pmatrix} \Big| s_a\, m_a,\, t_a\, \tau_a,\, T_A\, \tau_A,\, J_A\, M_A \Big\rangle$$

5.28

The Wigner-Eckart theorem is defined as

$$\langle J'M' | T_{KQ} | JM \rangle = (-)^{J-K+M'} \hat{J}\, i$$

$$\times \begin{pmatrix} J & K & J' \\ M & Q & -M' \end{pmatrix} \langle J' \| T_K \| J \rangle$$

and

$$\langle J' \| T_K \| J \rangle = \sum_{MQ} (-)^{J-K+M'} \hat{J}',$$

$$\times \begin{pmatrix} J & K & J' \\ M & Q & -M' \end{pmatrix} \langle J'M' | T_{KQ} | JM \rangle \quad 5.29$$

Using the Wigner-Eckart theorem we get

$$\langle a'A' | V | aA \rangle = \sum_{TLSJ} \sum_{\mu m \tau} (-)^{2\mu - m - S} (-)^{S_a + m_{a'} + J_A + M_{A'}}$$

$$(-)^{t_a + \tau_{a'} + T_A + \tau_{A'}} i^L Y_L^{m*}(\theta,\phi) \hat{J} \begin{pmatrix} L & S & J \\ m & \mu - m & -\mu \end{pmatrix}$$

$$\hat{S}_a \begin{pmatrix} S_a & S & S_a \\ m_a & m-\mu & -m_{a'} \end{pmatrix} \langle S_a \| S_S \| S_a \rangle \hat{t}_a \begin{pmatrix} t_a & T & t_a \\ \tau_a & -\tau & -\tau_{a'} \end{pmatrix} \langle t_a \| O_T \| t_a \rangle$$

$$\hat{J}_{A'} \hat{T}_{A'} \begin{pmatrix} J_A & J & J_{A'} \\ M_A & \mu & -M_{A'} \end{pmatrix} \begin{pmatrix} T_A & T & T_{A'} \\ \tau_A & -\tau & -\tau_{A'} \end{pmatrix}$$

$$\langle T_{A'} J_{A'} \| V_{LSJ}^{(T)} (r, \tau_A) \| T_A J_A \rangle$$

5.30

$$= \sum_{\substack{TLSJ \\ \mu m \tau}} (-)^{\mu - 2m} (-)^{S_a + m_a + J_A + M_{A'}} (-)^{t_a + \tau_{a'} + T_A + \tau_{A'}}$$

$$\times i^L Y_L^{m*}(\theta,\phi) \begin{pmatrix} L & S & J \\ m & \mu - m & -\mu \end{pmatrix} \begin{pmatrix} S_a & S_a & S \\ m_a & -m_{a'} & m-\mu \end{pmatrix}$$

$$\begin{pmatrix} J_A & J & J_{A'} \\ M_A & \mu & -M_{A'} \end{pmatrix} \begin{pmatrix} t_a & T & t_a \\ \tau_a & -\tau & -\tau_{a'} \end{pmatrix} \begin{pmatrix} T_A & T & T_{A'} \\ \tau_A & \tau & -\tau_{A'} \end{pmatrix}$$

$$\times \hat{J} \hat{S}_a \hat{t}_a \hat{J}_{A'} \hat{T}_{A'} \langle S_a \| S_S \| S_a \rangle \langle t_a \| O_T \| t_a \rangle \langle T_{A'} J_{A'} \| V_{LSJ}^{T} \| T_A J_A \rangle$$

5.31

The projection quantum numbers are related by

$$\begin{aligned} \mu - m &= m_a - m_{a'} \\ \tau &= \tau_{A'} - \tau_A = \tau_a - \tau_{a'} \\ \mu &= M_{A'} - M_A \\ m &= M_{A'} - M_A + m_{a'} - m_a \end{aligned}$$

so that

$$\langle a'A'|V|aA\rangle = \sum_{\substack{T L S J \\ \mu m \tau}} (-)^{s_a - 2m_{a'} + m_a + 2M_{A'} - M_A} (-)^{J_A + L - S - J}$$

$$(-)^{T_A + t_a - \tau_{a'} - \tau_{A'}} i^L Y_L^{m*}(\theta,\phi) \begin{pmatrix} L & S & J \\ m & m_a - m_{a'} & M_A - M_{A'} \end{pmatrix}$$

$$\begin{pmatrix} s_a & s_a & S \\ m_a & -m_{a'} & m_{a'} - m_a \end{pmatrix} \begin{pmatrix} J_A & J & J_{A'} \\ M_A & M_{A'} - M_A & -M_{A'} \end{pmatrix}$$

$$\begin{pmatrix} t_a & T & t_a \\ \tau_a & \tau_{A'} - \tau_A & -\tau_{a'} \end{pmatrix} \begin{pmatrix} T_A & T & T_{A'} \\ \tau_A & \tau_{A'} - \tau_A & -\tau_{A'} \end{pmatrix}$$

$$\hat{J}\,\hat{S}\,\hat{J}_{A'}\,\hat{t}_a\,\hat{T}_{A'}\; G^T_{LSJ}(r) \qquad 5.32$$

where

$$G^T_{LSJ}(r) = (-)^{L+S-J}\,\hat{s}_a/\hat{S}\,\langle s_a \| S_s \| s_a\rangle \langle t_a \| O_T \| t_a\rangle$$

$$\langle J_{A'}, T_{A'} \| V^{(T)}_{LSJ}(r) \| J_A, T_A\rangle \qquad 5.33$$

The spin tensor S_s is a tensor of rank S, where S may have one of the $2s_a + 1$ values between 0 and $2s_a$. Therefore, as in equation 5.24 we may say

$$S_0 = \underline{1} \qquad \text{and} \qquad S_1 = \underline{\sigma} \qquad 5.34$$

where $\underline{\sigma}$ is the Pauli spin operator.

$G^T_{LSJ}(r)$ can be expressed as the product of a spectroscopic amplitude A and a radial form factor F so that

$$G^T_{LSJ} = A^T_{LSJ}\, F^T_{LSJ} \qquad 5.35$$

A^T_{LSJ} depends on the type of nuclear model used, while F_{LSJ} depends on the form factor of

the nuclear potential and on the radial shape of the nuclear wave functions. A T-independant function G_{LSJ} may be defined

$$G_{LSJ} = \sum_{T} (-)^{t_a + T_A + \tau_{a'} + \tau_{A'}} \begin{pmatrix} t_a & T & t_a \\ \tau_a & \tau_A - \tau_{A'} & -\tau_{a'} \end{pmatrix} \begin{pmatrix} T_A & T & T_{A'} \\ \tau_A & \tau_{A'} - \tau_A & -\tau_{A'} \end{pmatrix} G^{T}_{LSJ} \qquad 5.36$$

It can be seen from equation 5.36 that the amplitudes for the various isospin values T add coherently, reflecting the fact that in practice one deals with isospin polarised particles. In general F^{T}_{LSJ} is independant of T, so that we may write

$$G_{LSJ}(r) = A_{LSJ} F_{LSJ}(r) \qquad 5.37$$

where

$$A_{LSJ} = \sum_{T} (-)^{t_a + T_A + \tau_{a'} + \tau_{A'}} \begin{pmatrix} t_a & T & t_a \\ \tau_a & \tau_A - \tau_{A'} & -\tau_{a'} \end{pmatrix} \hat{t}_a \hat{T}_{A'} \begin{pmatrix} T_A & T & T_{A'} \\ \tau_A & \tau_{A'} - \tau_A & -\tau_{A'} \end{pmatrix} A^{T}_{LSJ} \qquad 5.38$$

The expression for the transition amplitude T_{fi} of equation 5.2 may be written

$$T_{fi} = \langle \underline{k}_{a'}, s_a m_{a'}, t_a \tau_{a'}, T_A \tau_{A'}; J_A M_{A'} | V | \underline{k}_a, s_a m_a, t_a \tau_a, T_A \tau_A, J_A M_A \rangle$$

If there is coupling between the particle's spin and orbital angular momentum, the scattering wave functions are matrices in spin-space, so that

$$T_{fi} = \sum_{m_b m_{b'}} \int dr \; \psi^{(-)*}_{m_{b'} m_{a'}} \; \langle s_a m_{a'}, t_a \tau_{a'}, T_A \tau_{A'}, J_A M_{A'} | V |$$

$$s_a m_a, t_a \tau_a, T_A \tau_A, J_A M_A \rangle \; \psi_{m_b m_a}$$

5.39

$$= \sum_{\substack{m' m_{b'} m_b \\ LSJT}} (-)^{s_a - 2m_{b'} + m_b + 2M_{A'} - M_A} \; (-)^{J_A + L - S - J} (-)^{T_A + t_a - \tau_{a'} - \tau_{A'}}$$

$$\begin{pmatrix} L & S & J \\ m' & m_b - m_{b'} & M_A - M_{A'} \end{pmatrix} \begin{pmatrix} s_a & s_a & S \\ m_b & -m_{b'} & m_{b'} - m_b \end{pmatrix}$$

$$\begin{pmatrix} t_a & T & t_a \\ \tau_a & \tau_A - \tau_{A'} & -\tau_{a'} \end{pmatrix} \begin{pmatrix} T_A & T & T_{A'} \\ \tau_A & \tau_{A'} - \tau_A & -\tau_{A'} \end{pmatrix} \begin{pmatrix} J_A & J & J_{A'} \\ M_A & M_{A'} - M_A & -M_{A'} \end{pmatrix}$$

$$\int dr \; \psi_{m_{b'} m_{a'}}(k_{a'}) \, Y_L^{m'*} \, G^T_{LSJ} \, \psi_{m_b m_a}(k_A) \; \hat{J} \, \hat{S} \, \hat{t}_a \, \hat{J}_{A'} \, \hat{T}_{A'}$$

5.40

$$= \sum_{LSJ} (-)^{J_{A'} - J + M_{A'}} \begin{pmatrix} J_A & J & J_{A'} \\ M_A & M_{A'} - M_A & -M_{A'} \end{pmatrix} A_{LSJ}$$

$$\times \left\{ \sum_{m' m_{b'} m_b} (-)^{s_a - 2m_{b'} + m_b + M_{A'} - M_A} \; (-)^{L-S} \begin{pmatrix} L & S & J \\ m' & m_b - m_{b'} & M_A - M_{A'} \end{pmatrix} \hat{J} \, \hat{S} \, \hat{J}_{A'} \right.$$

$$\times \begin{pmatrix} s_a & s_a & S \\ m_b & -m_b & m_{b'} - m_b \end{pmatrix} \int dr \; \psi^{(-)*}_{m_{b'} m_{a'}}(\underline{r}, \underline{k}_{a'})$$

$$\left. i^L \, Y_L^{m'*}(\theta, \phi) \; F_{LSJ}(r) \; \psi_{m_b m_a}(\underline{r}, \underline{k}_a) \right\}$$

5.41

$$= \sum_{LSJ} \hat{J} \hat{J}_{A'} A_{LSJ} (-)^{J_A - J + M_{A'}}$$

$$\times \begin{pmatrix} J_A & J & J_{A'} \\ M_A & M_{A'} - M_A & -M_{A'} \end{pmatrix} \beta_{LSJ}^{m\, m_a m_{a'}} (\underline{k}_{a'}\, \underline{k}_a)$$

5.42

where

$$\beta_{LSJ}^{m, m_a m_{a'}} = \sum_{m' m_{b'} m_b} (-)^{s_a - 2m_{b'} + m_b} (-)^{L-S} (-)^{M_{A'} - M_A} \hat{S}$$

$$\begin{pmatrix} L & S & J \\ m & m_b - m_{b'} & M_A - M_{A'} \end{pmatrix} \begin{pmatrix} s_a & s_a & S \\ m_b & -m_{b'} & m_{b'} - m_b \end{pmatrix}$$

$$\int dr\; \psi^{(-)*}_{m_b m_{b'}} (\underline{k}_{a'}, \underline{r})\, i^{-L}\, Y_L^{m*}(\theta, \phi)\, F_{LSJ}(r)\, \psi^{(+)}_{m_b m_a} (k_a, r)$$

5.43

Section 5iv: The scattering wave functions and the evaluation of $\beta_{LSJ}^{m, m_a m_{a'}}$

The scattering wave functions $\psi^{(\mp)}$ are expanded in terms of partial waves

$$\psi^{(+)}_{m_b m_a} = \frac{4\pi}{k_a r} \sum_{l_a j_a \lambda_a} (\hat{j}_a)^2 \begin{pmatrix} l_a & s_a & j_a \\ \lambda_a & m_a & -(\lambda_a + m_a) \end{pmatrix}$$

$$\begin{pmatrix} l_a & s_a & j_a \\ \lambda_a + m_a - m_b & m_b & -(\lambda_a + m_a) \end{pmatrix} i^{l_a} Y_{l_a}^{\lambda_a}(\theta_{k_a}, \phi_{k_a})\, Y_{l_a}^{\lambda_a - m_a - m_b}(\theta_r, \phi_r)\, \psi_{l_a j_a}(k_a, r)$$

5.44

where $(\theta_{k_a}\, \phi_{k_a})$ are the angular coordinates of k_a, and (θ_r, ϕ_r) are the corresponding coordinates of r. The incoming and outgoing wave functions are related by time reversal considerations so that

$$\psi^{(-)}_{m_b' m_a'}(\underline{k}_{a'}, \underline{r}) = (-)^{m_{a'} - m_{b'}} \psi_{-m_{b'} - m_{a'}}(-\underline{k}_{a'}, \underline{r})$$

$$= \frac{4\pi}{k_{a'} r} \sum_{\ell_{a'} j_{a'} \lambda_{a'}} (\hat{j}_{a'})^2 \begin{pmatrix} \ell_{a'} & s_a & j_a \\ \lambda_{a'} & -m_a & m_{a'} - \lambda_{a'} \end{pmatrix} \begin{pmatrix} \ell_{a'} & s_a & j_a \\ \lambda_{a'} + m_{a'} - m_{b'} & -m_{b'} & m_{b'} - \lambda_{a'} \end{pmatrix}$$

$$(-)^{m_{a'} - m_{b'}} i^{-\ell_a} Y_{\ell_a'}^{\lambda_a' - m_{a'} + m_{b'}}(\theta_r, \phi_r) \psi_{\ell_a' j_a'}(k_{a'}, r) Y_{\ell_a'}^{\lambda_a' *}(\theta_{k_{a'}}, \phi_{k_{a'}})$$

5.45

where $\psi_{\ell_a j_a}(\underline{k}_a, \underline{r})$ are the solutions of Schroedinger's equation

$$\left\{ \frac{d^2}{dr^2} + k^2 - \frac{\ell(\ell+1)}{r^2} - \frac{2\mu}{\hbar^2} \left(U(r) + U_c + U_\ell^j \right) \right\} \psi_{\ell j} = 0 \qquad 5.46$$

U_c is the coulomb potential, U_ℓ^j the spin-orbit potential, and $U(r)$ the central nuclear potential. $U(r)$ is complex and may be written

$$U(r) = V(r) + i W(r).$$

Equation 5.43 can be written

$$\beta^{m, m_a m_{a'}}_{LSJ} = \hat{S} \sum_{m' m_b' m_b} (-)^{S_a - 2m_{b'} + m_b} (-)^{L-S} (-)^{M_{A'} - M_A}$$

$$\begin{pmatrix} L & S & J \\ m & m_b - m_{b'} & M_A - M_{A'} \end{pmatrix} \begin{pmatrix} s_a & s_a & S \\ m_b & -m_{b'} & m_{b'} - m_b \end{pmatrix} I \qquad 5.47$$

where

$$I = \int dr \, \psi^{(-)*}_{m_{b'} m_{a'}}(k_{a'}, r) \, i^{-L} Y_L^{m'*}(\theta, \phi) F_{LSJ}(r) \psi_{m_b m_a}(k_a, r)$$

$$= \frac{16\pi^2}{k_a k_{a'}} \sum_{\substack{\ell_a \ell_{a'} \\ j_a j_{a'} \\ \lambda_a \lambda_{a'}}} \begin{pmatrix} \ell_a & s_a & j_a \\ \lambda_a & m_a & -\lambda_a - m_a \end{pmatrix} \begin{pmatrix} \ell_a & s_a & j_a \\ \lambda_a + m_a - m_b & m_b & -\lambda_a - m_a \end{pmatrix}$$

P.T.O.

$$\times \begin{pmatrix} \ell_a' & S_a' & j_a' \\ \lambda_a' & -m_a' & m_a'-\lambda_a' \end{pmatrix} \begin{pmatrix} \ell_a' & S_a & j_a' \\ \lambda_a'-m_a'+m_b' & -m_b' & m_a'-\lambda_a' \end{pmatrix}$$

$$(\hat{j}_a \hat{j}_{a'})^2 \; i^{\ell_a - \ell_{a'} - L} \; Y_{\ell_a}^{\lambda_a *}(\theta_{ka}\phi_{ka}) \; Y_{\ell_{a'}}^{\lambda_{a'} *}(\theta_{ka'}\phi_{ka'}) \; (-)^{m_{a'}-m_{b'}}$$

$$\int d\Omega \; Y_{\ell_a}^{\lambda_{a'}+m_{b'}-m_{a'}}(\theta_r,\phi_r) \; Y_L^{m' *}(\theta_r,\phi_r) \; Y_{\ell_a}^{\lambda_a - m_b + m_a}(\theta_r\phi_r)$$

$$\int_0^\infty dr \; \psi_{\ell_{a'} j_{a'}}(k_{a'}, r) \; F_{LSJ}(r) \; \psi_{\ell_a j_a}(k_a, r) \qquad 5.48$$

$$= (-)^{m_{a'}-m_{b'}} \; \frac{16\pi^2}{k_a k_{a'}} \sum i^{\ell_a - \ell_{a'} - L} \; Y_{\ell_a}^{\lambda_a *}(\theta_{ka},\phi_{ka})$$

$$Y_{\ell_{a'}}^{\lambda_{a'}}(\theta_{ka}\phi_{ka}) \; \frac{\hat{\ell}_{a'}\,\ell_a}{(4\pi)^{\frac{1}{2}}\hat{L}} \; (\hat{L}\,\hat{j}_a\,\hat{j}_{a'})^2 \begin{pmatrix} \ell_a & S_a & j_a \\ \lambda_a & m_a & \lambda_a + m_a \end{pmatrix}$$

$$\begin{pmatrix} \ell_a & S_a & j_a \\ \lambda_a + m_a - m_b & m_b & \lambda_a + m_a \end{pmatrix} \begin{pmatrix} \ell_{a'} & S_{a'} & j_{a'} \\ \lambda_{a'} & -m_{a'} & m_{a'} - \lambda_{a'} \end{pmatrix}$$

$$\begin{pmatrix} \ell_{a'} & S_{a'} & j_{a'} \\ \lambda_{a'} - m_{a'} + m_{b'} & -m_{b'} & \lambda_{a'} - m_{a'} \end{pmatrix} \begin{pmatrix} \ell_a & \ell_{a'} & L \\ \lambda_a - m_b + m_a & \lambda_{a'} + m_{b'} - m_{a'} & -m' \end{pmatrix}$$

$$\begin{pmatrix} \ell_a & \ell_{a'} & L \\ 0 & 0 & 0 \end{pmatrix} (-)^{m'} \; f^{LSJ}_{\ell_a j_a \ell_{a'} j_{a'}}(k_a, k_{a'}) \qquad 5.49$$

where

$$f^{LSJ}_{\ell_a j_a \ell_{a'} j_{a'}} = \int dr \; \psi_{\ell_{a'} j_{a'}}(k_{a'} r) \; F_{LSJ}(r) \; \psi_{\ell_a j_a}(k_a, r) \qquad 5.50$$

We choose the z-axis to be along $\underline{k}_a$ and the y-axis is along $\underline{k}_a \wedge \underline{k}_{a'}$ so that

$$Y_{\ell_a}^{\lambda_a *}(0,0) = \delta_{\lambda_a,0} \frac{\hat{\ell}_a}{(4\pi)^{1/2}}$$

and

$$Y_{\ell_{a'}}^{\lambda_{a'} *}(\theta,0) = (-)^{\lambda_{a'}} \frac{\hat{\ell}_{a'}}{(4\pi)^{1/2}} \left\{ \frac{(\ell_{a'} - \lambda_{a'})!}{(\ell_{a'} + \lambda_{a'})!} \right\}^{1/2} P_{\ell_a}^{\lambda_{a'}}(\theta) \qquad 5.51$$

Thus

$$I = \frac{16\pi^2}{k_a k_{a'}} \frac{(-)^{m_{a'} - m_{b'}}}{(4\pi)^{3/2}} \sum_{\substack{\ell_a \ell_{a'} j_a j_{a'} \\ \lambda_{a'}}} (-)^{m' + \lambda_{a'}} i^{\ell_a - \ell_{a'} - L}$$

$$\hat{L} (\hat{\ell}_a \hat{\ell}_{a'} \hat{j}_a \hat{j}_{a'})^2 \left\{ \frac{(\ell_{a'} - \lambda_{a'})!}{(\ell_{a'} + \lambda_{a'})!} \right\} P_{\ell_{a'}}^{\lambda_{a'}}(\theta) \begin{pmatrix} \ell_a & s_a & j_a \\ 0 & m_a & -m_a \end{pmatrix}$$

$$\begin{pmatrix} \ell_a & s_a & j_a \\ m_a - m_b & m_a & -m_a \end{pmatrix} \begin{pmatrix} \ell_{a'} & s_{a'} & j_{a'} \\ \lambda_{a'} & -m_{a'} & m_{a'} - \lambda_{a'} \end{pmatrix}$$

$$\begin{pmatrix} \ell_{a'} & s_{a'} & j_{a'} \\ \lambda_{a'} - m_{a'} + m_{b'} & -m_{b'} & \lambda_{a'} - m_{a'} \end{pmatrix} \begin{pmatrix} \ell_a & \ell_{a'} & L \\ m_a - m_b & \lambda_{a'} + m_{b'} - m_{a'} & -m' \end{pmatrix}$$

$$\begin{pmatrix} \ell_a & \ell_{a'} & L \\ 0 & 0 & 0 \end{pmatrix} f^{LSJ}_{\ell_a \ell_{a'} j_a j_{a'}}(k_{a'} k_a). \qquad 5.52$$

As

$$m' = M_{A'} - M_A + m_{b'} - m_b$$

and

$$\lambda_{a'} = m' - m_{b'} + m_b + m_{a'} - m_a$$

then

$$\lambda_{a'} = M_{A'} - M_A + m_{a'} - m_a \equiv m$$

so that

$$\beta^{m\, m_a\, m_{a'}}_{LSJ}(k_{a'}, k_a) = \frac{16\pi^2}{k_a k_{a'}} \frac{1}{4\pi^{3/2}} \sum i^{\ell_a - \ell_{a'} - L} (\hat{\ell}_a \hat{\ell}_{a'})^2$$

$$(\hat{j}_a \hat{j}_{a'}) \; {}^{1}/_{\hat{J}} \; (-)^{m_a - s_a - m_{a'}} \left[\frac{(\ell_{a'} - m)!}{(\ell_a - m)!}\right]^{1/2} P^{m}_{\ell_{a'}}(\theta)$$

$$\begin{pmatrix} \ell_a & s_a & j_a \\ 0 & m_a & -m_a \end{pmatrix} \begin{pmatrix} \ell_{a'} & s_a & j_{a'} \\ m & -m_{a'} & m_{a'} - m \end{pmatrix}$$

$$\begin{pmatrix} \ell_a & \ell_{a'} & L \\ 0 & 0 & 0 \end{pmatrix} f^{LSJ}_{\ell_a \ell_{a'} j_a j_{a'}} \quad \Phi \qquad 5.53$$

where

$$\Phi = \sum_{m', m_b, m_{b'}} (-)^{m_b + m_{b'} + m_a - 2s_a + m + m' + L - S + M_{A'} - M_A}$$

$$\begin{pmatrix} L & S & J \\ m' & m_b - m_{b'} & M_A - M_{A'} \end{pmatrix} \begin{pmatrix} s_a & s_a & S \\ m_b & -m_{b'} & m_{b'} - m_b \end{pmatrix}$$

$$\begin{pmatrix} \ell_a & s_a & j_a \\ m_A - m_b & m_b & -m_a \end{pmatrix} \begin{pmatrix} \ell_{a'} & s_{a'} & j_{a'} \\ m - m_{b'} + m_b & -m_{b'} & -m + m_{a'} \end{pmatrix}$$

$$\cdot \begin{pmatrix} \ell_a & \ell_{a'} & L \\ m_a - m_b & m + m_{b'} - m_{a'} & -m' \end{pmatrix} \hat{J}\, \hat{S}\, \hat{j}_a\, \hat{j}_{a'}\, \hat{L}$$

5.54

Using the relation between 3-j and 6-j coefficients (reference 12)

$$\mathcal{J} = (-)^{m_a - m - 2m_{a'} J - 2S_a} \hat{J}\hat{S}\hat{j}_a\hat{j}_{a'}\hat{L} \begin{pmatrix} J & j_a & j_{a'} \\ M_{A'} - M_A & -m_a & -m+m_{a'} \end{pmatrix} \begin{pmatrix} J & j_a & j_{a'} \\ L & \ell_a & \ell_{a'} \\ S & S_a & S_a \end{pmatrix}$$

5.55

Equation 5.53 now becomes

$$\beta^{m\, m_a\, m_{a'}}_{LSJ}(k_{a'}, k_a) = \frac{16\pi^2}{k_a k_{a'}} \frac{1}{(4\pi)^{3/2}} (-)^{2m_a + m_{a'} - m + S_a} \hat{S}\hat{L}$$

$$\sum_{\ell_a \ell_{a'} j_a j_{a'}} (-)^{J} (\hat{\ell}_a \hat{\ell}_{a'} \hat{j}_a \hat{j}_{a'})^2 \left[\frac{(\ell_{a'} - m)!}{(\ell_{a'} + m)!}\right]^{1/2} P^m_{\ell_a}(\Theta)\, i^{\ell_a - \ell_{a'} - L}$$

$$\begin{pmatrix} J & j_a & j_{a'} \\ M_{A'} - M_A & -m_a & -m+m_{a'} \end{pmatrix} \begin{pmatrix} \ell_a & S_a & j_a \\ 0 & m_a & -m_a \end{pmatrix}$$

$$\begin{pmatrix} \ell_{a'} & S_a & j_{a'} \\ m & -m_{a'} & m-m_{a'} \end{pmatrix} \begin{pmatrix} \ell_a & \ell_{a'} & L \\ 0 & 0 & 0 \end{pmatrix}$$

$$\begin{pmatrix} J & j_a & j_{a'} \\ L & \ell_a & \ell_{a'} \\ S & S_a & S_a \end{pmatrix} f^{LSJ}_{\ell_a j_a \ell_{a'} j_{a'}}$$

5.56

Using the symmetry relations of 3-j coefficients (reference 12)

$$\beta^{m\, m_a m_{a'}}_{LSJ}(k_{a'} k_a) = \frac{16\pi^2}{k_a k_{a'} (4\pi)^{3/2}} (-)^{2m_a + m_{a'} - m} (-)^{S_a} \hat{S}\hat{L}$$

$$\times \sum_{\ell_a \ell_{a'} j_a j_{a'}} (-)^{2j_a - j_{a'} - J} (\hat{\ell}_a \hat{\ell}_{a'} \hat{j}_a \hat{j}_{a'})^2 \left[\frac{(\ell_a - m)!}{(\ell_a + m)}\right]^{1/2} P^m_{\ell_{a'}}(\Theta)$$

$$i^{l_a - l_{a'} - L} \begin{pmatrix} j_{a'} & J & j_a \\ m_{a'} - m & m - m_{a'} + m_a & -m_a \end{pmatrix} \begin{pmatrix} l_a & s_a & j_a \\ 0 & m_a & -m_a \end{pmatrix}$$

$$\begin{pmatrix} l_{a'} & s_a & j_{a'} \\ -m & m_{a'} & m - m_{a'} \end{pmatrix} \begin{pmatrix} l_{a'} & L & l_a \\ 0 & 0 & 0 \end{pmatrix}$$

$$\begin{pmatrix} J & j_a & j_{a'} \\ L & l_a & l_{a'} \\ S & s_a & s_a \end{pmatrix} f^{LSJ}_{l_a l_{a'} j_a j_{a'}}(k_a, k_{a'}) \qquad 5.57$$

We define

$$f'^{LSJ}_{l_a j_a l_{a'} j_{a'}}(k_a, k_{a'}) = \frac{2\pi^{1/2}}{k_a k_{a'}} f^{LSJ}_{l_a j_a l_{a'} j_{a'}}(k_a, k_{a'}) \qquad 5.58$$

so that

$$\beta^{m\, m_a m_{a'}}_{LSJ} = \sum_{l_a l_{a'} j_a j_{a'}} \lceil^{LSJ\; m\, m_a m_{a'}}_{l_a l_{a'} j_a j_{a'}} P^m_{l_{a'}}(\Theta) f'^{LSJ}_{l_{a'} l_a j_a j_{a'}} \qquad 5.59$$

where

$$\lceil^{LSJ\; m\, m_a m_{a'}}_{l_a l_{a'} j_a j_{a'}} = \hat{S}\hat{L}(\hat{l}_a \hat{l}_{a'} \hat{j}_a \hat{j}_{a'})^2 (-)^{l_{a'} + j_{a'}} (-)^{m_{a'} - m}$$

$$(-)^J i^{l_a - l_{a'} - L} \left[\frac{(l_{a'} - m)!}{(l_{a'} + m)!}\right]^{1/2} \begin{pmatrix} l_a & L & l_{a'} \\ 0 & 0 & 0 \end{pmatrix}$$

$$\begin{pmatrix} l_a & s_a & j_a \\ 0 & m_a & -m_a \end{pmatrix} \begin{pmatrix} l_{a'} & s_a & j_{a'} \\ -m & m_{a'} & m_{a'} - m \end{pmatrix}$$

P.T.O

$$\begin{pmatrix} j_{a'} & J & j_a \\ m_{a'}-m & m-m_{a'}+m_a & m_a \end{pmatrix} \begin{pmatrix} J & L & S \\ j_a & \ell_a & s_a \\ j_{a'} & \ell_{a'} & s_a \end{pmatrix} \quad 5.60$$

The various coefficients of equation 5.60 give the following selection rules:

$$\underline{\ell_{a'}} + \underline{\ell_a} = \underline{L} \; ; \quad \ell_a + \ell_{a'} + L = \text{even} ; \quad \underline{\ell_a} + \underline{s_a} = \underline{j_a} \; ;$$

$$\underline{\ell_{a'}} + \underline{s_a} = \underline{j_{a'}} ; \quad \underline{j_{a'}} + \underline{j_{a'}} = \underline{J} ; \quad \underline{J} + \underline{L} = \underline{S} \text{ and } \underline{s_a} + \underline{s_a} = \underline{S}$$

Section 5v: Calculation of cross-sections from the transition amplitude

The cross-section $d\sigma/d\Omega$ is related to the transition amplitude of equation 5.2 by

$$\frac{d\sigma}{d\Omega} = \frac{\mu_m^2}{(2\pi\hbar^2)^2} \frac{k_{a'}}{k_a} (\hat{J}_a \hat{s}_a)^{-2} \sum_{M_A M_{A'} m_a m_{a'}} |T_{fi}|^2 \quad 5.61$$

where μ_m is the reduced mass of the particle-target system.

From equation 5.42

$$T_{fi} = \sum_{LSJ} \hat{J} \hat{J}_A \; A_{LSJ} (-)^{J_A - J + M_{A'}} \begin{pmatrix} J_A & J & J_{A'} \\ M_A & M_{A'}-M_A & -M_{A'} \end{pmatrix} \beta_{LSJ}$$

$$= \sum_{JJ'} (-)^{J_A - J + M_{A'}} A_{LSJ} (-)^{J_A + J + J_{A'}} \begin{pmatrix} J_A & J_{A'} & J \\ M_A & -M_{A'} & M_{A'}-M \end{pmatrix} \beta_{LSJ}^{m m_a m_{a'}} (k_a k_{a'})$$

5.62

therefore

$$|T_{fi}|^2 = \sum_{JJ'} (-)^{2(J_A - M_{A'}) + 2(J_A + J_{A'})} (2J_A+1)(\hat{J}\hat{J}')$$

$$\begin{pmatrix} J_A & J_{A'} & J \\ M_A & -M_{A'} & M_{A'}-M_A \end{pmatrix}\begin{pmatrix} J_A & J_{A'} & J' \\ M_A & -M_{A'} & M_{A'}-M_A \end{pmatrix}$$

$$\left\{\sum_{LS} A_{LSJ}\,\beta_{LSJ}^{m\,m_a m_{a'}}\right\}\left\{\sum_{LS} A_{LSJ}\,\beta_{LSJ}^{m\,m_a m_{a'}}\right\}^{*}$$

5.63

As $2(J_A - M_{A'}) + 2(J_A + J_{A'}) = +1$ we can sum over the magnetic quantum numbers M_A and $M_{A'}$ using the orthogonality of 3-j coefficients

$$\sum_{M_{A'}} (2J+1)\begin{pmatrix} J_A & J_{A'} & J \\ M_A & -M_{A'} & M_{A'}-M_A \end{pmatrix}\begin{pmatrix} J_A & J_{A'} & J' \\ M_A & -M_{A'} & M_{A'}-M_A \end{pmatrix} = \delta_{JJ'} \qquad 5.64$$

so that

$$\frac{d\sigma}{d\Omega} = \frac{\mu^2}{(2\pi\hbar^2)^2}\,\frac{k_{a'}}{k_a}\left(\frac{\hat{J}_{A'}}{\hat{J}_A\,\hat{S}_a}\right)^2 \sum_{J\,m_a m_{a'} m} \left|\sum_{LS} A_{LSJ}\,\beta_{LSJ}^{m\,m_a m_{a'}}\right|^2$$

5.65

from which it can be seen that the various L and S values add coherently while the J values add incoherently. Often, in practice, the interference terms are negligible and we can write

$$\frac{d\sigma}{d\Omega} = \frac{\mu^2}{(2\pi\hbar^2)^2}\,\frac{k_{a'}}{k_a}\,\frac{2J_{A'}+1}{(2J_A+1)(2S_a+1)} \sum_{LSJ} |A_{LSJ}|^2 \sum_{m\,m_a m_{a'}} |\beta_{LSJ}|^2$$

$$= \frac{2J_A+1}{(2J_A+1)(2S_a+1)} \sum_{LSJ} |A_{LSJ}|^2 \sigma_{LSJ}(\Theta) \qquad 5.66$$

where

$$\sigma_{LSJ}(\Theta) = \frac{\mu^2}{(2\pi\hbar^2)^2} \frac{k_a'}{k_a} \sum_{m m_a' m_a} \left| \beta_{LSJ}^{m m_a' m_a} \right|^2 \qquad 5.67$$

Section 5vi: The Interaction

The interaction between the projectile and the target is assumed to take place through a sum of two-body forces between the projectile and the target nucleons. Thus the interaction may be written

$$V = \sum_i v_{ip}(|r_i - r_p|) - U \qquad 5.68$$

U is the optical potential generating the distorted waves. It does not contribute to the inelastic scattering as it is diagonal in the nuclear states. Thus we get for the interaction of equation 5.1

$$V = \sum_i v_{ip}(|r_i - r_p|)$$

where r_p and r_i are the respective coordinates of the projectile and the ith nucleon of the target.

The two-body interaction must be subject to the following restrictions. It must be invarient under translation, rotation, space reflection, time reversal and Galilean transformation.

It must also be Hermitian, charge independant and symmetric under permutation.

The most general form for v_{ip} is

$$v_{ip} = V_0 + (\sigma_i \cdot \sigma_p) V_1 + S_{ip} V_2 + \underline{L} \cdot \underline{S} V_3 + \tfrac{1}{2}[(\underline{\sigma_i} \cdot \underline{L})(\underline{\sigma_p} \cdot \underline{L}) + (\underline{\sigma_p} \cdot \underline{L})(\underline{\sigma_i} \cdot \underline{L})] V_4 + (\underline{\sigma_i} \cdot \underline{p})(\underline{\sigma_p} \cdot \underline{p}) V_5 + \text{Hermitian Conjugate} \quad 5.69$$

where

$$S_{ip} = \{ 3(\underline{\sigma_i} \cdot \underline{r})(\sigma_p \cdot r)/r^2 \} - \underline{\sigma_i} \cdot \underline{\sigma_p} \quad 5.70$$

The coefficients V_k are dependant on isospin, as well as on r^2, p^2 and L^2 and each term may be written

$$V_k = V_{k0} + V_{k1} (\tau_i \cdot \tau_p) \quad 5.71$$

where V_{k0} is the isospin singlet potential and V_{k1} the isospin triplet potential.

We shall be considering only the first two terms in equation 5.69 so that we can write

$$v_{ip} = V_{00} + V_{01} (\tau_i \cdot \tau_p) + V_{10} (\sigma_i \cdot \sigma_p) + V_{11} (\sigma_i \cdot \sigma_p)(\tau_i \cdot \tau_p) \quad 5.72$$

The coefficients V_{jk} of equation 5.72 are considered to be functions of $|\underline{r_i} - \underline{r_p}| = r$ only, and we take the same r-dependance for each term, so that

$$v_{ip}(r) = -V_N \{ a_{0\alpha} + a_{0\beta} (\tau_i \cdot \tau_p) + a_{i\alpha} (\sigma_i \cdot \sigma_p) + a_{1\beta} (\sigma_i \cdot \sigma_p)(\tau_i \cdot \tau_p) \} g(|r_i - r_p|) \quad 5.73$$

We can combine the singlet-spin singlet-isospin and the triplet-spin singlet-isospin terms to give the "isoscalar" interaction

$$-V_N \left(a_{0\alpha} + a_{1\alpha}(\sigma_i.\sigma_p)\right) g(|r_i - r_p|) \qquad 5.74a$$

Similarly, an isovector interaction may be constructed from the remaining singlet-spin triplet-isospin and triplet-spin triplet-isospin terms

$$-V_N \left(a_{0\beta} + a_{1\beta}(\sigma_i.\sigma_p)\right)(\tau_i.\tau_p)\, g(|r_i - r_p|) \qquad 5.74b$$

The multipole expansion of $G^T_{LSJ}(r)$ in equation 5.33 gave

$$G^T_{LSJ}(r) = (-)^{L+S-J} \hat{S}_a / \hat{S} \langle S_a || S_S || S_a \rangle \times \langle t_a || O_T || t_a \rangle \langle J_A' T_A' || V^{(r)}_{LSJ} || J_A T_A \rangle \qquad 5.75$$

where the interaction $V^{(r)}_{LSJ}$ acts only on the nuclear coordinates. As we are dealing with nucleon scattering with spin $\frac{1}{2}$ and isospin $\frac{1}{2}$ we get

$$\langle S_a || S_S || S_a \rangle = \langle \tfrac{1}{2} || S_S || \tfrac{1}{2} \rangle = \hat{S} \qquad 5.76a$$

and

$$\langle t_a || O_T || t_a \rangle = \langle \tfrac{1}{2} || O_T || t_a \rangle = \hat{T} \qquad 5.76b$$

so that

$$G^T_{LSJ} = (-)^{L+S-J} 2^{1/2} \hat{T} \langle J_A' T_A' || V^T_{LSJ} || J_A T_A \rangle = (-)^{L+S-J} 2^{1/2} \langle J_A' T_A' || V^0_{LSJ} \delta_{T0} + V^1_{LSJ} \delta_{T1} || J_A T_A \rangle \qquad 5.77$$

The interaction can now be written

$$V = \sum_T V^{(T)}.O_T = V^0 \underline{1} + V^1.\tau_p = V^{(0)} + V^{(1)}\tau_p \qquad 5.78$$

where τ_p is the Pauli isospin matrix for the projectile.

As we have now both expressions for the interaction in terms of an isoscalar and an

isovector potential we may compare equations 5.74 and 5.78 to get

$$V^{(0)} = -V_N \sum_i \left\{ a_{0\alpha} + a_{1\alpha} (\underline{\sigma}_i \cdot \underline{\sigma}_p) \right\} g(r_i r_p) \qquad 5.79a$$

and

$$V^{(1)} = -V_N \sum_i \left\{ a_{0\beta} + a_{1\beta} (\underline{\sigma}_i \cdot \underline{\sigma}_p) \right\} \tau_i \, g(r_i r_p) \qquad 5.79b$$

The radial form factor of the potential may be expanded in terms of multipoles so that

$$g(|\underline{r}_i - \underline{r}_p|) = 4\pi \sum_{LM} g_L(r_i, r_p) Y_L^M(\theta_i, \phi_i) Y_L^{M*}(\theta_p \phi_p) \qquad 5.80$$

where θ_i, ϕ_i and θ_p, ϕ_p are the angles of r_i and r_p.

Hence

$$V^{(0)} = -4\pi V_N \sum_i \left\{ \left[a_{0\alpha} + a_{1\alpha} (\sigma_i \cdot \sigma_p) \right] \sum_{LM} g_L(r_i r_p) Y_L^M(\theta_i \phi_i) Y_L^{M*}(\theta_p \phi_p) \right\} \qquad 5.81$$

and

$$V^{(1)} = -4\pi V_N \sum_i \left\{ \left[a_{0\beta} + a_{1\beta} (\sigma_i \cdot \sigma_p) \right] \left[\sum_{LM} g_L(r_i, r_p) Y_L^M(\theta_i \phi_i) Y_L^{M*}(\theta_p \phi_p) \right] \times \tau_i \right\} \qquad 5.82$$

But

$$V^{(T)} = \sum_{LSJN} (-)^N \, V^{(T)}_{LSJ,N}(r_i) \, T_{LSJ,-N}(\theta_p, \phi_p, r_p)$$

where

$$T_{LSJ,N} = \sum (-)^{L-S+N} i^L Y_L^M(\theta_p \phi_p) \, S_{S,N-m} \times \begin{pmatrix} L & S & J \\ m & N-m & -N \end{pmatrix} \qquad 5.83$$

and $S_0 = 1$; $S_1 = \sigma_p$

We may define a tensor S_ξ analogous to which acts on the internal coordinates of the target nucleons. As in equation 5.24 we get

$$S_\xi = \underline{1} \qquad \text{and} \qquad S_\tau = \underline{\sigma}_i$$

We can now write equation 5.81 in a condensed form

$$V^{(0)} = -4\pi V_N \sum_{\substack{L\hat{S}MS \\ N}} a_{s\alpha}\, g_L(r_i,r)\, Y_L^M(\theta_i,\phi_i)\, Y_L^{M*}(\theta_n,\phi_n)\, S_{\hat{S}N-M}\, S_{SM-N}(-)^{N-M} \qquad 5.84a$$

and

$$V^{(1)} = -4\pi V_N \sum_{\substack{L\hat{S}MS \\ N}} a_{s\beta}\, g_L(r_i,r)\, Y_L^M(\theta_i,\phi_i)\, Y_L^{M*}(\theta_n\phi_n) \times S_{\hat{S}N-M}\, S_{SM-N}\,(-)^{N-M} \qquad 5.84b$$

We define tensors $T_{L\hat{S}JN}$ corresponding to $S_{\hat{S}}$ so that

$$T_{L\hat{S}JN}(\hat{S}_i) = \sum_m (-)^{J-\hat{S}+N}\hat{J}\begin{pmatrix} L & \hat{S} & J \\ m & N-m & -N \end{pmatrix} \times i^L Y_L^m(\theta_i,\phi_i)\, S_{\hat{S}N-m}$$

As

$$i^L Y_L^M(\theta_i\phi_i)\, S_{\hat{S}N-m}(\hat{S}_i) = \sum_J (-)^{L-\hat{S}+N}\hat{J}\begin{pmatrix} L & \hat{S} & J \\ m & N-m & -N \end{pmatrix} T_{L\hat{S}JN}(\hat{S}_i)$$

we get

$$V^{(0)} = -4\pi V_N \sum_{L\hat{S}M_N} a_{s\alpha}\, g_L(r_i,r)\, i^{-L} Y_L^{M*}(\theta_n\phi_n)\, S_{SM-N}\,(-)^{N-M} \times \sum_J (-)^{L-\hat{S}+N}\hat{J}\begin{pmatrix} L & \hat{S} & J \\ M & N-M & -N \end{pmatrix} T_{L\hat{S}JN}$$

$$= 4\pi V_N \sum_{L\hat{S}J_N} a_{s\alpha}\, g_L\, T_{LSJ,N}(\hat{S}_i) \sum_M (-)^{2N-M}(-)^{L-S} i^L Y_L^{M*}(\theta_n,\phi_n)\, S_{S,M-N}\begin{pmatrix} L & S & J \\ M & N-M & -N \end{pmatrix} \qquad 5.85$$

as $\hat{S} = S$

From equation 5.26

$$T_{LSJ,-N} = \sum_m (-)^{-J}(-)^{N-M}\hat{J}\begin{pmatrix} L & S & J \\ m & N-m & -N \end{pmatrix} i^L Y_L^{m*} S_{S,m-N}$$

so that

$$V^{(0)} = -4\pi V_N \sum_{LSJN} a_{s\alpha}\, g_L\, T_{LSJ,N}(\xi_i)\, T_{LSJ,-N}(\xi_p)(-)^{L+S-J-N} \qquad 5.86$$

From this equation we get

$$V^{(0)}_{LSJN} = -4\pi V_N (-)^{L+S-J} \sum_i a_{s\alpha}\, g_L(r_i, r_p)\, T_{LSJ,N}(\xi_i)$$

Similarly

$$V^{(1)}_{LSJ,N} = -4\pi V_N (-)^{L+S-J} \sum_i a_{s\beta}\, g_L(r_i, r_p)\, T_{LSJ,N}(\xi_i)\, \tau_i$$

Thus we get

$$G^T_{LSJ}(r) = -4\pi V_N\, 2^{1/2} \langle J_A T_A \| \sum_i \{ a_{s\alpha}\, \delta_{T0} + 3^{1/2} a_{s\beta}\, \tau_i\, \delta_{T1} \}\, g_L(r_i, r_p)\, T_{LSJ} \| J_A T_A \rangle$$

$$= A^T_{LSJ}(A)\, F_{LSJ}(r) \qquad 5.87$$

Chapter 6

The results of the experiments described in Chapter 3 are presented in this chapter. The theoretical analysis of the data has been carried out in terms of the theory described in Chapters 4 and 5. The results and conclusions of this analysis are also discussed in this chapter.

Section 6i: The Optical Model analysis of the elastic scattering data.

Introduction

The analysis of the elastic scattering cross-sections and polarisations was carried out using the automatic parameter search code described in Chapter 4. The scattering amplitude was calculated over 15 partial waves and an integration step length of 0.1 fermis was used.

In order to avoid searching over the whole area of χ^2 space, the values of the parameters used as an initial central guess were chosen to give results which were expected to be fairly close to the minimum. The elastic scattering of protons at 40 MeV. by a range of nuclei including Zr^{90} has been studied by Fricke et al. (reference 13). In this analysis, best fit parameters were found for each nucleus. In addition, an average geometry for all the nuclei was obtained. Parameter values

similar to both the average geometry and the best fit potentials were used as starting values in the analysis of the present data. Similar results were obtained with either potential. In both cases, slight modifications were required before a satisfactory fit could be obtained. In particular, a considerable improvement in the results was obtained by increasing the strength of the volume absorbtion.

Initial attempts to fit the data by varying all the parameters simultaneously proved unsuccessful. This was because of ambiguities between the depths of the potential wells and their radii. The angular distributions for a given value of $V_n r_n^x$ were basically the same for a wide range of values of V_n and r_n. Hence it was neccesary to avoid varying certain of the parameters simultaneously. The principal effect on the potentials of a change of incident energy would be seen in the strengths of the potentials rather than in the geometry. The well depths were therefore varied first, the geometry parameters being kept constant. The well depths were then kept constant and first the radii, and then the diffusivities were varied. The radii and diffusivities were then varied simultaneously. In case the resulting geometry required different

potential strengths, the search over the well depths was repeated. Finally, the radii and diffusivities were again varied simultaneously.

This procedure was not infallible. Although in most cases it led quickly to potentials which were fairly close to the optimum, occasionally it produced results which were clearly non-physical. However, in such cases it was nearly always possible to repeat the fit satisfactorily using a different set of initial parameters.

Results

The optical model proved to be very successful in predicting the angular distributions of both cross-sections and polarisations for each of the nuclei under consideration. In addition to the thirteen parameter potentials of the form of equation 4.7, the data was also fitted with potentials having purely volume and purely surface absorbtion. The coulomb radius used in these calculations was initially set at 1.25 fermis. However some of the preliminary fits suggested that a smaller coulomb radius might be appropriate. The analysis was therefore repeated for r_c = 1.2, 1.15 and 1.115 fermis.

One of the disadvantages of the restrictions made in the above procedure is that there was no

certainty that the final result was near the minimum of χ^2. To check the efficiency of the fitting procedure, a further trial was performed in some of the cases, allowing all the parameters to vary simultaneously. As the improvement in χ^2 was usually of the order of only a few per cent, and the changes in the parameters were of a similar order, it was concluded that the procedure gave potentials which were reasonably near the optimum.

The results of these analyses are summarised in tables 6.1 to 6.5. Where indicated the angular distribution of the cross-sections and polarisation is illustrated in the appropriate figure. The thirteenth set of parameters in each table is the result of varying all the parameters simultaneously using set 10 as a base. The fourteenth and fifteenth sets are the results of attempts to find an average geometry for all the isotopes. In addition, the best-fit and average geometry parameters of Fricke are reproduced in parameter sets 16 and 17 respectively on table 6.1.

It can be seen from the tables and from the angular distributions that the results for the different isotopes are very similar. The potentials with both volume and surface components produced

the best fits, although in some cases the predictions for the second and third peaks in the cross-section angular distribution were slightly smaller than experiment.

The trend of the results seems to indicate that most of the absorbtion takes place within the nucleus. Indeed, only a slight deterioration in the quality of the fit was produced by setting the surface potential to zero, although there is an increased disparity in the heights of the second and third peaks in the angular distributions. The volume potential was increased to a value roughly equal to the sum of the volume and surface terms in the previous case, and there was an increase in the imaginary radius, and a decrease in the diffusivity. The other geometry parameters remained practically unchanged, though the real potential was slightly increased. There was little effect on the polarisation angular distributions. On the other hand, although a purely surface absorbtion gave slightly better agreement with the second peak of the angular distribution the general fit was worse and there were corresponding increases in the value of χ^2. The imaginary radius was much reduced and the diffusivity increased indicating that the program was attempting to spread the potential over

the volume of the nucleus. The real and spin orbit potentials were somewhat reduced and there were slight changes in r_{so} and a_{so}.

No conclusions could be drawn on the best value of the coulomb radius as both the cross-sections and the parameters seemed to be practically insensitive to it.

The symmetry term

Systematic variations in the depths of the real potential with atomic number have been revealed in comparisons of optical model analyses of a range of nuclei at the same energy. Lane has suggested an isotopic spin dependance in the optical potential (reference 14). Thus, the real part of the potential may be written

$$V_r = V_0 + V_1 \left(\frac{t \cdot T}{A} \right) \qquad 6.1$$

where t and T are the isospins of the projectile and target respectively. For protons this becomes

$$V_r = V_0 + \frac{1}{4} \left(\frac{N - Z}{A} \right) V_1 \qquad 6.2$$

The isotopes studied in this work had isotopic spin projections ranging from 5 to 8. Provided the isotopes were all fitted with the same geometry parameters, the real potentials should lie on a straight line when plotted against

the quantities $(N-Z)/A$. The gradient of this graph could then be used to find the value of the coefficient V_1 in equation 6.2. Such a technique has been applied to Zirconium by Ball et al (reference 15) using 22.5 MeV. proton scattering. A value of -43.4 MeV. was obtained for V_0 and 27.8 MeV. for V_1.

A set of average geometry parameters was calculated by obtaining the mean values of parameter set 13 in each of tables 6.1 to 6.5. The values of the potential depths for each isotope which gave the best fit to the angular distributions were then found. The results are given in the tables (parameter set 14). As can be seen, there was no correlation between isospin and the strength of the real potential. In case this was an effect of the geometry parameters, a new set was obtained (parameter set 15) which gave better individual fits in most cases. Again, no correlation was observed.

It appears therefore that it is not possible to evaluate the symmetry term using the present data. The above method would have doubtful efficiency in any case, as it does not involve isospin polarisation measurements, which would require (p,n) reaction cross-sections. The method is analogous to attempting to evaluate the spin-orbit term in the

optical potential without making polarisation measurements.

Section 6iii: Inelastic Scattering

Predictions of the inelastic scattering cross-sections were made using both the collective model and the shell model of the nucleus. In both cases the shape of the angular distribution is broadly characteristic of the orbital angular momentum transfer, although details of the distribution will depend on the shape of the radial form factor F_{LSJ} of equations 5.37 and 5.87. The collective model uses the non-spherical part of a deformed optical potential to generate the form factors whereas the shell model evaluates the nuclear matrix elements directly, by integrating the potential V of equation 5.2 over the nuclear wave functions. It follows, therefore, that while the general features of the predictions for a given angular momentum transfer will be the same for both models the details of the angular distributions will depend, in the case of the collective model, on the parameters of the optical model potential. The shell model predictions, on the other hand, will depend on the form and range of the interaction and the configurations of the initial and final states.

Collective model

Theoretical cross-sections were calculated for the majority of levels in Zr^{90}, Zr^{92} and Zr^{94} for which angular distributions had been obtained. The magnitude of the cross-sections was determined by the deformation parameter β_L. It can be seen from equation 5.13 that

$$\frac{d\sigma}{d\Omega} \propto \beta_L^2$$

The value of β_L which gave the minimum value of χ^2 was found where

$$\chi^2 = \sum_{i=n}^{m} (X_i - Y_i)/\Delta X_i \qquad 6.3$$

and X_i, Y_i and ΔX_i are defined as in equation 4.26. The sumnation was taken over a limited range of angles. These were chosen so that the resulting fit followed the trend of the angular distributions and did not neccesarily give the minimum value of χ^2 over the whole range.

The calculations were performed by a computer program made available by H.Sherif. The program used the same optical model parameters to obtain the interaction as it used to generate the distorted waves. Consequently, the radial form factors calculated by the program were usually complex, although it was possible to suppress the imaginary component.

Facilities in the program allowed the use of a deformed spin-orbit potential of either the full Thomas term type of equations 5.9 and 5.10 or the simplified Oak-Ridge form of equation 5.8. In either case, it was possible to vary the spin-orbit deformation parameter β_{so} independantly of the deformation of the real and imaginary terms. This was facilitated by the definition of a quantity A_{def} where

$$A_{def} = \beta_{so} / \beta_L \qquad 6.4$$

Thus the spin-orbit contribution could be suppressed by setting $A_{def} = 0$.

Results

The results of the collective model analysis are summarised in table 6.6, and the corresponding angular distributions are illustrated in figures 6.6 to 6.19. The table contains the value of β_L obtained for each angular distribution and an indication is given of the form and parameters of the interaction.

The Zr^{90} nucleus

Angular distributions for A_{def} = 0.0, 1.0 and 2.0 were calculated for the 2.18 MeV. 3- level in Zr^{90} with both Oak-Ridge and full Thomas term spin-orbit deformations. The cross-sections were not significantly dependant on the form of the

interaction although the asymmetries were considerably affected. Therefore, without polarisation data it was not possible to decide which form of the spin-orbit interaction was appropriate. The cross-sections were more sensitive to the strength of the spin-orbit term, particularly at large angles. However, the results for the 2^+ and 3^- levels were conflicting. For the 2^+ level, the best agreement was obtained with a value of $A_{def} = 2.0$ whereas better results for the 3^- level were obtained with $A_{def} = 0.0$, although for both levels the effect was marginal. In either case the value of β_L was reduced for increasing A_{def}.

A more drastic effect on the cross-sections was obtained by suppressing the imaginary component in the form factor. The oscillations in the cross-section with angle for real form factors had a considerably smaller amplitude than those for complex form factors and the angular distributions resembled those of the shell model.

Various sets of optical model parameters were used, but most of the calculations were performed using parameter set 13 of table 6.1. The effects of using a potential with a different coulomb radius (set 1) or with purely volume absorbtion (set 11) were found to be negligible. This was not unreasonable

as the elastic scattering was insensitive to the choice of potential, and the form factors are unlikely to be much affected by the coulomb radius or the presence of surface absorbtion. On the other hand, the angular distributions were affected by using parameters for purely surface absorbtion. Here, the imaginary component of the form factor would be peaked at a significantly greater radius than for volume absorbtion. Such a potential did give slightly better fit to the 3^- level, though not to the 2^+ level. Surface absorbtion only, however, did not give good fits to the elastic scattering, and the investigations were not carried any further.

Finally, a contribution to the scattering from coulomb excitation was included. This did not affect the shape of the angular distributions but produced an increase of the order of 3% in the value of β_L for the 3^- level, and a similar though slightly larger increase for the 2^+ level.

The collective model was quite successful at predicting the angular distributions of both the 2^+ and the 3^- levels. The effects of the changes discussed above were all fairly small and did not lead to any conclusive results. Therefore, for the remaining levels, the angular distributions were

calculated using a standard form of the interaction. The full Thomas term spin-orbit deformation was implemented, with $A_{def} = 1.0$. Optical model parameter set 13 for Zr^{90} was used and the contribution of coulomb excitation was included.

Of the excited states of Zr^{90} in the energy range considered only the 2.75 MeV. 3^- level, which may be considered as an octopole vibration, showed a marked collective nature with a β_L of 0.139. The other levels have values of β_L between 0.07 and 0.02. For the remaining levels, the 3.07 MeV. 4^+ and the 3.45 MeV. 6^+ levels corresponding to the 2^+ level were also well described by the model. The 3.57 MeV. 8^+ level has a very low cross-section and the errors in the measurement of individual cross-sections may be greater than allowed for in Section 3v. The predictions for the 2.30 MeV. 5^- level were also in good agreement with experiment. In all these cases, however, the forward angle points were not well fitted. This was probably because of slit scattering which appeared at small angles. This principally affected the high energy end of the spark chamber spectrum.

The remaining levels are probably either simple hole-particle excitations or mixtures of a small number of such states. The collective model would not be expected to be appropriate in such cases.

However, there was still good agreement between the theory and experiment for many of the levels. The angular distributions are principally characteristic of the angular momentum transfer and the analysis was of use in assigning L-values to the various levels. In some cases none of the values of L produced very good agreement with the experimental cross-sections. In these cases, such as for the 4.05 MeV. and 4.89 MeV. levels, the values of L which appeared most probable have been used in the quoted results. Such levels are probably mixtures of transitions with different values of L and other angular momentum transfers cannot be ruled out.

A case of particular interest is the 3.37 MeV. level. In the shell model picture, this level possibly includes a contribution from an $L = 0$ transition. In figure 6.7c angular distributions for both $L = 0$ and $L = 2$ are depicted. In this case neither angular distribution fits the data very well and the results are inconclusive. Most of the angular momentum transfer assignments for the remaining levels agree with the suggestions made for 19 MeV. proton scattering. One exception however, is the 4.22 MeV. level. At 19 MeV. this was tentatively assigned $L = 5$. The present data gives considerably better agreement with $L = 2$. The 4.66 MeV. level is shown with $L = 2$ and

$L = 3$, although $L = 2$ appears to be more appropriate. In all, seven of the higher levels have angular distributions consistent with $L = 3$. Of these, however, only in the 4.46 MeV. level and to a lesser extent the 4.54 MeV. level is the assignment relatively unambiguous. In the case of the 4.05 MeV. and 4.89 MeV. levels equally good or better results were obtained with $L = 4$. In the 4.79, 4.99 and 5.07 MeV. levels the fit was very poor although no other value of L gave any improvement. Of the remaining levels, the 4.32 is reasonably well predicted with $L = 4$, and there can be little doubt in the assignment of $L = 5$ to the 3.95 MeV. level.

The Zr^{92} and Zr^{94} nuclei

The angular distributions for Zr^{92} and Zr^{94} were calculated using the same parameters as the Zr^{90} cross-sections, with the appropriate optical potentials; that is, set 13 in tables 6.3 and 6.4. The results were similar to those for Zr^{90}. It was not possible to obtain angular distributions for the 1.43 MeV. and 2.03 MeV. states in Zr^{92}, but the results for most of theremaininglevels are summarised in table 6.6.

The 2^+ levels at about 0.93 MeV. and the 3^- levels at 2.33 and 2.07 MeV. respectively in Zr^{92} and Zr^{94} were fitted with values of $A_{def} = 0.0, 1.0$

and 2.0. The angular distributions exhibited the same behaviour as in the case of Zr^{90}, best results being obtained with $A_{def} = 2.0$ for the $L = 2$ levels and with $A_{def} = 0.0$ for the 3^- levels.

For the remaining levels, ambiguities in the value of the angular momentum transfer were more difficult to resolve, as the cross-sections were measured at intervals of 5°. However, where it was possible to make tentative assignments, these agreed with the suggestions of previous workers, with the exception of the 2.83 MeV. level in Zr^{92}, which the present data indicates should be $L = 5$ rather than $L = 2$, and the 2.34 MeV. level in Zr^{94} which appears to be more consistent with $L = 4$, against $L = 2$ for 19 MeV. proton scattering.

The values of β_L for both nuclei followed a similar pattern to Zr^{90}, with the exception of the 2^+ levels at about 0.93 MeV. The levels, believed to have $(2d_{5/2})^2$ and $(2d_{5/2})^{-2}$ configurations for Zr^{92} and Zr^{94} respectively, appeared to have a fairly strong collective nature, with corresponding values of β_L of 0.12 and 0.09. These are larger than any of the other levels, except the highly collective 3^- states.

In general, the angular distributions are reasonably well fitted, even for excitations which

would not normally be regarded as collective. Again, some of the levels may involve several values of the angular momentum transfer, and the values quoted in table 6.6 do not exclude the possibility of contributions from other values of L.

The Shell Model

In Chapter 5 the differential cross-section was expressed in terms of a sum over spectroscopic factors A_{LSJ} and reduced cross-sections σ_{LSJ}. In most of the cases encountered in this study there is a unique value of the angular momentum transfer L and a single configuration in the initial and final states. The sum in equation 5.66 therefore reduces to two terms corresponding to $S = 1$ and $S = 0$ and the expression for the cross-section becomes

$$\frac{d\sigma}{d\Omega}(\theta) = 4\pi (2J+1) \left\{ V_0^2 M_{L0L}^2 + V_1 M_{L1J}^2 \right\} \sigma_{LSJ}(\theta) \qquad 6.5$$

where V_0 and V_1 are the strengths of the Wigner and "spin-flip" interactions averaged over the isospin (see Appendix 2). The reduced cross-sections were evaluated by a computer code in terms of a radial form factor $F_L(r)$. It was found that, to a good approximation, the angular variation of σ_{LSJ} was independant of S and J. The shape of the angular distribution for a given L

therefore depends on the shape of the radial form factor which in turn depends on the range and form of the interaction and on the radial parts of the single particle wave functions. The evaluation of $F_L(r)$ is described in appendix 3.

The magnitude of the cross-sections is determined by the strength of the interaction and by the spin-angle reduced matrix elements M_{LSJ}. Methods for calculating the M_{LSJ} are described in appendix 2 and the values for the cases discussed below are given in table 6.7.

The $(g_{9/2})^2$ configuration

In the Zr^{90} nucleus the shell model picture gives the neutron shells filled up to the $1g_{9/2}$ orbit and the proton shells up to the $2p_{1/2}$ orbit. Excited states may be formed by two protons in the $1g_{9/2}$ shell with angular momenta coupled to 0, 2, 4, 6 and 8. Such states could not normally be excited by the transition of a single particle. However, there is mixing between the 0^+ ground state and the first 0^+ state of the above configuration. Thus we may write the ground state wave function

$$a\,|p_{1/2}{}^2\rangle + b\,|g_{9/2}{}^2\rangle$$

All transitions involving these configurations will therefore be affected by the value of a and b. For the purposes of this analysis the values were

taken to be those of reference 16, that is, $a^2 = 0.64$, $b^2 = 0.36$. The ratio b/a is believed to be negative.

Therefore, most of the observed levels in the lower part of the spectrum can be explained in terms of recoupling of the $g_{9/2}$ protons. Levels with odd J are not allowed and there is no spin-flip contribution. In this case, the expression for the cross-section is

$$\frac{d\sigma}{d\Omega}(\theta) = b^2 (2L+1) M^2_{LoL} V_o^2 \sigma_{LSJ}(\theta) \qquad 6.6$$

The form factors were calculated using a Yukawa interaction

$$V = V_o \frac{e^{-\alpha r}}{r} \qquad 6.7$$

The proton wave functions were calculated for bound states in a Saxon-Woods potential. The depth of the well was chosen to give a binding energy for the $g_{9/2}$ proton of 5.29 MeV., obtained from the proton separation energy of Nb^{91}. The radius of the well was taken to be $1.35A^{1/3}$ fermis with a diffusivity of 0.6. In addition, a spin-orbit potential of strength 7.04 MeV. similar to the optical potential with a radius of $1.25A^{1/3}$ fermis and diffusivity 0.6 and the coulomb potential of a uniformly changed sphere of radius 1.25 fermis

were also included. A variety of values of these parameters were used initially to calculate the wave functions but the shape of the form factors was largely independant of any of the parameters except the radius of the well r_n. To a large extent the magnitude of the form factors was also independant of these parameters. However, increasing the well radius from $1.25A^{1/3}$ fermis to $1.35A^{1/3}$ fermis moved the position of the form factor peak outwards by about 0.3 fermis and also broadened it slightly. The amplitude was reduced by about 10%.

The other factor which had a marked effect on the form factors was the range of the interaction. Although decreasing values of α had little effect on the position of the form factor peak, the width of the peak was considerably increased. The amplitude of the form factor was strongly dependant on α. This may be clearly seen in figure 6.29 where the $L = 2$ radial form factors for values of α ranging from 0.6 to 1.4 are portrayed. Form factors for $\alpha = 0.6$ and values of $L = 0$, 2, 4, 6 and 8 and the real part of the collective model form factor are shown in figure 6.30. The degree of dependance was different for each value of the angular momentum transfer, but for $L = 2$, the following empirical relation was obtained

$$(F_{LSJ})_{MAX} \propto \alpha^{-2.2} \qquad 6.8$$

The value of α therefore, will alter the relative strengths of the angular distributions. This was important when attempting to fit the cross-sections of a number of levels with a single interaction strength.

The dependance of the strenth of theoptical potential on the incident energy observed in elastic scattering studies, has been explained by a number of workers in terms of a non-local term in the potential. Non-local contributions to the optical and shell model potentials also arise in studies of correlations in nuclear matter (reference 17). The treatment of such potentials is simplified by using the local energy approximations, where an equivalent local potential is generated to take account of the non-local contribution. A convenient expression for relating the local (V_L) and non-local (V_N) potentials is (reference 7)

$$V_N(r) = V_L(r) \exp\left[Ma^2/2\hbar^2 (E - V_L(r))\right] \qquad 6.9$$

The wave functions of particles in such potentials are related by a similar expression

$$u_N(r) = \beta\, u_L(r)\, e^{-Ma^2 V_L(r)/2\hbar^2} \qquad 6.10$$

where B is a normalisation constant, M is the reduced mass and a the non-locality range. For free nucleon

scattering the value of B is unity. However, the exponential factor in equation 6.9 reduces the wave function in the interior of the nucleus. In order that the wave functions should remain normalised so that

$$B^2 \int u_N^2(r)\, dr = 1$$

the value of B must be greater than unity and the tail of the wave functions will be increased. Thus the effect of including non-locality was to produce form factors which were peaked at greater radii than those calculated with purely local potentials. The calculations in this work were performed by a computer program written by S.M.Perez (reference 18). The range a, of the non-locality correction, used in these calculations was 0.85 fermis, the value observed by Perey and Buck to give the best empirical agreement with the energy dependance of the potential. In practice, the effect of non-locality on the angular distributions was fairly small compared with the effect of the range of the interaction and the radius of the well. The distorted waves used in the calculation were evaluated using the optical model parameters of section 6.1. In all cases, parameter set 13 of table 6.1 was employed.

Results

The shell model was not as successful as the

collective model in predicting the angular distributions of the states of the $(g_{9/2})^2$ configuration. This was partly because instead of using an arbitrary normalisation, chosen to give the best agreement with experiment as in the case of the collective model, the relative strength of the shell model cross-sections was determined by the features of the model itself and by the strength of the interaction potential V_o. However, the shell model did not produce good agreement with the shapes of the angular distributions either. As indicated above, the shape of the angular distributions depended mainly on the radius of the shell model potential well and on the range of the interaction. It was found that a value of $r_n = 1.35A^{1/3}$ fermis was required to give angular distributions which were peaked at about the right angles. Decreasing the value of the range parameter α produced more structure in the angular distributions and altered the relative strengths of the different levels. The best individual fits to the experimental data were obtained with $\alpha = 0.6$. The angular distributions with this value of α and with $r_n = 1.35A^{1/3}$f. for the 4^+, 6^+ and 8^+ levels are shown in figure 6.20. The strength of the interaction V_o was fixed at 85 MeV. A lower potential appeared more appropriate

for the 2^+ level and the continuous line in figure 6.20A represents the angular distribution for a strength of 50 MeV. The broken line on the same graph is for a potential of 85 MeV. The 4^+ and 6^+ levels were reasonably well fitted though the 8^+ predictions were considerably lower than experiment. Little improvement in the fitting of the 8^+ level was achieved for any combination of α and r_n. The experimental cross-sections of this level are themselves very small and may include contributions from the background and from levels in other nuclei present as impurities in the target. Including non-locality when calculating the form factors slightly improved the shape fits but had little effect on the magnitude of the cross-sections.

A value of $\alpha = 1.0$ and $V_o = 230$ MeV. gave slightly better agreement with the relative strengths of the cross-sections but the individual fits were rather worse. This potential, however, agrees with the value of 205 MeV. obtained at 18.8 MeV. (reference 1) provided the effect of increasing the radius of the shell model potential r_n is taken into account. It can be seen from figure 6.20 that the quality of the fit in individual cases would not be seriously affected by changes of up to 20% in the strength of the potential.

A possible reason for the poor agreement between theory and experiment for the shell model may be understood by comparing the results to those of the collective model, with particular regard to the shape and form of the radial form factors. In the case of the $(g_{a_{1_2}})$ configuration, the general shape of the form factors for both models were similar but the collective model form factors were peaked at a greater radius. The effect of increasing r_0 and decreasing α was tending to improve the resemblance between the models (see figure 6.30). The collective model form factors, of course, have in addition complex and spin-orbit components. The shell model reproduced the positions of the various peaks in the experimental angular distributions fairly well, but the predicted amplitude of the peaks was generally too small. In the case of the collective model, which normally gave good agreement with the details of the shape of the angular distributions, it was found that the amount of structure was considerably reduced by suppressing the imaginary component in the interaction. The effect of the spin-orbit contribution is discussed above.

There are reasons for believing that the shell model form factors should also be complex. In the first place, a real interaction does not allow for

the effect of excitations to continuum states. Secondly, and possibly more important, there might be core polarisation effects which would also lead to complex terms in the form factor.

The 0^+ level

The 0^+ level has not been included in the above discussion as it is probably a complementary mixture to the ground state. Hence its wave function may be written

$$|0^+\rangle = a\,|(g_{9/2})^2\rangle - b\,|(p_{1/2})^2\rangle \qquad 6.11$$

and the matrix element for the transition from the ground state is

$$\langle 0^+(1.75\,\mathrm{MeV})\,||\,V_{000}\,||\,0^+(g.s)\rangle$$

$$= ab\left\{\langle (g_{9/2})^2\,||V_{000}||\,(g_{9/2})^2\rangle - \langle (p_{1/2})^2\,||V_{000}||\,(p_{1/2})^2\rangle\right\} \qquad 6.12$$

The reduced cross-sections $\sigma_{000}(\theta)$ must then be evaluated in terms of a form factor equal to the difference between the $1g_{9/2}$ - $1g_{9/2}$ and $2p_{1/2}$ - $2p_{1/2}$ form factors. Using the expressions of appendix 2, the differential cross-section may be written

$$\frac{d\sigma}{d\Omega}(\theta) = \frac{1}{\hat{\pi}^{1/2}}\,ab\,\sigma_{000}(\theta).$$

The experimentally observed cross-sections of the 0^+ level were very small and could not be measured at the same time as the cross-sections of the other levels in the Zr^{90} spectrum. However

the following procedure was used to make measurements at 15° and 20°. A spectrum extending over an energy range from about 1 MeV. to about 3 MeV. including the 2.75 MeV. 3^- level was accumulated until there were about 200,000 events in the 3^- peak. At 20°, a peak was observed in a position roughly corresponding to 1.75 MeV., the expected energy of the 0^+ level (see reference 1). The area of this peak, when compared with the 3^- peak, corresponded to a cross-section of 45 ∓ 10 μbarns. At 15°, the peak could not be distinguished from the slit-scattering background. However, an upper limit was estimated by taking half the total of events in the appropriate channels. The value obtained in this way was ≤ 200 μbarns.

A theoretical angular distribution for the 0^+ level was obtained with form factors calculated using the same parameters as for the ($g_{9/2}$) states. The interaction strength was again set at 85 MeV. Both the theoretical predictions and the experimental points are displayed in figures 6.27. As can be seen the predictions are up to three orders of magnitude too large.

The contribution from core-excitation, which would be greater for low angular momentum transfers has not been taken into account. It is possible that

the core transition amplitudes may be out of phase with the single particle amplitude and may account for the very large disparity between theory and experiment. There may also be similar destructive interference with the amplitude from multiple scattering. However, calculations at 19 MeV. have shown that at that energy, these effects are small (reference 19).

The $(2p_{1/2}\ 1g_{9/2})$ configuration

In addition to the $(g_{9/2})^2$ levels considered above, states with $L = 4$ or $L = 5$ may be excited by the transitions of a $2p_{1/2}$ or $1g_{9/2}$ proton to either the $1g_{9/2}$ or the $2p_{1/2}$ orbit. Thus the expression for the cross-section will have two terms representing each part of the transition. Since the single particle matrix elements involved are related by

$$\langle \ell' j' \| T_{LSJ} \| \ell j \rangle = \hat{j}/\hat{j'} \quad \langle \ell j \| T_{LSJ} \| \ell' j' \rangle (-)^{J-S} \qquad 6.13$$

the cross-sections are given by

$$\frac{d\sigma}{d\Omega} = (2J+1)(4\pi 2^{1/2} M_{LSJ} V_0)^2 \times \sigma_{LSJ} (a + (-)^{J-S} 5^{1/2} b) \qquad 6.14$$

In the case of the 5^- level, there is also a contribution from the spin-flip term in the interaction. This would not affect the shape of the angular distribution, only the magnitude of the cross-sections.

The 4^- level, on the other hand, may be excited only by the spin-flip term.

Results

The shell model wave function for the $g_{9/2}$ orbit was calculated using the same well depth as before, that is 50.17 MeV. This gave a binding energy of 6.74 MeV. compared with the proton separation energy from Y^{89} of 7.07 MeV. As with the $(g_{9/2})^2$ levels, the wave functions were not very sensitive to the value used for the binding energy. The effect of changing the various parameters of the effective interaction was investigated in the same way as for the $(g_{9/2})^2$ states, leading to the same conclusions. It was found that $\alpha = 0.6F^{-1}$ and $r_0 = 1.35F$ gave the best results. In fact, for a potential strength of 85 MeV. and zero spin-flip potential, the agreement between theory and experiment was better for the 5^- level than for most of the other levels. The results are illustrated in figure 6.21.

The predictions of the shell model in this case are again similar to those of the collective model (figure 6.7A). However, as in the case of any transition involving shell model wave functions with $n>1$, it is not possible to make the same comparison as above between the radial form factors. It can be seen from figures 6.31 and 6.29 that these

are very different. As for the $(g_{9/2})^2$ states, the collective model cross-sections show more structure than those of the shell model, although in this case the shell model gives slightly better agreement with the experimental data.

It is not possible to draw firm conclusions about the strength of the spin-flip term in a study of this level. Again, the data allows a certain amount of latitude in the total strength of the predicted cross-sections. The results, however, are certainly consistent with $V_s << V_o$. The 4^- level, which would give an unambiguous indication of the value of the spin-flip strength is completely obscured by the nearly degenerate and highly excited 3^- level at 2.75 MeV.

Harmonic oscillator potential form factors

In addition to the calculations using Saxon-Woods potentials to describe the shell model wave functions, form factors were also calculated for a harmonic oscillator potential well of the form

$$\tfrac{1}{2}\delta r^2 \qquad 6.15$$

where δ is a parameter specifying the width of the well. Provided a suitable value of δ was chosen, the wave functions produced by this potential were very similar to the Saxon-Woods wave functions. In figure 6.32, the $1g_{9/2}$ and $2p_{1/2}$ wave functions for

a potential with $\delta = 0.0925$ are compared with the corresponding Saxon-Woods wave functions. The mean square radius defined as

$$\langle r^2 \rangle = \frac{\int u_{n'l'}(r)\, u_{nl}(r)\, r^2 dr}{\int u_{n'l'}(r)\, u_{nl}(r)\, dr}$$

$$= \frac{11}{4\delta} \quad \text{(for the } (g_{9/2})^2 \text{ configuration)}$$

For $\delta = 0.0925$, $\langle r^2 \rangle = 29.9$ fermis corresponding to $\langle r_0 \rangle = 1.19$ fermis, which compares with $\langle r_0 \rangle = 1.185$ fermis for the Saxon-Woods potential. While the shape of the form factors was practically independant of the choice of single particle wave functions, the amplitude was increased by about 10% by the use of harmonic oscillator wave functions.

Particle hole states

In addition to the configurations involving only the outer protons in the $1g_{9/2}$ or $2p_{1/2}$ orbits, excited states may be formed by the transition of one of the core nucleons to an unfilled orbit. The energy levels observed experimentally will probably consist of a mixture of such configurations and more than one value of the orbital angular momentum transfer may be involved. The analysis of the remaining levels in Zr^{90} in terms of single particle-hole configurations therefore was an oversimplification. Nevertheless, such a description should help to confirm the tentative assignations of L-transfers made during

the collective model analysis. Furthermore, the possible correspondance between the number, strengths and L-values of the predicted single configuration states may give some information about the actual configurations making up the levels.

The configurations expected to give excited states in the energy range 0 MeV. to about 5 MeV. are given in table 6.8. In the case of proton excitations from the $1f_{5/2}$ and $2p_{3/2}$ orbits to the $2p_{1/2}$ orbits, the odd protons are left coupled to zero in the $1g_{9/2}$ orbit and the cross-sections are given by equation 6.6. For corresponding excitations to the $1g_{9/2}$ orbit, the protons are in the $2p_{1/2}$ orbit and the expression for the cross-section must be multiplied by a^2/b^2. For neutron excitations the expression is multiplied by $1/b^2$.

The angular distributions for the normal parity states were calculated for the same value of α and r_0 used in the analysis of the $(g_{9/2})^2$ levels. The depth of the shell model potential was set to 51 MeV. Where appropriate, both proton and neutron single particle wave functions were calculated. Apart from producing a much greater binding energy, the effect of replacing protons by neutrons on the form factor was relatively small. The neutron wave functions for the $1g_{9/2}$ and $2p_{1/2}$

states are shown for comparison in figure 6.32.

The comparisons between the experimental data and the angular distributions for some of the configurations are illustrated in figures 6.22 to 6.26. The key to these graphs is given in table 6.9. In each case, the theoretical cross-sections have been normalised to give the best agreement with the experimental data, using the same criteria as in the collective model analysis. The strength of the interaction corresponding to each normalisation was calculated using the spin-angle matrix elements M_{LSJ} of table 6.7. Also given in table 6.7 are the theoretical cross-sections at 30° calculated for a potential of 85 MeV. The results of the analysis are summarised in table 6.9. The angular distributions for all of the possible L-values for the normal parity states of each configuration were also calculated using harmonic oscillator wave functions with $\delta = 0.0925$. These cross-sections with normalisations corresponding to an interaction strength of 85 MeV. are illustrated in figure 6.28. They were calculated for an excitation energy of about 1.5 MeV. It was found that the magnitude of the cross-sections decreased by about 5% for every 1 MeV. increase in the excitation but the shape remained practically unchanged. They were also increased by about 10% by

the use of harmonic oscillator wave functions.

Results

For many of the levels, there was quite good agreement between the shapes of the experimental angular distribution and the predictions of at least one of the configurations. However, it can be seen from table 6.9 that in most cases the required interaction strength is considerably lower than the 85 MeV. required to account for the $(g_{9/2})^2$ levels. The number of normal parity states agrees approximately with the number of levels observed experimentally but there is less agreement between the numbers of states with a given L-transfer.

Four of the experimental states have angular distributions consistent with L = 2, compared with only three such levels predicted by the simple picture above. Although none of the experimental levels are particularly well fitted by any of the configurations, the predictions of D and E, which are fairly similar give better agreement on the whole than those of configuration C. The strengths of all the theoretical cross-sections are considerably greater than those of any of the experimental levels and it is not possible to make definite allocations of configurations to particular levels on this basis. However, it would appear that all the levels are

predominantly D or E configuration.

In the case of the $L = 3$ levels, the situation is complicated by the presence of the highly collective 2.75 MeV. 3^- level. In the shell model picture, this state is a combination of many particle-hole states and would be expected to absorb much of the available $L = 3$ strength. In all, eight of the experimental angular distributions appear to be consistent with $L = 3$, but of these, the 4.05 MeV. and to a lesser extent, the 4.89 MeV. are more likely to be $L = 4$. Of the remaining six levels, the 4.54, 4.79 and 5.06 MeV. levels were better fitted by configuration A which was also more consistent with the 2.75 MeV. level. Apart from this level, all of the experimental levels had cross-sections much lower than predicted for this configuration. The cross-sections of the 2.75 MeV. level however, were almost four times greater. The 4.45 and 4.95 MeV. levels were better fitted with either B or G configurations. The strength of the 4.45 MeV. level which was very well fitted by configuration B was about twice the predicted strength, and it is possible that this level is predominantly B with some G added. If this is so, then the 4.88 MeV. level would probably be predominantly G. The combined strength of all the configurations is unable to account for the total strength of the observed

levels if the 2.75 MeV. is included. It is possible, however, that other configurations not included in this analysis may take part in the excitation of this level.

Excited states with $L = 4$ are predicted by both configurations E and F. The angular distributions in both cases are very similar in shape though the former configuration produces cross-sections about 50% greater than the latter.

The 4.05, 4.32, 4.88 and perhaps the 4.54 MeV. levels were found by the collective model to be consistent with $L = 4$. There is no means of discriminating between the configurations but the strength of the F configuration is close to that of the 4.32 Level. Unfortunately, in this case there is very poor agreement between the shapes of the angular distributions. The total strength of the remaining levels is less than that of configuration E. They are reasonably well fitted by either configuration.

Only one of the experimental angular distributions was consistent with $L = 5$, although contributions from $L = 5$ transitions may well appear in some of the levels where the allocation of an L-transfer was ambiguous. Both configurations A and B predict $L = 5$ states but in either case the predicted strength is only half

the observed strength. Configuration A clearly gives the best agreement with the data but a mixture of A and B would produce the required strength while remaining in fairly good agreement with experiment.

Angular distributions for higher angular momentum transfers predicted by these configurations were expected to have low cross-sections ≤ 0.1 mbarn at 30° and were unlikely to be seen in the present experiment.

Finally, a strong $L = 1$ state is expected from configuration H. This was stronger than any of the observed levels and may possibly appear at higher energies than those considered here.

The above discussion has been confined to normal parity states and the spin-flip interaction was assumed to be zero. If a Serber mixture with $V_1 = V_0$ was assumed, a number of non-normal parity states would be expected in addition to those considered above. In particular there is an $L = 0$ transition to the 1^+ level of configuration C. The level most likely to include such a configuration is the 3.37 MeV. state. In figure 6.22A the angular distribution for this transition is compared with that of the 3.37 MeV. level. The quality of the fit is about as good as for $L = 2$, but the interaction strength required

is only 8 MeV., a factor of ten less than predicted.

It appears therefore that the number, type and strength of the levels observed in the experiment is more or less consistent with $V_1 << V_0$.

Another problem ignored by the above discussion is the confusion caused by the lack of information about the strength of the isovector potential. In the analysis it was assumed that the potential used to excite a proton was the same as used to excite a neutron, that is, $V_\beta = 0$. Nothing in the results sheds any light on whether this assumption was justified.

Conclusion and discussion

Both the shell model and the collective model gave an adequate account of the angular distributions for most of the energy levels in Zr^{90} excited by proton inelastic scattering. It was found that a two body interaction with a range parameter of 0.6 fermis^{-1} and a Wigner strength of 85 MeV. gave reasonably accurate predictions of the shape and strengths of the cross-sections of the $(g_{9/2})^2$ and $g_{9/2}\, p_{1/2}$ states, although better results were obtained for the 2^+ level with a potential of 50 MeV. Little difference was found between the predictions made using Saxon-Woods single particle wave functions and corresponding harmonic oscillator functions.

The collective model gave a consistently more realistic description of the angular distributions of all the levels except the 5^- level. This was shown to be principally due to the use of a complex form factor. Mathematically, this is not unreasonable as the additional structure observed in cross-sections calculated with complex form factors probably arises from interference between the amplitudes of the real and imaginary components. As the two parts of the form factor are generally peaked at different radii (the optical model consistently gave $r_I > r_R$) the corresponding scattering amplitudes may be slightly out of phase, producing a more marked diffraction pattern. Physically, the introduction of an imaginary component in the interaction is not unreasonable either, as mentioned above, a complex interaction arises naturally to take into account the polarisation of the core and excitation of particles to the continuum states.

The study of 19 MeV. proton scattering (reference 1) has led to similar conclusions to those of the present analysis, with the exception of the 2.18 MeV. 2^+ state. In the case of this level, the agreement with the 19 MeV. experimental angular distributions was improved by increasing the interaction strength, the reverse of the effect seen at

50 MeV. As at 19 MeV., the present data shows the cross-sections observed for the 8^+ level to be larger than the predictions, though to a greater extent than at 19 MeV. The 0^+ cross-sections were very much lower than the predictions, which also agreed with the findings at 19 MeV., but for the present data, the effect was an order of magnitude greater. If, as is probable, the disparity between theory and experiment for the 8^+ level is due to the presence of levels in other nuclei present in the target as impurities, there is little reason to expect any correspondance between the two sets of results. On the other hand, the poor agreement of the 0^+ predictions with experiment is possibly caused by destructive interference between the core polarisation and the configuration discussed above. Such core excitation would be expected to increase with greater incident energy, when the incoming proton is more likely to penetrate the core. Core polarisation was also suggested as a reason for the enhanced interaction strength required for the 2^+ level at 19 MeV. However, the change of these effects with energy is unlikely to explain the very different results obtained in this analysis. It is also possible that other defects of the model such as the neglect of total antisymmetrisation between the projectile

and the nucleons of the target may play a part.

Section 6iii: Energy Levels

According to the shell model, the zirconium isotopes are depicted as a Zr^{90} core with neutrons filling the $2d_{5/2}$ shell. Thus, with the exception of Zr^{90} itself, the energy levels in all of the isotopes are mainly obtained by exciting one of the outer neutrons to a neighbouring orbit. The situation in practice is more complicated however, as there will probably be contributions from proton configurations of the Zr^{90} core. These have been extensively discussed in previous sections, where it was shown that the excited states could be explained in terms of $(g_{9/2})^2$, $(g_{9/2}p_{1/2})$ or hole particle configurations. The observed energy levels of Zr^{90} are illustrated in figure 6.34. These were obtained using the method of section 3v. A typical fitted spectrum is illustrated in figure 6.33. Also in figure 6.34 for comparison, the results of 19 MeV. proton inelastic scattering (reference 1) are shown (set B). It can be seen that there is good agreement between number and energy of the levels observed in the two experiments except that the 5.47 and 5.50 MeV. levels have not been seen in the present work. The tentative assignments of the L-transfer have been made on the basis of the foregoing collective

and shell model analyses. The strongly excited 3^- collective level at 2.75 MeV. was also seen in the other even isotopes; at 2.34 MeV. in Zr^{92}, at 2.064 in Zr^{94} and at 1.86 MeV. in Zr^{96}.

In Zr^{91}, the only odd nulide in the group, the energy levels are expected to be mainly due to the excitation of the odd nucleon. The comparison of the results of the present work (set A) with the Nuclear Data sheets (set B), 19 MeV. proton inelastic scattering (set D: reference 20) and (d,p) reactions in Zr^{90} (set C: reference 21) is illustrated in figure 6.35. The energy levels were obtained using the method of section 3v. The spectrum at 20° is shown in figure 6.39. The agreement of the present data with previous work is rather poor. Reasons for this are given in section 3iv. However, the number of levels agrees with those for (d,p) reactions although many of the levels seen in 19 MeV. proton scattering studies have not been observed.

Zr^{92} and Zr^{94} are expected to have similar sets of energy levels as they have complementary structures and the low lying excited states may be dominated by the $(d_{5/2})^2$ and $(d_{5/2})^{-2}$ neutron configurations respectively. However, proton excitations of the core also play an important part. For instance, the 0.93 MeV. 0^+ level is believed to be primarily $(g_{9/2})^2$ configuration.

The energy level diagrams are illustrated in figures 6.36 and 6.37. In both cases, the results of 19 MeV. proton scattering (set B: reference 23); and inelastic deuteron scattering (set C: reference 24) are also shown. In addition, the levels excited by (d,p) reactions on Zr^{91} are shown for Zr^{92} (set D: reference 25). As in the case of Zr^{90} there is good agreement between the present data and previous work, except that for Zr^{92} at higher energies rather more levels have been observed in the present work. The L-value assignments for some of the levels have tentatively been made on the basis of the collective model analysis.

Finally, the energy levels obtained for Zr^{96} are shown in figure 6.38. Sets B, C and D are for (t,p) reactions on Zr^{94} (reference 26), (d,d) scattering (reference 24) and (p,p') scattering at 19 MeV. (reference 27) respectively. As in the case of Zr^{91} the method of section 3iv was used and the agreement between the results is poor. The energy spectrum recorded at 40° is shown in figure 6.40. There will be similarities between the Zr^{96} energy levels and those of Zr^{92} as the excitation of a $d_{5/2}$ neutron from the closed shell in Zr^{96} leaves a $d_{5/2}^{-1}$ hole. There is some correspondance although not as marked as between Zr^{92} and Zr^{94}.

Appendix A1: A Non-linear Parameter Search program for Spectrum Stripping

A non-linear parameter search program, written in FORTRAN IV by Mr.G.S.Mani for an IBM 360/75 computer was used to calculate the areas of the peaks in the experimental spectra. The operation of the program is summarised in figure A1.

The program first reads in a set of numbers which enable it to define the initial set of parameters on which the set is based. These parameters consist of a set of heights, widths and positions corresponding to the various peaks and a background parameter. They may be specified explicitly, or, more usually, only the peak positions are supplied to the program. The height of each peak is then estimated from the experimental spectrum and the width set to a standard value, usually 5 or 6 channels. The amount of data required by the program may be further reduced by defining a standard spectrum. This spectrum is treated first, and any subsequent spectra which have a similar basic structure may be specified by using the relative displacement to the standard spectrum.

The progress of the fitting procedure is governed by other parameters, also read in initially. These are CHIMIN, the minimum value of χ^2; CHIDIF, the minimum permissable change in χ^2, NROLL, MCUT

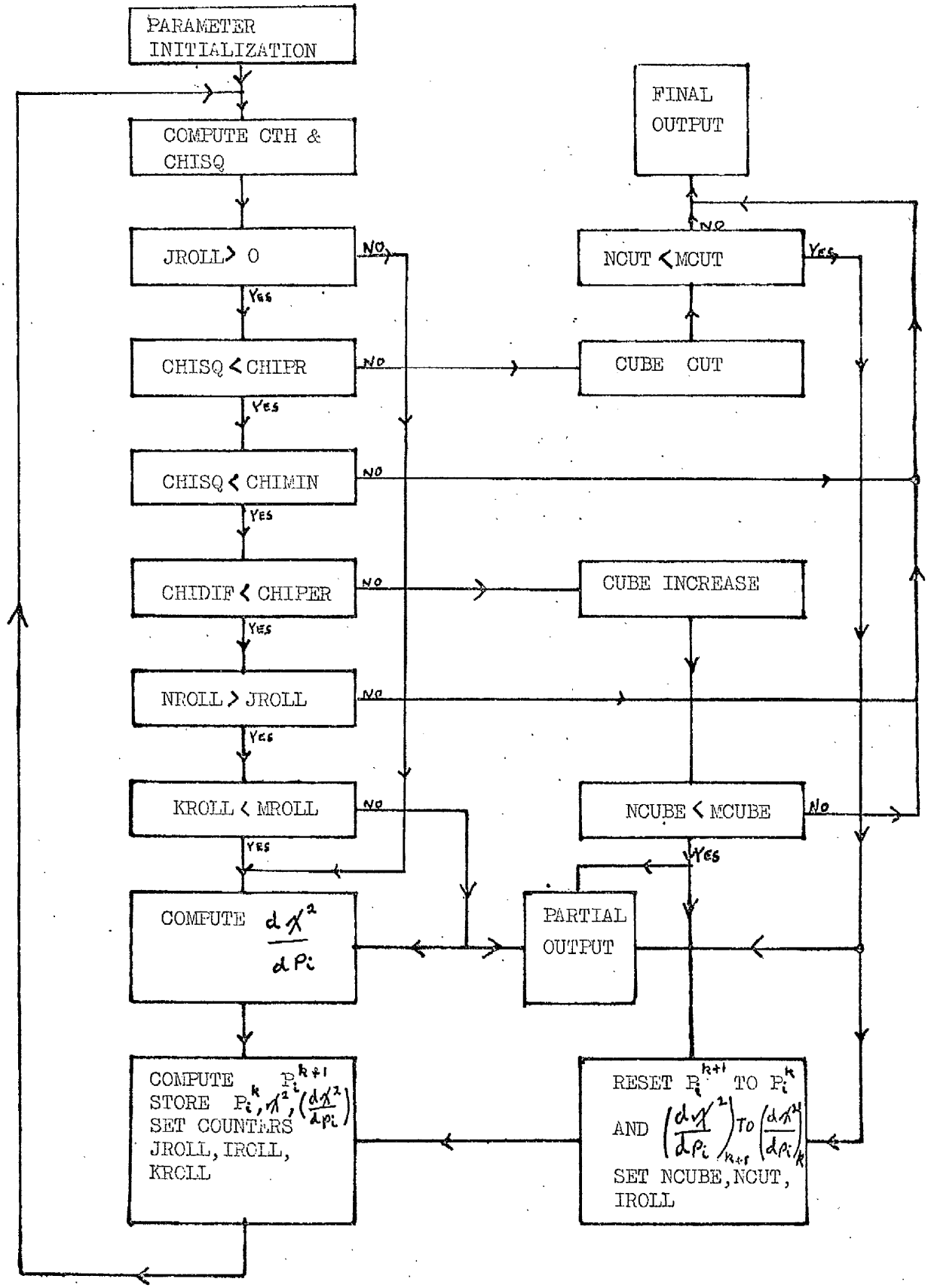

Figure A1 Logic Diagram for Spectrum Stripping Program.

and MCUBE which govern the total number of iterations, step-length reductions or increases, NMAG, the position of the spectrum on the magnetic tape and MROLL which controls output.

The program reads the appropriate spectrum from magnetic tape or disk. It then uses the initial parameters $(P_i^K)_{K=1}$ to calculate a theoretical spectrum (CTH) and the values of χ^2 (CHISQ) from equations 3.19 and 3.20. In the first iteration the program proceeds directly to calculate the values of $d\chi^2/d\rho_i$ and uses these values to obtain a new set of parameters P_i^{k+1} where

$$P_i^{k+1} = P_i^K + \Delta\rho_i \frac{d\chi^2/d\rho_i}{(d\chi^2/d\rho_j)_{max}} \qquad A1$$

$(d\chi^2/d\rho_j)$ max is the largest valued $d\chi^2/d\rho_i$ and $\Delta\rho_i$ is the step-length. This may be set explicitly, or by default the program takes standard values: 1 channel for the position and 10% of the width and height. The counters JROLL, IROLL and KROLL are incremented by one.

Using the new parameters, CTH and χ^2 are recalculated and the latter compared with the previous value. If the new value is greater, the step-length is too long and the program enters the cube cut section. The step-lengths are then reduced according to the equation

$$\Delta \rho_i = \Delta \rho_i \times \frac{0.5\, d\chi^2/d\rho_i}{(d\chi^2/d\rho_i)_{max}} \qquad A2$$

The parameters ρ_i^{k+1} are recalculated from the original and the values of CTH and χ^2 recomputed. The NCUT counter is increased by 1.

If, on the other hand, the new value of was less than the previous value, but by an amount less than CHIDIF, the parameters are not changing quickly enough and the program enters the cube increase stage. Here, the step-lengths are increased according to the equation

$$(\Delta \rho_i)_{new} = \Delta \rho_i \times 2.0 \qquad A3$$

The NCUBE counter is incremented and CTH and recalculated as in the cube cut section.

If both the above tests are negative, the program proceeds directly to the next iteration.

Output

The program is provided with facilities for output, both at the end of the calculation and at any intermediate stage. These intermediate or partial outputs occur at intervals determined by KROLL, which produces an output every MROLL iterations and whenever the cube increase or cube cut stage is entered. On later versions of the program the partial output has been suppressed.

Final output can occur in four ways: if the

present minimum value of χ^2 is achieved, if the total number of iterations exceeds NROLL, and if the number of cube cuts or increases exceeds MCUBE and MCUT respectively.

On final output, the values of the final parameters are printed out and the areas of each peak calculated. A brief summary of the fitting procedure is also printed out. Finally the theoretical and experimental spectra are printed out in graphical form to facilitate comparison.

Later versions of the program take the calculation a step further. Sufficient information is supplied to the program to enable it to calculate absolute cross-sections using equation 3.6. The channel number is converted to energy and the cross-section, error, centre of mass angle and energy of the peak are all output on a single punched card. A second program is then used to correlate the results from a number of similar spectra to produce a single angular distribution and a set of energy levels.

Appendix A2: The Nuclear Matrix Elements

In Chapter 5 an expression was derived for the interaction V of equation 5.2 in terms of a sum of two body forces over the nucleons of the target. The radial part of the nuclear matrix element $G^{T}_{LSJ}(r)$ can then be expressed in terms of the matrix elements of the isoscalar and isovector operators. These are one body operators in the space of the target nucleons. Hence they will connect shell model configurations which differ by, at most, the state of one nucleon. If we limit the discussion to the case of a single configuration in the initial and final states we may separate the matrix elements into radial and spin-angle factors. Therefore we may write

$$G^{T}_{LSJ} = 4\pi 2^{1/2} \langle J_{A'} T_{A'} || V_{S\alpha} \delta_{T0} + V_{S\beta} \delta_{T1} 3^{1/2} \tau || J_A T_A \rangle \qquad A1$$

where $V_{S\alpha}$ and $V_{S\beta}$ respectively are the strengths of the isoscalar and isovector potentials.

Two particle configurations

First we consider the case of ground state with two particles outside an inert core, both in the same shell with angular momentum j coupled to give a total angular momentum J_A. An excited state with angular momentum $J_{A'}$ may be obtained by

the transition of one of the particles to the j' orbit. Considering only the isoscalar term at present, we may write

$$\langle j\, j' \| T_{LSJ}\, g_L(r_p, r) \| j^2\, J_A \rangle = (-)^{J_A' - J}$$

$$\hat{J}_A\, \hat{j}\, W(j' j\, J_A' J_A\, j\, J j) \langle j' \| T_{LSJ}\, g_L(r_p) \| j \rangle \qquad \text{A2}$$

The last factor in this equation is the single particle matrix element. This describes the excitation of a single particle outside an inert spinless core from an initial orbit j to the j' orbit. T_{LSJ} is a composite tensor consisting of the product of spin and angle tensors (equation 5.26). The wave function may also be expanded in terms of radial, spin and angular parts. Hence

$$|n \ell j\rangle = \sum_N \langle \ell s\; m-N\; m | J N \rangle u_{n\ell}(r)\, Y_\ell^{m-N}\, \chi_s \qquad \text{A3}$$

Using the relations of reference 12 we obtain for the single particle matrix element

$$\langle n' \ell' j' \| T_{LSJ}\, g_L(r_p) \| n \ell j \rangle = \langle \ell' \tfrac{1}{2}\, j' \| T_{LSJ} \| \ell \tfrac{1}{2}\, j \rangle \mathcal{I}_L(r)$$

$$= \hat{j}\, \hat{J}\, \hat{\ell}\, \hat{\tfrac{1}{2}} \begin{pmatrix} j' & j & J \\ \ell' & \ell & L \\ \frac{1}{2} & \frac{1}{2} & S \end{pmatrix} \langle \ell' \| Y_L \| \ell \rangle \langle \tfrac{1}{2} \| S_S \| \tfrac{1}{2} \rangle \mathcal{I}_L(r)$$

where $\mathcal{I}_L(r) = \int g_L(r)\, u_{n\ell}(r)\, u_{n'\ell'}(r)\, dr$ A4

S may have the values 0 or 1. Using the standard expression for the various quantities in this equation we may write

$$\langle \ell' j' \| T_{LSJ} \| \ell j \rangle = i^{L+\ell+\ell'} (-)^{j+\ell-1/2} \hat{L}\hat{j} \times \begin{pmatrix} j' & j & J \\ \frac{1}{2} & -\frac{1}{2} & 0 \end{pmatrix} \frac{b_{LSJ}}{4\pi}$$

where

$$b_{L0L} = 1$$

$$b_{L1L} = (x-y')/\hat{L} \qquad b_{L1L-1} = -\hat{L}\frac{(L+x+y)}{L^{1/2}}$$

$$b_{L1L+1} = \hat{L}(\ell+1-x-y)/(L+1)^{1/2}$$

and $x = (\ell-j)(2j+1)$, $x' = (\ell'-j')(2j'+1)$. A5

The $(g_{9/2})^2$ configuration

In this case a number of excited states may be obtained by recoupling the angular momenta of the two particles in the $1g_{9/2}$ shell. Here $J_A = 0$, $j = j'$ and $S = 0$. If we identify $I_L(r)$ with the F_{LSJ} of equation 5, we may write

$$A^{(0)}_{LSJ} = 4\pi 2^{1/2} M_{LSJ} \qquad \text{where } J = L \quad \text{A6}$$

where $M_{L0L} = 2\hat{L}\langle \ell j \| Y_L(\theta,\phi) \| \ell j \rangle$ A7

The factor of 2 in this equation occurs because both particles in the $g_{9/2}$ shell may take part in the transition.

The $(p_{1/2}\ g_{9/2})$ configuration

Here we consider one of the n particles in the $p_{1/2}$ shell, excited to the $g_{9/2}$ shell. In the cases arising in this study, $n = 2$ allowing the use of the above expressions. When antisymmetrisation between the particle left in the $p_{1/2}$ state and the particle in the $g_{9/2}$ state is taken into account a factor of $2^{-\frac{1}{2}}$ is introduced into equation 2. Again,

both particles may take part in the transition so that

$$M_{LSJ} = \frac{2^{1/2}}{\hat{J}\,\hat{j}}\,\hat{j}'\,\langle \ell j' \| T_{LSJ} \| \ell j \rangle \qquad \text{A8}$$

Particle hole states

Apart from the states formed by the particles outside the closed shells, excited states may be obtained by the transition of a particle from a filled shell to an unoccupied orbit. The matrix elements for such hole particle pairs is given by (references 28 and 29)

$$M_{LSJ} = (-)^{S-1}\,\hat{j}\,\frac{2^{1/2}}{\hat{J}}\,\langle \ell j' \| T_{LSJ} \| \ell j' \rangle \qquad \text{A9}$$

Isospin dependance

In the above discussion, no account has been taken of isospin. The matrix elements of the isovector operator lead to similar expressions to equations 7, 9 and 10, multiplied by a factor depending on the isospin of the nucleus. However, for nucleons, it turns out that this quantity is always balanced by a quantity contributed by the Clebsch-Gordon coefficients, of equation 5.36. Provided, therefore, that the strength of the nucleon-nucleon potential is averaged over the isospin, we may neglect the effect of isospin altogether so that $A_{LSJ} = V_S\, 4\pi\, 2^{1/2}\, M_{LSJ}$ A10 where $V_S = V_{S\alpha} + V_{S\beta}$ for the excitation of a proton and $V_S = V_{S\alpha} - V_{S\beta}$ for neutron states.

Appendix A3: The Radial Form Factors

In equation 4 of Appendix 2, the radial part of the nuclear matrix element was factorised out of the expression and written as

$$I_L(r) = \int g_L(r,r_1)\, u_{nl}(r_1)\, u_{n'l'}(r_1)\, dr_1 \qquad A1$$

u_{nl} and $u_{n'l'}$ are the initial and final shell model wave functions and $g_L(r)$ is the radial part of the Lth term of the multipole expansion of the interaction. The wave functions were calculated both for a harmonic oscillator potential and for a Saxon-Woods potential similar to the real part of the optical potential. Both sets of wave functions were approximately equivalent. The interaction used in the present analysis had a Yukawa form

$$V = \frac{V_0\, e^{-\alpha r}}{r} \qquad A2$$

This expression may be written in terms of spherical Bessel and Hankel functions such that the radial term $g_L(r, r_1)$ may be written

$$\begin{aligned} g_L(r) &= j_L(ikr_1)\, h_L(ikr) \qquad r_1 > r \\ &= j_L(ikr)\, h_L(ikr_1) \qquad r > r_1 \end{aligned} \qquad A3$$

The Saxon-Woods wave functions were evaluated by the program described in reference 18. The harmonic oscillator wave functions were evaluated by a series expansion in terms of δr, where δ is the range parameter. Suitable expressions are given in reference

30. The spherical Bessel and Hankel functions were evaluated by upward recursion for $|ikr| \geq 1$ and by series expansion for lower values. The integration of equation 1 was carried out upto r_c = 20 fermis using a step length of 0.05 fermis. These values proved to give the required accuracy.

	V_r	r_r	a_r	W_s	W_d	r_i	a_i	V_{so}	r_{so}	a_{so}	r_c	χ^2	
1.	47.53	1.1608	0.7478	6.53	1.70	1.3954	0.5430	5.70	1.0582	0.7100	1.115	308	Fig.6.1B
2.	48.77	1.1677	0.7495	9.07		1.4099	0.4970	5.65	1.0754	0.7179	1.115	401	
3.	43.36	1.2173	0.6763		8.21	1.1401	0.7151	5.35	1.1408	0.7054	1.115	687	Fig.6.2A
4.	47.52	1.1634	0.7377	6.41	1.81	1.3877	0.5708	5.80	1.0473	0.7422	1.15	319	
5.	48.76	1.1661	0.7511	9.10		1.4075	0.5088	5.75	1.0762	0.7321	1.15	395	
6.	45.58	1.1966	0.6782		9.42	1.1009	0.7060	5.25	1.1321	0.7131	1.15	780	
7.	47.02	1.1635	0.7430	6.71	1.60	1.3939	0.5479	5.90	1.0524	0.7296	1.20	306	
8.	48.26	1.1690	0.7500	9.03		1.4117	0.4950	5.75	1.0768	0.7229	1.20	385	
9.	45.40	1.2201	0.6687		9.61	1.1163	0.6756	5.70	1.1199	0.7095	1.20	794	
10.	47.60	1.1624	0.7531	7.69	1.26	1.3902	0.5092	5.80	1.0737	0.6783	1.25	305	
11.	48.10	1.1690	0.7535	9.07		1.4128	0.4856	5.75	1.0800	0.7076	1.25	387	
12.	39.84	1.2388	0.6628		6.92	1.1043	0.8652	4.65	1.1310	0.7700	1.25	687	
13.	47.52	1.1633	0.7490	7.57	1.25	1.3965	0.5005	5.8	1.0704	0.6838	1.25	303	Fig.6.1A
14.	48.33	1.1489	0.7527	7.11	1.53	1.3717	0.6140	5.9	1.0512	0.7220	1.25	355	
15.	47.71	1.1487	0.7739	6.45	1.94	1.3679	0.6123	6.05	1.0530	0.7153	1.25	396	
16.	45.95	1.186	0.674	3.21	5.25	1.300	0.655	6.92	1.002	0.861	1.25		
17.	47.76	1.16	0.75	4.69	3.46	1.37	0.63	6.04	1.064	0.738	1.25		

Table 6.1 Optical ModelParameters for Zr^{90}

	V_r	r_r	a_r	W_s	W_d	r_i	a_i	V_{so}	r_{so}	a_{so}	r_c	χ^2
1.	47.83	1.1560	0.7636	8.22	1.22	1.3542	0.6726	5.85	1.0436	0.7159	1.115	259
2.	48.88	1.1573	0.7725	10.44		1.3599	0.6548	5.80	1.0393	0.7569	1.115	298
3.	44.05	1.1847	0.7337		6.85	1.0877	0.9557	4.00	1.0107	0.5410	1.115	840
4.	47.65	1.1550	0.7654	8.06	1.36	1.3503	0.6793	6.00	1.0309	0.7328	1.150	256
5.	48.69	1.1582	0.7768	9.98		1.3884	0.5825	5.95	1.0674	0.7111	1.150	285
6.	44.05	1.1973	0.6875		10.13	1.0959	0.7121	5.10	1.1179	0.6261	1.150	757
7.	47.70	1.1556	0.7687	8.58	1.05	1.3587	0.6520	6.05	1.0405	0.7221	1.200	250
8.	48.61	1.1564	0.7761	10.09		1.3792	0.6108	6.05	1.0476	0.7224	1.200	276
9.	45.09	1.1912	0.7079		10.28	1.0253	0.7990	5.25	1.0283	0.8621	1.200	543
10.	48.02	1.1543	0.7700	8.80	1.10	1.3610	0.6145	5.90	1.0627	0.6839	1.250	253
11.	48.46	1.1566	0.7818	10.12		1.3855	0.5798	6.10	1.0565	0.7077	1.250	274
12.	44.78	1.1875	0.7243		10.26	0.9964	0.8455	5.20	1.0430	0.8469	1.250	508
13.	49.18	1.1437	0.7814	8.83	7.09	1.3686	0.5893	6.10	1.0588	0.6891	1.250	243
14.	48.21	1.1489	0.7527	7.94	1.55	1.3717	0.6140	6.3	1.0512	0.7220	1.25	304
15.	48.36	1.1487	0.7739	8.55	1.17	1.3679	0.6123	6.35	1.0530	0.7153	1.25	248

Fig.6.2B

Table 6.2 Optical Model Parameters for Zr^{91}

	V_r	r_r	a_r	W_s	W_d	r_i	a_i	V_{so}	r_{so}	a_{so}	r_c	χ^2
1.	47.01	1.1514	0.7693	7.99	2.11	1.3338	0.7444	5.85	1.0487	0.6864	1.115	271
2.	48.54	1.1526	0.7721	11.96		1.3454	0.7221	5.60	1.0576	0.6821	1.115	449
3.	43.69	1.1765	0.7386		6.86	1.0690	1.1179	4.6	1.0453	0.6681	1.115	508
4.	47.15	1.1518	0.7680	8.79	1.62	1.3448	0.7214	5.85	1.0511	0.6797	1.15	266
5.	48.09	1.1544	0.7710	11.21		1.3740	0.6903	5.75	1.0643	0.6863	1.15	379
6.	44.49	1.2015	0.7042		11.70	1.0855	0.7244	5.4	1.1150	0.6158	1.15	610
7.	46.72	1.1530	0.7695	8.62	1.72	1.3426	0.7234	5.85	1.0506	0.6817	1.2	262
8.	47.84	1.1535	0.7697	11.14		1.3726	0.7064	5.75	1.0584	0.6806	1.2	364
9.	44.21	1.2012	0.7083		11.51	1.0665	0.7482	4.95	1.1060	0.6846	1.2	580
10.	47.04	1.1526	0.7743	9.43	1.33	1.3526	0.6869	5.75	1.0615	0.6593	1.25	274
11.	47.66	1.1545	0.7728	11.26		1.3707	0.6922	5.9	1.0488	0.7013	1.25	370
12.	43.86	1.2039	0.6975		11.55	1.0718	0.7436	5.05	1.0988	0.6789	1.25	570
13.	48.55	1.1334	0.7901	8.95	1.28	1.3685	0.6900	6.1	1.0321	0.6810	1.25	248
14.	47.81	1.1489	0.7527	9.19	1.53	1.3717	0.6147	6.30	1.0512	0.7220	1.25	422
15.	47.72	1.1487	0.7739	9.06	1.64	1.3679	0.6123	6.25	1.0530	0.7153	1.25	326

Fig.6.3A

Table 6.3 Optical Model Parameters for Zr^{92}

	V_r	r_r	a_r	W_s	W_d	V_i	a_i	V_{so}	r_{so}	a_{so}	r_c	χ^2	
1.	47.19	1.1569	0.7718	7.75	2.25	1.3484	0.6811	5.65	1.0758	0.7590	1.115	319	
2.	49.54	1.1531	0.7857	11.68		1.3598	0.6778	4.90	1.0812	0.7713	1.115	581	
3.	43.71	1.1980	0.7138		8.37	1.1067	0.8810	5.15	1.1301	0.7585	1.115	466	
4.	46.92	1.1575	0.7728	7.68	2.29	1.3559	0.6576	5.80	1.0678	0.7449	1.15	321	
5.	48.50	1.1587	0.7774	11.21		1.3701	0.6840	5.45	1.0412	0.8595	1.15	514	Fig.6.4A
6.	44.93	1.2071	0.6862		11.67	1.1307	0.6546	5.20	1.1436	0.6377	1.15	800	
7.	46.67	1.1578	0.7725	7.67	2.31	1.3537	0.6617	5.70	1.0764	0.7425	1.2	314	
8.	48.37	1.1583	0.7792	11.13		1.3828	0.6488	5.45	1.0757	0.7476	1.2	526	
9.	44.50	1.2078	0.6868		11.66	1.1272	0.6577	5.2	1.1317	0.6708	1.2	758	
10.	46.45	1.1584	0.7722	7.92	2.09	1.3610	0.6538	5.75	1.0743	0.7445	1.25	313	
11.	48.87	1.1555	0.7863	11.68		1.3653	0.6565	5.25	1.0630	0.7936	1.25	560	Fig.6.4B
12.	42.97	1.2017	0.7057		8.73	1.0971	0.8741	5.5	1.1132	0.7790	1.25	469	
13.	48.16	1.1414	0.7896	8.04	2.06	1.3665	0.6353	5.95	1.0625	0.7411	1.25	301	Fig.6.3B
14.	47.81	1.1489	0.7527	8.26	2.00	1.3717	0.6147	5.80	1.0512	0.7220	1.25	435	
15.	47.59	1.1487	0.7739	7.95	2.25	1.3679	0.6123	5.80	1.0530	0.7153	1.25	339	

Table 6.4 Optical Model Parameters for Zr^{94}

	V_r	r_r	a_r	W_s	W_d	r_i	a_i	V_{so}	r_{so}	a_{so}	r_c	λ^2	
1.	48.43	1.1535	0.7624	7.41	2.23	1.3547	0.6466	6.35	1.0442	0.7898	1.115	154	
2.	49.91	1.1581	0.7712	10.75		1.3746	0.6328	5.75	1.0469	0.8380	1.115	383	
3.	44.25	1.1938	0.6944		7.40	1.0767	1.0046	5.70	1.0760	0.8554	1.115	324	
4.	48.33	1.1522	0.7663	7.39	2.20	1.3603	0.6333	6.30	1.0449	0.7742	1.15	158	
5.	48.75	1.1640	0.7625	10.29		1.3867	0.6359	6.20	1.0273	0.8707	1.15	326	
6.	45.11	1.2052	0.6867		10.67	1.0914	0.7233	5.80	1.1163	0.7658	1.15	332	Fig.6.5B
7.	48.27	1.1524	0.7705	7.79	1.99	1.3662	0.6115	6.35	1.0555	0.7630	1.20	165	
8.	48.58	1.1632	0.7622	10.15		1.3928	0.6330	6.00	1.0487	0.8212	1.20	318	Fig.6.5C
9.	44.83	1.2042	0.6853		10.59	1.0726	0.7529	5.55	1.1070	0.7884	1.20	342	
10.	47.56	1.1581	0.7632	7.73	2.06	1.3584	0.6303	6.20	1.0494	0.7817	1.25	165	
11.	49.15	1.1603	0.7730	10.77		1.3745	0.6295	5.65	1.0452	0.8237	1.25	395	
12.	44.53	1.2049	0.6846		10.55	1.0751	0.7535	5.65	1.1106	0.7711	1.25	338	
13.	46.59	1.1629	0.7583	7.16	2.24	1.3586	0.6581	6.60	1.0322	0.8154	1.25	149	Fig.6.5A
14.	48.22	1.1489	0.7527	7.72	1.95	1.3717	0.6147	6.30	1.0512	0.7220	1.25	220	
15.	48.07	1.1487	0.7739	7.44	2.21	1.3679	0.6123	6.35	1.0530	0.7153	1.25	179	

Table 6.5 Optical ModelParameters for Zr^{96}

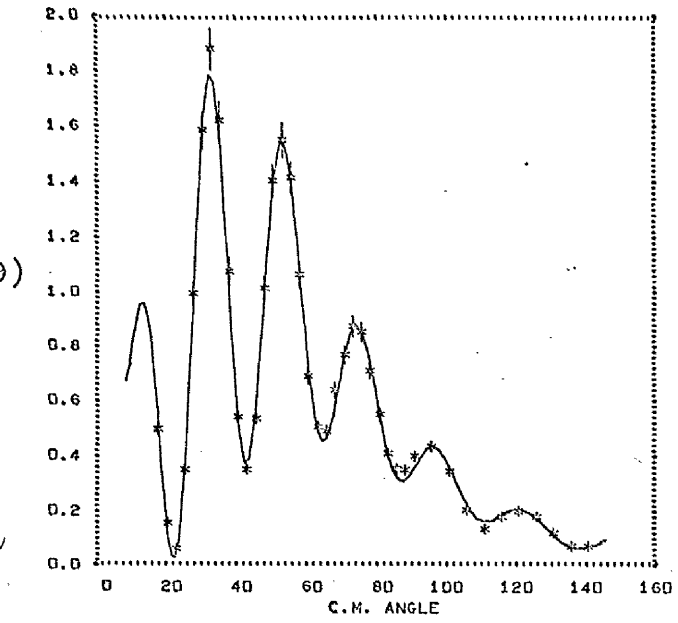

A. Zr^{90} Parameter Set 13.

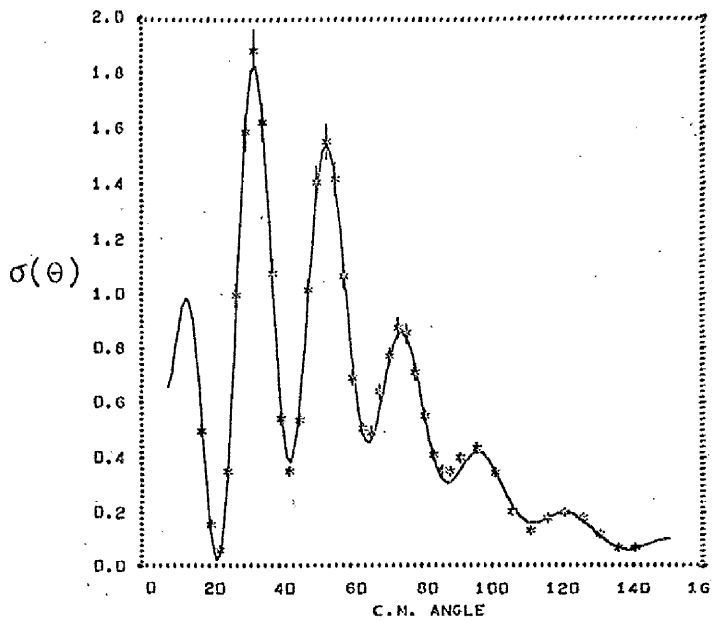

B. Zr^{90} Parameter Set 1.

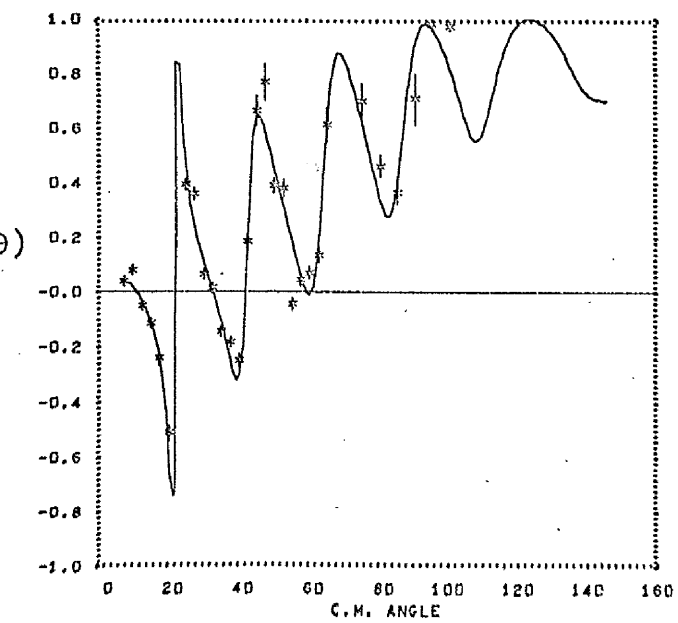

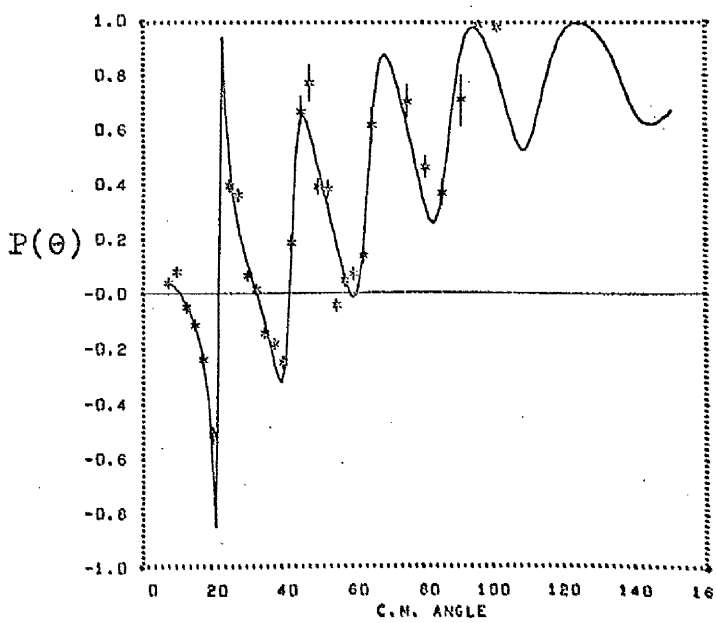

Figure 6.1 Optical Model Predictions for Cross-sections and Polarisations of Elastic Scattering.

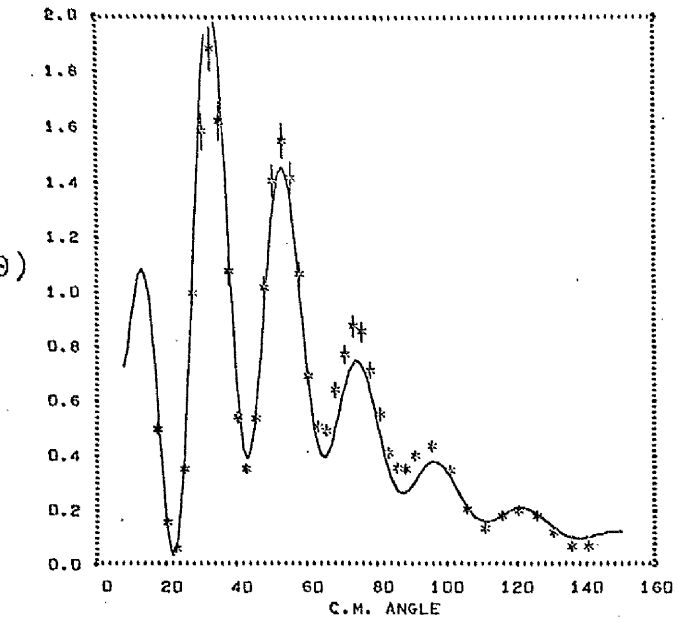

A. Zr^{90}, Parameter Set 3.

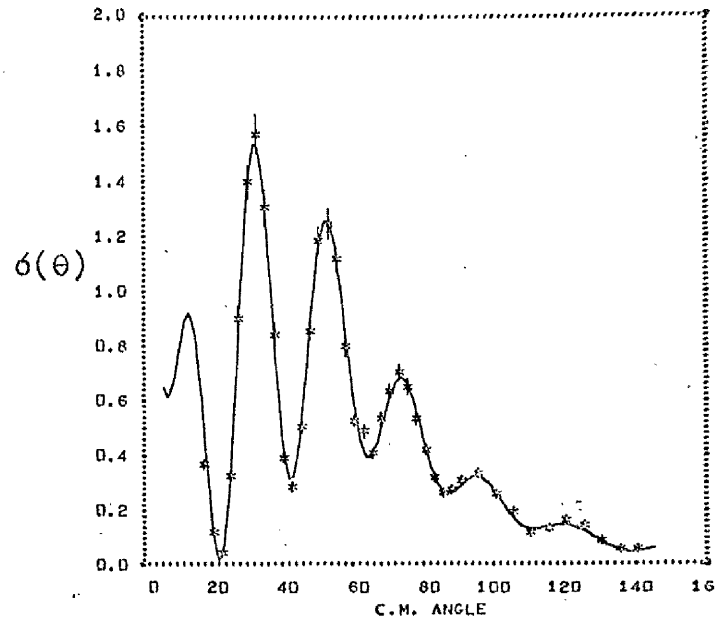

B. Zr^{91}, Parameter Set 13.

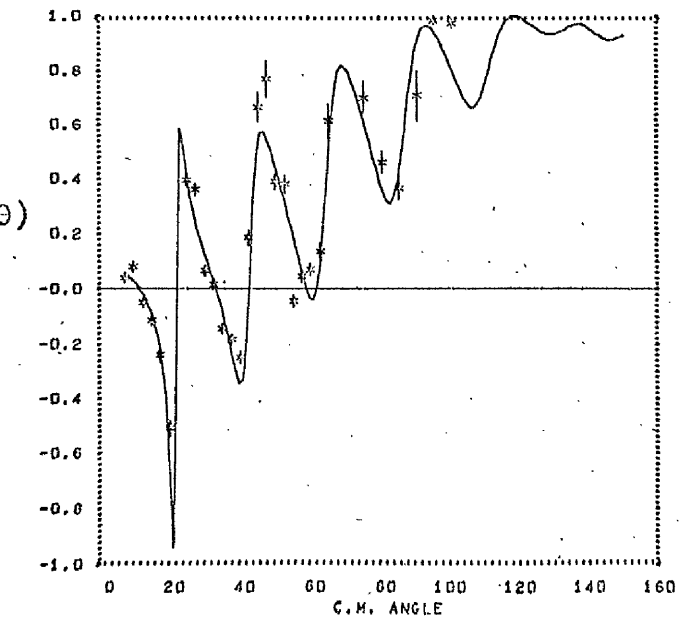

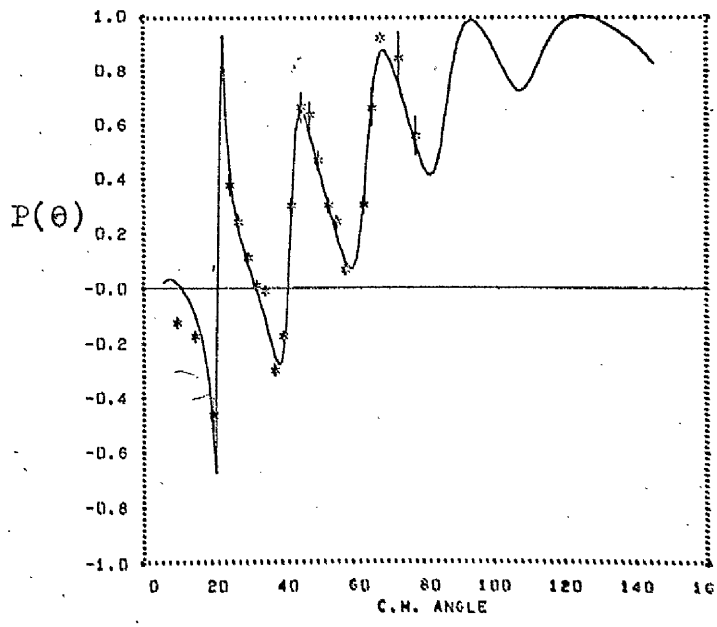

Figure 6.2 Optical Model Predictions for Cross-section and Polarisation of Elastic Scattering.

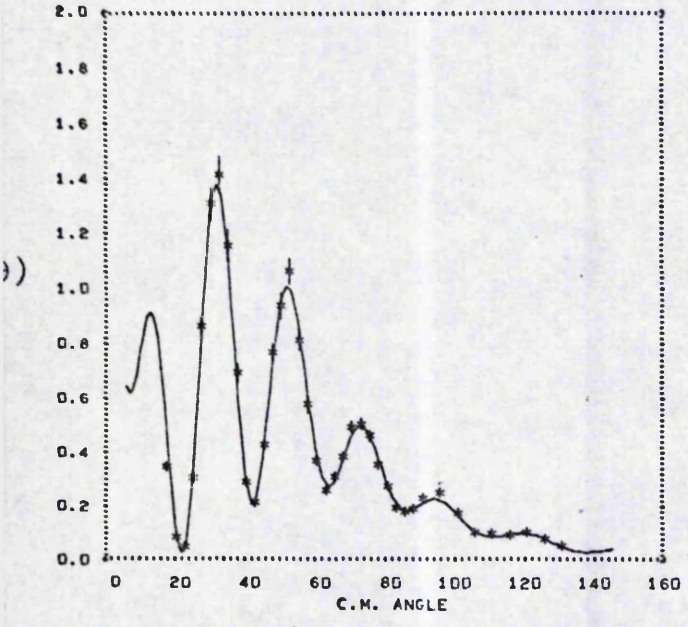

A. Zr^{92}, Parameter Set 13

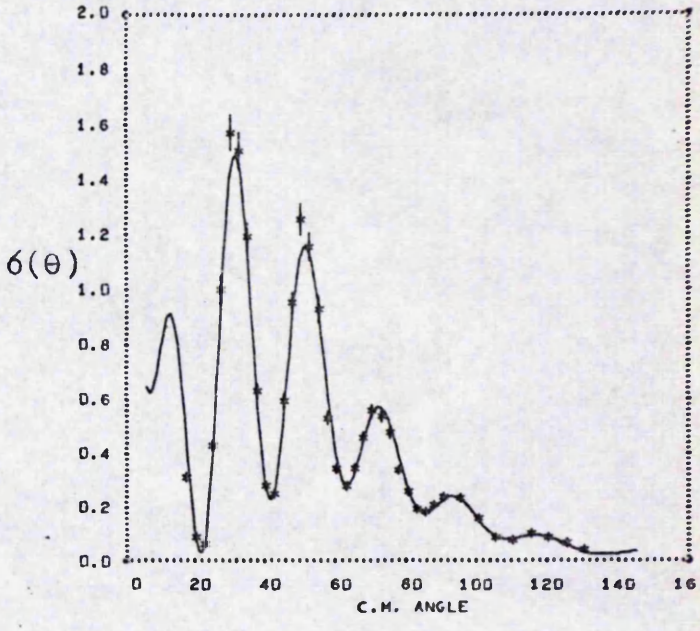

B. Zr^{94}, Parameter Set 13

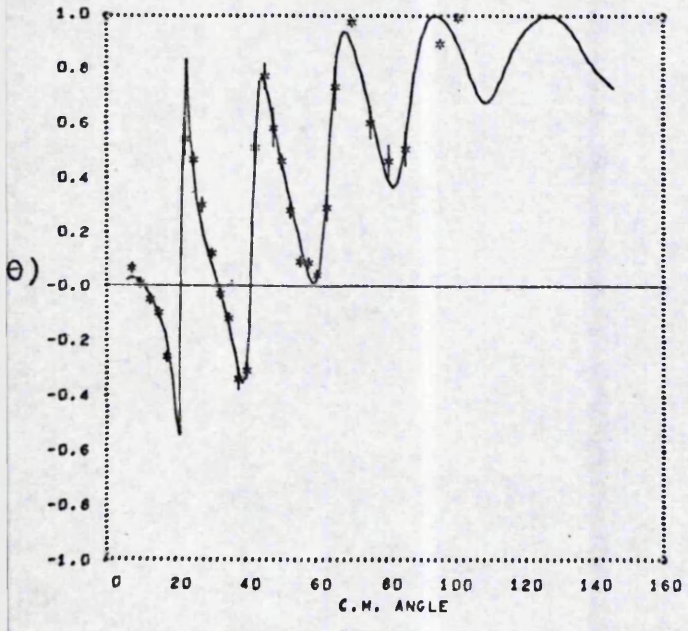

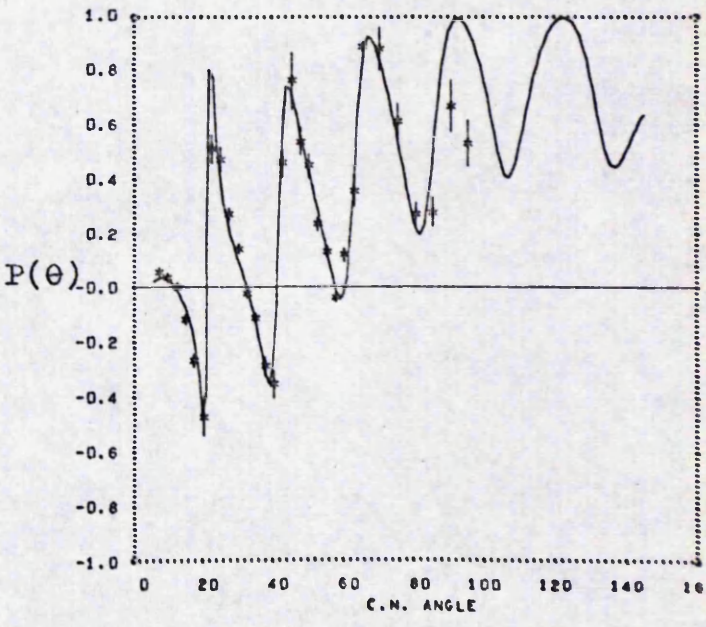

Figure 6.3 Optical Model Predictions for Cross-section and Polarisation of Elastic Scattering.

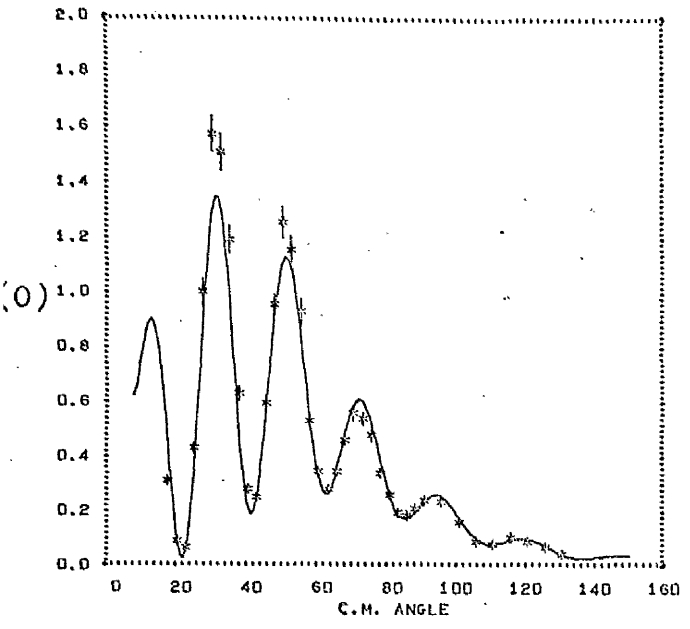

A. Zr^{94}, Parameter Set 5.

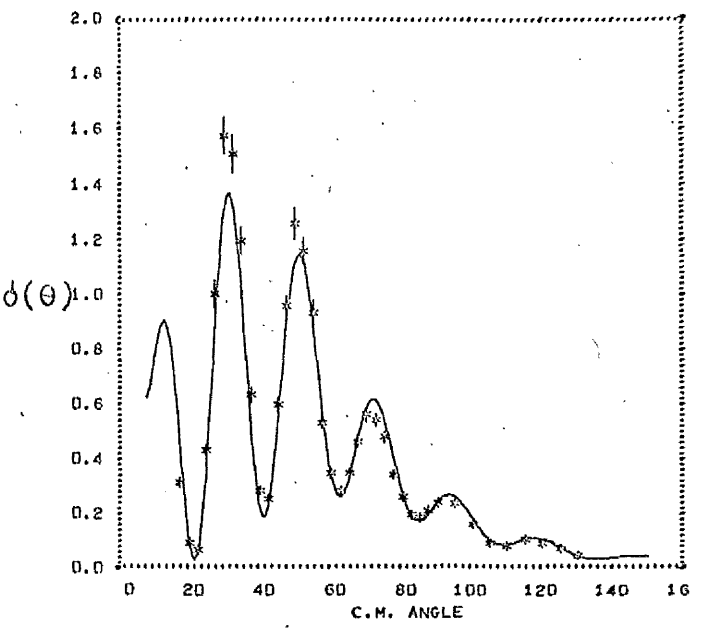

B. Zr^{94}, Parameter Set 11

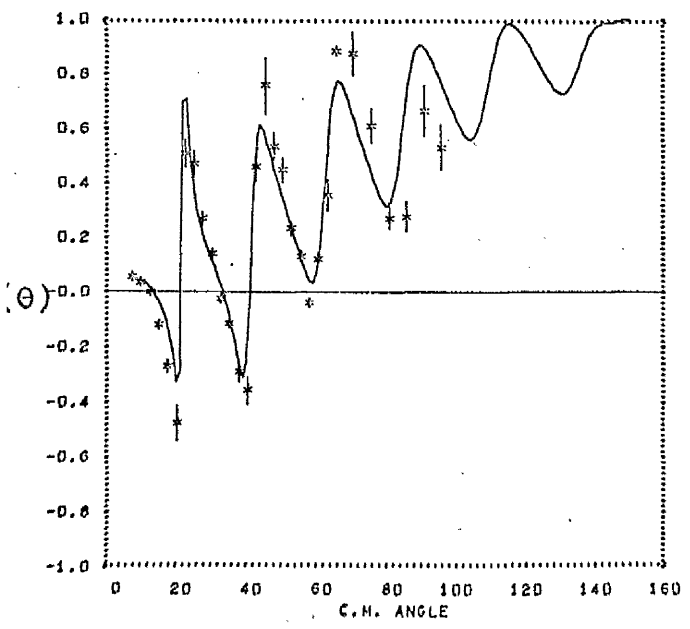

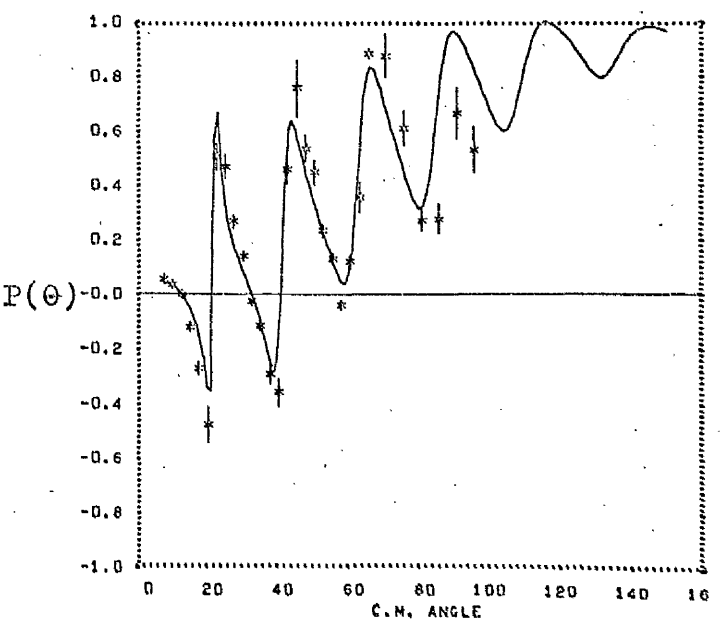

Figure 6.4 Optical Model Predictions for Cross-sections and Polarisations of Elastic Scattering.

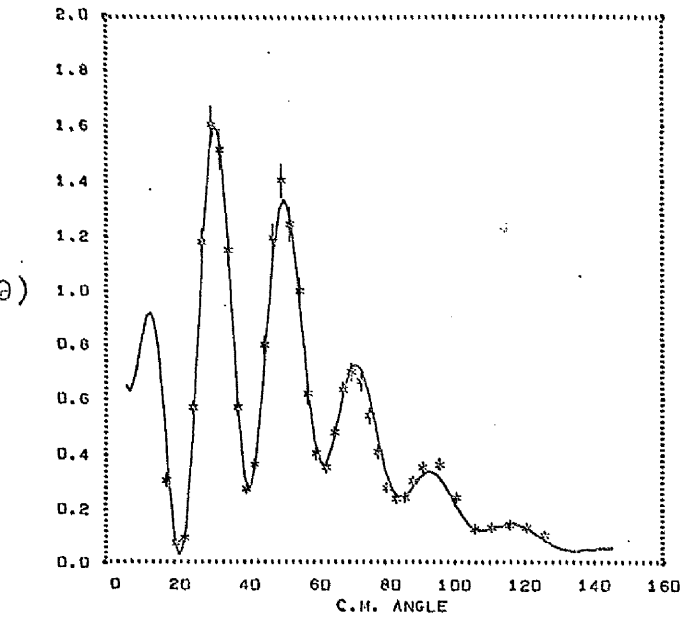

A. Zr^{96}, Parameter Set 13.

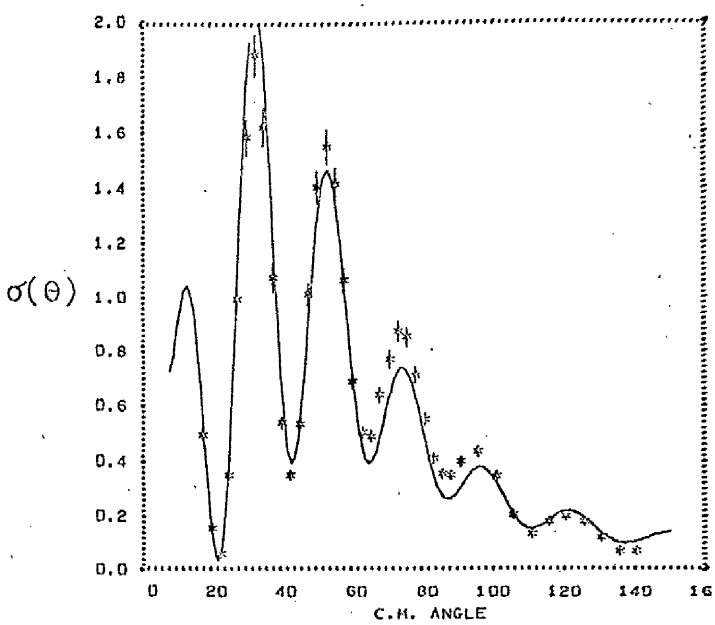

B. Zr^{96}, Parameter Set 6.

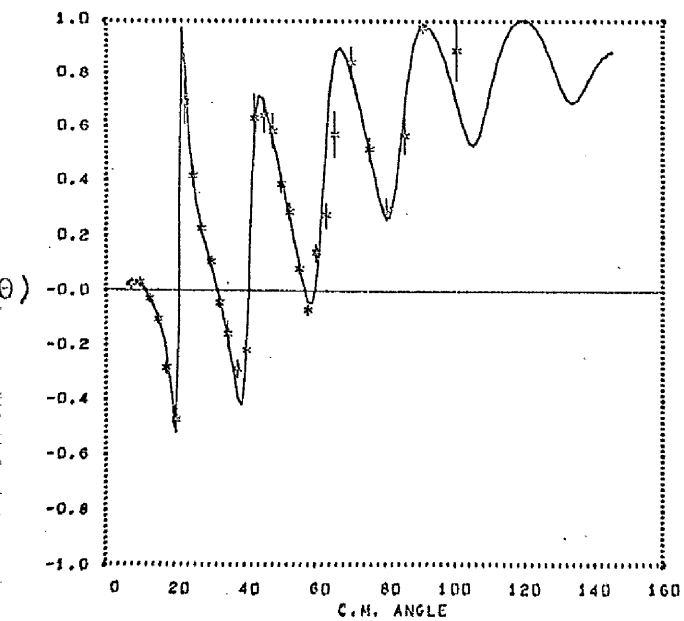

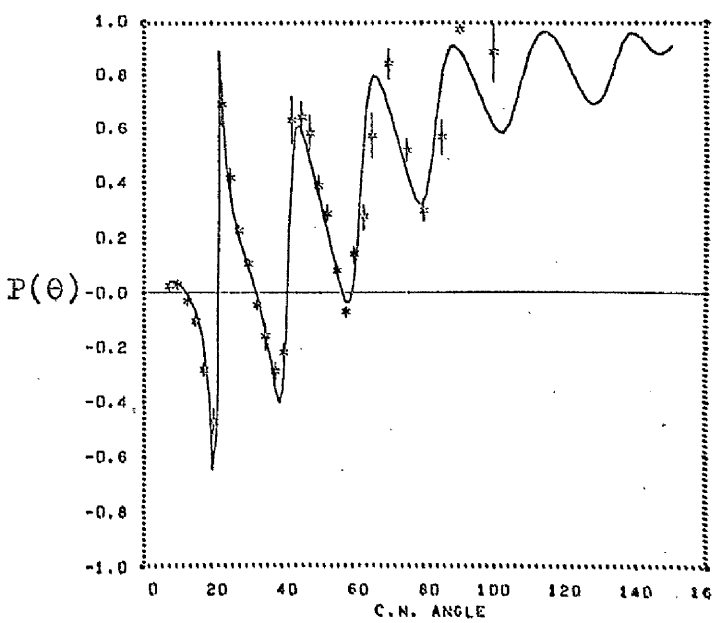

Figure 6.5 Optical Model Predictions for Cross-section and Polarisation of Elastic Scattering.

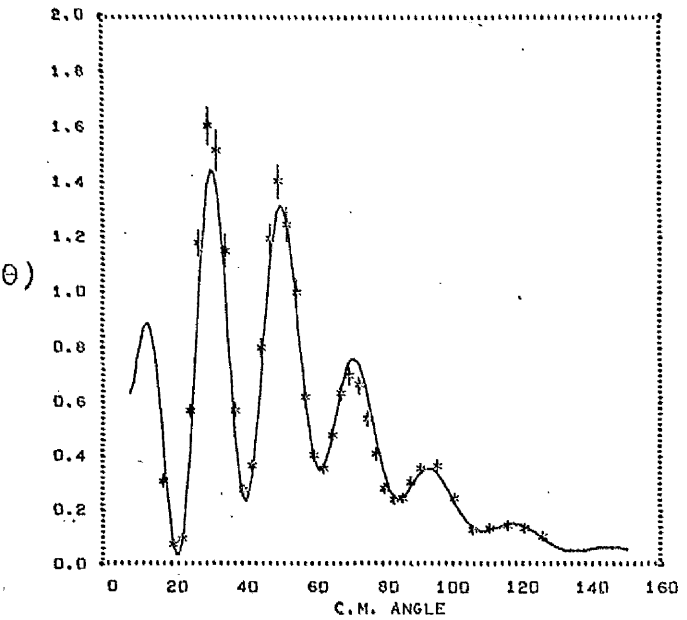

C. Zr^{96}, Parameter Set 8.

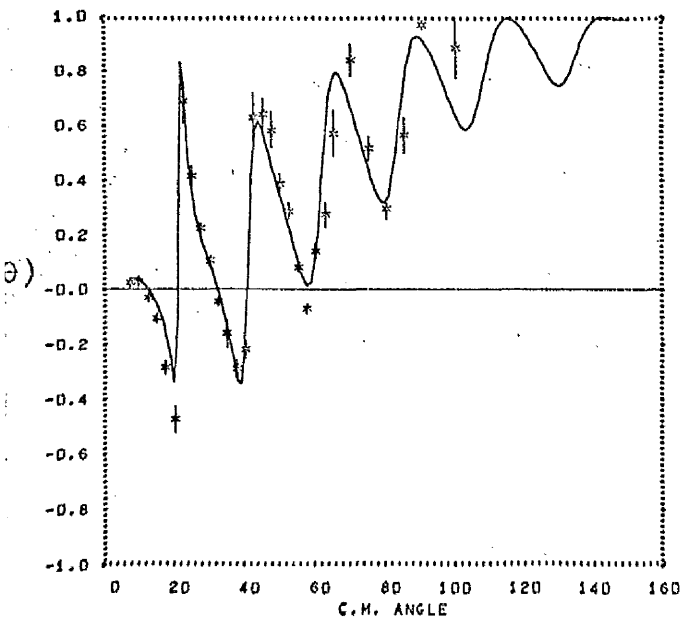

Figure 6.5 Optical Model Predictions for Cross-section and Polarisation of Elastic Scattering.

Excitation Energy	L	Figure	Beta
2.18	2	6.6A	0.063
2.18	2	6.6A*(1)	
2.18	2	6.6B(2)	0.059
2.75	3	6.6C(3)	0.144
2.75	3	6.6D	0.139
2.75	3	6.6D*(1)	
2.30	5	6.7A	0.056
3.07	4	6.7B	0.037
3.37	0	6.7C	0.023
3.37	2	6.7C*	0.042
3.45	6	6.7D	0.018
3.57	8	6.8A	0.017
3,84	2	6.8B	0.040
3.95	5	6.8C	0.045
4.05	3	6.8D	0.030
4.05	4	6.8D*	0.030
4.22	2	6.9A	0.038
4.32	4	6.9B	0.068
4.46	3	6.9C	0.041
4.54	3	6.9D	0.027
4.54	4	6.9D*	0.030
4.66	2	6.10A*	0.025
4.66	3	6.10A	0.032
4.79	3	6.10B	0.023
4.89	3	6.10C	0.018
4.89	4	6.10C*	0.023
4.99	3	6.10D	0.021
5.07	3	6.11A	0.033

* indicates a broken line on the graph
(1) Real Form Factors only
(2) $A_{def} = 2.0$
(3) $A_{def} = 0.0$

Table 6.6a Index to the Graphs Illustrating the Collective Model Analysis for Proton Inelastic Scattering by Zr^{90}.

P.T.O

Excitation Energy(MeV)	L	Figure	Beta
0.92	2	6.11B	0.090
1.40	4	6.11C	0.034
1.62	2	6.11D	0.064
2.07	3	6.12A	0.182
2.34	4	6.12B	0.039
2.62	5	6.12C	0.047
2.89	4	6.12D	0.070
3.13	3	6.13A	0.057
3.22	4	6.13B	0.067
3.22	5	6.13B*	0.060
3.32	3	6.13C	0.046
3.48	4	6.13D	0.047
3.48	5	6.13D*	0.048
3.59	4	6.14A	0.040
3.59	5	6.14A*	0.040
3.72	4	6.14B	0.055
3.72	5	6.14B*	0.050
3.80	4	6.14C	0.048
3.91	3	6.14D	0.030
4.21	4	6.15A	0.040
0.93	2	6.15B	0.123
1.89	2	6.15C	0.028
2.33	3	6.15D	0.188
2.44	4	6.16A	0.078
2.44	5	6.16A*	0.084
2.73	4	6.16B	0.042
2.83	5	6.16C	0.050
2.92	5	6.16D	0.043
3.00	2	6.17A	0.043
3.08	2	6.17B	0.057
3.18	5	6.17C	0.061
3.29	3	6.17D	0.059
3.35	3	6.18A	0.042
3.48	2	6.18B	0.032
3.64	2	6.18C	0.027
3.64	3	6.18D	0.032
3.74	5	6.19A	0.056
3.85	4	6.19B	0.057

Table 6.6b Index to the Graphs Illustrating the Collective Model Analysis for Zr^{92} (figures 6.15B to 6.19B), and for Zr^{94} (figures 6.11B to 6.15A).

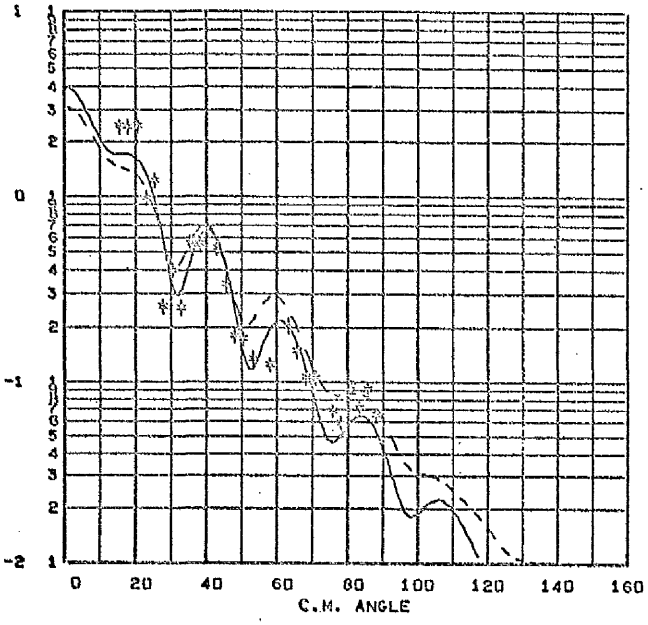

A.

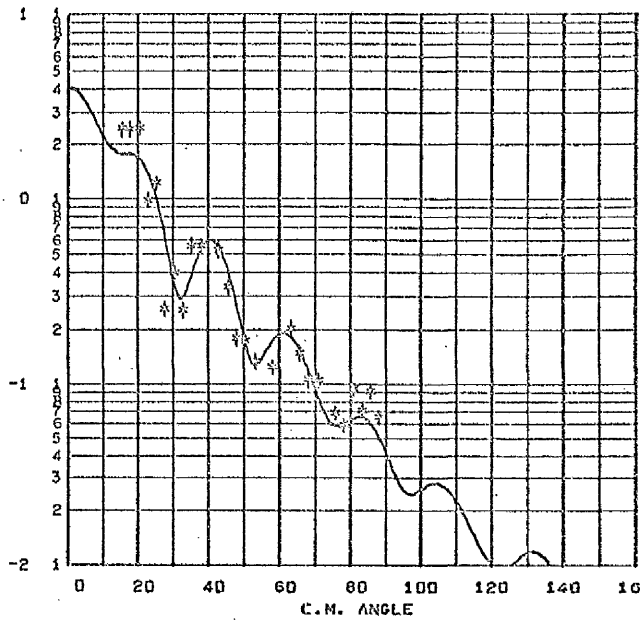

B.

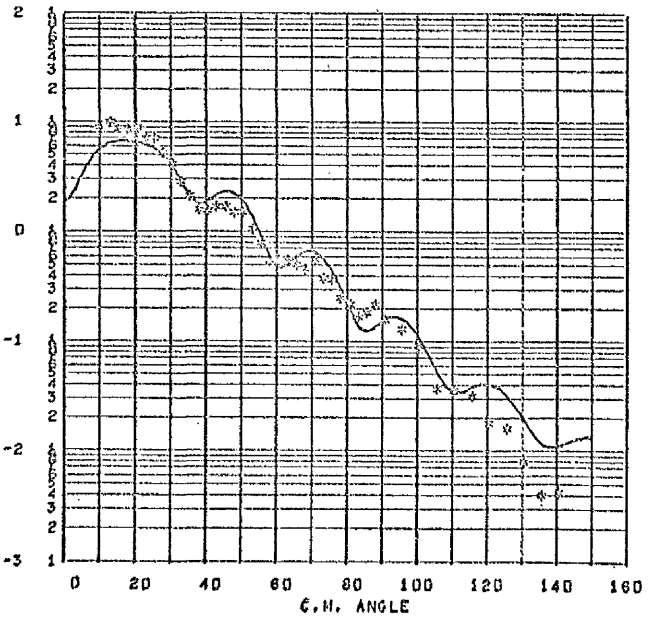

C.

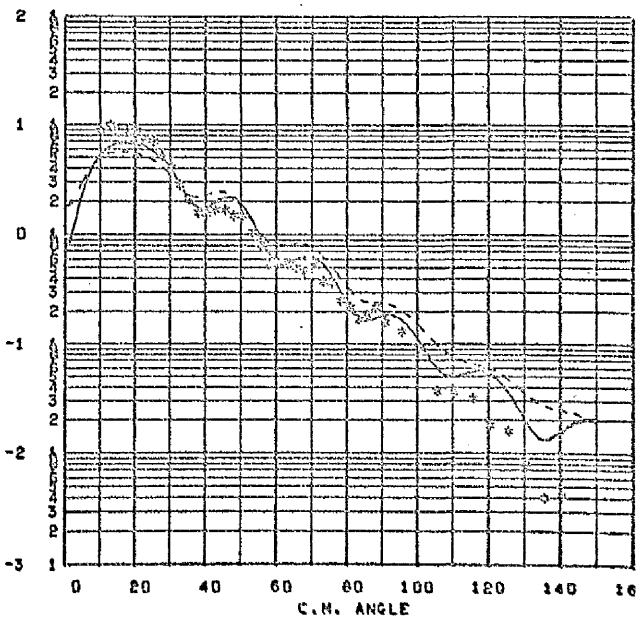

D.

Figure 6.6

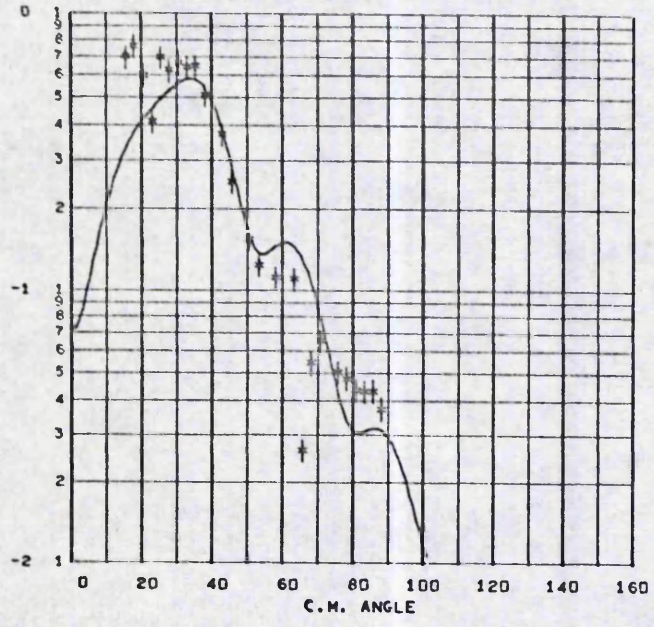

A.

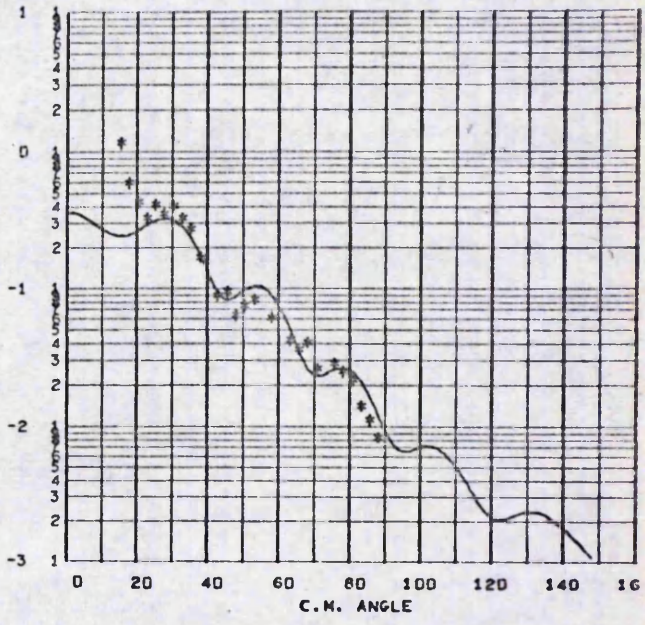

B.

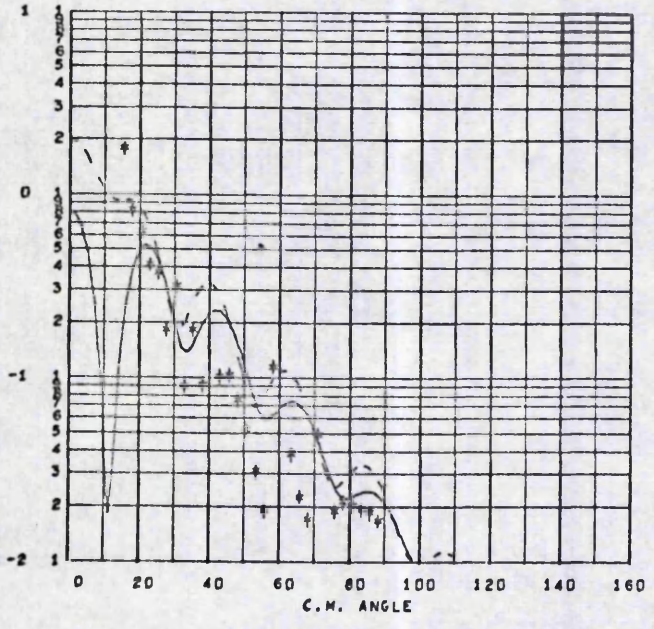

C.

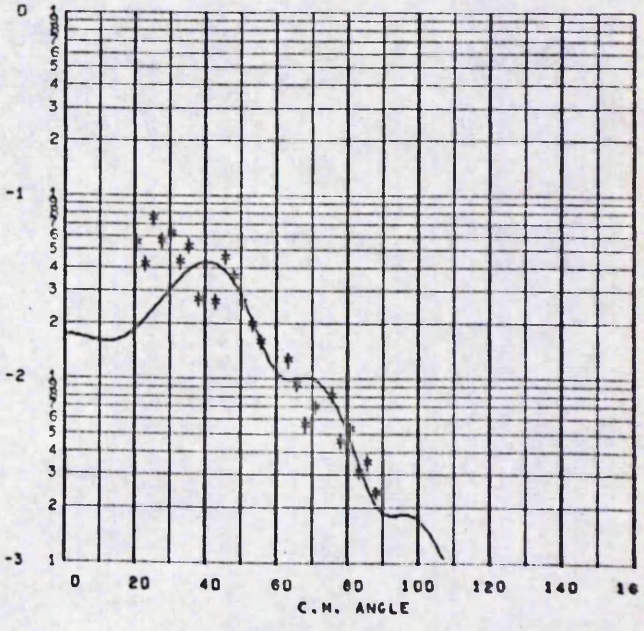

D.

Figure 6.7

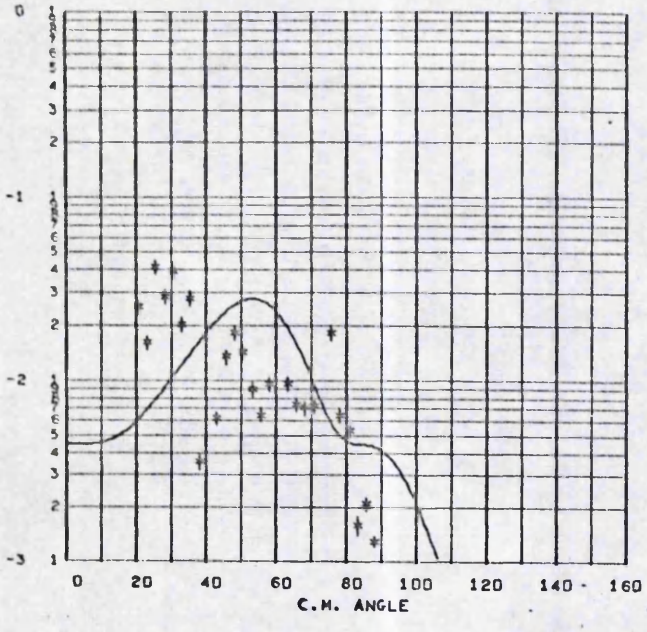

A.

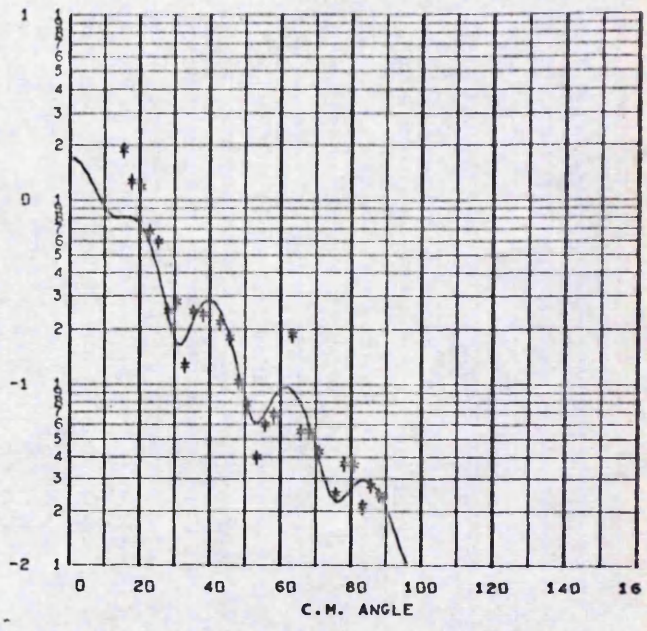

B.

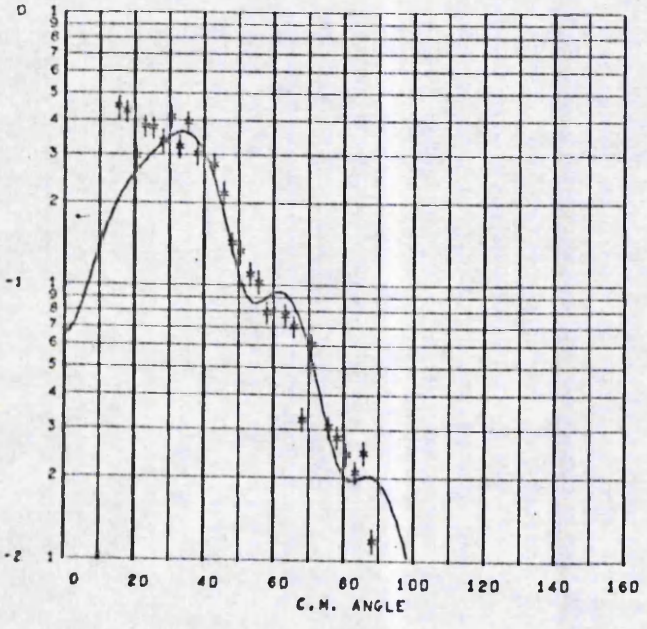

C.

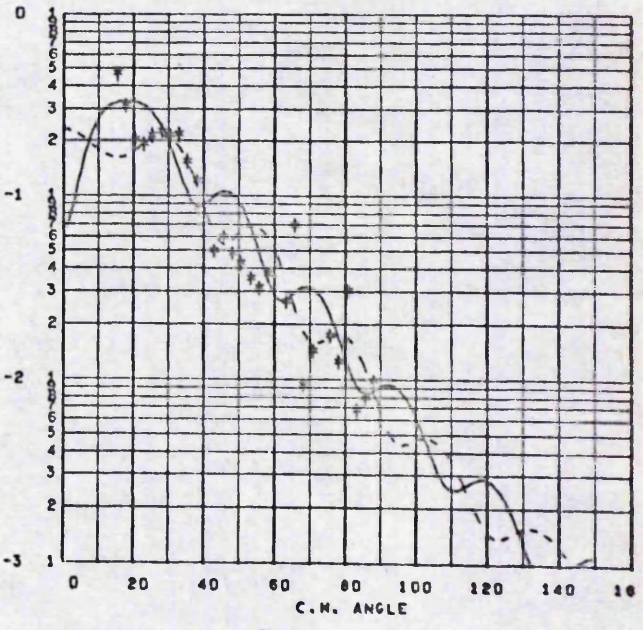

D.

Figure 6.8

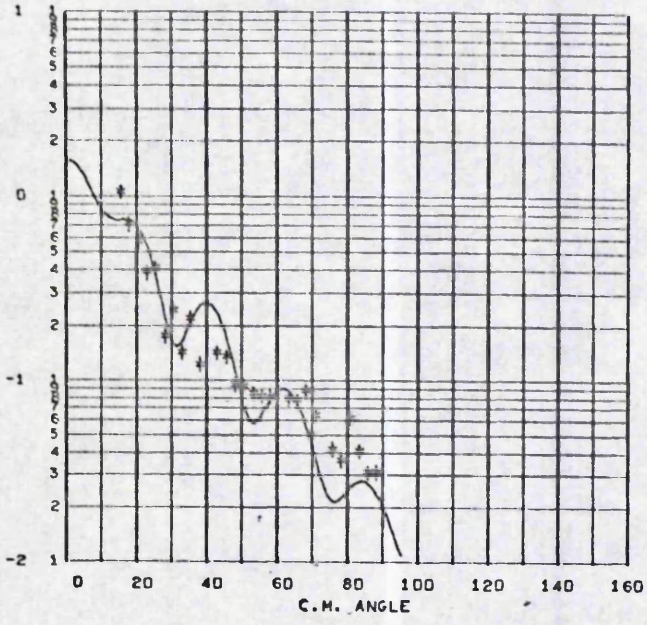

A.

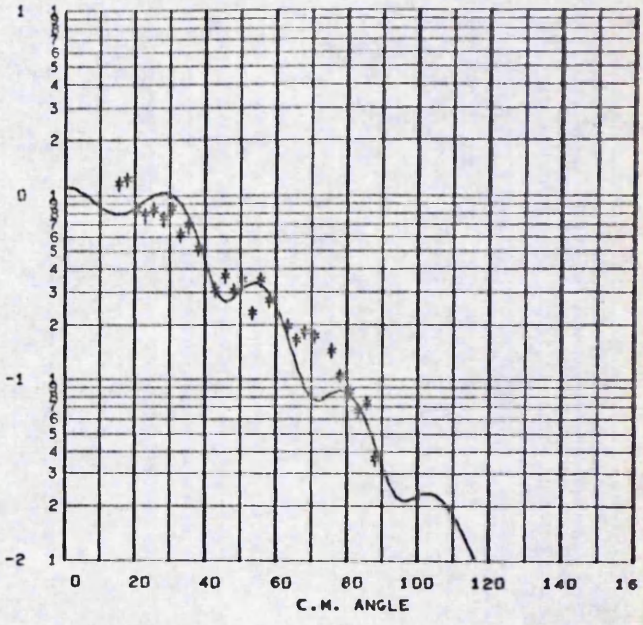

B.

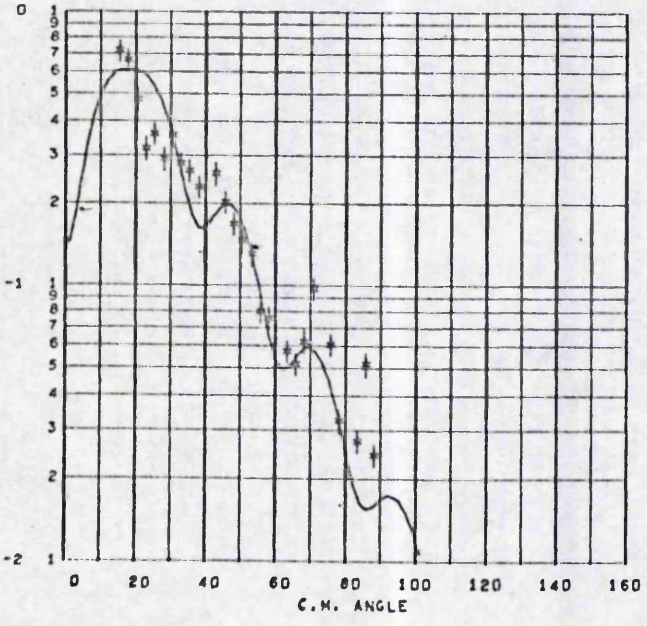

C.

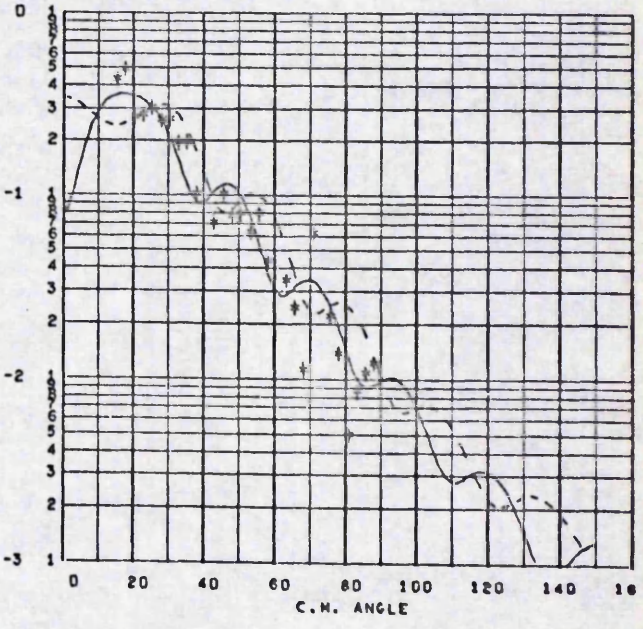

D.

Figure 6.9

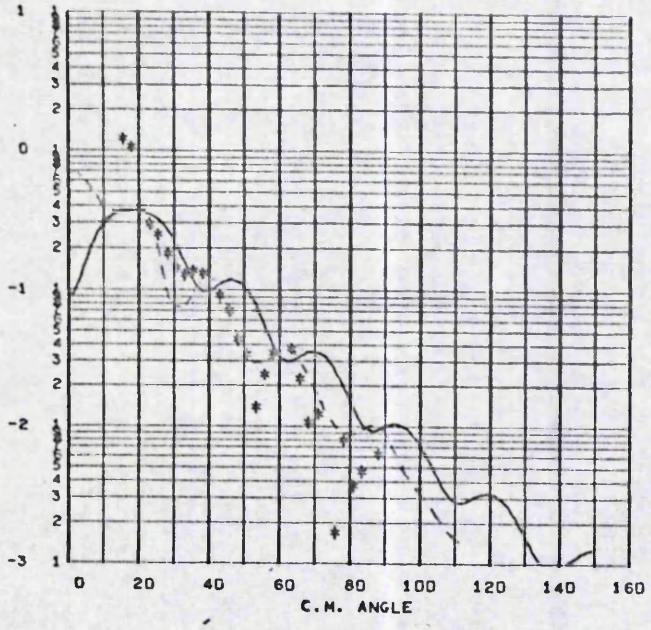

A.

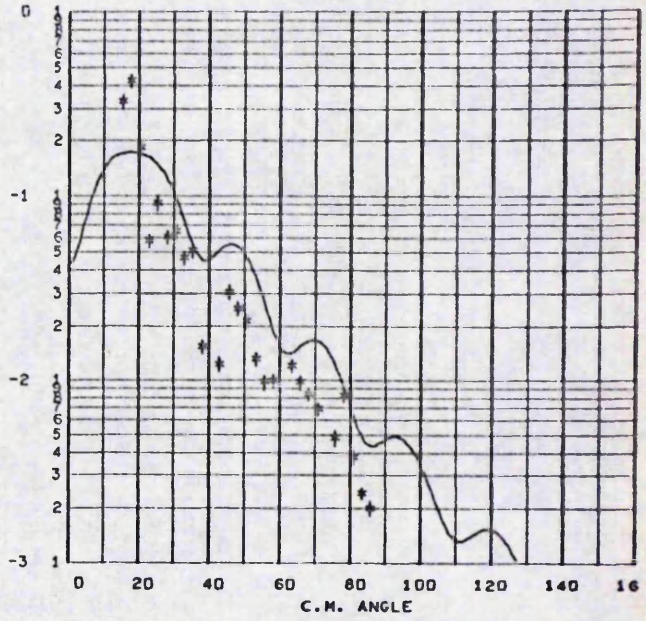

B.

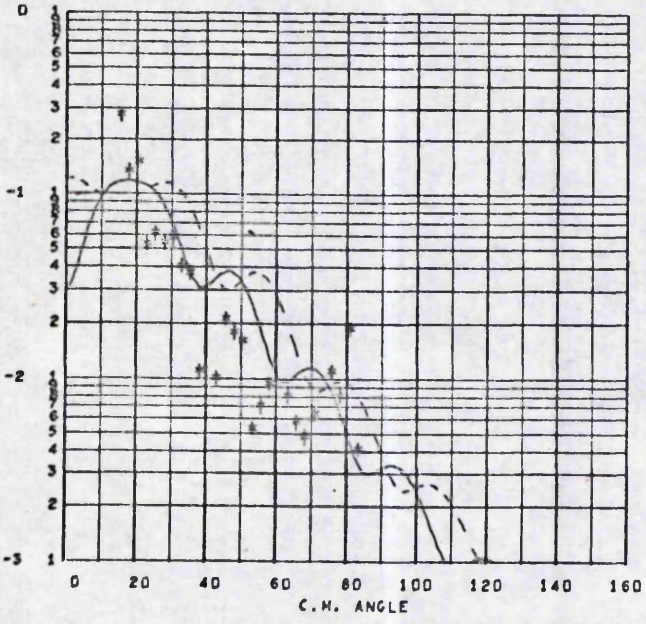

C.

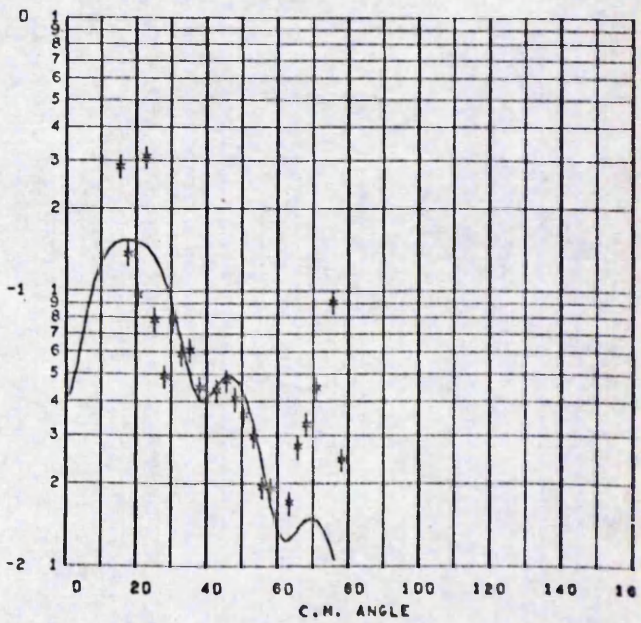

D.

Figure 6.10

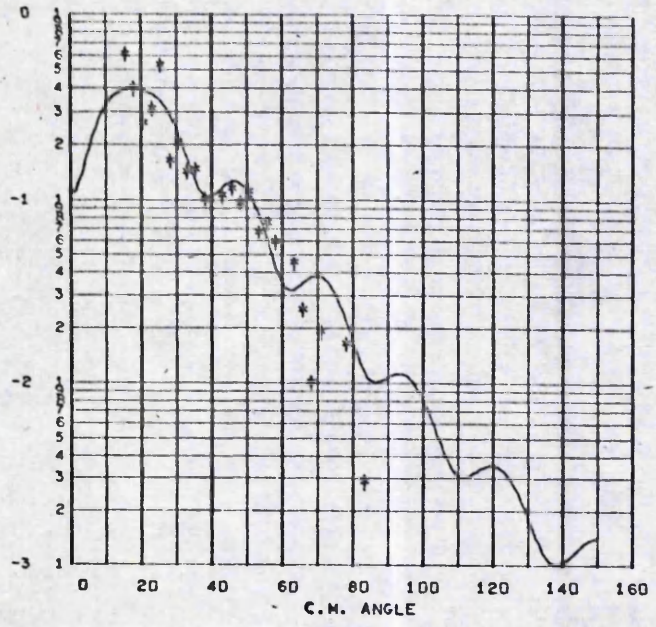

A.

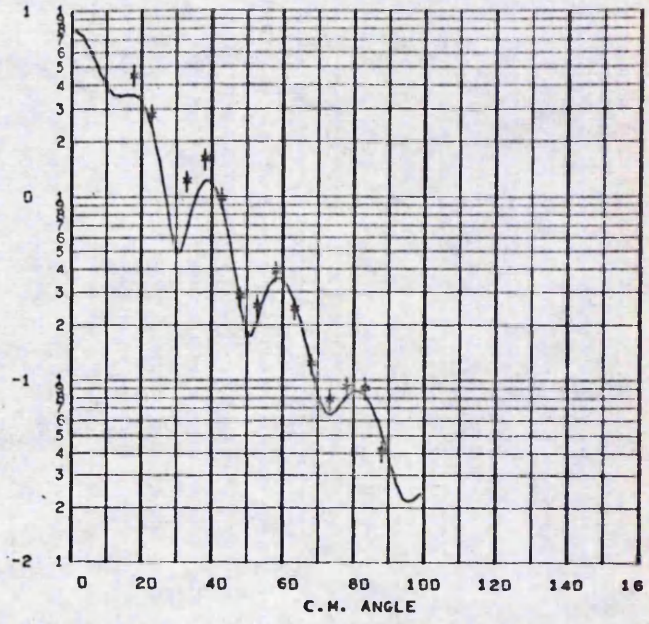

B.

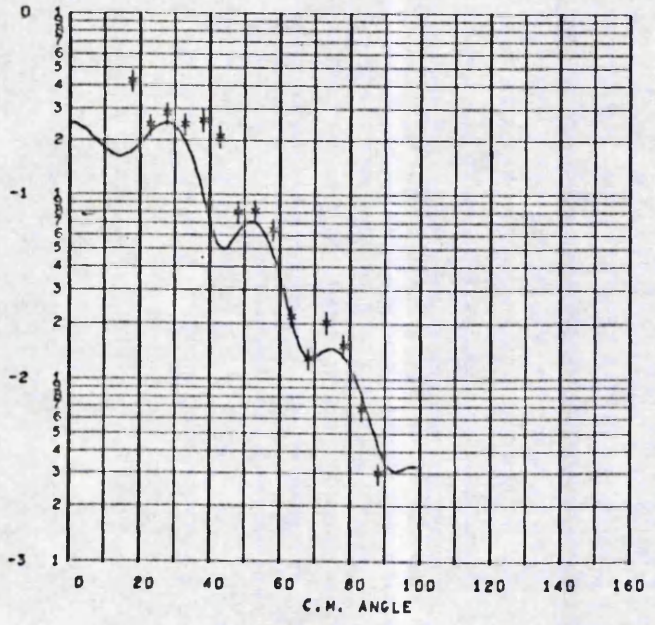

C.

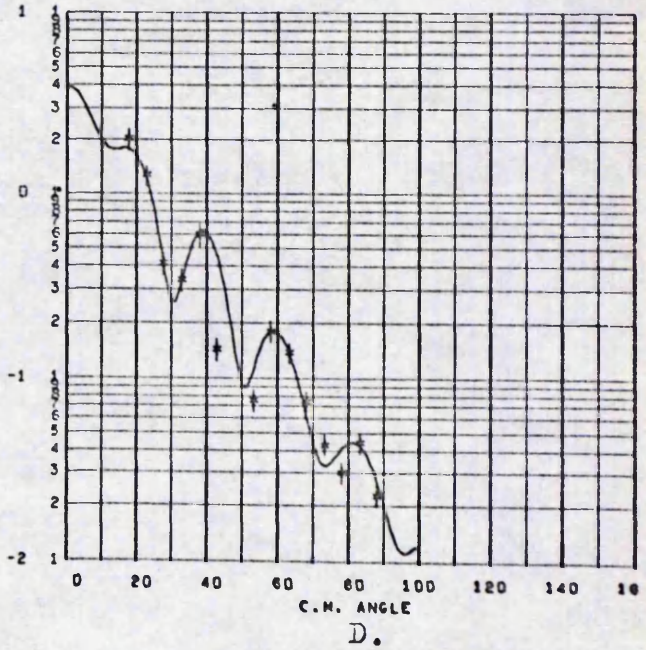

D.

Figure 6.11

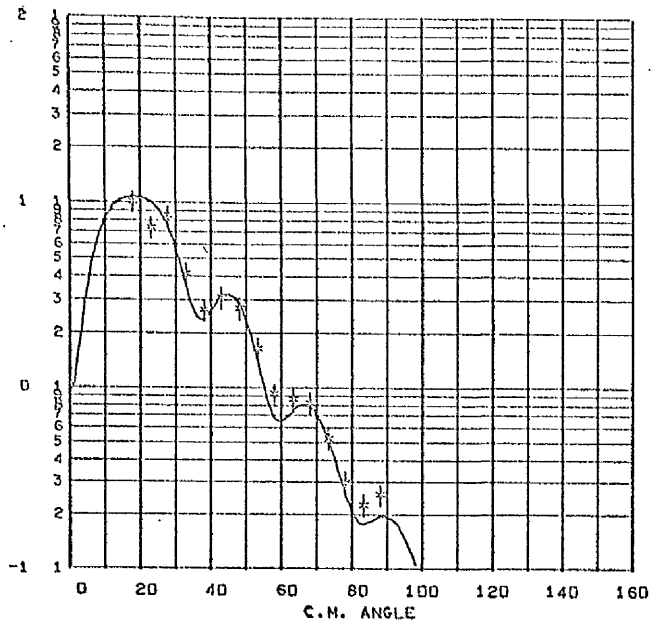

A.

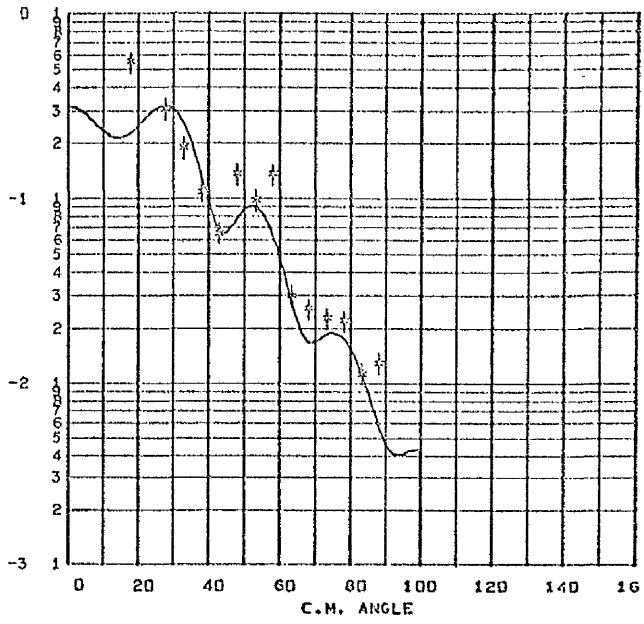

B.

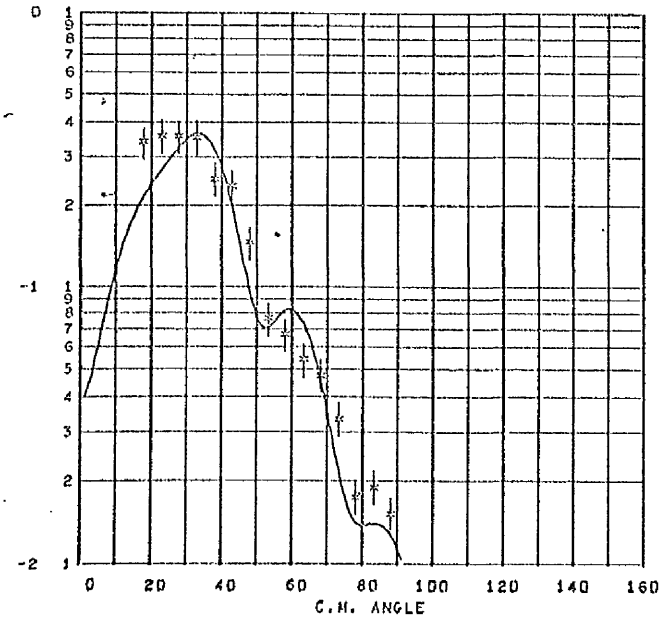

C.

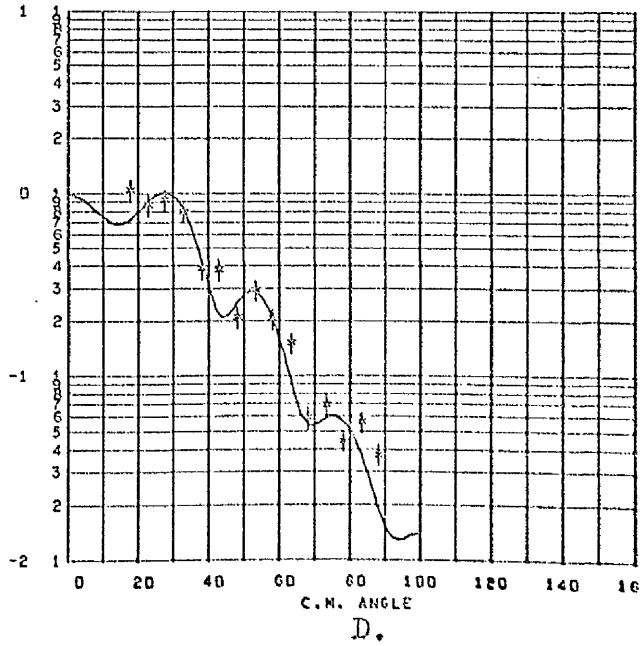

D.

Figure 6.12

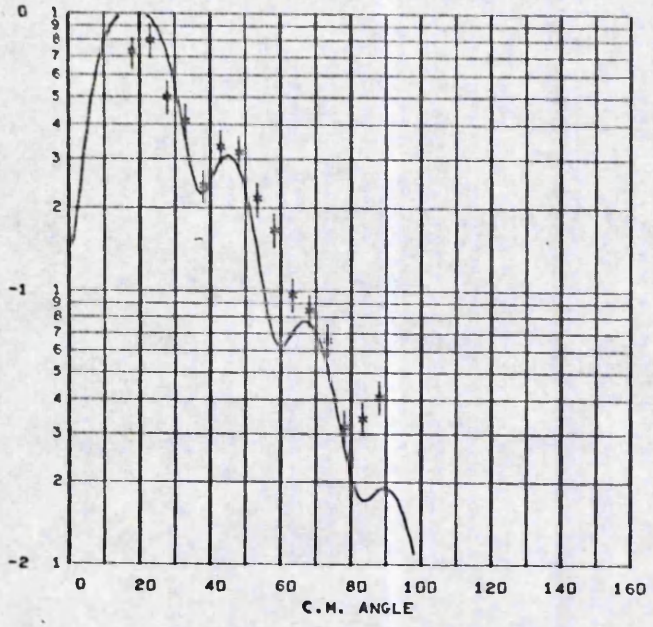

A.

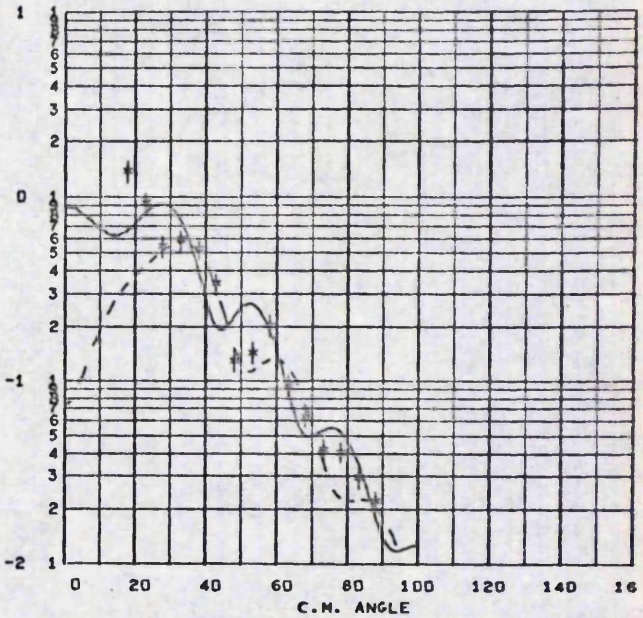

B.

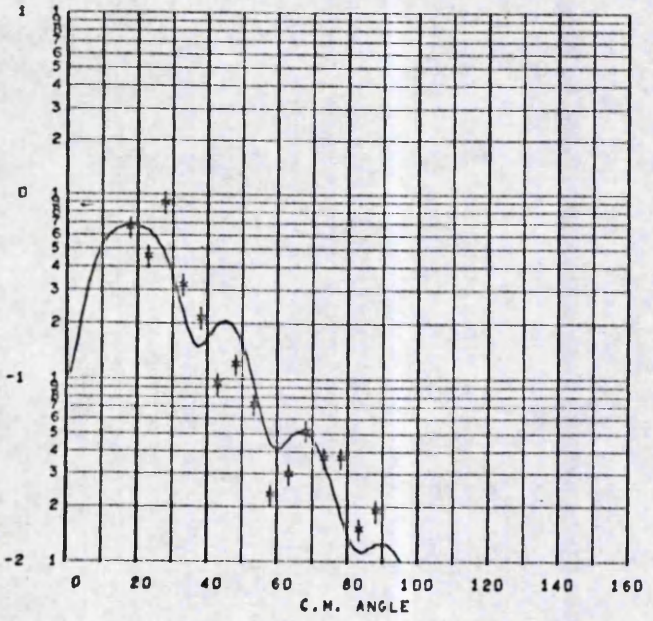

C.

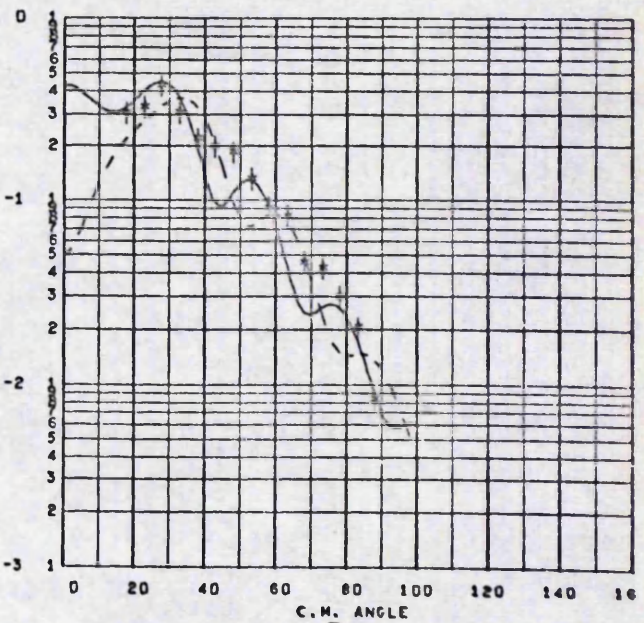

D.

Figure 6.13

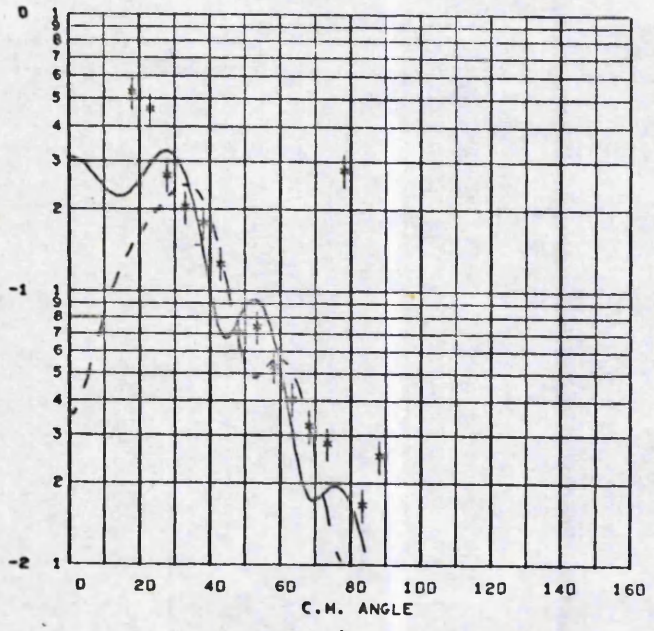

A.

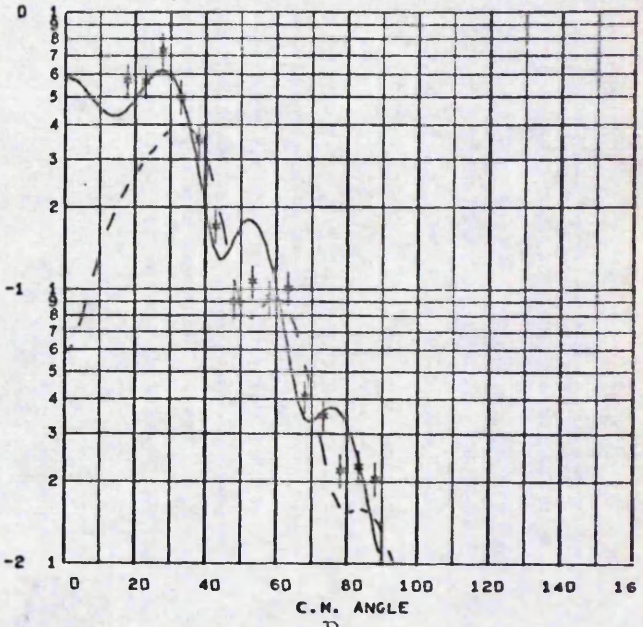

B.

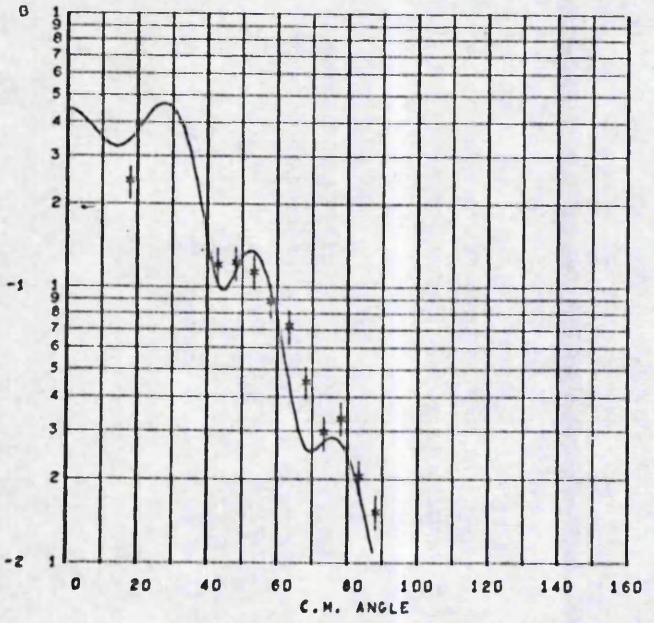

C.

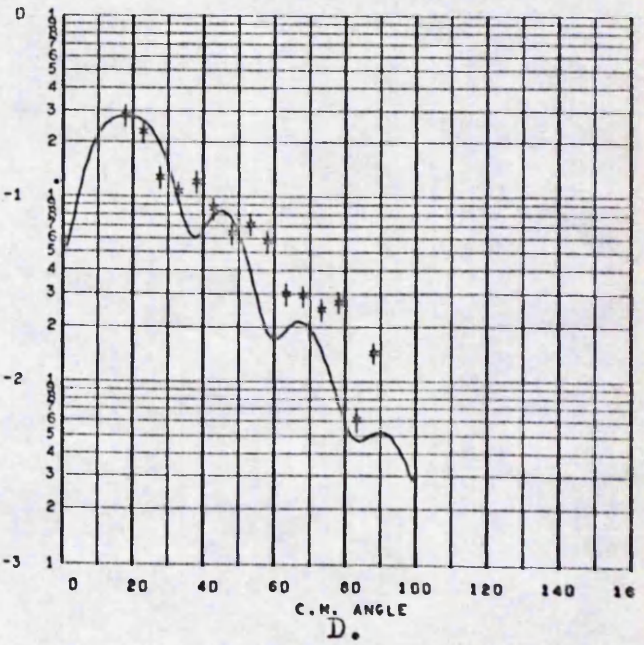

D.

Figure 6.14

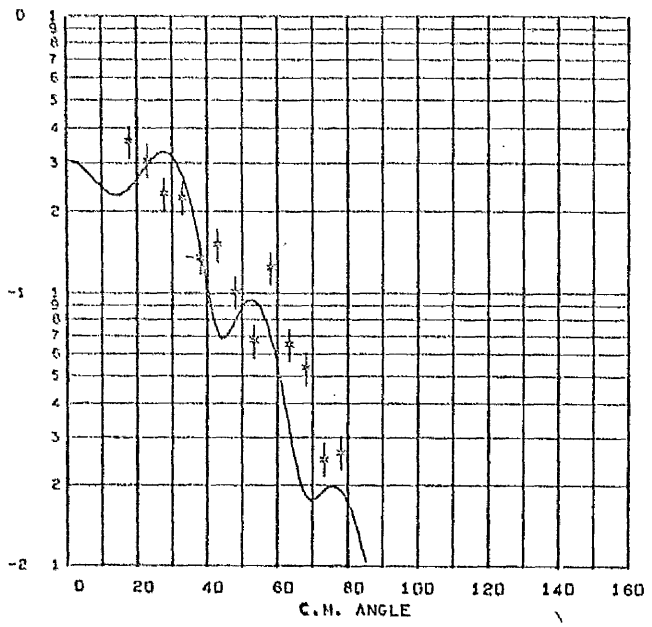

A.

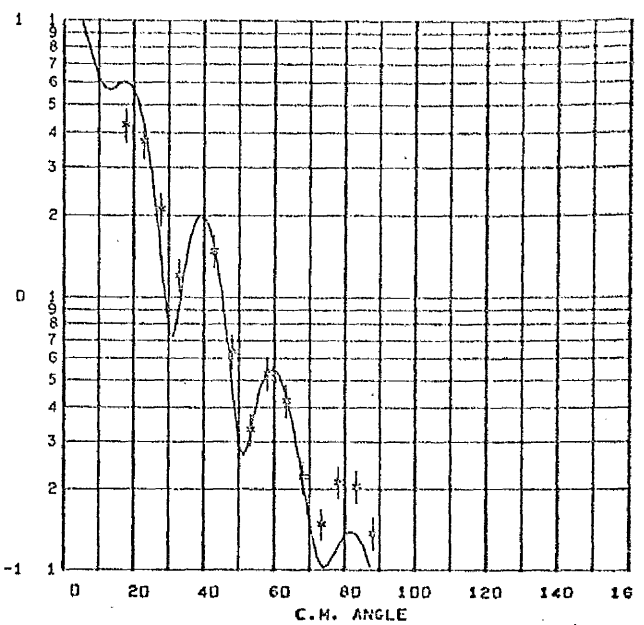

B.

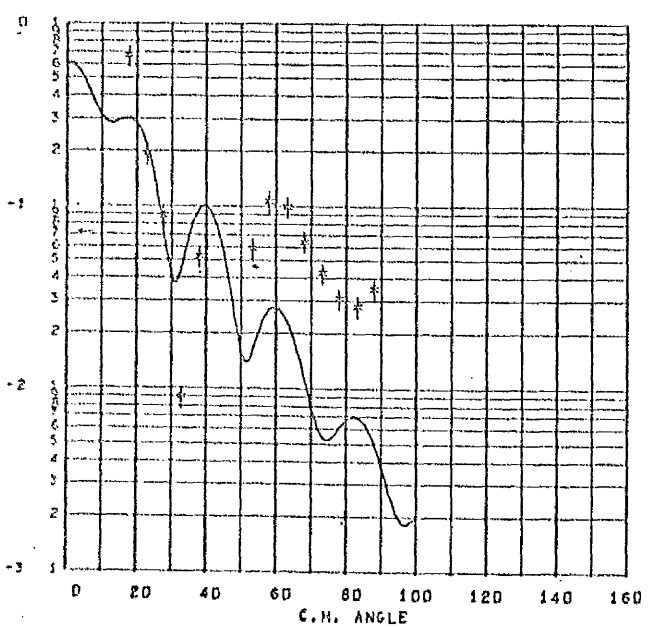

C.

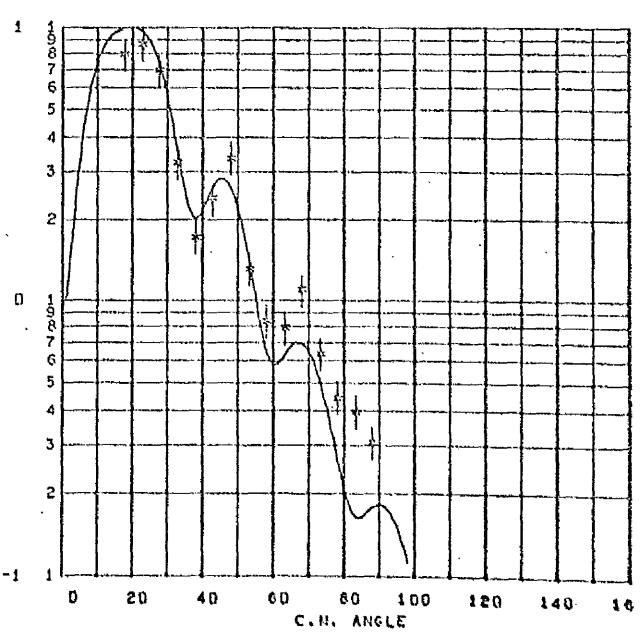

D.

Figure 6.15

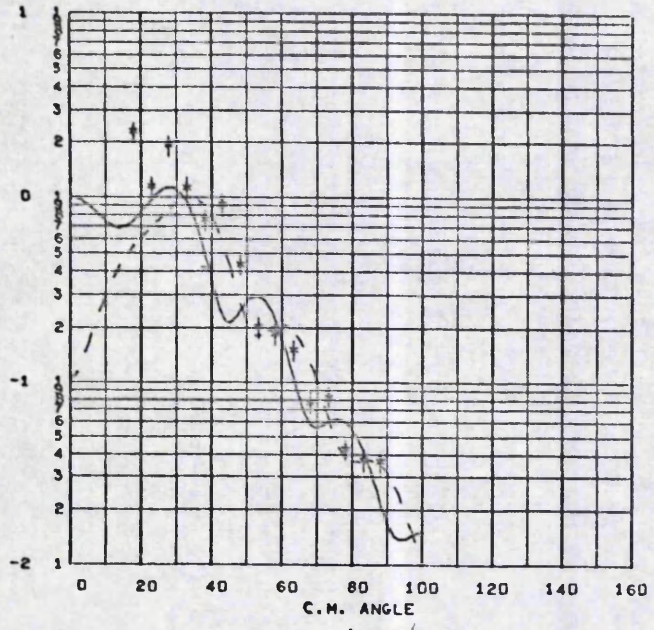

A.

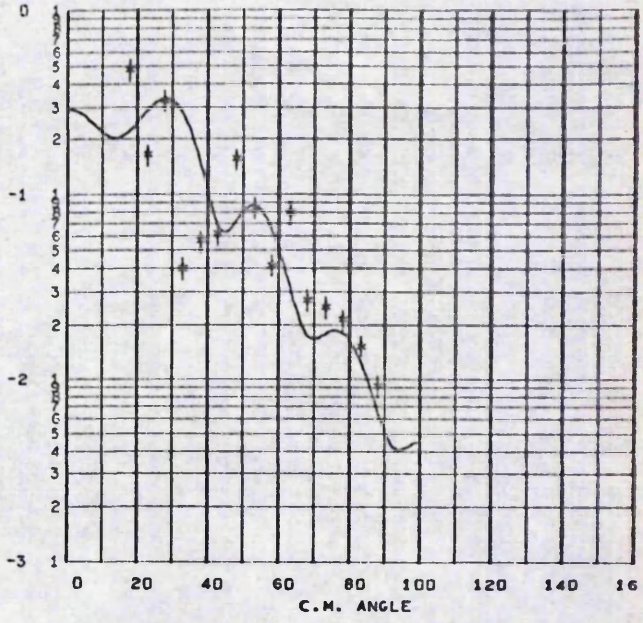

B.

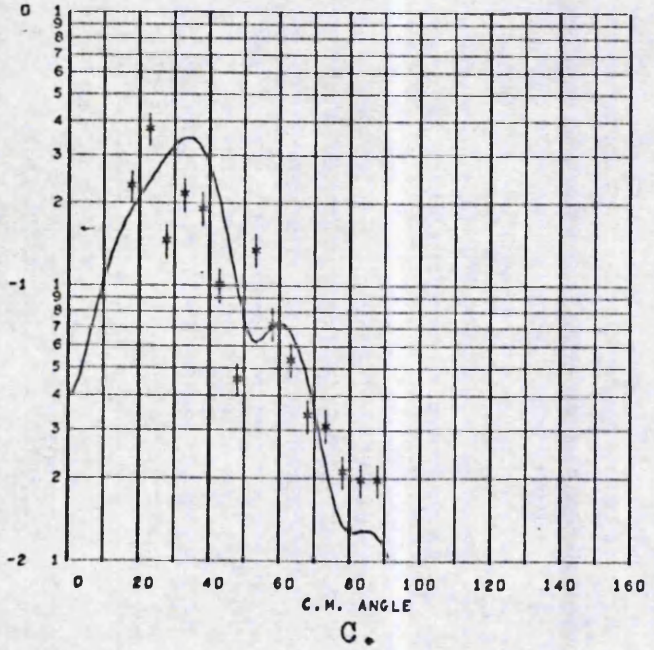

C.

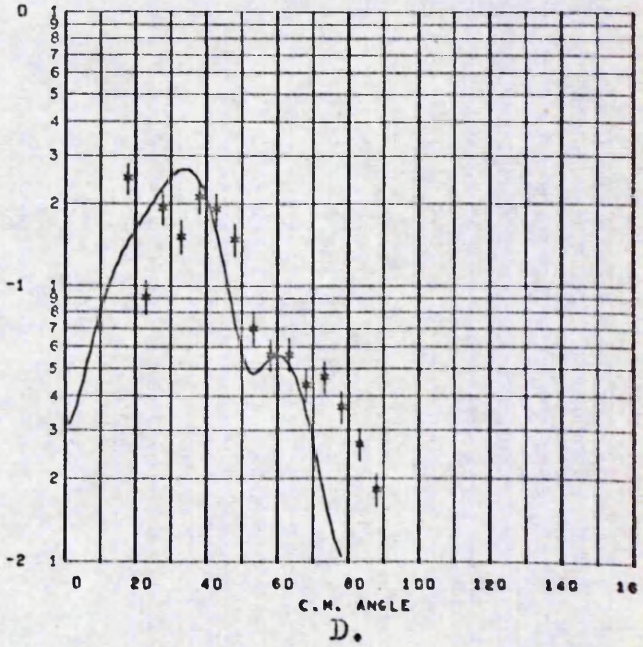

D.

Figure 6.16

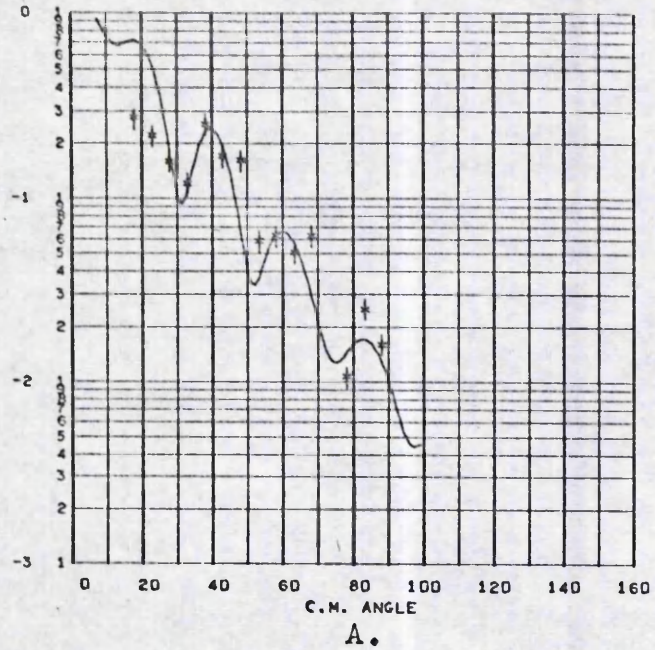

A.

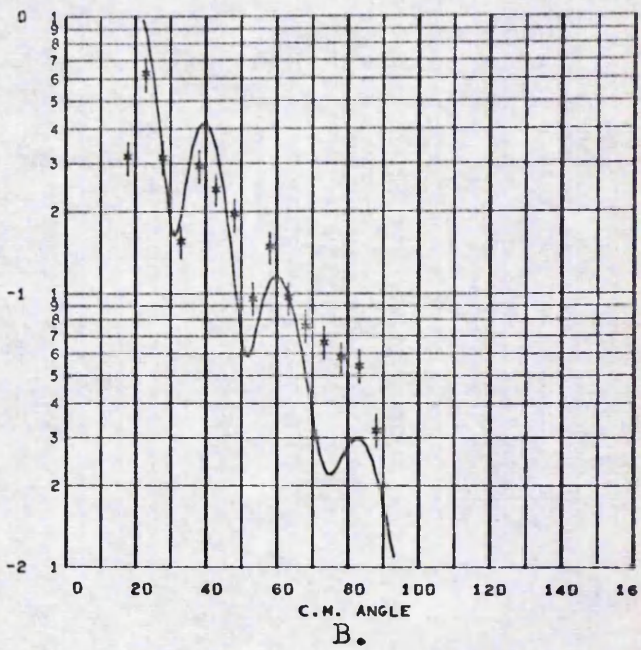

B.

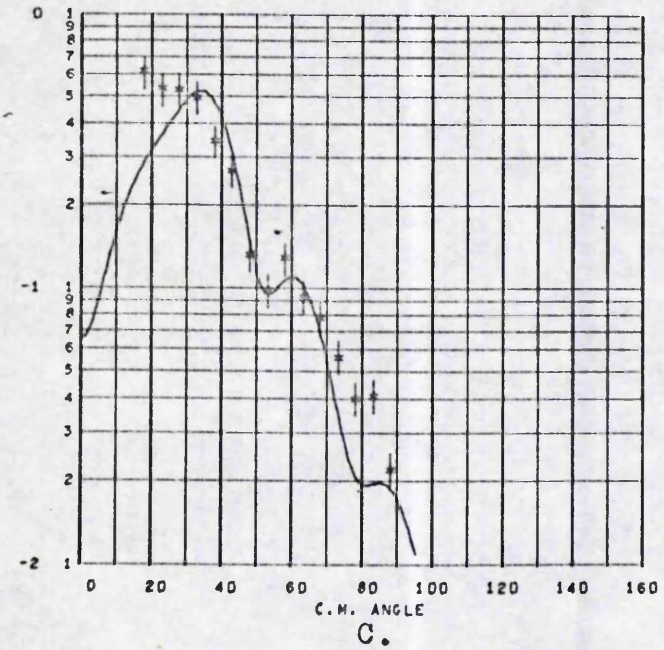

C.

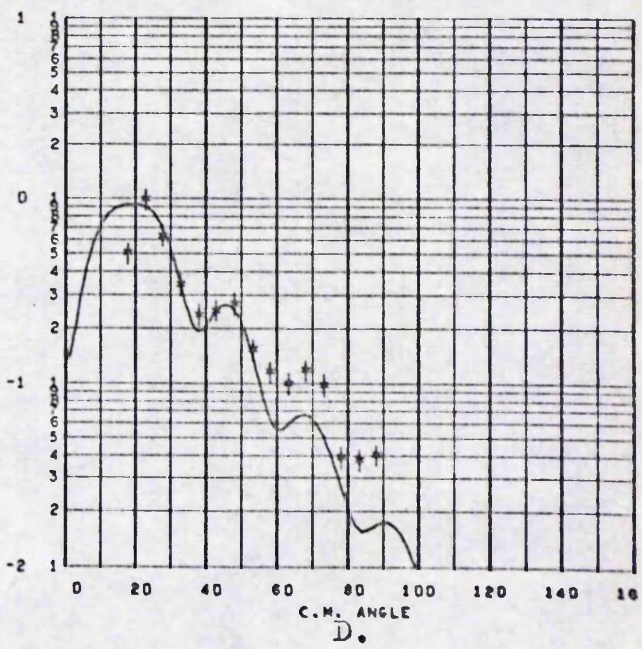

D.

Figure 6.17

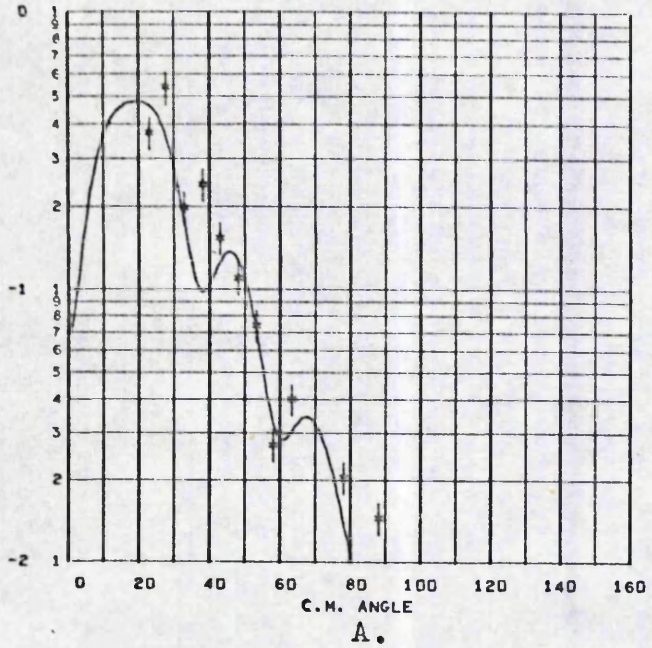

A.

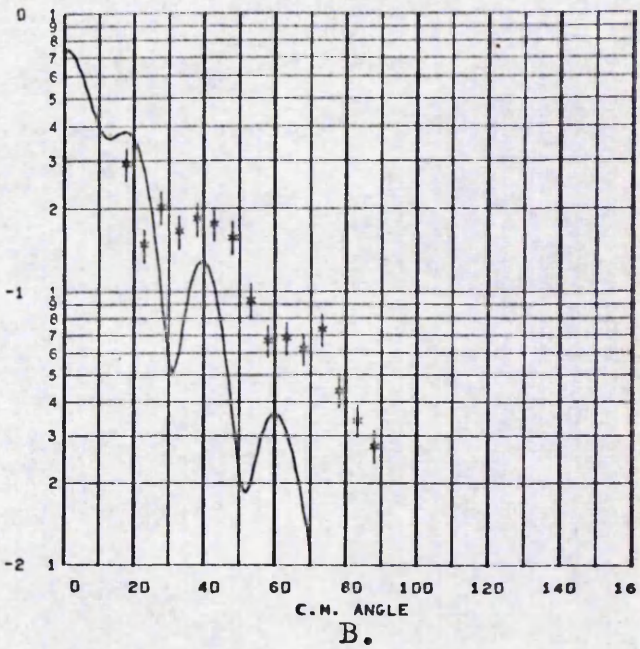

B.

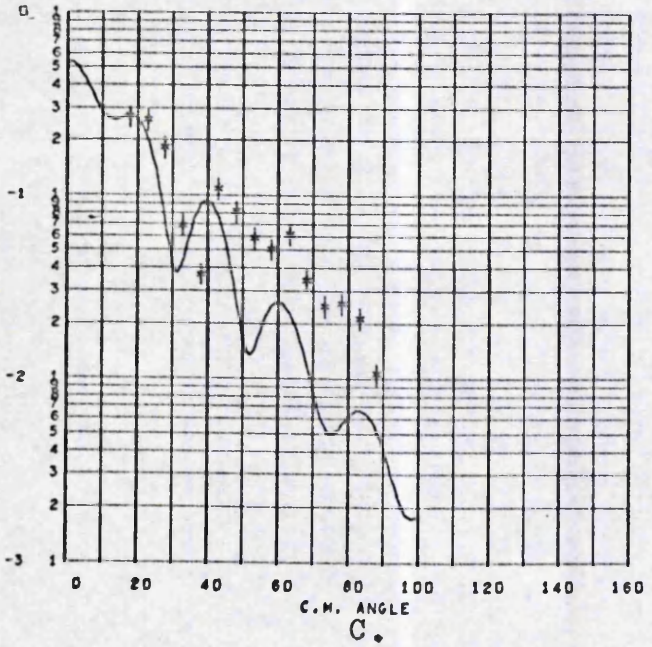

C.

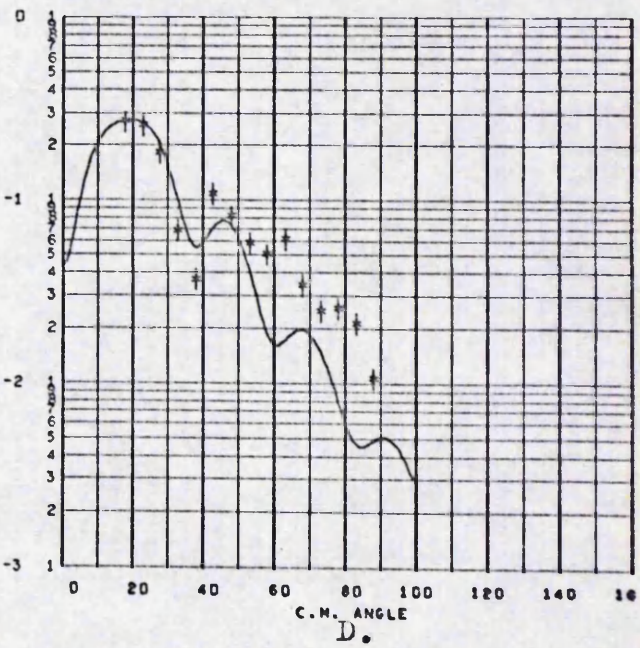

D.

Figure 6.18

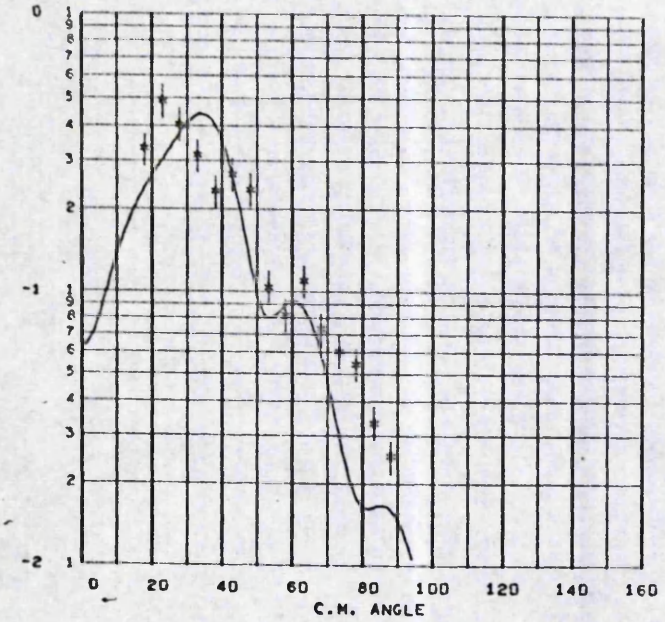

A.

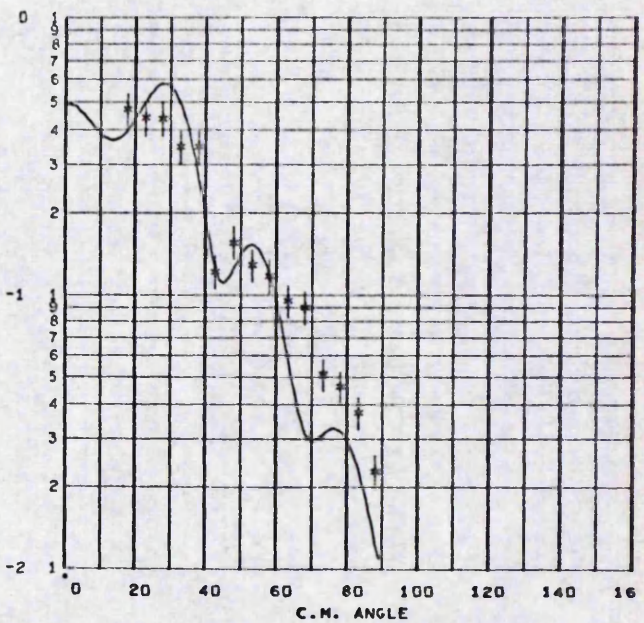

B.

Figure 6.19

Configuration	LSJ	M_{LSJ}	$\frac{d\sigma}{d\Omega}(30°)$ (V =85MeV)
$(g_{9/2})^2$	202	0.2778	
	404	0.2002	
	606	0.1541	
	808	0.1133	
$p_{1/2}\, g_{9/2}$	314	0.3960	
	505	0.2690	
	515	0.2946	
	514	0.0440	
$p^{-1}_{3/2} g_{9/2}$	303	0.3893	1.32
	313	0.3372	
	314	0.3287	
	505	0.2196	0.20
	515	0.1203	
	514	0.0535	
	516	0.4658	
$f^{-1}_{5/2} g_{9/2}$	112	0.6031	
	303	0.1438	0.14
	313	0.3320	
	312	0.1231	
	314	0.2875	
	505	0.2110	0.16
	515	0.3082	
	514	0.1286	
	516	0.1788	
	707	0.3418	0.05
	717	0.3654	
	716	0.1034	
$p^{-1}_{3/2} p_{1/2}$	011	0.3761	
	202	0.2523	0.81
	212	0.3090	
$f^{-1}_{5/2} p_{1/2}$	202	0.3090	0.58
	212	0.2523	
	213	0.0570	
	413	0.3948	
$g^{-1}_{9/2} d_{5/2}$	202	0.4768	2.30
	212	0.3893	
	213	0.3451	
	404	0.2875	0.80
	414	0.1286	
	413	0.1087	
	415	0.3698	
	606	0.1973	0.07
	616	0.0609	
	615	0.0519	
	617	0.5004	
$g^{-1}_{9/2} s_{1/2}$	404	0.2974	0.80
$p^{-1}_{1/2} d_{5/2}$	112	0.5530	
	303	0.3700	0.85
	313	0.4260	
	312	0.1130	
$p^{-1}_{1/2} s_{1/2}$	101	0.3260	5.94
	111	0.4610	
	110	0.5640	

Table 6.7 Nuclear Matrix Elements

Configuration	Normal Parity States	Non-normal Parity States
$(g_{9/2})^2$	0^+	
	2^+	
	4^+	
	6^+	
	8^+	
$p_{1/2}\, g_{9/2}$	5^-	4^-
A. $p_{3/2}^{-1}\, g_{9/2}$	3^-	4^-
	5^-	6^-
B. $f_{5/2}^{-1}\, g_{9/2}$	3^-	2^-
	5^-	4^-
	7^-	6^-
C. $p_{3/2}^{-1} p_{1/2}$	2^+	1^+
D. $f_{5/2}^{-1} p_{1/2}$	2^+	3^+
E. $g_{9/2}^{-1} d_{5/2}$	2^+	3^+
	4^+	5^+
	6^+	7^+
F. $g_{9/2}^{-1} s_{1/2}$	4^+	5^+
G. $p_{1/2}^{-1} d_{5/2}$	3^-	2^-
H. $p_{1/2}^{-1} s_{1/2}$	1^-	0^-

Table 6.8 Shell Model Configurations in Zr^{90} Expected to Give States in the 0-5MeV. Energy Range

Excitation Energy	Configuration	LSJ	V (MeV)	Figure	Cross-sect. at 30°
2.18	$(g_{9/2})^2$	202	85	6.20A*	
		202	50	6.20A	
3.08		404	85	6.20B	
3.45		606	85	6.20C	
3.57		808	85	6.20D	
2.30	$(g_{9/2} p_{1/2})$	505	85	6.21	
3.37	C	011	18	6.22A	0.14
	C	202	36	6.22A*	
	D	202	47	6.22B	
	E	202	22	6.22B*	
3.84	C	202	44	6.22C	0.20
	D	202	57	6.22C*	
	E	202	27	6.22D	
3.95	A	505	146	6.23A	0.45
	B	505	124	6.23A*	
4.05	A	303	27	6.23B	0.21
	B	303	86	6.23C	
	E	404	52	6.23C*	
4.22	C	202	45	6.23D	0.22
	D	202	59	6.23D*	
	E	202	26	6.24A	
4.32	E	404	116	6.24B	0.90
4.45	A	303	39	6.24C	0.30
	B	303	111	6.24C*	
4.54	A	303	32	6.24D	0.25
	B	303	87	6.25A	
	E	404	67	6.25A*	
4.65	C	202	30	6.25B	0.15
	D	202	37	6.25B*	
	E	202	18	6.25C	
4.79	A	303	17	6.25D	0.55
	B	303	55	6.25D*	
4.88	A	303	16	6.26A	0.50
	B	303	159	6.26B	
	E	404	27	6.26B*	0.54
4.99	A	303	19	6.26C	
	B	303	56	6.26C*	
5.06	A	303	29	6.26D	0.25
	B	303	74	6.26D*	

Table 6.9 Key to Figures 6.20 to 6.26 with values of V_o.

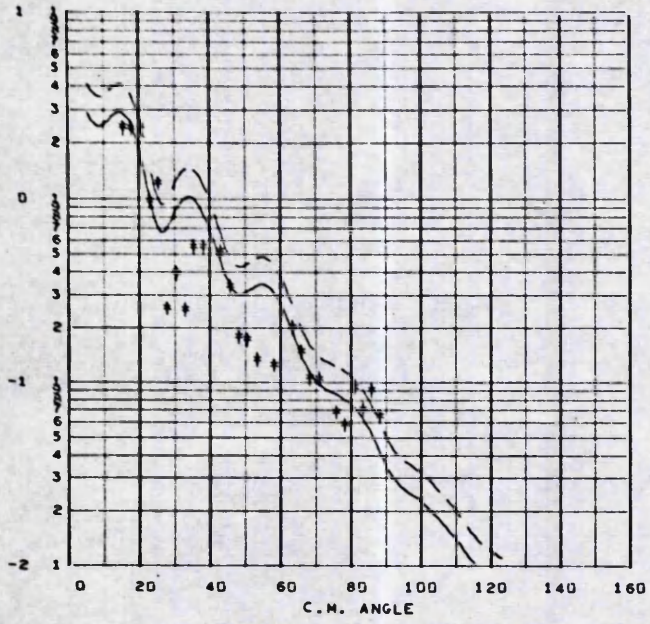

A.

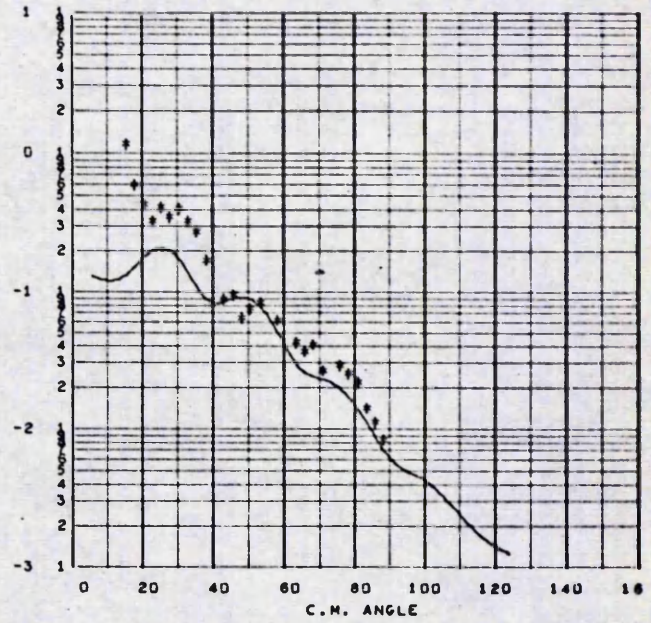

B.

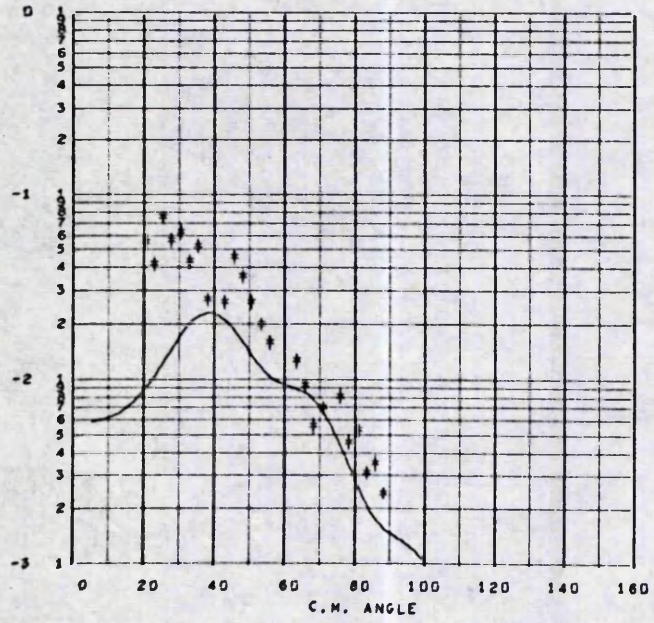

C.

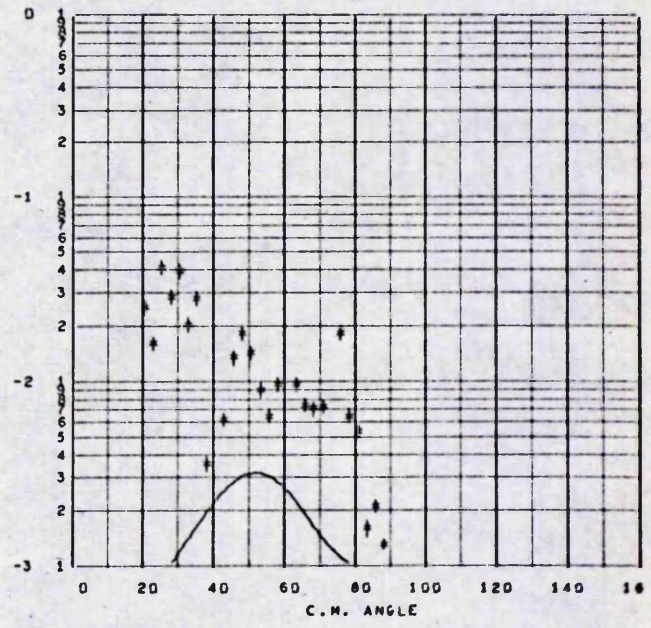

D.

Figure 6.20

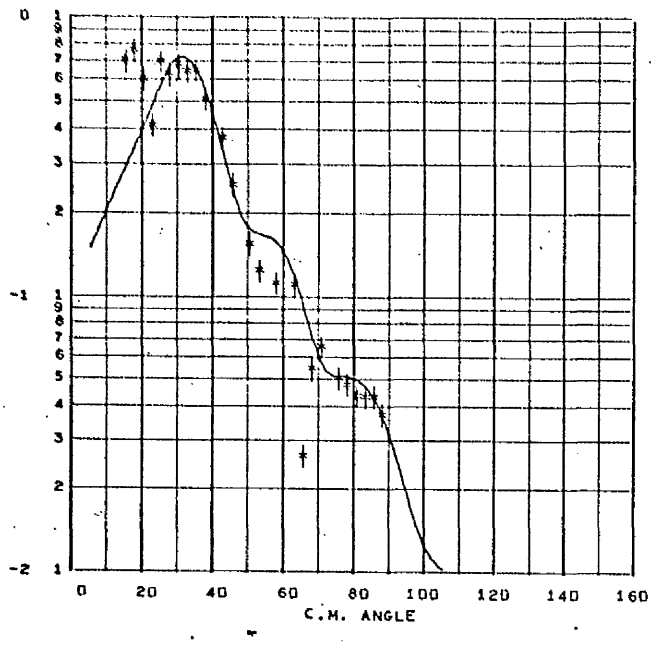

Figure 6.21

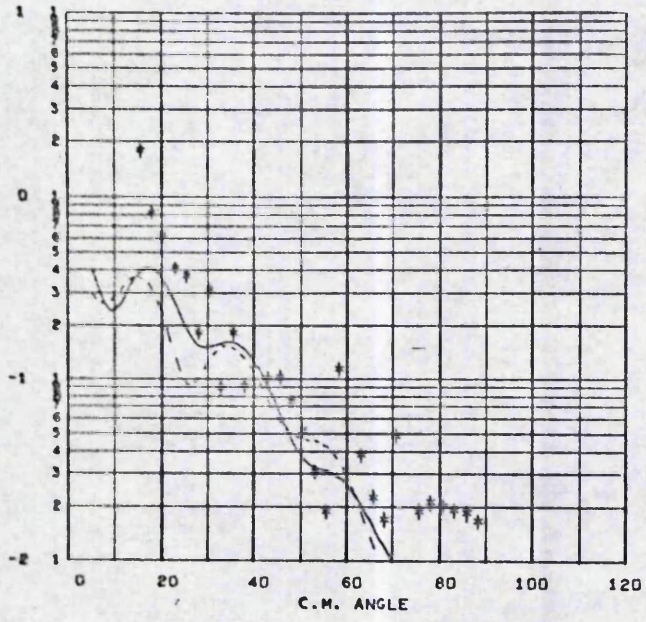

A.

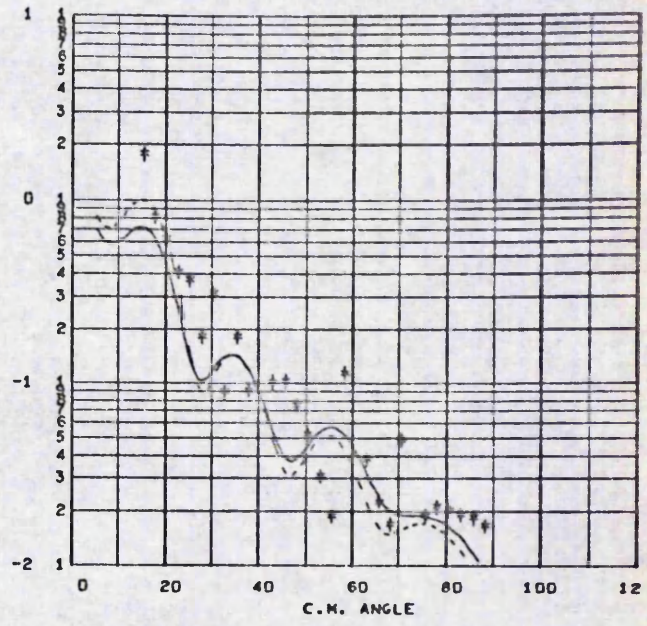

B.

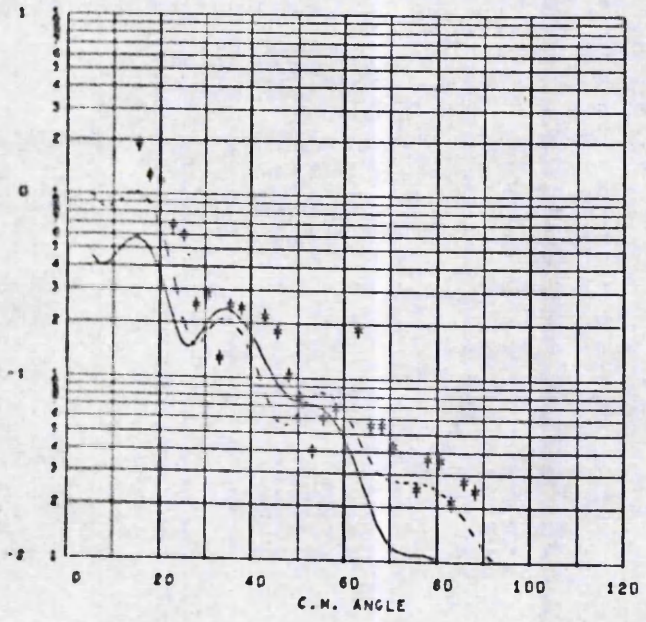

C.

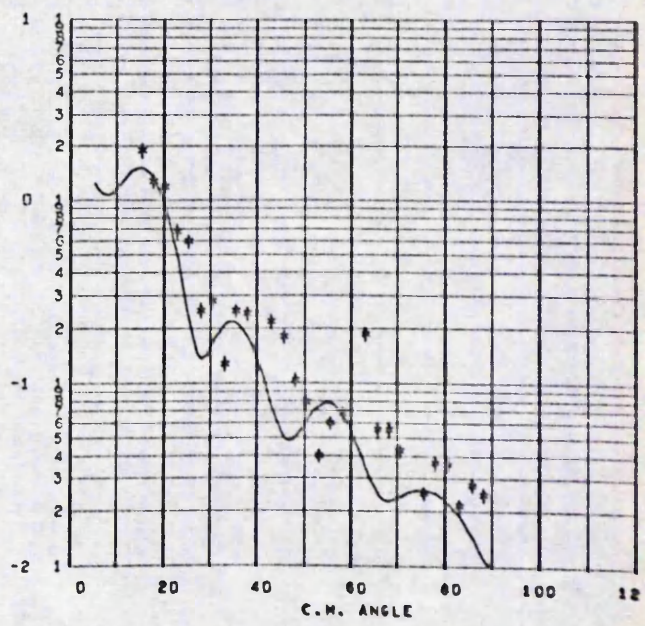

D.

Figure 6.22

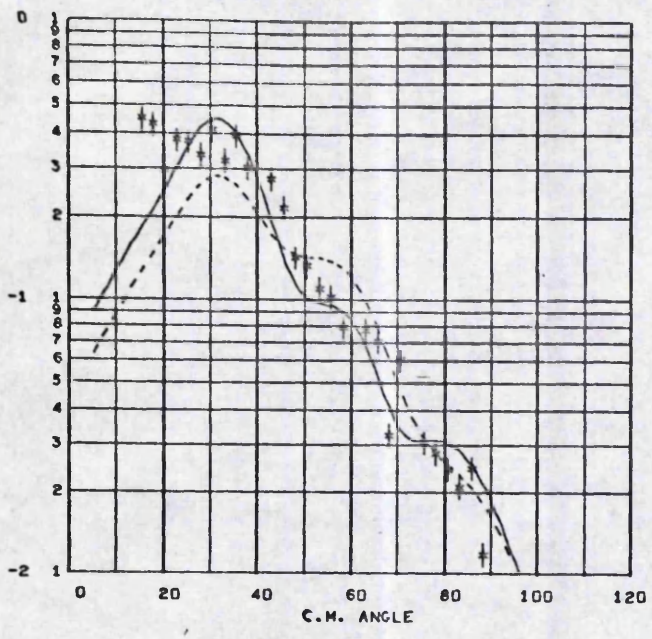

A.

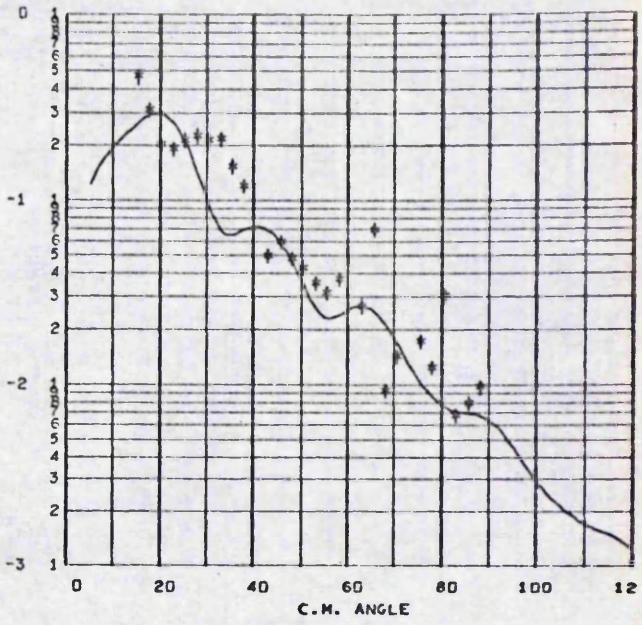

B.

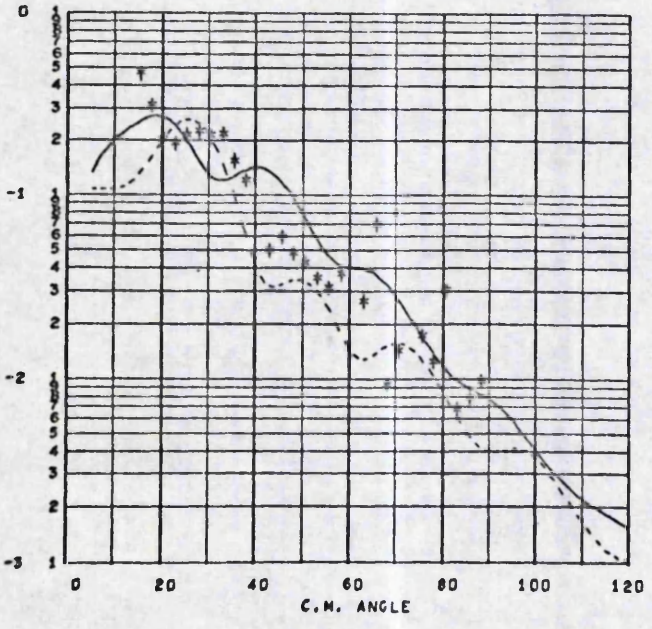

C.

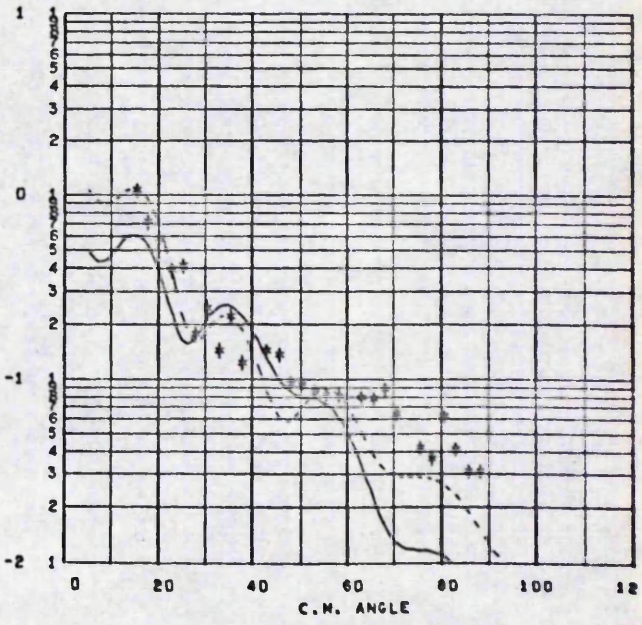

D.

Figure 6.23

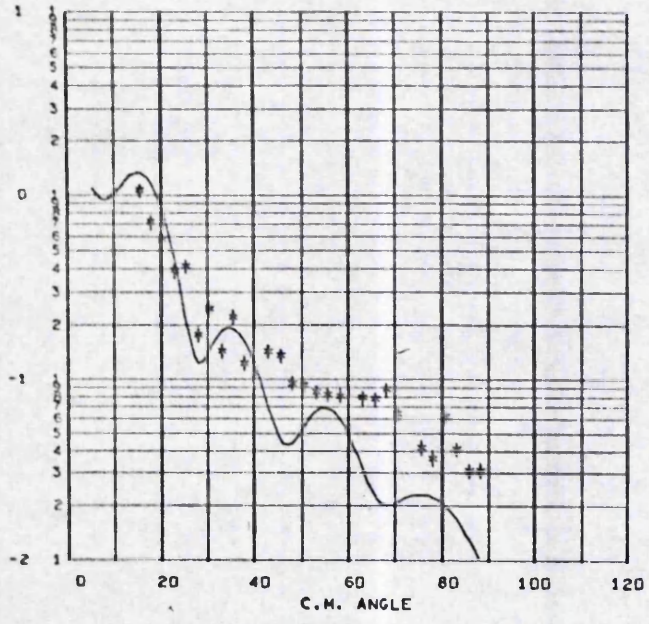

A.

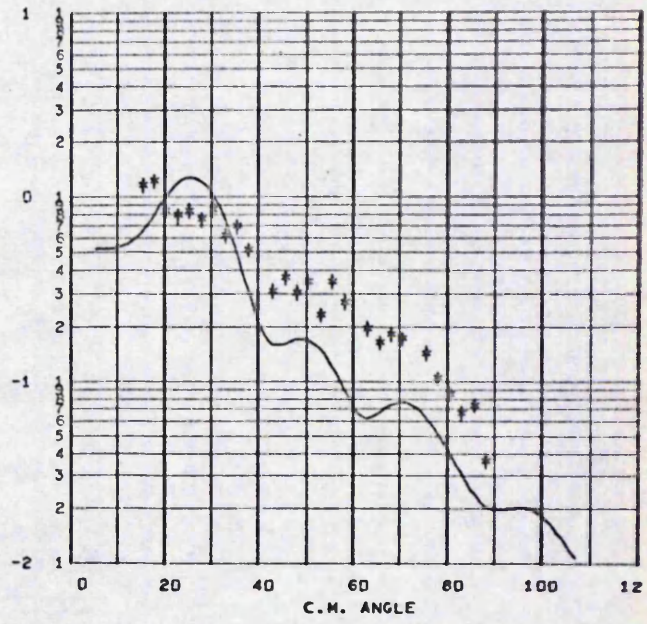

B.

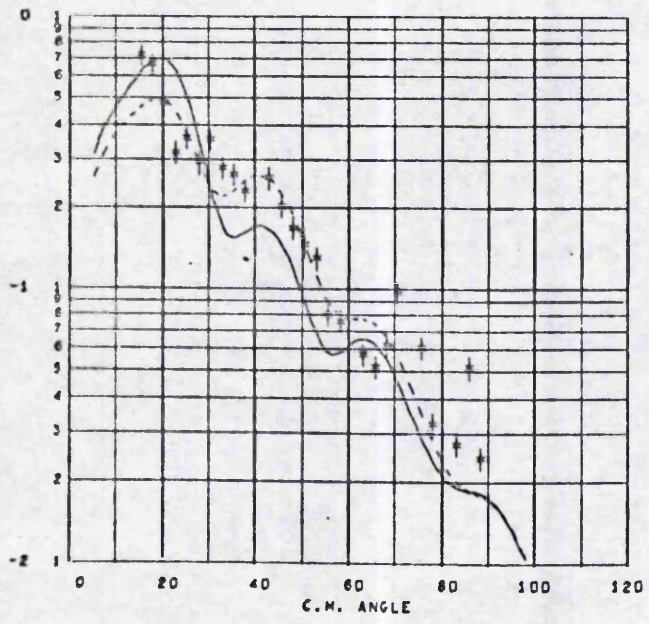

C.

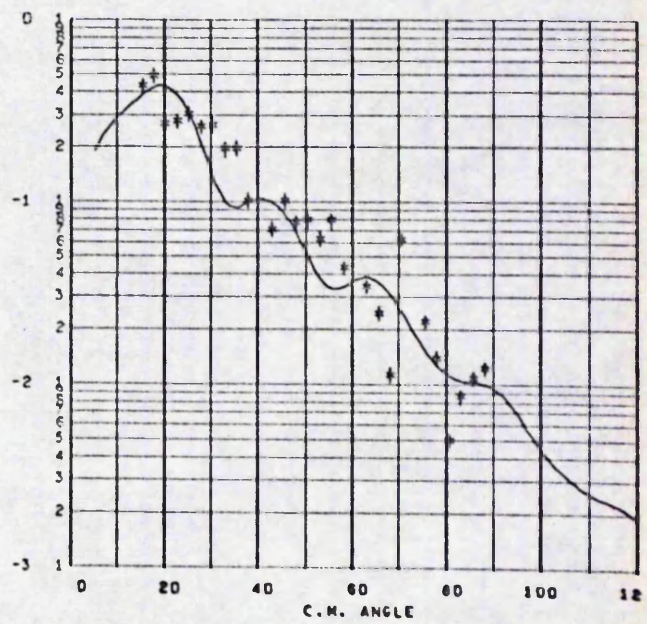

D.

Figure 6.24

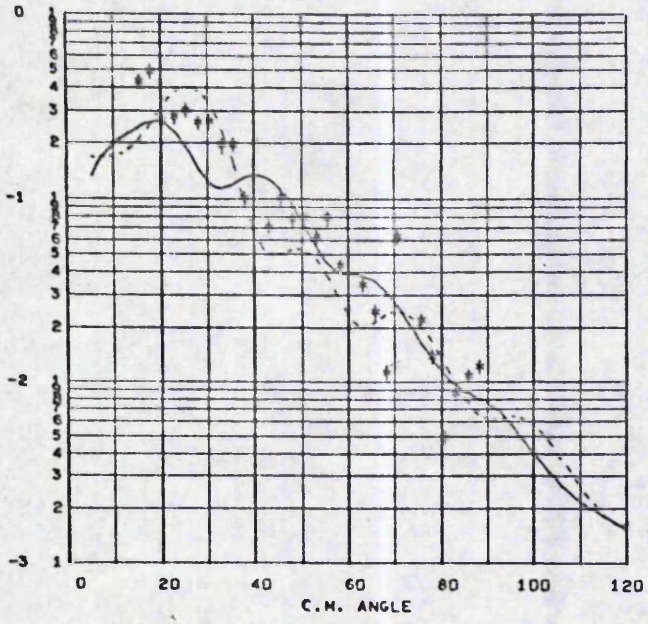

A.

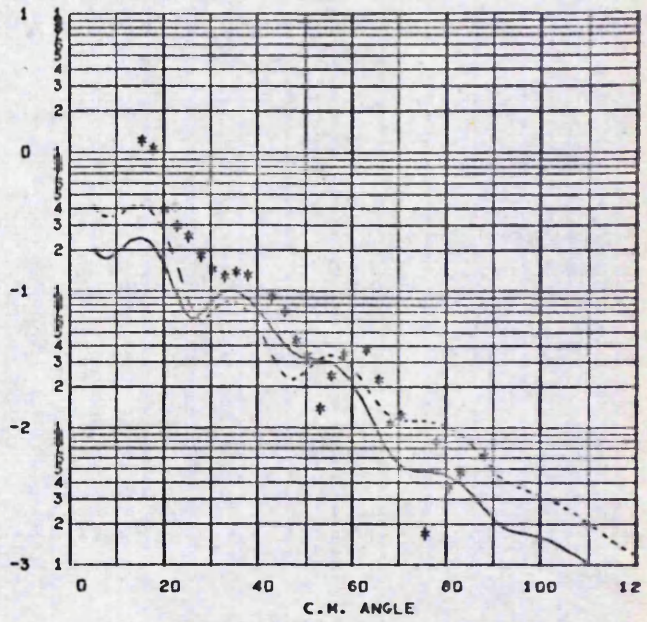

B.

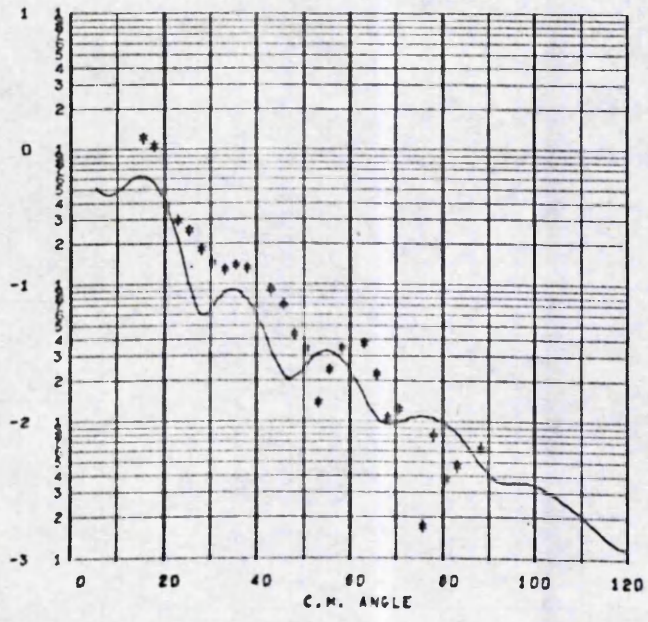

C.

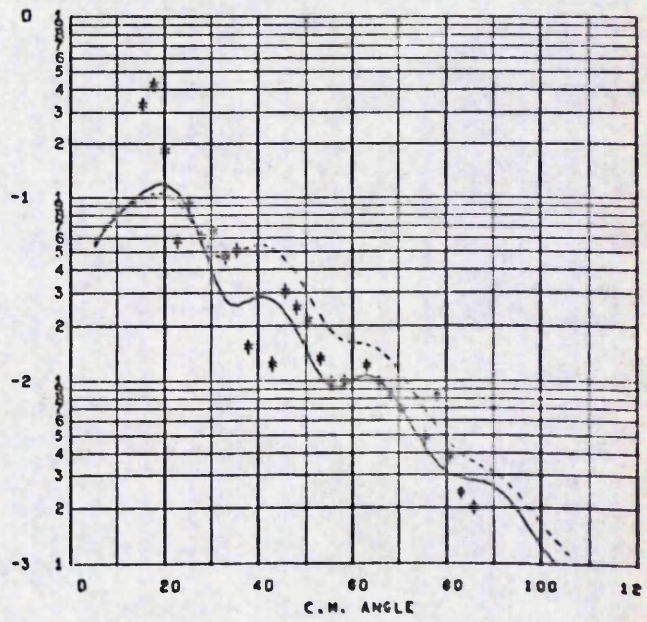

D.

Figure 6.25

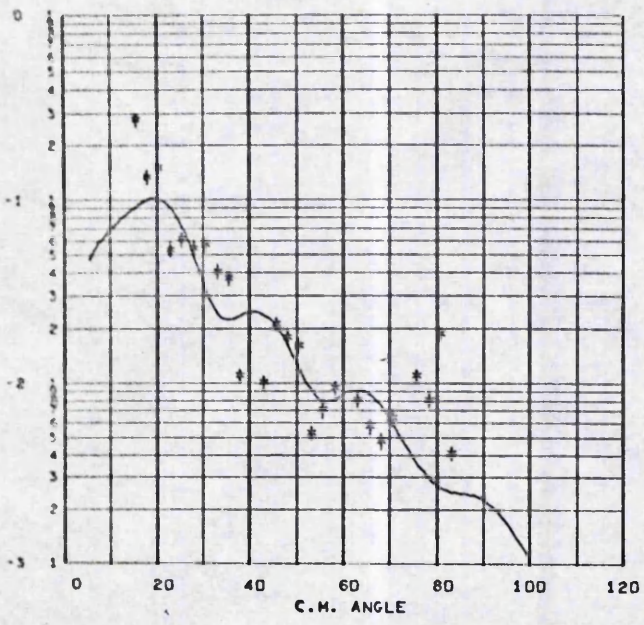

A.

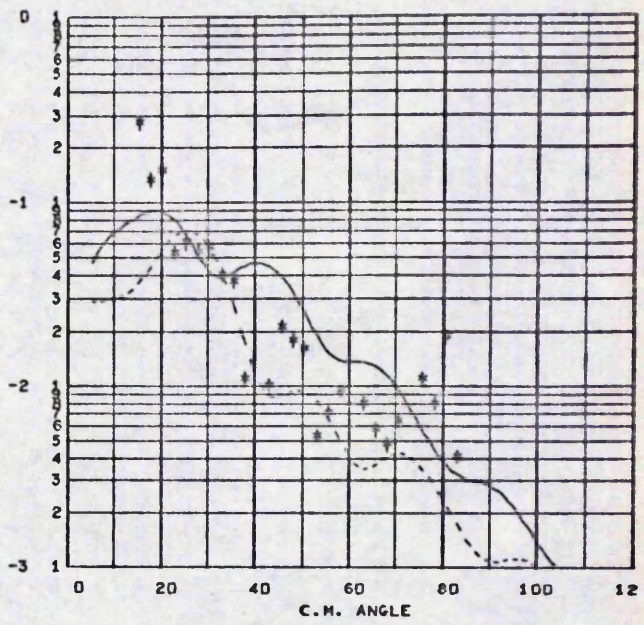

B.

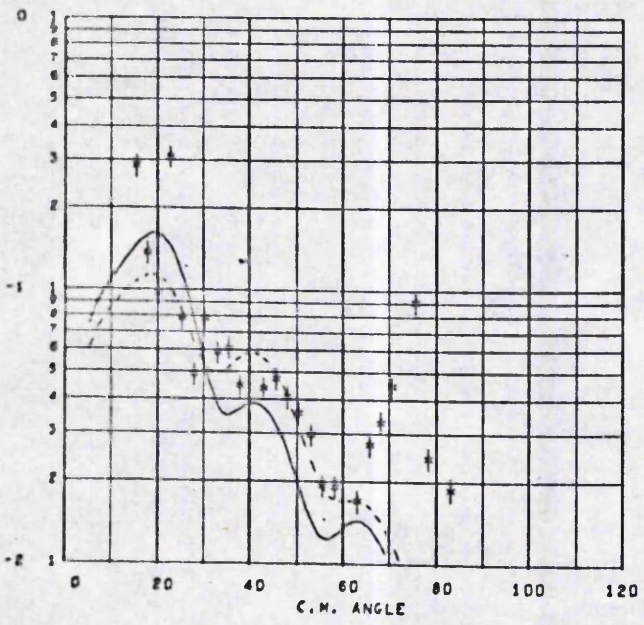

C.

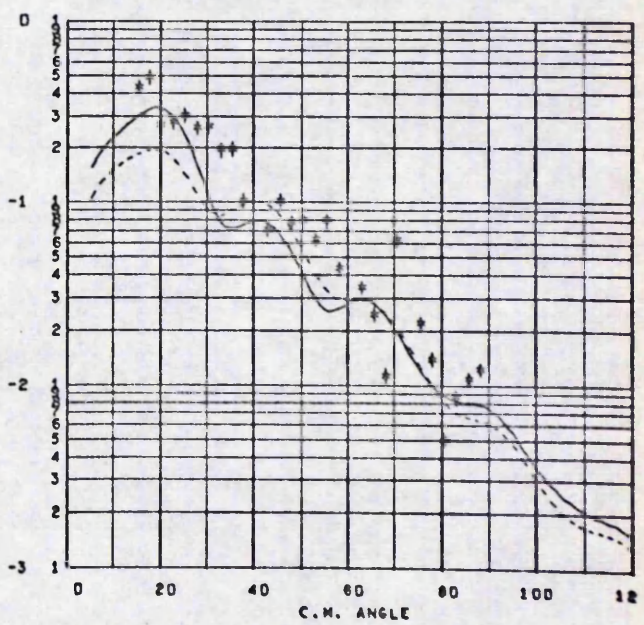

D.

Figure 6.26

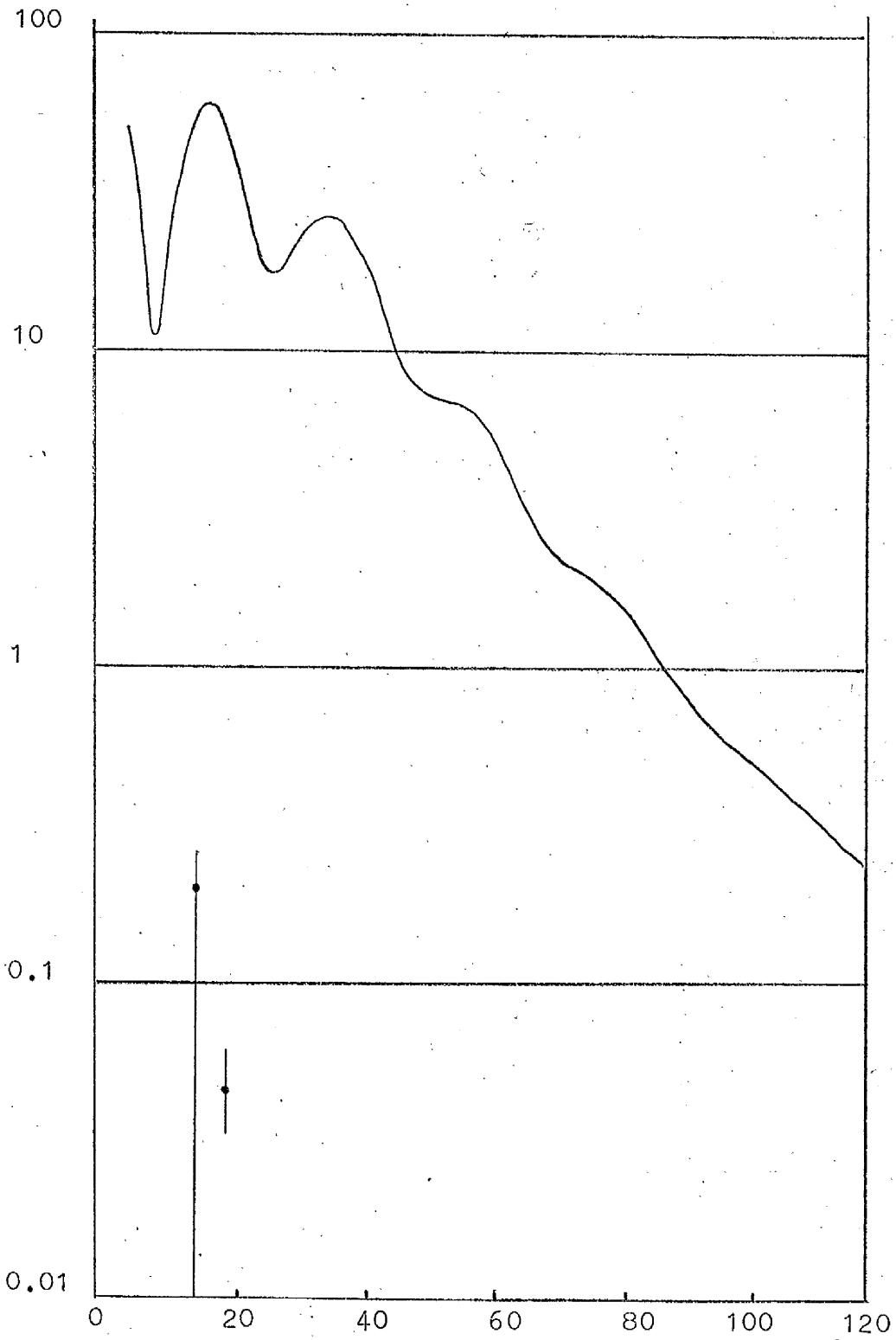

Figure 6.27 Shell Model Predictions for the 0^+ Level

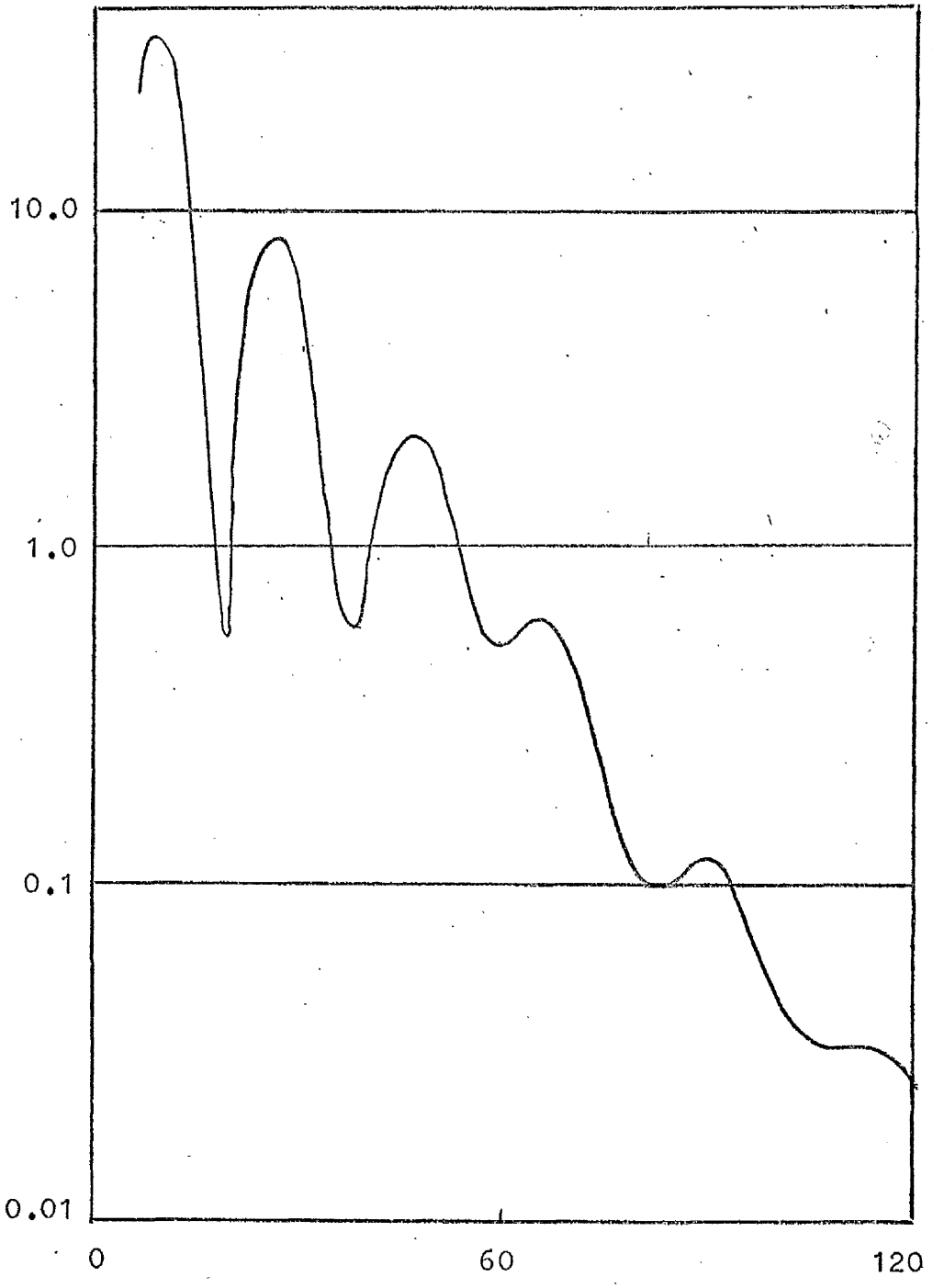

Figure 6.28A. Angular distribution for the H101 configuration.(V = 85MeV)

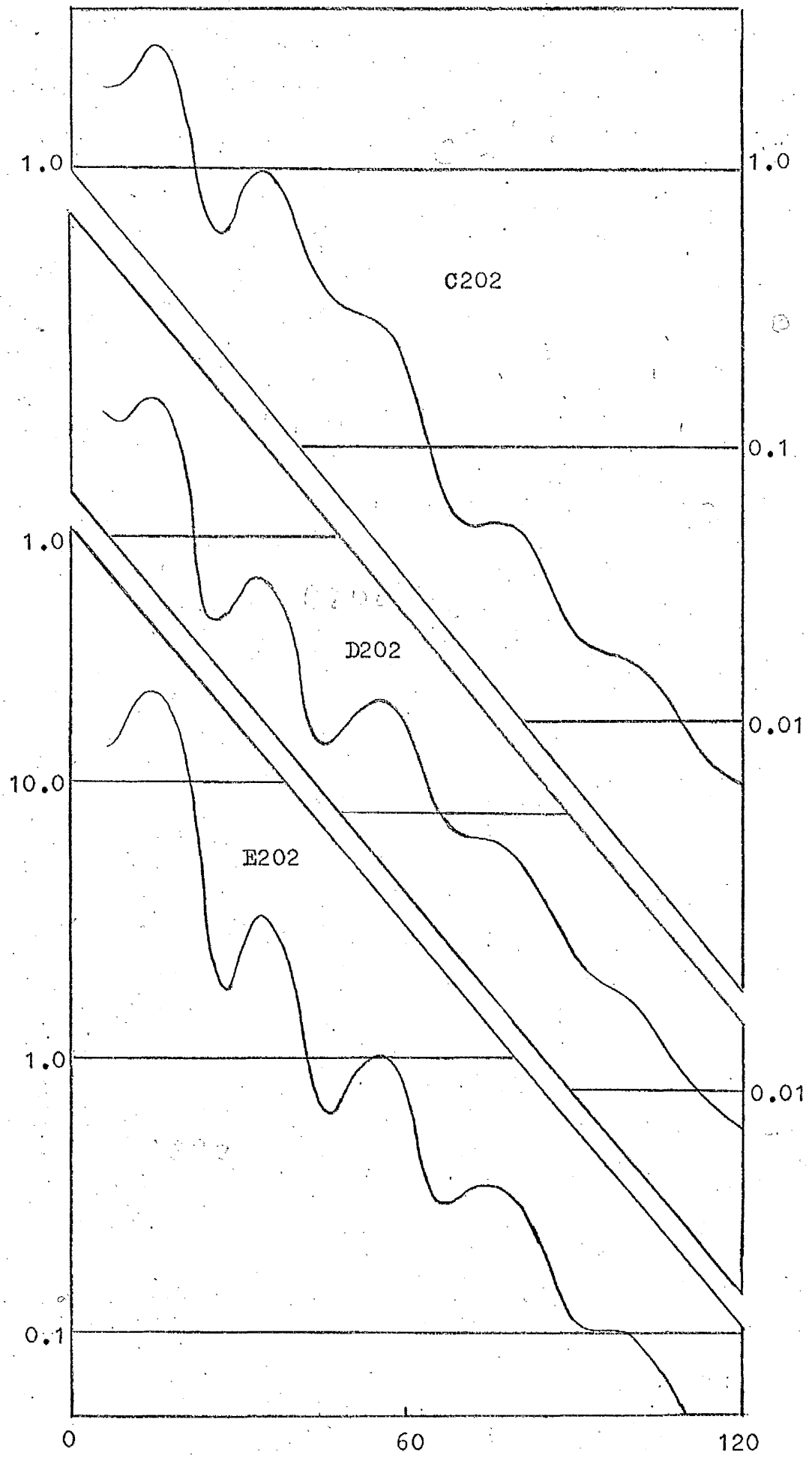

Figure 6.28B. Angular Distribution for the L=2 Configurations

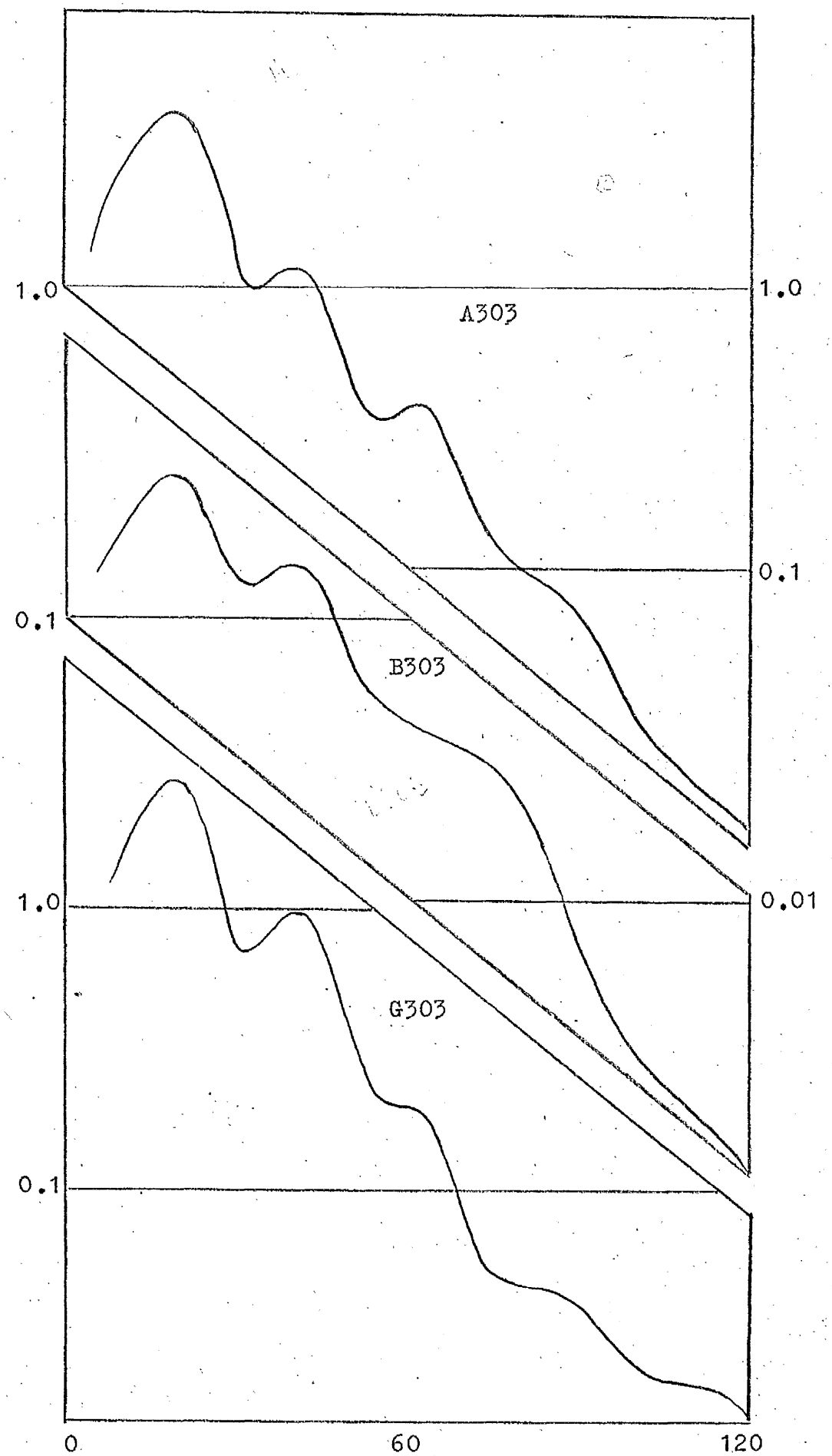

Figure 6.28c. Angular Distributions for the L=3 configurations.

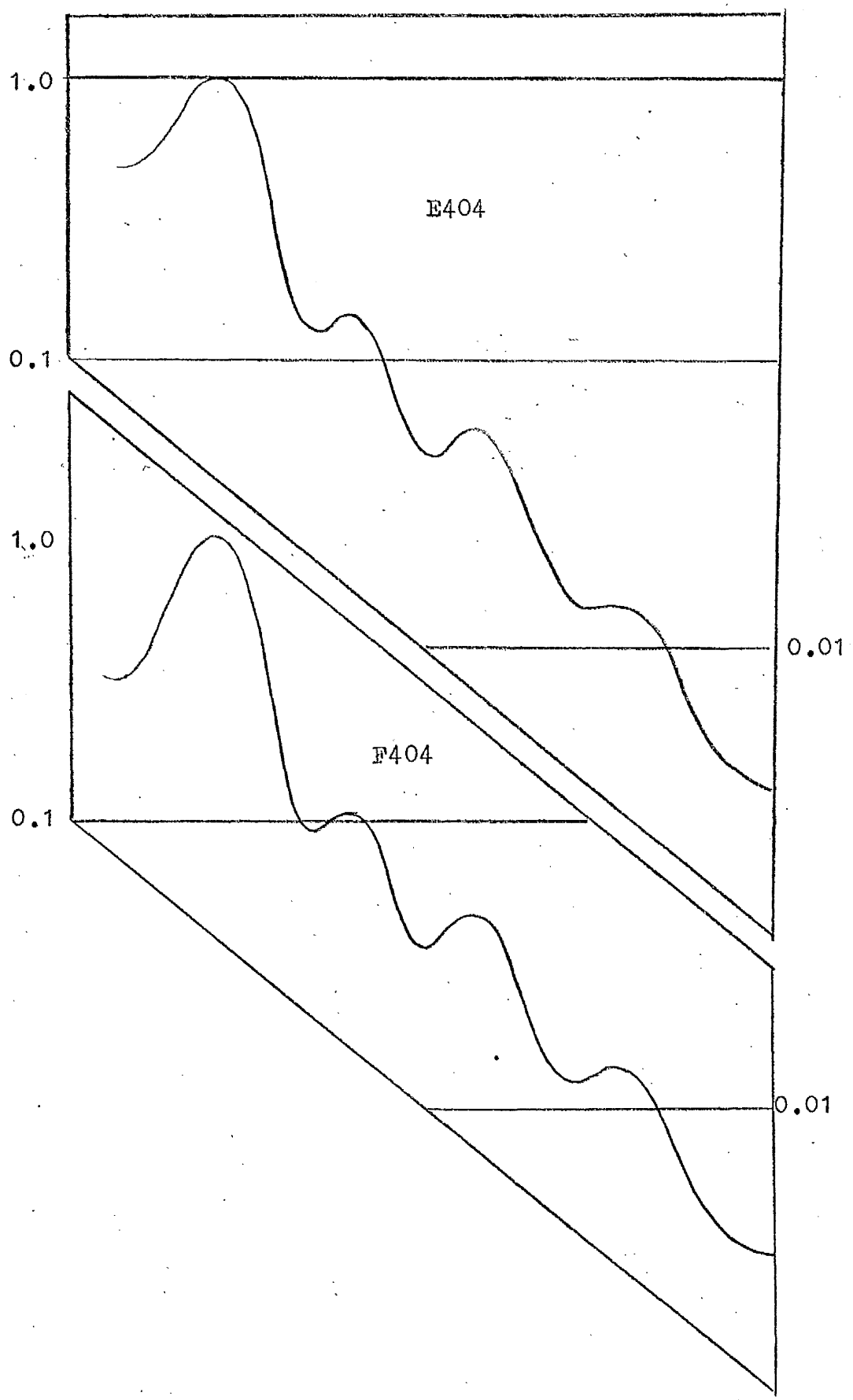

Figure 6.28D Angular Distribution for the L=4 Configurations.

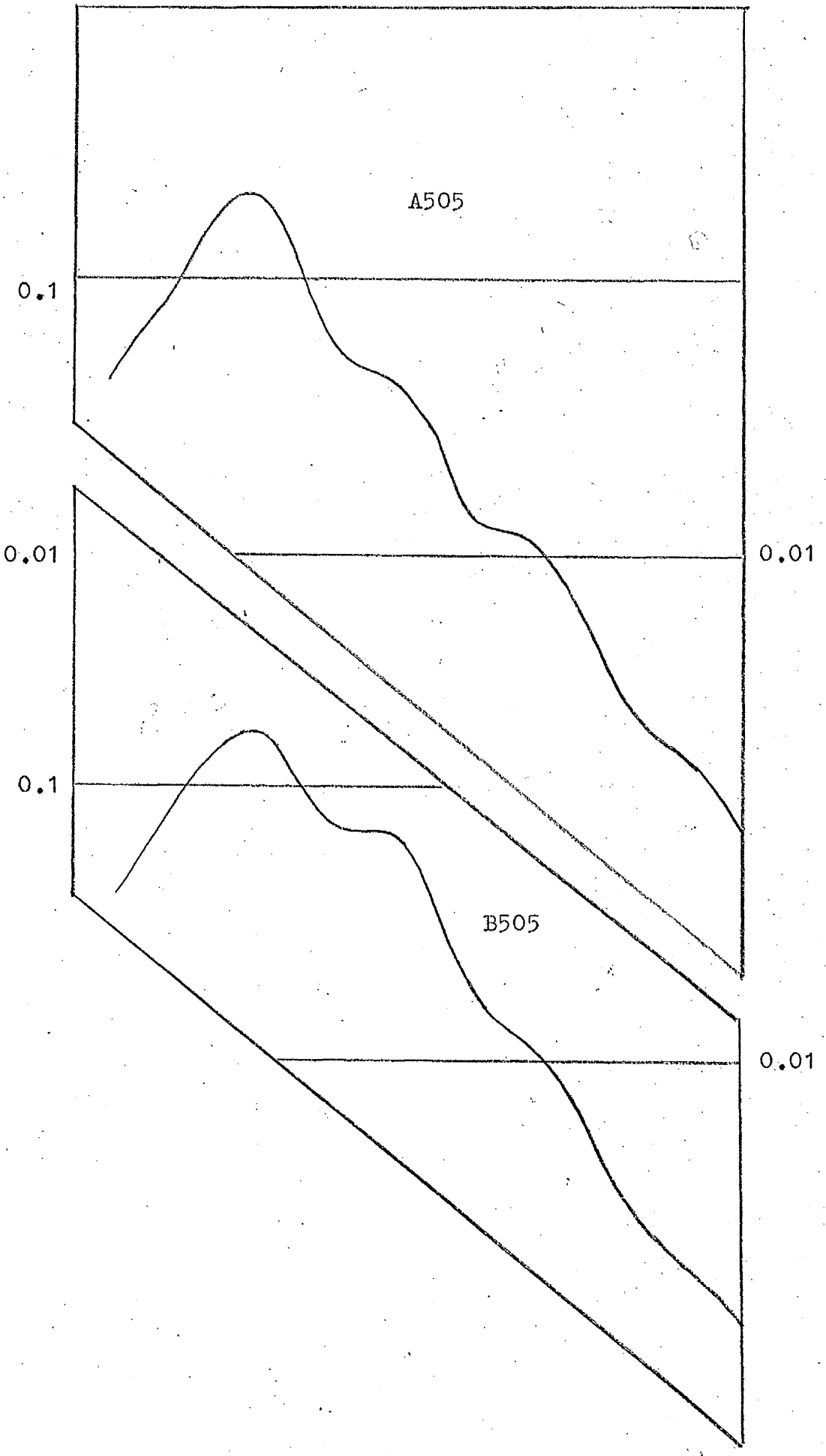

Figure 6.28E. Angular Distributions of the L=5 Configurations.

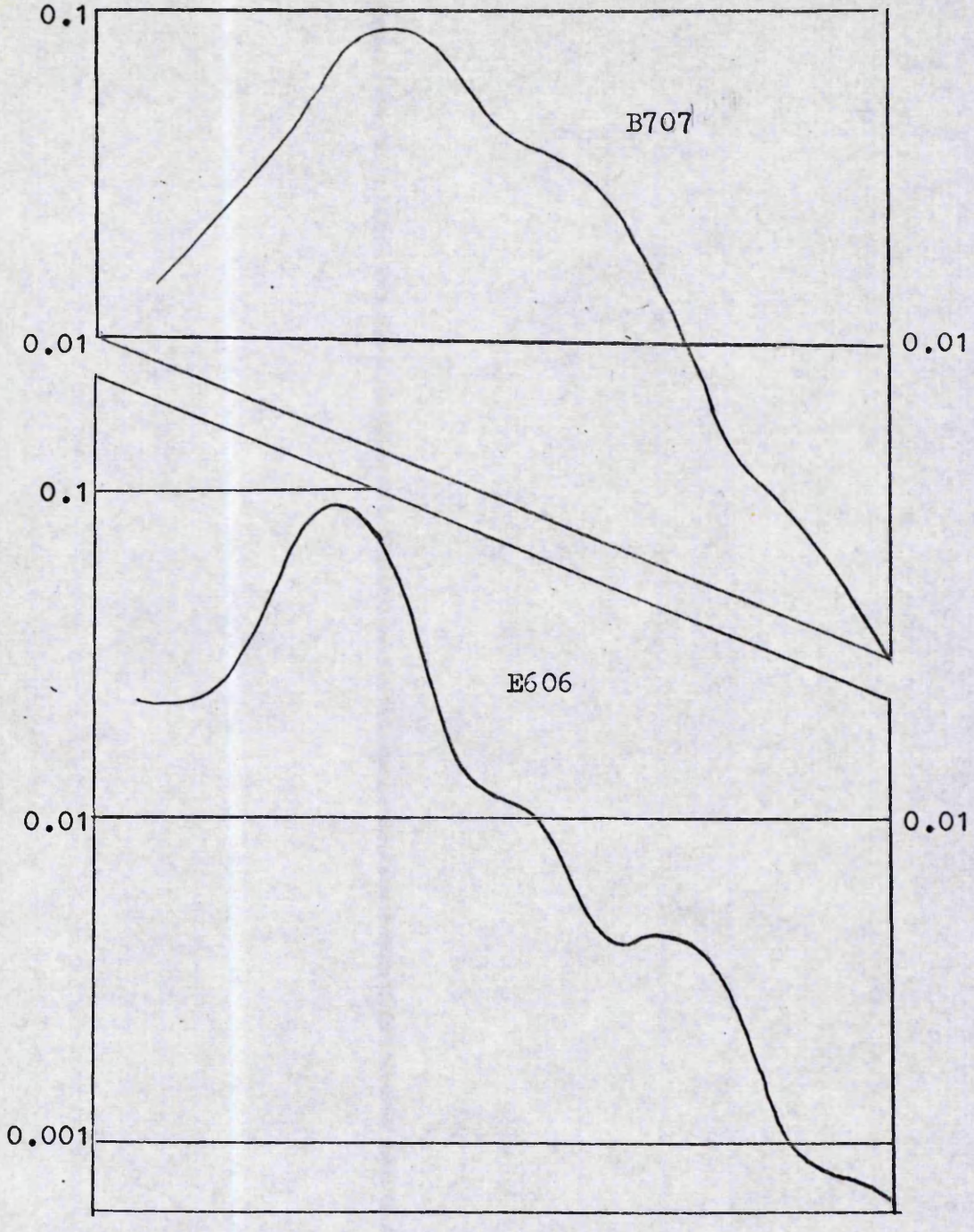

Figure 6.28F. Angular Distributions of the L=6 and L=7 Configurations

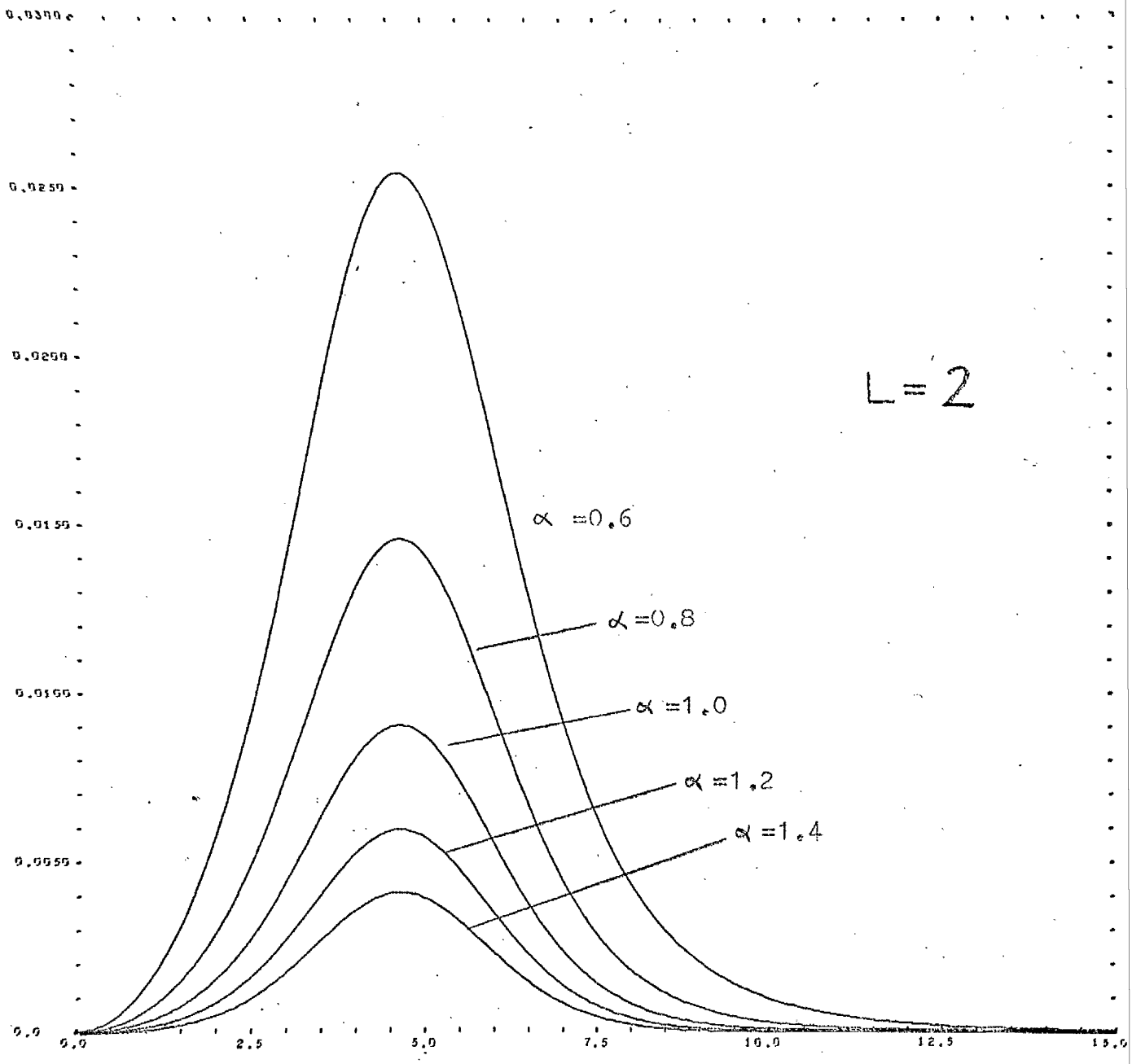

Figure 6.29 Effect on Radial Form Factors of Varying ∝

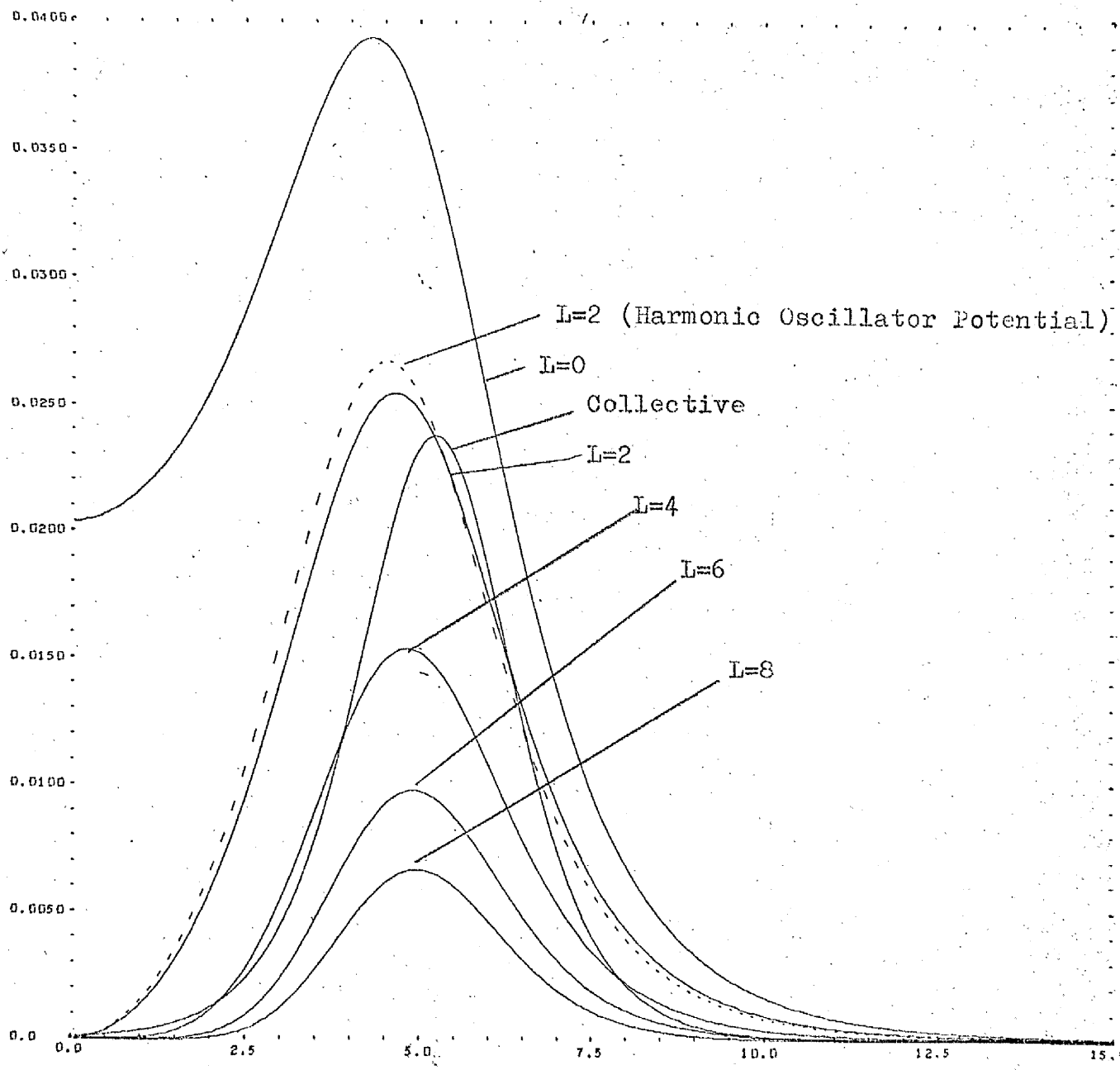

Figure 6.30 Radial Form Factors for the $(g_{9/2})$ levels in Zr^{90}.

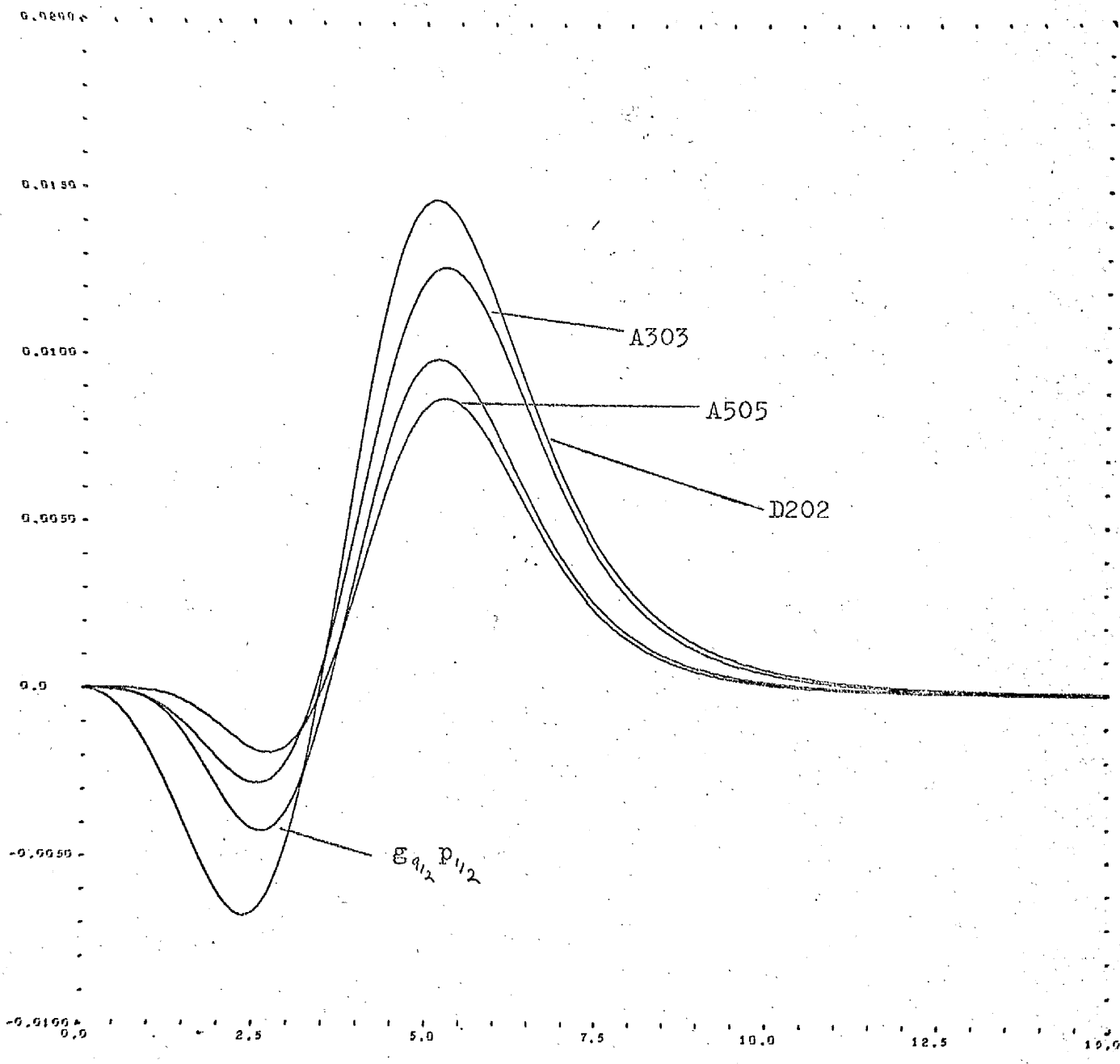

Figure 6.31 Form Factors for some of the other Configurations

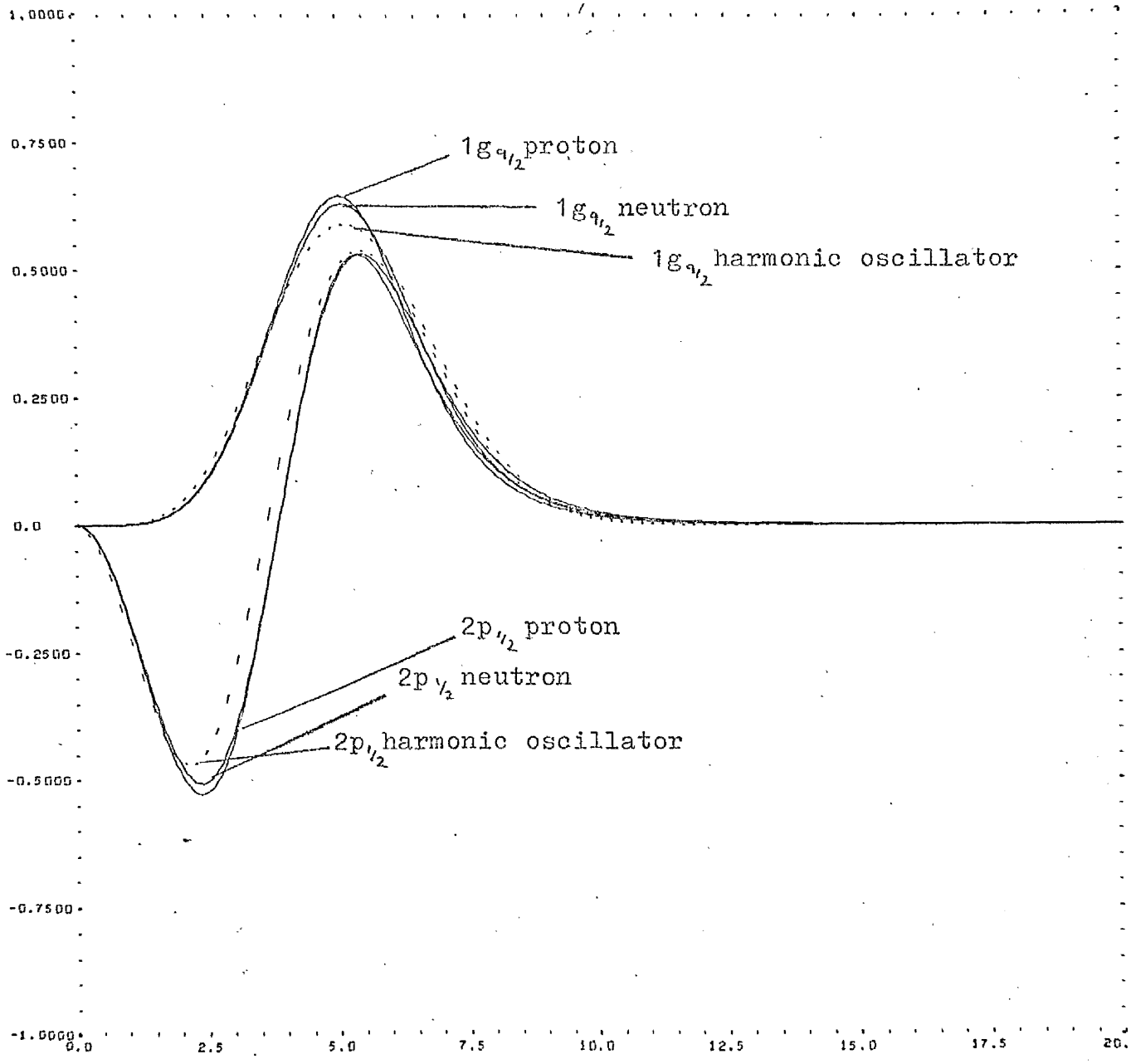

Figure 6.32 Shell model Single Particle Wave Functions

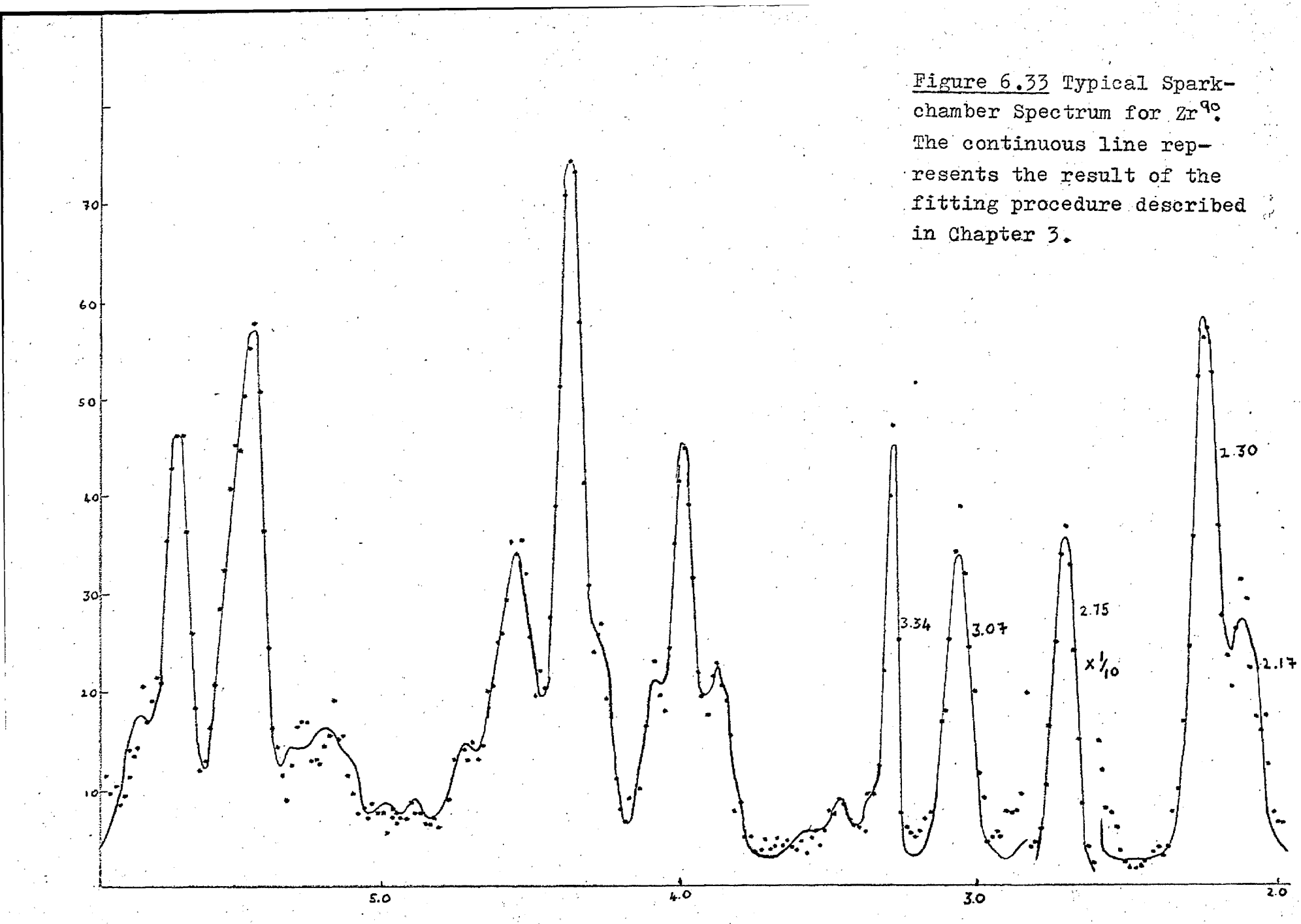

Figure 6.33 Typical Spark-chamber Spectrum for Zr^{90}. The continuous line represents the result of the fitting procedure described in Chapter 3.

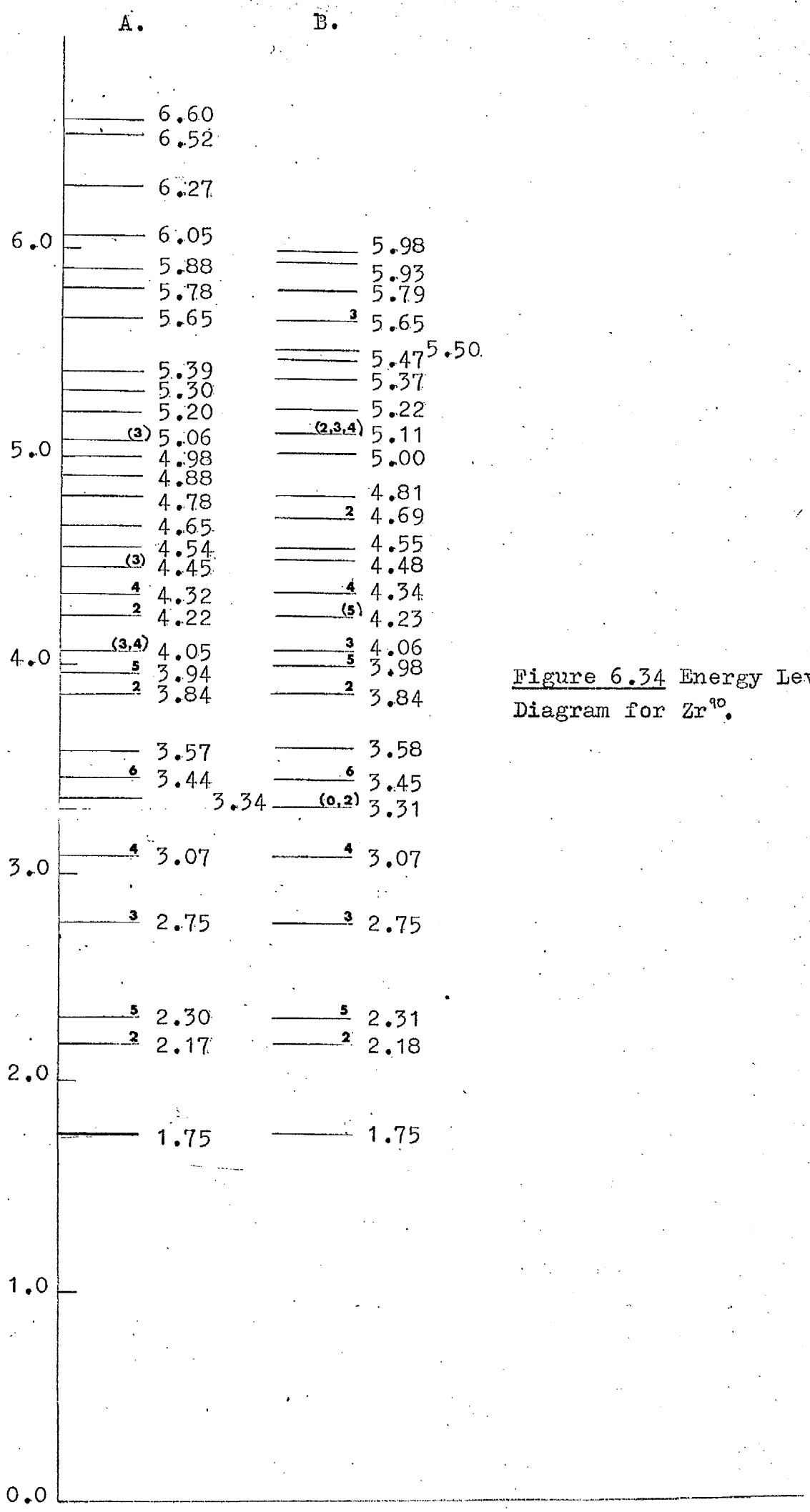

Figure 6.34 Energy Level Diagram for Zr^{90}.

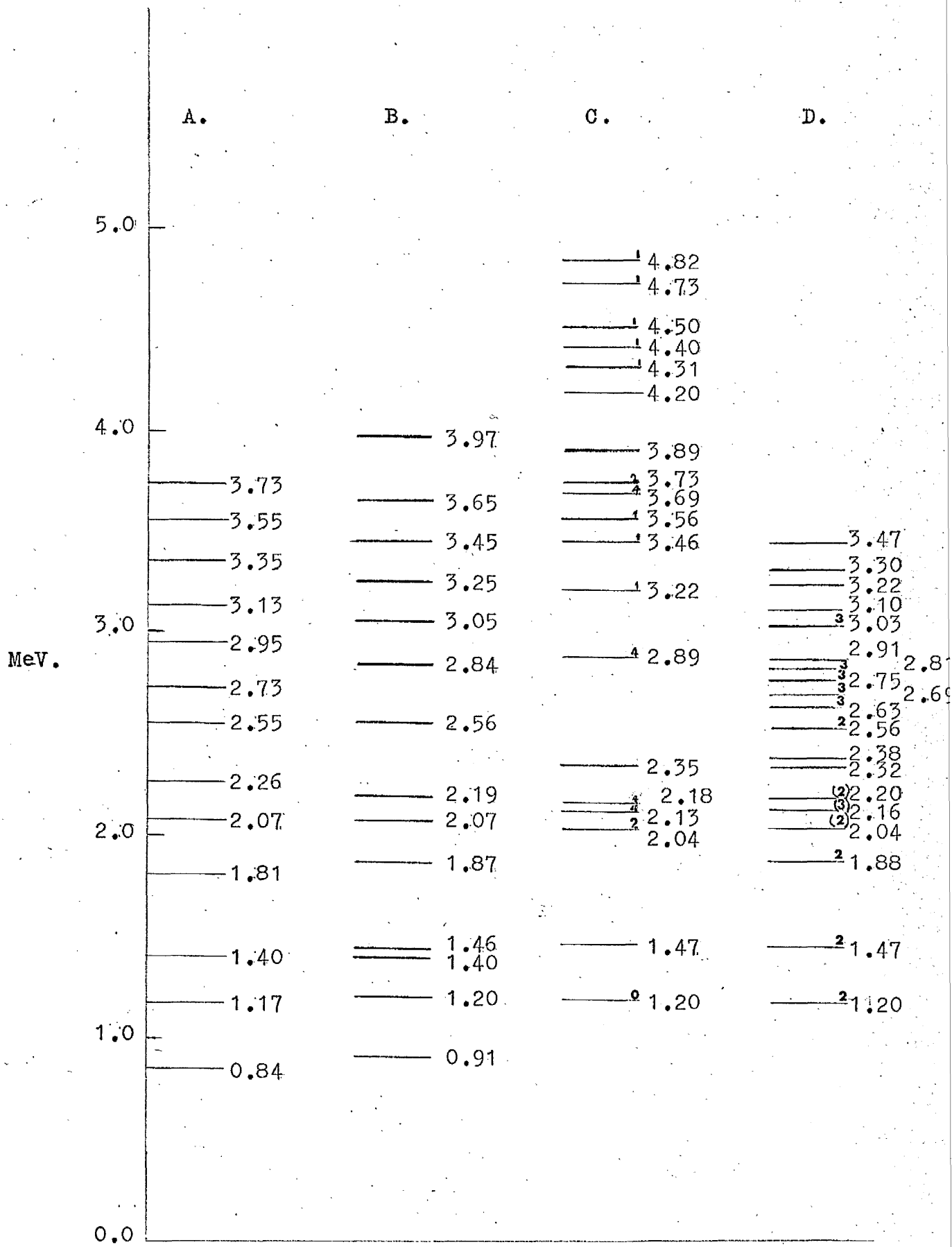

Figure 6.35 Energy Level Diagram for Zr^{91}.

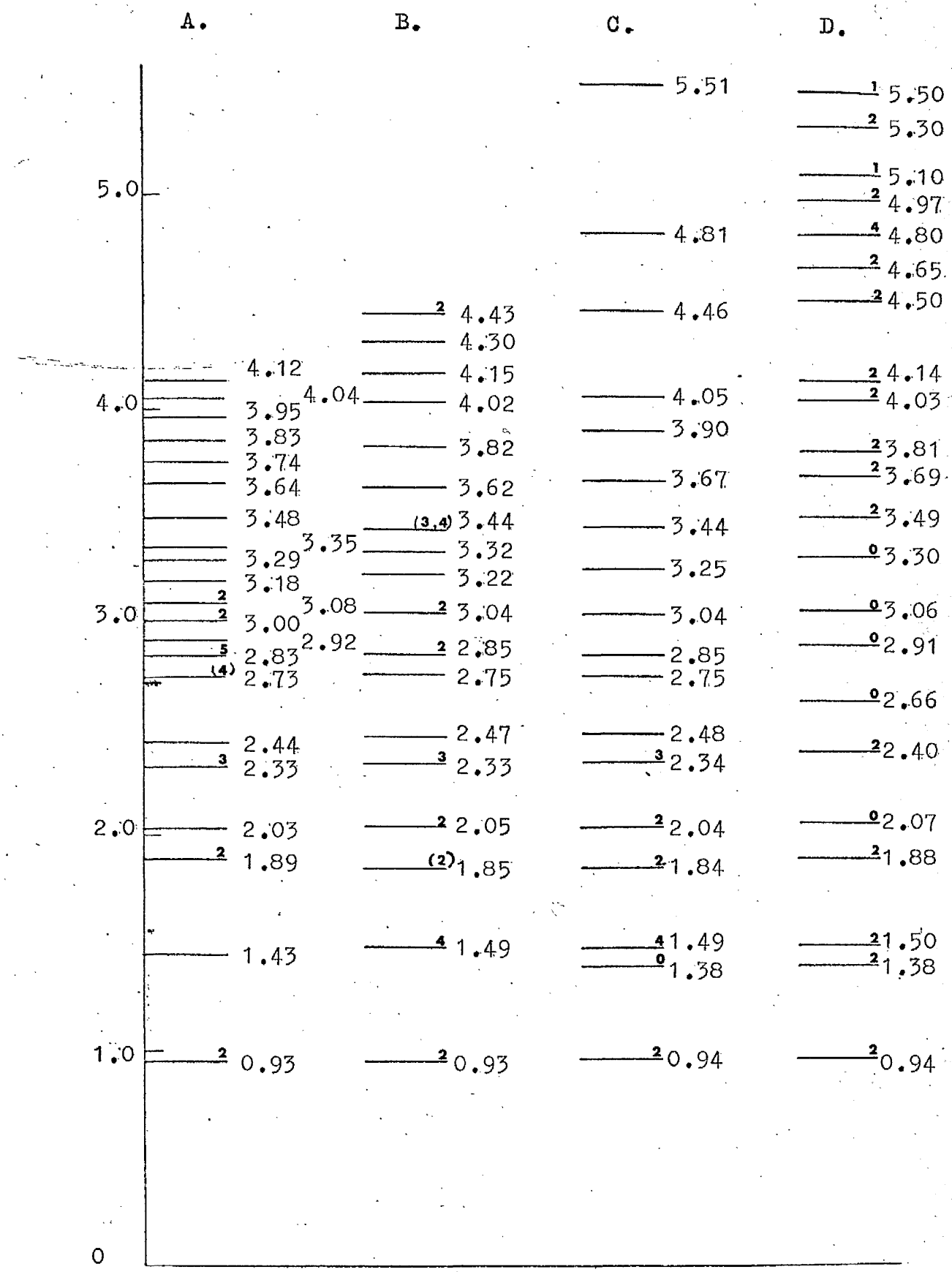

Figure 6.36 Energy Level Diagram for Zr^{92}.

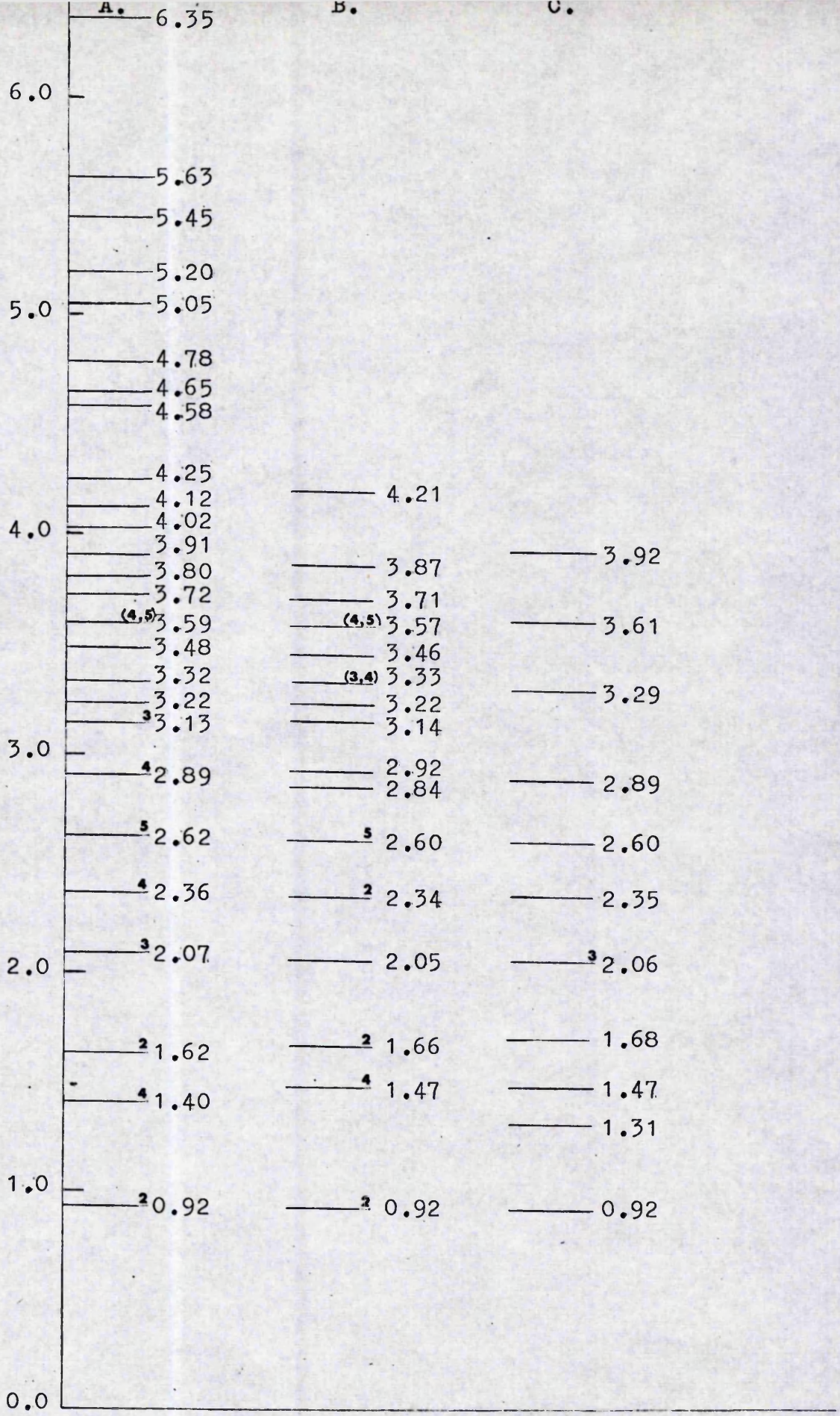

Figure 6.37 Energy Level Diagram for Zr^{94}.

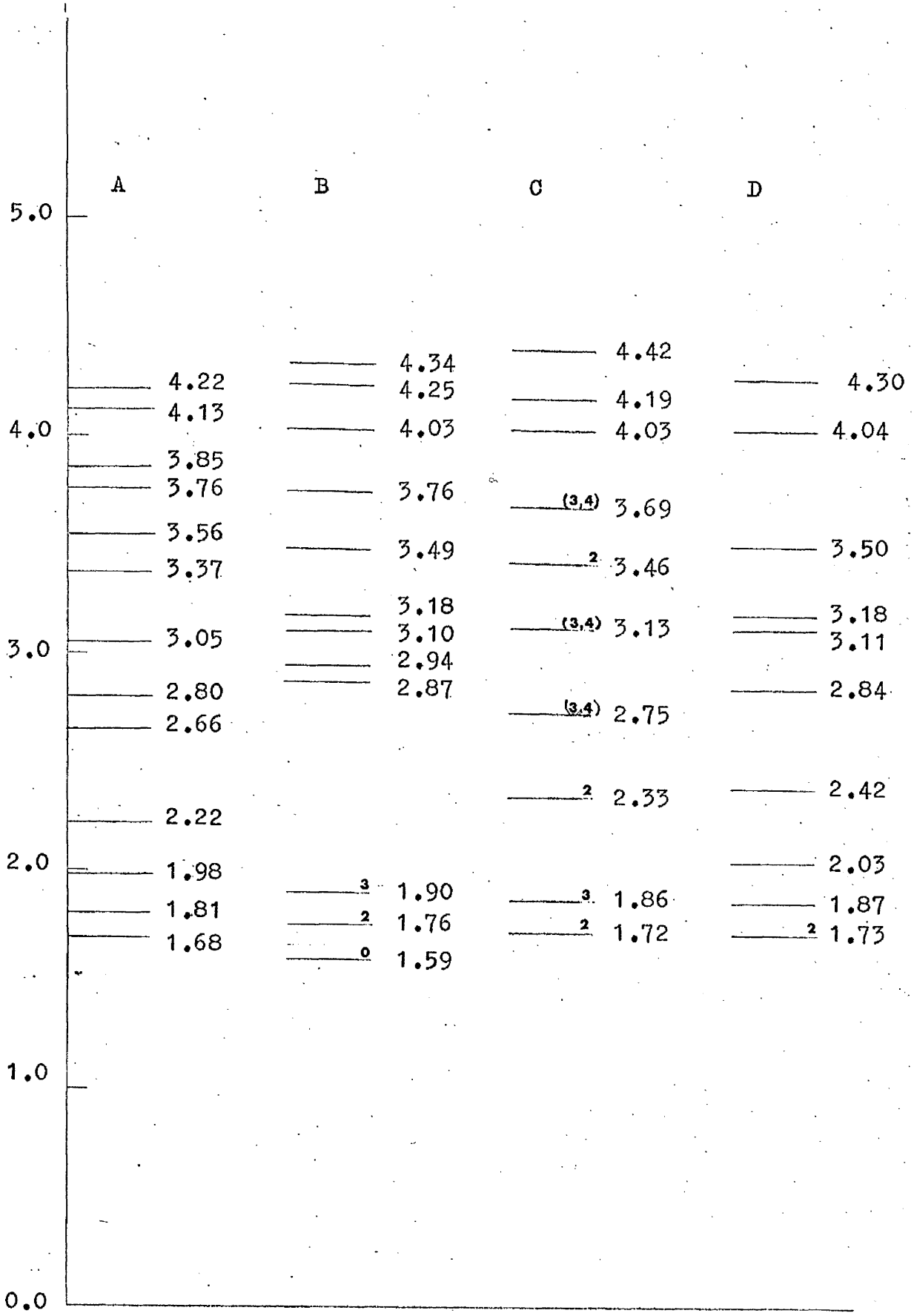

Figure 6.38 Energy Level Diagram for Zr^{96}

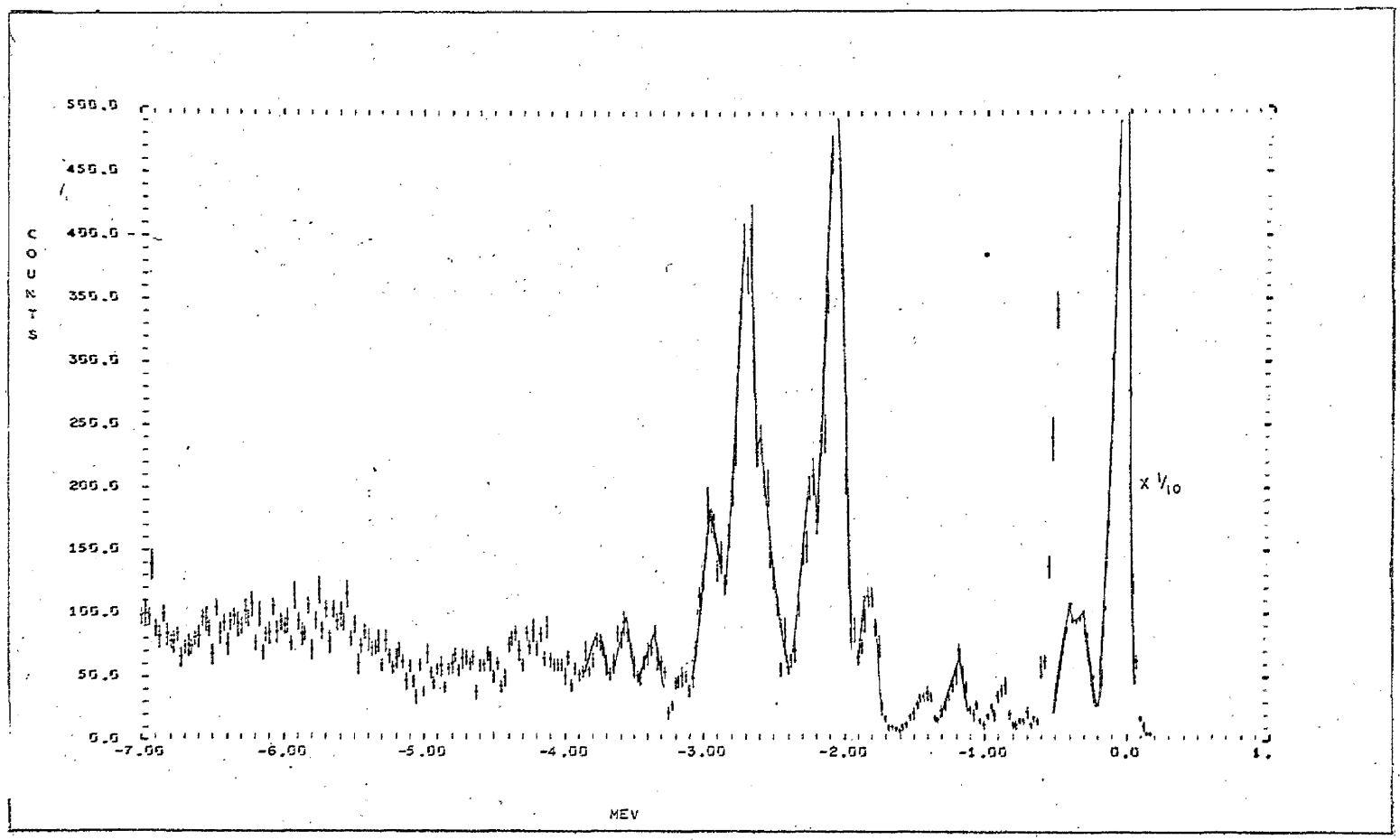

Figure 6.39 Energy Spectrum of Protons Scattered at 20° by Zr^{91}

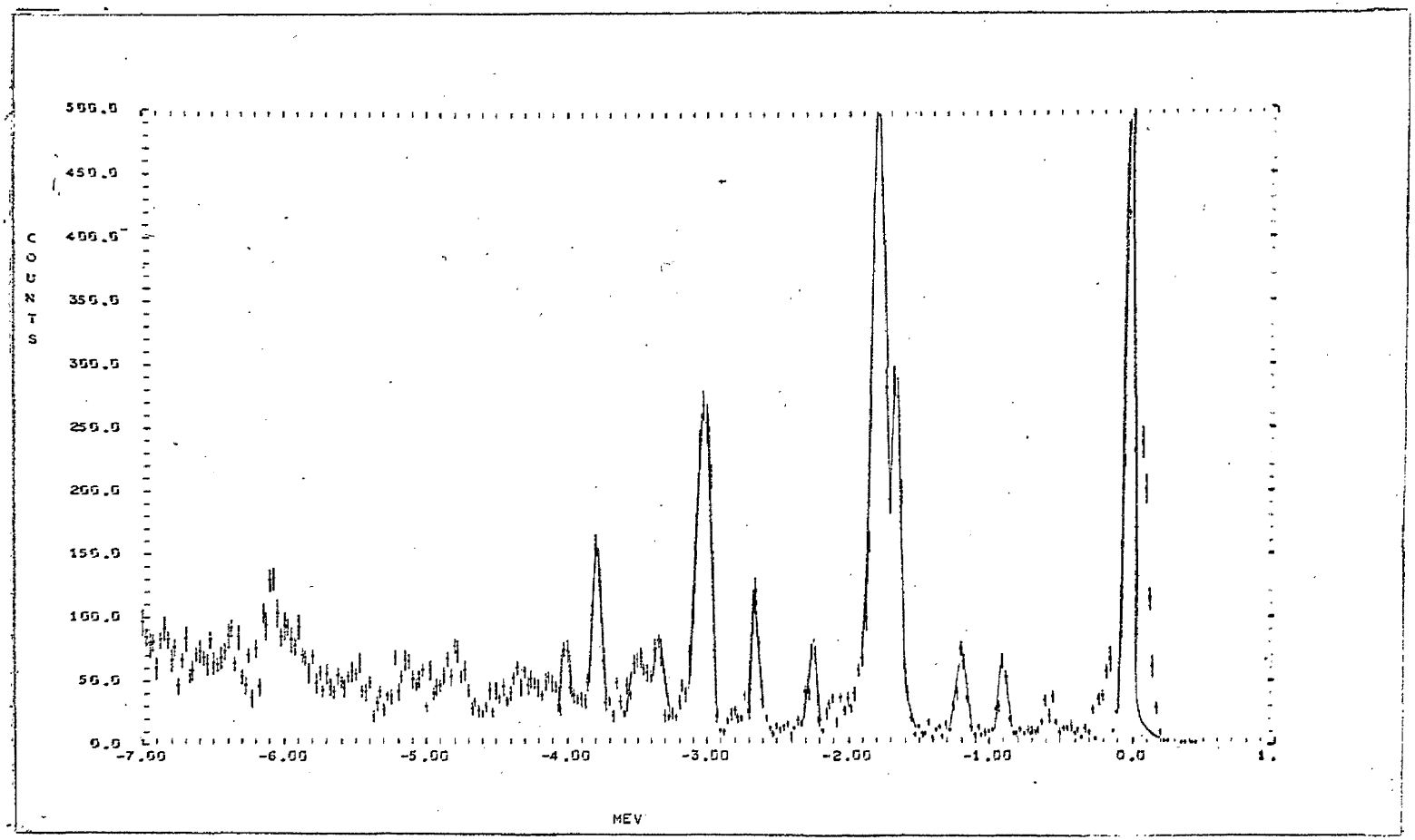

Figure 6.40 Energy Spectrum of Protons Scattered at 40° by Zr^{96}

References

1. W.S.Gray, R.A.Kenefick, J.J.Kraushaar and G.R.Satchler, Physical Review 142 (1966) No.3 p.735.
2. P.L.A. Progress Reports 1961 to 1969, Rutherford High Energy Laboratory.
3. A.D.B.Dix, Ph.D. thesis, University of Manchester May 1969.
4. User guide to the P.L.A. beam ancilliaries, Ed. F.J.Swales, RHEL/M109.
5. J.A.Fannon, E.J.Burge, D.A.Smith and N.K.Ganguly Nuclear Physics A97 (1967) p.263.
6. J.A.Fannon, Ph.D. thesis, University of London Oct. 1966.
7. P.E.Hodgson, "The Optical Model of Elastic Scattering", Oxford University Press 1963.
8. F.G.Perey, Oak Ridge National Laboratory Report No.ORNL-3429.
9. F.G.J.Perey and B.Buck, Oak Ridge National Laboratory, Neutron Physics Progress Report, ORNL-3193.
10. H.Sherif, Ph.D. thesis, (Seattle, Washington) 1968.
    H.Sherif and J.S.Blair, Physics Letters 26B (1968) p.489.
11. M.P.Fricke, E.E.Gross and A.Zucker, Physical Review 163 (1967) p.1153.

12. D.M.Brink and G.R.Satchler, "Angular Momentum" Oxford University Press 1962.
13. M.P.Fricke, E.E.Gross, B.J.Morton and A.Zucker Physical Review 156 (1967) p.1207.
14. A.M.Lane, Physical Review Letters 8 (1962) p.171.
15. J.B.Ball, C.B.Fulmer and R.H.Bassel, Physical Review 135 p.B706.
16. B.M.Preedom, Thesis, (University of Tennessee) 1967 ORNL TM-1860.
17. M.A.Preston, "Physics of the Nucleus" Addison Wesley Publishing co. (1962).
18. S.M.Perez, Atlas Program Library Report No.10.
19. W.G.Love, G.R.Satchler and T.Tamura, Physics Letters 22 No.3 (1966) p.325.
20. H.P.Blok, G.D.Thijs, J.J.Kraushaar and M.M.Stautberg Nuclear Physics A127 (1969) p.188.
21. J.B.Ball and C.B.Fulmer, Physical Review 172 (1968) p.1199.
22. Nuclear Data Sheets, published by the National Acadamey of Sciences, National Research Council Washington, NRC(60-4-26).
23. M.M.Stautberg, J.J.Kraushaar, Physical Review 151 (1966) p.969.
24. R.K.Jolly, Physical Review 139 (1965) p.B318. R.K.Jolly, E.K.Lin and B.L.Cohen, Physical Review 128 (1962) p.2292.

25. B.L.Cohen and O.V.Chubinsky, Physical Review 131 (1963) p.2184.
C.H.J.Martin Jnr., M.B.Sampson and R.L.Preston Physical Review 125 (1962) p.942.
26. J.Beery, Los Alamos Scientific Laboratory Report No. LA 3958.
27. M.M.Stautberg, R.R.Johnson, J.J.Kraushaar and B.W.Radley, Nuclear Physics A104 (1967) p.67.
28. D.M.Brink and G.R.Satchler, Nuovo Cimento 4 (1956) p.549.
29. G.R.Satchler, Nuclear Physics 77 (1966) p.481
30. A.de Shalit and I.Talmi, "Nuclear Shell Theory" Academic Press (1963).

Acknowledgements

I would like to express my appreciation to Mr.G.S.Mani for his assistance and encouragement during the course of work contained in this thesis. I would also like to thank the University of Manchester and in particular Professor J.C.Wilmott for providing me with the opportunity to undertake post graduate research.

I also wish to express my gratitude to the Science Research Council, Dr.T.G.Pickavance and Professor W.D.Allen for allowing me to use the facilities of the Rutherford High Energy Laboratory, in particular the IBM 360/75 computer and the Proton Linear Accelerator. I would like to acknowledge the considerable help and support given to me by all members of the P.L.A. group.

I would like to thank my colleagues, A.D.B.Dix and D.Jacques, J.G.Ballard and other members of the University of Manchester for their assistance in the collection and analysis of the experimental data. I wish to thank Mrs.M.Jones for her assistance in the preparation of the thesis.

The work in this thesis was carried out under a research studentship from the Science Research Council.